Pedro Manuel Duarte Gonçalves Amaro
M.Sc. in Physics Engineering

Study of Forbidden Transitions in Atomic Systems

A Thesis submitted for the co-tutelle degree of Doctor in Physics at Universidade Nova de Lisboa and Université Pierre et Marie Curie

Supervisor:	José Paulo dos Santos, Professor com Agregação, Faculdade de Ciência e Tecnologia da Universidade Nova de Lisboa
Supervisor:	Paul Indelicato, Directoire de le recherche, Université Pierre et Marie Curie, École Normale Supérieure, Laboratoire Kastler Brossel

Examination committee

Chair:	Prof. Maria Adelaide de Almeida Pedro de Jesus
Examiner:	Prof. Michel René Jean Godefroid
Examiner:	Prof. Joaquim Marques Ferreira dos Santos
Other Members:	Prof. Alfred Maquet
	Prof. José Paulo Moreira dos Santos
	Prof. Fernando António de Freitas Costa Parente

FACULDADE DE CIÊNCIAS E TECNOLOGIA
UNIVERSIDADE NOVA DE LISBOA

December 2011

THÈSE DE DOCTORAT EN COTUTELLE

Discipline : Physique

présentée par

Pedro Manuel Duarte Gonçalves AMARO

ÉTUDE DES TRANSITIONS INTERDITES DANS SYSTÈMES ATOMIQUES

---

pour obtenir le grade de Doctor de
Université Pierre et Marie Curie et
Universidade Nova de Lisboa

Dirigée par José Paulo dos Santos et Paul Indelicato

Soutenue le 20 december 2011 devant le jury composé de:

Maria Adelaide DE JESUS	Universidade Nova de Lisboa	président
Michel Godefroid	Université Libre de Bruxelles	examinateur
Joaquim dos Santos	Universidade de Coimbra	examinateur
Alfred Maquet	Université Pierre et Marie Curie	rapporteur
José Paulo dos Santos	Universidade Nova de Lisboa	directeur de thèse
Paul Indelicato	Université Pierre et Marie Curie	directeur de thèse
Fernando Parente	Universidade Nova de Lisboa	rapporteur

Study of Forbidden Transitions in Atomic Systems

Pedro Manuel Duarte Gonçalves Amaro

FCT-UNL UPMC

December 2011

Declaration

Study of Forbidden Transitions in Atomic Systems.

Dedicado a S.I.M. ☺.

Acknowledgements

I start my acknowledgements by expressing my deepest gratitude to my supervisor, Prof. J. P. Santos, who introduced me to the world of science and physics. During the last years, his suggestions and guidance were crucial for bringing my work to a good port.

Next, I give my sincere gratitude to my co-supervisor, Dr. P. Indelicato for accepting and welcoming me in the LKB at Paris. His corrections and critics are highly acknowledged. During my stay in Paris I had many discussions that helped me overcome the various problems of the lab and improved my understanding of the involved physics. Therefore, I express my gratitude to Dr. Alexandre Gumberidze, Dr. Alexandre Vallette, Dr. Csilla, Dr. Eric, Dr. Martino, and Dr. Sophie. Additionally, I would like to thank Prof. Andrey and Dr. Filippo for welcoming me in Heidelberg and for the nice scientific discussions.

Pelo ambiente amigável na FCT, quero agradecer aos meus colegas, Diana, Diogo, Mauro, Dr. Rodrigo, Rui, Sandro e Vitor.

Não me podia esqueçer das pessoas mais queridas. Agradeço à minha familia pela motivação e suporte. Aos meus sobrinhos, por toda a alegria e mimos que me dão. A minha mãe merece um obrigado especial. Com todos os problemas que o destino lhe apresentou, sempre me deu o maior apoio, atenção e amor. Pelos momentos felizes que construimos juntos, agradeço-te, Susana. Sem a vossa atenção e carinho não era possível concluir este trabalho.

To everyone who helped me performing this work, I give many thanks.

Institutional Acknowledgements

The work reported in this Thesis was performed in collaboration with:

- Centro de Física Atómica (CFA) group of Faculdade de Ciências e Tecnologia (FCT) of Universidade Nova de Lisboa (UNL).
- Métrologie des Systèmes Simples et tests Fondamentaux group of the Laboratoire Kastler Brossel (LKB). LKB is a unité mixte de recherche n° 8552 of the École Normale Supérieure ENS, Centre National de la Recherche Scientifique (CNRS) and Université Pierre et Marie Curie UPMC.
- APIX group in Heidelberg University.

Support for performing this Thesis was provided by:

- Acções Integradas Luso-Alemãs (Contract nº A-19/09)
- Fundação de Ciências e Tecnologia (FCT), contract SFRH/BD/37404/2007. FCT belongs to the Portuguese Ministry of Science, Technology and Superior Education (MCTES). Funds from Programa Operacional Potencial Humano (POPH/FSE) and European Union social fund.

Abstract

One active topic in Atomic Physics is the study of highly charged ions (HCI). These physical systems have a strong Coulomb field that provides a unique opportunity to investigate and validate relativistic, Quantum ElectroDynamics (QED), and many-body effects. Moreover, fundamental test on symmetries and parity violation gives clues to the physics beyond the Standard Model. Thus, nowadays, a primary goal of Atomic Physics is the existence of precise experimental data and accurate theoretical calculations for these systems.

In this thesis I focus on the investigation of forbidden radiative transitions in HCI. The main emphasis of this work is on atomic transitions, in which the selection rules forbids the emission of electric dipole photons. In this special type of radiative transition, the electron decays mainly through the emission of a single magnetic dipole photon, or two electric dipole photons. Both types of decay are investigated either experimentally or theoretically.

The two-photon decay is only theoretically investigated, using a full relativistic formalism, in HCI with one or two electrons. Several physical effects in the two photon decay, such as resonances, the Dirac's negative continuum or angular correlations are considered. Related with the decay, two-photon excitation is also investigated. According to these evaluations, I stress the importance of relativistic and nondipolar effects. Moreover, a new approach based on the B-polynomials basis set is employed on two-photon transitions.

The second part of the work is devoted to the precise measurement of transitions in highly charged Ar with two to four electrons. For that matter, I describe the technical features of a double crystal spectrometer used to perform those measurements in HCI for the first time. This kind of spectrometer is able to perform absolute and precise measurements with an accuracy never achieved in these systems, which enables a comparison with recent QED calculations. I describe a Monte-Carlo code developed with the purpose of studying several systematic errors, as well as testing the various methods of retrieving physical quantities from raw data. Finally, I present the first absolute 2 ppm measurements on HCI with this spectrometer, paying special attention on the forbidden magnetic dipole transition in He-like Ar.

Keywords: Forbidden transitions, HCI, QED, Multi-photon processes, ECRIS, X-ray spectroscopy, Monte-Carlo simulation.

Pacs : 32.70.Fw, 32.80.Wr, 31.15.-p, 31.30.Jv, 32.90.+a, 32.80.Rm, 31.10.+z, 32.30.Rj, 31.30.J-, 12.20.Fv.

Résumé

L'étude des ions fortement chargés connaît un fort développement en physique atomique. Ces systèmes physiques permettent d'étudier et valider la théorie de l'électrodynamique quantique en champ fort, et les méthodes du problème à n-corps relativiste. Par ailleurs, réaliser des tests de physique fondamentale sur les symétries, comme par exemple la violation de la parité peut donner des indications sur une éventuelle physique au-delà du Modèle Standard. Un des principaux objectifs de la physique atomique moderne est ainsi d'obtenir des données expérimentales précises et pour tester les calculs théoriques sur ces systèmes.

Cette thèse est consacrée à l'étude des transitions radiatives interdites dans les ions lourds multichargés. En particulier, j'ai étudié les transitions atomiques, dans lesquelles les règles de sélection interdisent les désexcitations de type dipolaire électrique. Dans ces transitions interdites, les états excités métastables se désexcitent par transition dipolaire magnétique, ou par des transitions à deux photons de type électrique dipolaire. Les deux types de désexcitation ont été étudiés expérimentalement et théoriquement dans les années récentes.

Dans ce travail, j'ai réalisé l'étude théorique de la désexcitation à deux photons pour des ions très chargés avec un ou deux électrons, en utilisant un formalisme relativiste. J'ai considéré plusieurs effets physiques dans l'étude de ces phénomènes, tels que celui des résonances, du continuum négatif de Dirac ou des corrélations angulaires. J'ai aussi étudié l'effet inverse, l'excitation à deux photons. Grâce à ces calculs j'ai pu mettre en évidence l'importance des effets relativistes et des multipoles d'ordre supérieur. Par ailleurs, j'ai développé une nouvelle approche numérique fondée sur l'utilisation d'une nouvelle famille de fonction de base appelée B-polynmes pour le calcul de la transition à deux photons.

La deuxième partie de la thèse est consacrée à la mesure précise d'énergies de transitions radiatives dans des ions Ar très chargés, avec de deux à quatre électrons. Dans cette partie, je décris les caractéristiques techniques d'un spectromètre à deux cristaux plans, que nous avons utilisé pour effectuer ces mesures, ce qui une première pour des ions très chargés. Ce type de spectromètre permet d'effectuer des mesures absolues avec une précision jamais atteinte dans ces systèmes, ce qui permet une comparaison avec des calculs de QED les plus récents. Je décris le code de simulation du spectromètre, basé sur la méthode de Monte-Carlo, que j'ai développé dans le but d'étudier plusieurs erreurs systématiques, ainsi que pour tester les différentes méthodes d'extraction de l'énergie et de la largeur des raies à partir des données brutes. Enfin, je présente les résultats des premières mesure absolue d'énergies de rayons X à 2.5 ppm sur des ions très chargés

d'argon avec ce spectromètre, en accordant une attention particulière à la transition interdite dipolaire magnétique dans l'argon à deux électrons.

Mots-clés: Transitions interdites, HCI, QED, Processus de multi-photon, ECRIS, Spectroscopie de rayons X, Simulation de Monte-Carlo.

List of Publications and Manuscripts

The work performed in this Thesis was published in the following list, which contains also manuscripts for publication.

- P. Amaro, J. P. Santos, F. Parente, A. Surzhykov, and P. Indelicato. *Resonance effects on the two-photon emission from hydrogenic ions*. Phys. Rev. A, 79(6):062504, 2009.

- A. Surzhykov, J. P. Santos, P. Amaro, and P. Indelicato. *Negative-continuum effects on the two-photon decay rates of hydrogenlike ions*. Phys. Rev. A, 80(5):052511, 2009.

- P. Amaro, A. Surzhykov, F. Parente, P. Indelicato, and J. P. Santos. *Calculation of two-photon decay rates of hydrogen-like ions by using B-polynomials*. J. Phys. A: Math. Theor., 44(24):245302, 2011.

- A. Surzhykov, P. Indelicato, J. P. Santos, P. Amaro, and S. Fritzsche. *Two-photon absorption of few-electron heavy ions*. Phys. Rev. A, 84(2):022511, 2011.

- P. Amaro, F. Fratini, S. Fritzsche, P. Indelicato, J. P. Santos and A. Surzhykov. *Parametrization of the angular and polarization in two-photon decays of hydrogen-like ions*. Manuscript for publication.

- P. Amaro, S. Schlesser, M. Guerra, E. O. Le Bigot, J. M. Isac, P. Travers, J. P. Santos, C. I. Szabo, A. Gumberidze, and P. Indelicato, *Absolute measurement of the "relativistic M1" transition energy in heliumlike argon*. Submitted to Physical Review Letter.

- P. Amaro, C.I. Szabo, S. Schlesser, A. Gumberidze, E.O. Le Bigot, M. Guerra, J. P. Santos, and P. Indelicato, *A double crystal spectrometer and ECRIS combination for precise and absolute measurements of X-ray energies from HCI*. Manuscript for publication.

List of Contents

List of Figures

LIST OF FIGURES

List of Tables

Nomenclature

Vector notations

- Symbols in bold represents vectors, e.g., $\boldsymbol{p}$ in pag. 12.

- Bold symbols with a circumflex hat are unitary vectors, e.g., $\hat{\boldsymbol{k}}_{\boldsymbol{j}} = \frac{\boldsymbol{k_j}}{|k_j|}$ in pag. 23.

List of Variables

The following list of the *most* used variables are sorted by order of appearance. A given symbol can have a different meaning if defined in a particular part of the text not related with the global definition.

Z	Atomic number	Pag. 1
$n_{i(f)}$	Initial (final) quantum principal number in one-electron orbitals	Pag. 7
$j_{i(f)}$	Initial (final) angular momentum in one-electron orbitals	Pag. 7
c	Light speed	Pag. 12
$\boldsymbol{p}$	Momentum operator	Pag. 12
$\boldsymbol{\alpha}$	Dirac Matrices	Pag. 12
$\boldsymbol{A}$	Vector potencial	Pag. 13
H_D	One electron Dirac hamiltonian	Pag. 13
$V(r)$	Nuclear potencial	Pag. 13
Y_{lm}	Spherical harmonics	Pag. 14
$l_{i(f)}$	Initial(final) orbital momentum in one-electron orbitals	Pag. 14
κ	Quantum number of the K operator	Pag. 15

$P_{n\kappa}$	Large radial component	Pag. 15
$Q_{n\kappa}$	Small radial component	Pag. 15
α	Fine structure	Pag. 16
G	*Gauge* parameter	Pag. 23
$\hat{\boldsymbol{e}}$	Polarization vector	Pag. 23
$\boldsymbol{k}$	Wavenumber vector	Pag. 23
L	Order of the Multipole	Pag. 24
$\boldsymbol{r}$	Vector position	Pag. 24
j_L	Spherical Bessel function	Pag. 25
ω	Frequency of a photon	Pag. 27
$J_{i(f)}$	Total initial (final) angular momentum	Pag. 27
$L_{i(f)}$	Total initial (final)orbital angular momentum	Pag. 28
$S^{j}(2,1)$	Reduced two-photon matrix elements	Pag. 28
$\overline{W}$	Two-photon decay rate	Pag. 29
R	Radius of the region defining the atom in numerical methods	Pag. 31
W^{C}	Two-photon angular correlation	Pag. 41
P_L	Degree of linear polarization	Pag. 43
α_0	Two-photon absorption parameter	Pag. 51
D^{L}_{Mq}	Wigner rotation matrix	Pag. 52
λ	Photon wavelength	Pag. 103
θ_{B}	Bragg angle	Pag. 103
d	Inter-planar distance	Pag. 103
θ_{C}	Angle between the optical center and crystal surface	Pag. 110
θ_{F}	First crystal position angle	Pag. 110
θ_{T}	Angle between the table axis and the X-ray source optical center	Pag. 110
$P_{\pm}$	Antiparallel (+) or parallel (-) rocking curve	Pag. 121

List of Acronyms and Abbreviations

The list of the most used acronyms and abbreviations follows the order of appearance.

HCI	Highly Charged Ions	Pag. 1
QED	Quantum ElectroDynamics	Pag. 1
CI	Configuration Interaction	Pag. 1
RMBPT	Relativistic Many Body Perturbation Theory	Pag. 2
MCDF	MultiConfigurational Dirac-Fock	Pag. 2
DCS	Double Crystal Spectrometer	Pag. 4
HFI	HyperFine Interaction	Pag. 4
CMB	Cosmic Microwave Background	Pag. 7
PNC	Parity Non-Conservation	Pag. 8
LAPACK	Linear Algebra PACKage	Pag. 32
LPA	Line Profile Approach	Pag. 44
TLA	Two-Loop self-energy Approach	Pag. 44
ECRIS	Electron Cyclotron Resonance Ion Sources	Pag. 101
FWHM	Full Width at Half Maximum	Pag. 105
XOP	X-ray Oriented Programs	Pag. 115

Chapter 1

Forbidden Transitions

In atomic physics, a radiative *forbidden* transition is an electronic transition between two states that is not permitted by electric dipole selection rules, i.e., it cannot occur by radiative emission of an electric dipole photon ($E1$). In this case, the electron decays by the next allowed multipole (magnetic dipole $M1$ or electric quadropole $E2$), or by a two-photon decay ($2E1$). On the other hand, if the radiative emission of an electric dipole photon is possible by selection rules, then the transition is called *allowed*. Another type of transition that can be classified as forbidden is an induced electric dipole transition, which only occurs when the atom is influenced by a weak perturbation, such as an applied electric field, or a nuclear magnetic moment.

Forbidden transitions were first considered in a classical paper by *Breit* and *Teller* [1], where it is shown that the $2s$ state of hydrogen and the $1s2s\ ^1\mathrm{S}_0$ state of helium decay primarily by two-photon emission ($2E1$), while the $1s2s\ ^3\mathrm{S}_1$ state of helium decays by a magnetic dipole transition ($M1$). These forbidden transitions have very low transition rates in neutral or few-ionized atoms compared with the rates of the allowed ones. A state that has a forbidden transition as the main decay channel, is known as a metastable state due to it's long lifetime. However, for ions with few electrons, the decay rate of allowed transitions scales approximately with the atomic number as Z^4 compared with the scale $Z^6 - Z^{10}$ of these forbidden transitions, which makes them comparable for highly charged ions (HCI).

In Fig. 1.1 it is shown an overview of allowed and forbidden transitions between energy levels in H-like and He-like ions. In the case of He-like ions, the latest values of the energy levels are given in Refs. [2, 3], while for H-like the latest values can be found in Ref. [4]. These energy levels were obtained considering both relativistic, quantum electrodynamics (QED) and many-body effects (for He-like ones).

The evaluation of the many-body effects, or the electron-correlation, is performed using the relativistic configuration interaction (CI) method [5], the relativistic many body perturbation theory

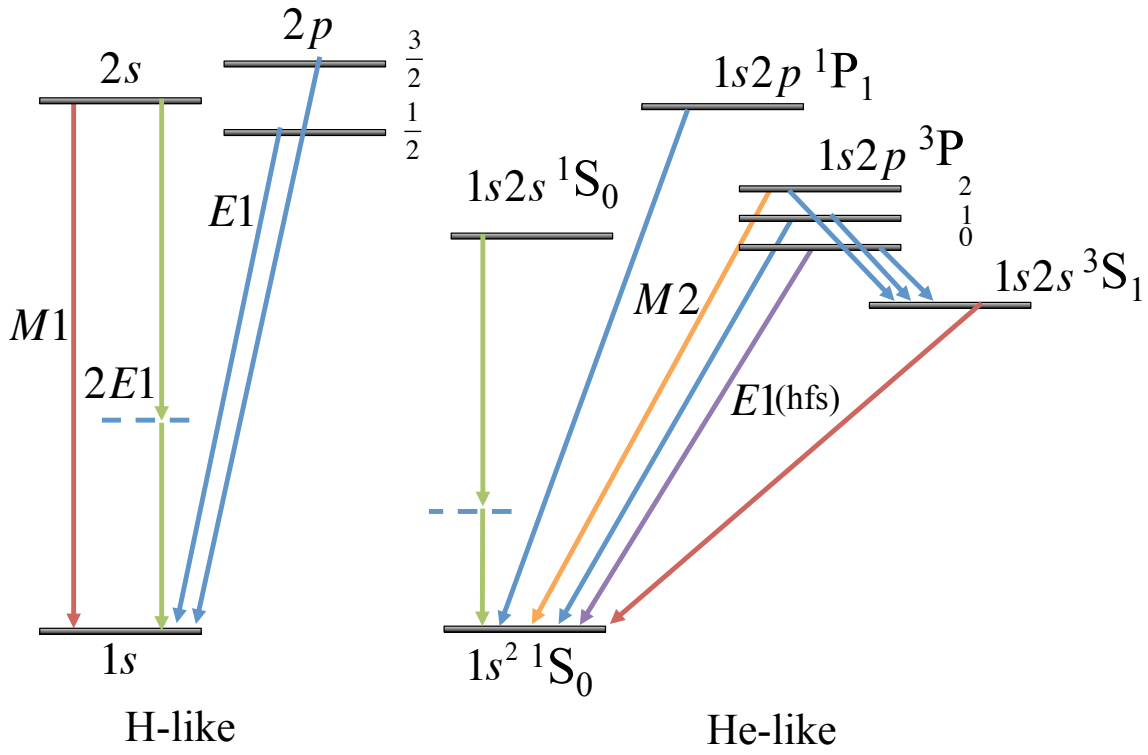

Figure 1.1: Allowed and forbidden transitions in H-and He-like ions - Each arrow represents a transition between two states. Only initial orbital states lower than three ($n_i < 3$). On each transition is labeled the most dominant decay channel. In case of the transition $2s \rightarrow 1s$ the $2E1$ is dominant for lower values of atomic number, while the $M1$ is dominant for higher Z's. The multipole terms have the colors according to: blue- $E1$; red- $M1$; green- $2E1$; orange- $M2$; purple- E1 (HFI). If the dominant multipole term of the transition is an $E1$ then the transition is allowed, otherwise is forbidden.

method (RMBPT) [6], or the multiconfigurational Dirac- Fock (MCDF) method [7, 8, 9]. These methods share the same main features: their treatment is based on the no-pair Hamiltonian and the electron correlation is taken into account within the Breit approximation. Exact relativistic effects are provided by using the Dirac equation for each electron orbital (cf. Sec. 3.1). QED theory deals with energy corrections for several physical quantum fluctuations (cf. Sec. 3.2).

The $2s$ state in H-like ions decays by a magnetic dipole transition ($M1$) or by a two electric dipole transition ($2E1$) to the ground state. These decay rates scale approximately as $2.50\times10^{-6}Z^{10}$ s^{-1} [10] and $8.226Z^{6}$ s^{-1} [1], respectively. For lower values of Z, the $2E1$ rate dominates the $M1$ rate, they are equal at approximately $Z = 41$ [11, 12], and for higher values of Z the main decay channel is the $M1$.

The transition rate of the $M1$ multipole can only be calculated within Dirac theory since in non-relativistic theory this calculation reduces to the orthogonally condition of wavefunctions. That's why this multipole is refereed as the relativistic induced $M1$. There is also a non-relativistic $M1$ due to a transition between hyperfine levels in hydrogen or deuterium [13].

The transition $1s2s\ ^1\mathrm{S}_0 \rightarrow 1\mathrm{s}^2\ ^1\mathrm{S}_0$ can also proceed by a two-photon decay. Moreover, no single photon decay is possible due to selection rules (cf. Sec. 3.3.1), which forbids $J_i = 0 \rightarrow J_f = 0$ single-photon transitions. Therefore, the two-photon decay is necessarily the main decay channel, which is similar to the H-like case. Since the $1s$ electron does not participate in the transition but acts as a spectator, it shields the nuclear charge for the active electron. This decay scales approximately as $16.45 \times (Z - \sigma)^6\ \mathrm{s}^{-1}$, with σ being a shielding parameter. Accurate values of this decay and the most recent measurement can be found in Refs. [14, 15].

The $1s2s\ ^3\mathrm{S}_1$ state also exhibits a $M1$ decay to the $1s^2\ ^1\mathrm{S}_0$ ground state, as first established from astrophysical observations [16]. *Gabriel* and *Jordan* emphasize the importance of this decay, by relating its decay rate with the electron density in the solar corona [17]. This transition rate scales approximately with Z as $1.66 \times 10^{-6} \times Z^{10}\ \mathrm{s}^{-1}$ and precise values can be found in Ref. [18, 19, 20].

The states $1s2p\ ^3\mathrm{P}_{2,1,0}$ decay by an $E1$ transition to the $1s2s\ ^3\mathrm{S}_1$. The state $1s2p\ ^3\mathrm{P}_2$ also makes a $M2$ forbidden transition to the ground state, as pointed out by *Mizushima* [21]. These calculations were extended by *Garstang* to spectral lines of interest in the de-excitation of atoms in the solar corona [22]. This rate scales as Z^8, and already at He-like Ar ($Z = 18$) the $M2$ and $E1$ decay modes are equally probable. This is a rare circumstance in atomic physics, where a $M2$ decay dominates over an $E1$ decay channel. Because of the spin-orbit interaction the wave functions of the $1s2p\ ^3\mathrm{P}_1$ and $1s2p\ ^1\mathrm{P}_1$ are mixed, opening the spin-forbidden $E1$ decay $1s2p\ ^3\mathrm{P}_1 \rightarrow 1\mathrm{s}^2\ ^1\mathrm{S}_0$. This transition is also useful in the determination of the electron densities in the solar corona [17]. When the nuclear spin I differs from zero and the total angular momentum, F ($F = J + I$), is equal to I for the state $1s2s\ ^3\mathrm{P}_0$, then the latter state mixes with the $1s2p\ ^3\mathrm{P}_1$. Thus, $E1$ transitions of $1s2p\ ^3\mathrm{P}_0 \rightarrow 1\mathrm{s}^2\ ^1\mathrm{S}_0$ are possible due to hyperfine interaction (HFI). This HFI significantly shortens the $1s2p\ ^3\mathrm{P}_0$ lifetime [23, 24].

A more detailed description of forbidden transitions can be found in the classical review of *Marrus* and *Mohr* [25], while a recent review related with forbidden and allowed transition lifetimes was reported in Ref. [26].

1. FORBIDDEN TRANSITIONS

Having made a general description of several forbidden transitions in H- and He-like ions we now describe the objective and organization of this Thesis.

- Part I is devoted to the theoretical evaluation of two-photon transitions in H-like ions, which have higher transition rates in forbidden transitions. Several physical effects are analyzed, being stressed the importance of relativistic and nondipole effects in this kind of decay channel.
- In Part II I describe the experimental work done to perform an energy measurement of a forbidden transition in He-like Ar. Due to its narrow natural width, it is possible, not only to increase further the accuracy of the measurement, but also to study the response function of the used instrument. We used a double crystal spectrometer (DCS), which was never used with HCI, nor forbidden transitions. This instrument provides accurate and absolute measurements of X-ray energies, thus making a reference-free comparison with *state of art* QED and many-body theory calculations reported in the literature.

Part I

Two-Photon Transitions

Chapter 2

Introduction to Two-Photon Transitions

Somewhat analogous to single-photon processes, two-photon emission can be spontaneous or stimulated, whereas two-photon absorption is only stimulated. However, since each photon carries one unit of angular momentum in the dipolar approximation, certain transitions between atomic energy levels, forbidden in single-photon processes, are allowed in two-photon processes. Another important distinction lies in the fact that the spectrum of spontaneous two-photon processes is continuous unlike the spectrum in the single-photon processes. A continuous spectrum is possible because energy conservation requires only that the sum of both photon energies equals the energy of the transition. For the

$$(n_i, j_i) \rightarrow \left(n_f, j_f\right) + \omega_1 + \omega_2 \tag{2.1}$$

transition in H-like ions, where (n_i, j_i) and $\left(n_f, j_f\right)$ denote the quantum numbers that identify the initial and final states, respectively, and ω_1 and ω_2 are the energies of each photon, the conservation of the energy states leads to the condition

$$E_f - E_i = \omega_1 + \omega_2 \, , \tag{2.2}$$

where E_i and E_f are the energies of the initial and final states, respectively.

Two-photon emission decay rates in hydrogen and H-like ions are under investigation since the seminal works of *Goeppert-Mayer* and of *Breit* and *Teller* [1, 27]. The early interest on these transitions from metastable states of hydrogen and helium steamed mainly from astrophysics [28, 29, 30]. Hydrogen recombination is the main process responsible for the thermal fluctuations of the cosmic microwave background (CMB), which is partially controlled by two-photon emission from the $2s_{1/2}$ state. More precisely, during the early universe, the $2p - 1s$ transition, being reabsorbed, reemitted, and again reabsorbed, did not allow the radiation to escape from the interaction with matter. When the universe density became lower, the $2s \rightarrow 1s$ transition presents one of the main channels for the

radiation escaping from the interaction with matter. Recently, *Chluba* and *Sunyaev* [31] revived the astrophysics interest in two-photon transitions [1].

Most of todays two-photon studies are focused on the determination of fundamental constants, such as the Rydberg constant [32, 33], measurement of the Lamb-shift [33, 34], in testing Bell's inequality [35, 36], in molecular spectroscopy [37], tissue imaging [38] and protein structure analysis [39].

Another interest in two-photon transitions relies on the study of parity non-conservation (PNC) in H-like and He-like ions [40, 41, 42, 43, 44, 45, 46]. Parity non-conservation or parity violation in an atom or ion, follows from the *Standard Model*, which describes, among others, the electroweak interaction between leptons and nucleons. This effect was predicted by *Weinberg* and *Salam* [47, 48], and first-time evaluated for the case of atoms or ions by *M. A. Bouchiat* and *C. C. Bouchiat* [40, 41]. PNC consists in states of different parity being mixed due to the interaction of the electron and the nucleus, mediated by the exchange of a virtual neutral massive particle, called Z-boson. Therefore, the mixed states have no define parity. The level of mixing is very small and depends on two factors: the amount of overlap of the electron wavefunction with the nuclear wavefunction and the energy difference between two adjacent states of opposite parity. For example, the two-photon $E1M1$ $2p_{1/2} \rightarrow 1s$ transition in H-like ions plays the role of the basic transition, while the parity-violating $2E1$ transition becomes admixed by PNC electroweak interaction [42]. Moreover, in recent years, two-photon transitions in heavy He-ions have attracted much attention as a promising tool for studying atomic PNC effects [45, 46]. In He-like heavy ions the overleap between the electron and nuclear wavefunctions is a sizable fraction of the nucleus and the two levels $1s2p\ ^3\mathrm{P}_0$ and $1s2s\ ^1\mathrm{S}_0$ happens to be almost degenerate for $Z = 64$ (gadolinium) and 90 (thorium), thus enhancing the PNC effects significantly [43].

The possibility of forbidden two photon transition, $J_i = 1 \rightarrow J_f = 0$ with two equal energy sharing being induced by HFI was considered as a possible route to measure violations in Bose-Einstein statistics [49, 50].

The two-photon spectral distribution of the $2s \rightarrow 1s$ transition in H-like ions has recently been used for precise efficiency calibration of solid-state X-ray detector as it has a known shape for a large distribution of energies [51].

From a theoretical point of view, the $2s \rightarrow 1s$ two-photon transition rate in H-like ions has been calculated and discussed many times using different approaches. An historical overview from both theoretical and experimental point of view can be found in the article by *Santos et al.* [12]. In that work, B-splines basis set techniques were applied to the evaluation of two-photon amplitudes based on the Dirac equation and were discussed relativistic and non dipolar effects. Meanwhile, a similar

[1] A review of the Cosmological Recombination Epoch and the role of the two-photon decay can be visualized in this URL link (online version).

work was performed by *Szymanowski et al*. based in the Sturmian expansion of the Coulomb-Dirac Green's function [52].

In the non-relativistic framework, other transitions were studied, for instance, by *Tung et al.* [53] and *Klarsfeld* [54], who performed calculations for transitions from an arbitrary state (n_i, l_i) to an arbitrary state (n_f, l_f). *Florescu et al.* [55] developed a theory for two-photon transitions in H-like systems, including the $3s \rightarrow 1s$ and $3d \rightarrow 1s$ transitions.

The first relativistic inner-shell calculation of two-photon for bound states was made by *Mu* and *Crasemann* [56] followed by *Tong et al.* [57]. *Surzhykov et al.* [58] performed another relativistic calculation to study the angular correlations in the two-photon decay of H-like ions.

Recently, *Labzowsky et al*. [59] evaluated the $2E1$ contribution for the $2s \rightarrow 1s$ transition and the $E1M1$ and $E1E2$ contributions for the $2p_{1/2} \rightarrow 1s$ transition. They derived an expression similar to the one obtained by *Goldman* and *Drake* [60] in the QED framework. Also in this framework, *Nganso et al.* [61] carried out the treatment of the S matrix for bound-bound transitions.

The $1s2s\ ^1\mathrm{S}_0 \rightarrow 1\mathrm{s}^2\ ^1\mathrm{S}_0$ two-photon decay in He-like Tin was recently measured by *Trotsenko et al*. [15] using a novel method of populating the $1s2s\ ^1\mathrm{S}_0$ based in relativistic collisions of Li-like projectiles with low-density gas. The high statistics and accuracy inherent to the method enabled the observation of relativistic effects for the first time.

Also this two-photon decay rate in He-like have been recently calculated by *Volotka et al*. [62] with the inter-electric interaction evaluated within the QED framework of the two-time Green function.

The use of polarization correlations properties of the emitted two-photons was recently considered by *Fratini et al*. as a route for measuring atomic PNC and studying entanglement correlations [63, 64].

As for two-photon absorption or excitation, a series of highly accurate measurements has been performed on two-photon excitation of neutral hydrogen and deuterium atoms [33, 65, 66, 67], which reveal QED effects and determine the Rydberg constant and Lamb-shift with a record accuracy. Apart from hydrogenic systems, studies on two-photon excitation of low- and medium-Z neutral atoms have been reported in Refs. [68, 69, 70, 71]. These studies were interesting not only for improving our understanding of the electronic structure of complex atoms, but also for the diagnostics of laboratory plasmas. In contrast to neutral hydrogen and rather light atoms, less attention on studying two-photon absorption processes has been paid in the past to medium- and high-Z atoms and ions. With the help of modern sources of coherent-vacuum ultraviolet and x-ray radiation, however, such experiments become feasible today. They may provide valuable insight into relativistic, many-body, and QED phenomena in strong electromagnetic fields and, hence, may serve as a complementary technique to the well-established X-ray absorption spectroscopy. While two-photon absorption was only studied

in the infrared, visible, and ultraviolet regime, recently, it was observed for the first time by *Doumy et al*. in the X-ray regime [72] using an highly intense X-ray Free-Electron Laser (XFEL).

Recent technical advances in polarization and position-sensitive detectors have opened up the possibility of investigating angular and polarization properties of the radiation emitted in atomic decays [73, 74]. It is foreseen measurements of two-photon angular correlations will be therefore performed, within the near future, at GSI in Darmstadt [75, 76], which will test quantum correlations of the photon pair [63] and PNC in He-like ions [64].

After I made an introduction to this kind of transition in atomic physics, the rest of this part is organized as follows: in Chapter 3 we give a review of the background theory involving in a two–photon emission, which also includes numerical methods necessary for the evaluation of the reduced two-photon amplitudes. In Chapter 4 we present the results obtained in this work. Several physical effects in a two-photon decay, such as resonances, the negative continuum contribution and angular correlations were evaluated and discussed in this chapter. Two-photon absorption was also considered. Moreover, a novel basis-set was introduced for calculating two-photon transitions. The conclusions are given in Chapter 5.

Chapter 3

Theory of Two-photon Transition

Since all the evaluations in this work were done in a relativistic framework of the Dirac equation, this equation is presented in Sec. 3.1 along with a description of the relativistic effects of an electron in an HCI nucleus. Then, we make a description of the formalism necessary for deducing two-photon properties in Sec. 3.2 and apply it to the case of spontaneous two-photon emission in Sec. 3.3.

Afterwards, we describe some numerical methods for evaluating the reduced two-photon amplitudes in Sec. 3.4. Emphasis will be done to the *finite basis set* since it was the method used in the work. Along with the well-stablished *B-splines* basis set, we introduce a novel basis set, so-called *B-polynomials*. The method presented in this section was published in Ref. [77].

The method of *finite basis set* enables the separation of the *negative-energy* intermediate states from the summation over the Dirac spectrum, which is present in second order perturbation expressions, such as two-photon decay rates. Therefore, in Sec. 3.5, special attention is paid to the effects on the two-photon transition rates arising from removing these states. Expressions of semi-relativistic estimates of the negative continuum contribution, published in Ref. [78], are presented in this section.

The angular correlation between the two photons are consider in Sec. 3.6. In particular, the expressions for the angular correlation are expanded in terms of $\cos\theta$-polynomials, whose coefficients depend on the atomic number and the energy sharing of the photon pair. The work presented in this section is in manuscript form for publication.

In Sec. 3.2 we consider the physical changes between *non-resonant* and *resonant* transitions in the two-photon emission. While the former type has no real intermediate states between the final and initial state of the decay, like the $2s_{1/2} \rightarrow 1s_{1/2}$ transition, in the resonant transitions, the two-photon transition has also a decay channel related with the cascade one-photon de-excitation process. The theoretical discussion was published in Ref. [79].

In Sec. 3.8 we describe the necessary expressions for evaluating two-photon excitation, also

known as two-photon absorption. The theoretical description of this section is given in Ref. [80].

In all the theoretical description presented in this chapter, it was used atomic units. A brief description of those units can be found in *Santos's* Thesis [81].

3.1 One electron Dirac equation

Relativistic Quantum Mechanics can be found in several textbooks [82, 83, 84, 85]. In this section, we restrict to a brief description and further details can be traced back to the references already mentioned.

3.1.1 Free electron

The relativistic invariant equation that describes the dynamic of a single electron, was obtained by *Dirac* in 1928 [86, 87]. At that time, *Dirac* was searching for a relativistic invariant wave equation of the Schrödinger form with a positive-defined probability density. Back then, there were doubts concerning the Klein-Gordon equation [88, 89], which were obtained in a similar way of the Schrödinger equation, setting the Hamiltonian H of a free electron, as

$$H^2\psi = (c^4 + c^2\boldsymbol{p}\cdot\boldsymbol{p})\psi = -\frac{\partial^2\psi}{\partial t^2} \ . \tag{3.1}$$

Here $\boldsymbol{p} = -i\boldsymbol{\nabla}$ is the momentum operator and c is the light speed (in atomic units $c = 137.03599911$ [90]). Such approach did not yield a satisfactory probability density, since it can have both positive and negative values. A reason of this fact is that the Klein-Gordon equation is of second order in time. *Dirac* proposed that the Schrödinger-like equation of the free electron motion, which is linear in time, should also be linear in the spatial components. Hence, Dirac proposed that the dynamic of a single free electron obeys the equation

$$i\frac{\partial\psi}{\partial t} = (-ic\ \boldsymbol{\alpha}\cdot\boldsymbol{\nabla} + c^2\beta)\psi \ . \tag{3.2}$$

The coefficients $\boldsymbol{\alpha}$ and β must not be simple numbers, otherwise these coefficients define a direction for the partial derivatives and this equation will not be invariant with respect to spatial rotations. To overcome this problem, those coefficients can be defined as square matrices, and hence, the wave-function as column matrices. By doing so, Eq. (3.2) becomes a system of linear first-order differential equations. The exact expressions of these matrices are obtained from the restriction that the free electron must have a relativistic energy. This is equivalent to consider each component of the matrix ψ a solution of the free-electron Klein-Gordon equation (Eq. (3.1)). It can be proved that this consideration is equivalent to impose a set of commutation relations that those matrices must follow [83].

It also restricts the dimension of those matrices to an even number greater than three. One possible representation, among others, is given by

$$\boldsymbol{\alpha} = \begin{pmatrix} 0 & \boldsymbol{\sigma} \\ \boldsymbol{\sigma} & 0 \end{pmatrix}, \quad \beta = \begin{pmatrix} I & 0 \\ 0 & -I \end{pmatrix}, \tag{3.3}$$

where $\boldsymbol{\alpha}$ and β are known as Dirac matrices. The cartesian components of $\boldsymbol{\sigma}$ are the Pauli matrices and I is the unitary matrix given by

$$\begin{aligned} \sigma_x &= \begin{pmatrix} 0 & 1 \\ 1 & 0 \end{pmatrix}, \quad \sigma_y = \begin{pmatrix} 0 & -i \\ i & 0 \end{pmatrix}, \\ \sigma_z &= \begin{pmatrix} 1 & 0 \\ 0 & -1 \end{pmatrix}, \quad I = \begin{pmatrix} 1 & 0 \\ 0 & 1 \end{pmatrix}. \end{aligned} \tag{3.4}$$

By doing so, it can also be demonstrate that the particle density, $\psi^\dagger\psi$, follows the continuity equation and Eq. (3.2) is invariant to a Lorentzian transformation [83].

3.1.2 One electron in a nucleus potencial

In case the electron being immersed in an external electromagnetic field, the electromagnetic interaction is included in the Dirac equation using the *minimal coupling* [91],

$$\begin{aligned} E &\rightarrow E - V \ , \\ \boldsymbol{p} &\rightarrow \boldsymbol{p} - \frac{\boldsymbol{A}}{c} \ . \end{aligned} \tag{3.5}$$

This substitution assures not only *gauge* invariance of the Maxwell equations, but also a Lorentz force acting on the electron. E is the free electron energy, V is a scalar potential and $\boldsymbol{A}$ is the vector potential. The *gauge* transformation is defined by

$$\mathbf{A}'(\mathbf{r}, t) \rightarrow \mathbf{A}(\mathbf{r}, t) + \nabla\vartheta(\mathbf{r}, t) \ , \tag{3.6}$$

and is a consequence of charge conservation. ϑ is an arbitrary function, that keeps the electrical and magnetic fields invariant to that transformation.

If the external electromagnetic field is due to the nucleus of an atom then an additional term, $V(r)$, is included next to $c^2\beta$ in Eq. (3.2), i.e., $\boldsymbol{A} = \mathbf{0}$ and $V = V(r)$.

$$i\frac{\partial\psi}{\partial t} = \left[-ic\ \boldsymbol{\alpha}\cdot\boldsymbol{\nabla} + c^2\beta + V(r)\right]\psi = H_{\mathrm{D}}\psi \ . \tag{3.7}$$

The term $V(r)$ is the radial potential of the nucleus and is given according to the nucleus model used. In case of a point nucleus model, it is given by the well-known expression of a point-like source $V^{\mathrm{p}}(r) = -Z/r$, where r is the distance to the nucleus and Z the atomic number or the number of protons. The next upgrade of this simple model is considering the nucleus as a uniform distribution of charges. Thus, the nuclear potential is given by

$$V^{\mathrm{U}}(r) = \begin{cases} \frac{Z}{2R_{\mathrm{N}}}\left[\left(\frac{r}{R_{\mathrm{N}}}\right)^2 - 3\right] & r \leq R_{\mathrm{N}} \\ -\frac{Z}{r} & r > R_{\mathrm{N}} \end{cases} , \tag{3.8}$$

where R_{N} is the nucleus radius given by

$$R_N = 2.2677 \times 10^{-5}\sqrt[3]{A}\,, \tag{3.9}$$

where in this case, A in Eq. (3.9) is the atomic mass number. Other charge density of the nucleus can be considered, for instance a Fermi distribution [4]. All the evaluations done in this work were done using a nucleus uniform distribution (Eq. (3.8)) and a point nucleus was used only for comparison with analytical results based in that approximation.

Those spherical potentials (e.g. Eq. (3.8)) does not depend on time, so we can use the stationary version, $H_{\mathrm{D}}\psi = E\psi$. Because of the spherical symmetry of the potential, the square of the total angular momentum, $\boldsymbol{j} = \boldsymbol{l} + \boldsymbol{s}$, and the relativist parity operator, $\Pi = e^{i\varphi}\beta(\boldsymbol{r} \to -\boldsymbol{r})$ commutes with Dirac Hamiltonian. Thus, as in the case of the non-relativistic Schrödinger equation, the wavefunction consists of a product of the angular part, which depends on the direction of the vector position, $\hat{\boldsymbol{r}}$, and a radial part that depends on $r = |\boldsymbol{r}|$. Furthermore, the angular part is an eigenfunction of the $\boldsymbol{j}^2$, j_z and Π. Following the angular quantum rules of combining two angular momentum operators to form a third, the spherical spinor is made by combining spherical harmonics, $Y_{l,m}$, which are eigenfunctions of $\boldsymbol{l}^2$ and l_z, and spinors, which are eigenfunctions of $\boldsymbol{s}^2$ and s_z. Those spherical spinors are defined by [92]

$$\Omega_{jlm} = \sum_{m_s=-1/2}^{m_s=1/2} \left\langle l\; m - m_s, \frac{1}{2}\; m_s \middle| j\; m \right\rangle Y_{l,m-m_s}(\hat{\boldsymbol{r}})\chi_{m_s}\,. \tag{3.10}$$

Here the two spinor χ_{m_s} ($m_s = 1/2,\ -1/2$), are eigenfunctions of the spin operator $\boldsymbol{s}^2 = \boldsymbol{\sigma}^2/4$ and $S_z = \sigma_z/2$. They are given explicitly by

$$\chi_{\frac{1}{2}} = \begin{pmatrix} 1 \\ 0 \end{pmatrix}, \quad \chi_{-\frac{1}{2}} = \begin{pmatrix} 0 \\ 1 \end{pmatrix}. \tag{3.11}$$

The eigenvalues equations, already refereed for the spherical spinor, are given by

$$\begin{aligned} \boldsymbol{j}^2\Omega_{jlm} &= j(j+1)\Omega_{jlm}\,, \quad j_z\Omega_{jlm} = m\Omega_{jlm}\,, \\ \boldsymbol{l}^2\Omega_{jlm} &= l(l+1)\Omega_{jlm}\,, \quad \boldsymbol{s}^2\Omega_{jlm} = \tfrac{3}{4}\Omega_{jlm}\,. \end{aligned} \tag{3.12}$$

The spherical spinors are also eigenfunctions of $K = 1 + \boldsymbol{\sigma} \cdot \boldsymbol{L}$ and Π, with eigenvalues

$$\kappa = \begin{cases} l & \text{if} \quad j = l - 1/2 \\ -(l+1) & \text{if} \quad j = l + 1/2 \end{cases} , \tag{3.13}$$

and $(-1)^l$, respectively. The values in Eq. (3.13) can be summarized as $\kappa = \mp(j - 1/2)$ for $j = l \pm 1/2$. The values of κ determine both j and l. Consequently, a more compact notation $\Omega_{jlm} = \Omega_{\kappa m}$ can be used. By making the following ansatz for the stationary Dirac equation,

$$\psi = \frac{1}{r} \begin{pmatrix} iP_\kappa(r)\Omega_{\kappa m} \\ Q_\kappa(r)\Omega_{-\kappa m} \end{pmatrix} , \tag{3.14}$$

we may eliminate the angular part in both sides of the equation and obtaining the differential equations for the radial functions $P_\kappa(r)$ and $Q_\kappa(r)$,

$$\begin{bmatrix} V(r) & c\left(\frac{d}{dr} - \frac{\kappa}{r}\right) \\ -c\left(\frac{d}{dr} + \frac{\kappa}{r}\right) & V(r) - 2c^2 \end{bmatrix} \begin{bmatrix} P_\kappa(r) \\ Q_\kappa(r) \end{bmatrix} = (E_{n\kappa} - c^2) \begin{bmatrix} P_\kappa(r) \\ Q_\kappa(r) \end{bmatrix} . \tag{3.15}$$

$V(r)$ can be any spherical potential and $\epsilon_\kappa = E_\kappa - c^2$ is defined in order to compare with non-relativistic energies. In fact, by expanding Eq. (3.15) in powers of $1/c$ and by retaining only the first term, we obtain the radial Schrödinger equation applied to $P_\kappa(r)$ with $\kappa(\kappa + 1) = l(l + 1)$ and

$$Q_\kappa(r) \simeq -\frac{1}{2c}\left(\frac{d}{dr} + \frac{\kappa}{r}\right) P_\kappa(r) . \tag{3.16}$$

Therefore, since $P_\kappa(r)$ and $Q_\kappa(r)$ are equal to the non-relativistic radial wavefunction and zero for $c \to \infty$, respectively, they are called the large and small components. If in some numerical method, the large and small components are restricted by Eq. (3.16), they are refereed to be *kinetically balanced*. The normalization condition of the wavefunctions for the large and small components is given by

$$\int_0^\infty \left[P_{n\kappa}(r)^2 + Q_{n\kappa}(r)^2\right] dr = 1 . \tag{3.17}$$

The spectrum of the eigenvalues in Eq. (3.15) consists of a discrete spectrum of bound states that covers the energy range $-2c^2 < \epsilon_\kappa < 0$ and a continuous spectrum for $\epsilon_\kappa > 0$, which corresponds to an oscillating wave function at large distance from the origin in complete analogy with the non-relativistic case. There is also a second continuous spectrum characteristic of the relativistic theory for $\epsilon_\kappa < -2c^2$. The notion of a negative energy lead to a physical dilemma: if there is an electron in some bound state, which its energy is in agreement with experiments, why does it not lose energy by successive decay and continuos emission? If so, this would make the atom unstable, and, furthermore, this kind of decay was never observed. The first interpretation of this negative spectrum was provided

Orbital	$1s_{\frac{1}{2}}$	$2s_{\frac{1}{2}}$	$2p_{\frac{1}{2}}$	$2p_{\frac{3}{2}}$	$3s_{\frac{1}{2}}$	$3p_{\frac{1}{2}}$	$3p_{\frac{3}{2}}$	$3d_{\frac{3}{2}}$	$3d_{\frac{5}{2}}$
n	1	2	2	2	3	3	3	3	3
κ	-1	-1	1	-2	-1	1	-2	2	-3
j	$\frac{1}{2}$	$\frac{1}{2}$	$\frac{1}{2}$	$\frac{3}{2}$	$\frac{1}{2}$	$\frac{1}{2}$	$\frac{3}{2}$	$\frac{3}{2}$	$\frac{5}{2}$
l	0	0	1	1	0	1	1	2	2
Parity	1	1	-1	-1	1	-1	-1	1	1

Table 3.1: Classification of one electron orbitals in H-like ions - The bound states of the electron, or orbitals, are classified according to the quantum numbers n and κ. The quantum numbers j and l are given according Eq. (3.13). The parity is equal to $(-1)^l$. The next letter for $l = 4$ is f.

by *Dirac* [93], assuming that all the states of negative energy are occupied with electrons. In this interpretation, the vacuum is defined by the absence of real electrons in bound states and positive energy states, and all the negative energy states filled with electrons. This vacuum is sometimes refereed as the Dirac sea. Because of the Pauli exclusion principle, which forbids two particles of half spin with the same quantum numbers being at the same state, that decay it is not possible, and hence making the lowest energy bound state also the ground state. On the other hand, the electron of negative energy can absorb a photon with energy greater then $2c^2$ and excite for a state of positive energy. The hole behaves like an electron with the same mass, spin and opposite charge and was named positron. The positron was experimentally observed in 1933 by Carl D. Anderson [94] and made it's discovery, the antiparticle of the electron, one of the greatest triumphs of theoretical physics.

The eigenvalues, $\epsilon_{n\kappa}$, of the bound states obtained after solving the eigenvalue equation (3.15) are given by the Sommerfeld formula

$$\begin{aligned}
\epsilon_{n\kappa} &= c^2\left(\frac{1}{\sqrt{1+\dfrac{(\alpha Z)^2}{n-|\kappa|+\sqrt{\kappa^2-(\alpha Z)^2}}}}-1\right), \qquad (3.18)\\
n &= 1,2,3,\ldots,\\
l &= 0,1,\ldots,n-1,\\
\kappa &= \pm\left(j+\frac{1}{2}\right)=\pm1,\pm2,\pm3,\ldots,
\end{aligned}$$

where a point-like of the nucleus was used for the spherical potential. The α value is the fine structure constant, which in atomic units is $\alpha = 1/c$. This energy levels only depends on $|\kappa|$ and n, as a consequence of the spherical potential. Consequently, these numbers are the necessary quantum numbers for describing an one-electron state or an orbital. In Table 3.1 is shown the nomenclature used for describing one-electron orbitals.

Those eigenvalues having the same value of n and j, but different values of l are degenerate in energy. For example, the $2s_{1/2}$ and $2p_{1/2}$ orbitals are degenerate. By contrast, orbitals with the

same n and l but different values of j, such as the $2p_{1/2}$ and $2p_{3/2}$ orbitals, have different energies. The separation between two such levels is called fine structure interval, which can be observed in Fig. 1.1. Furthermore, the degeneracy between the $2s_{1/2}$ and $2p_{1/2}$ could be lifted if the QED effects are considered (Lamb-shift). Usually the subscript $j = 1/2$ in the $s_{1/2}$ orbitals are omitted since it is always 1/2.

For $\alpha Z > 1$, Eq. (3.18) becomes imaginary, which indicates that there is no bound states for those atomic numbers. This is due to the energy of the $1s_{1/2}$ being embedded in the negative continuum $\epsilon_{n\kappa} < -2c^2$ for $\alpha Z > 1$ in a point-like nucleus model. As in the *Klein paradox* [83], this phenomena can be understood in the framework of the hole theory as electron-positron pair creation at the potential barrier. It becomes energetically favorable for the electron-positron pair not recombining, and thus, emitting a positron.

For lower values of αZ, Eq. (3.18) can be expanded as

$$\epsilon_{n\kappa} = -\frac{Z^2}{2n^2}\left[1 + \frac{(\alpha Z)^2}{n}\left(\frac{1}{\kappa} - \frac{3}{4n}\right)\right], \tag{3.19}$$

where the first term represents the Bohr formula for the electronic energy levels calculated according to the Schrödinger equation, which scales as Z^2. Accordingly, relativistic corrections for the energy levels are of order $\alpha^2 Z^4$. These corrections are significantly for small principal quantum numbers and in HCI. Moreover, the radial electron distribution shifts towards the nucleus if the Dirac equation is considered rather than the non-relativistic Schrödinger equation.

Having made a description of the one-electron Dirac equation, we will give a brief description of the QED formalism necessary for obtaining the two-photon expressions.

3.2 QED

QED can be found in several textbooks [82, 83, 85]. In this section, we restrict to a brief description and further details can be traced back to the references already mentioned. As refereed previously, the Lamb-shift is an energy shift between the $2s_{1/2}$ and the $2p_{1/2}$. This splitting was first discovered by *Lamb* and *Retherford* in 1947 using precise microwave absorption techniques [95]. Since it was done for hydrogen, the effect of the nuclear model was too small to explain this splitting. This lead to believe that these effects could be due to quantum fluctuations in the electromagnetic field or fluctuations in the vacuum Dirac sea (spontaneous electron-positron pair creation). *Bethe* calculated an estimative based in the calculation of the vacuum fluctuations of the electromagnetic field with the concept of renormalization [96]. These fluctuations can be interpreted as spontaneous emission and subsequent absorption of a photon by an electron, which is known as the self-energy of the electron. Classically, this corresponds to the interaction of the charge density with itself.

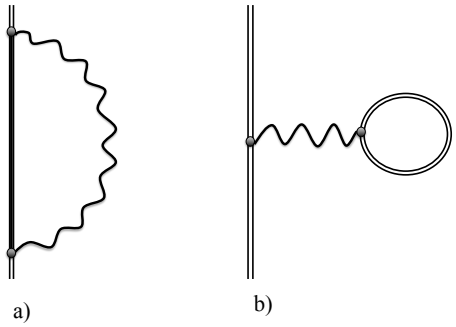

Figure 3.1: Self-energy and vacuum polarization Feynman diagrams - a) is refereed to the self-energy diagram while b) is the vacuum polarization diagram. The straight double line represents a bound electron and the oscillating line a photon

Calculations in QED are done in perturbative theory of the fine structure α. The terms of this perturbative expansion can be represented by Feynman diagrams. The first terms of the expansion, that gives the main contribution of the Lamb-shift, are the self-energy and the vacuum polarization terms. In Fig. 3.1 is shown a representation of these diagrams. The vacuum polarization corresponds to the interaction of the bound electron with an electron-positron pair, which is a quantum fluctuation of the Dirac sea.

The QED corrections on the atomic energy levels can be divided in one-electron corrections, where these fluctuations affects each electron independently, and two-electron corrections, which affects the interaction between two electrons. Self-energy and vacuum-polarization [97, 98] are one-electron corrections that gives the main contribution to the Lamb-shift. Other one-electron corrections, with less contribution to the Lamb-shift, are the two-loop self-energy [99] and two-loop vacuum-polarization [100]. A recent review can be found in Ref. [101]. As for the two electron corrections, they are calculated within the two-time Greens function [102] formalism, which evaluates the vacuum-polarization screening correction [103], the two-photon exchange correction [104], as well as the self-energy screened by a spherically symmetric part of the electron-electron interaction [105].

3.2.1 S Matrix in interaction representation

QED deals with dynamical system consisting of the electromagnetic field and the electron-positron field. Such systems can be defined by an Hamiltonian made of the sum of the field Hamiltonians without mutual interaction and the operator of the interaction between the fields [85]. With such separation of the mutual interaction, the interaction representation can be introduced in QED. This representation is frequently used in Quantum mechanics for obtaining approximate solutions within

the framework of perturbation theory.

In this representation, the state vector is expressed by

$$\Phi(t) = S(t, t_0)\Phi(t_0), \tag{3.20}$$

where $\Phi(t_0) = \Phi(t = t_0)$ and $S(t, t_0)$ is an operator defined by [85]

$$\begin{aligned} S(t, t_0) &= \sum_{n=0}^{\infty} \frac{(-i)^n}{n!} \int_{t_0}^{t}\int_{t_0}^{t}\int_{t_0}^{t} \ldots \int_{t_0}^{t} T\left[V_I(t_1')V_I(t_2')V_I(t_3')\ldots V_I(t_n')\right] dt_n' \ldots . dt_3' dt_2' dt_1' \\ &= T\left[e^{-i\int_{t_0}^{t} V(t')dt'}\right] = \sum_{n=0}^{\infty} S_n(t, t_0)\ , \end{aligned} \tag{3.21}$$

with

$$S_n(t, t_0) = \frac{(-i)^n}{n!} \int_{t_0}^{t}\int_{t_0}^{t}\int_{t_0}^{t} \ldots \int_{t_0}^{t} T\left[V_I(t_1')V_I(t_2')V_I(t_3')\ldots V_I(t_n')\right] dt_n' \ldots . dt_3' dt_2' dt_1'\ . \tag{3.22}$$

The Dyson chronological operator T is defined by

$$T\left[V(t_1)\,V(t_2)\right] = \begin{cases} V(t_1)\,V(t_2) & \text{if} \quad t_1 \geq t_2 \\ V(t_2)\,V(t_1) & \text{if} \quad t_1 < t_2 \end{cases}\ . \tag{3.23}$$

The operator $S(t, t_0)$ is called the Scattering matrix, or simply S matrix. It operates on the initial state vector $\Phi(t_0)$ and the result is the state $\Phi(t)$ at an instant t.

3.2.2 Quantified field

There are two formalisms for defining a quantum system in QED. One of such formalisms defines the system Hamiltonian through de use of path integrals and a variational principle that identifies the stationary paths of a classical system[1]. The other approach, which is equivalent to the last one, defines a field for a given particle which is the *quantum* of the field[2]. According to this concept, the ground state of a field is the vacuum, while an excitation of the field corresponds to a particle creation. In the case of the electromagnetic field, it consists in the electromagnetic field quantification, in which the four-vector potencial $\boldsymbol{A}_\mu$ is expanded in plane waves of polarity $\hat{\boldsymbol{e}}$ and wavenumber $\boldsymbol{k}$. A plane wave corresponds to a solution of the Maxwell equations without charges. The expansion coefficients are defined not as numerical quantities, but rather as unitary operators that can be identified as creation or destruction of a single photon with polarity $\hat{\boldsymbol{e}}$ and wavenumber $\boldsymbol{k}$ [85]. As for the electron case, it consists in the electron-positron field quantification, i.e., in the expansion of the functions ψ and

[1] Developed by *Feynman* [106, 107]

[2] Developed by *Tomonaga*, *Schwinger* and *Dyson* [108, 109, 110, 111, 112]

$\overline{\psi}$ that satisfies the Dirac equation (3.7). Like in the case of the electromagnetic field, the expansion coefficients corresponds to the creation or destruction of an electron or positron.

The commutation relations of these operators are constructed in such way that the each field follows a given statistics. In the case of the electromagnetic field, the photons obey the Bose-Einstein statistics, i.e., the number of particles in a given state is arbitrary. On the other hand, the electrons and positrons obey the Pauli exclusion principle and follow the Fermi-Dirac statistics; a state contains only zero or one particle.

Using this principles, it can be deduced that the interaction operator between the electromagnetic field and the electron-positron field is given by [85]

$$V(t) = \int j^{\mu}(\boldsymbol{x}) A_{\mu}(\boldsymbol{x}) dV \, , \tag{3.24}$$

where $\boldsymbol{A}(\boldsymbol{x})$ is the four-vector potential and $\boldsymbol{j}(\boldsymbol{x})$ is the four-vector electron flux defined by

$$j_{\mu}(\boldsymbol{x}) = iN\left(\overline{\psi}(\boldsymbol{x})\gamma_{\mu}\psi(\boldsymbol{x})\right) \, , \tag{3.25}$$

where N is an operator that sorts the operators in order to the creation operators being at the right and the destruction ones to the left. It also multiplies by one or minus one for an even or odd number of switches. Here, $\boldsymbol{x}$ is the space-time four-vector $(\boldsymbol{r}, -it)$.

Using the Eqs. (3.24) and (Eq. (3.25)), the matrix S can be rewritten as

$$\begin{aligned} S(t, t_0) &= \sum_{n=0}^{\infty} \frac{(-i)^n}{n!} \int\int\int ... \int T\left[U(\boldsymbol{x}_1)U(\boldsymbol{x}_2)U(\boldsymbol{x}_3)...U(\boldsymbol{x}_n)\right] d^4\boldsymbol{x}_n ... d^4\boldsymbol{x}_3 d^4\boldsymbol{x}_2 d^4\boldsymbol{x}_1 \\ &= T\left[\exp(-i\int U(\boldsymbol{x}) d^4\boldsymbol{x})\right] \, , \end{aligned} \tag{3.26}$$

where

$$U(\boldsymbol{x}) = -iN\left(\overline{\psi}(\boldsymbol{x})\gamma^{\mu}A_{\mu}(\boldsymbol{x})\psi(\boldsymbol{x})\right) = -iN\left(\overline{\psi}(\boldsymbol{x})\hat{A}(\boldsymbol{x})\psi(\boldsymbol{x})\right) \, . \tag{3.27}$$

A given interaction mode between the electromagnetic field and the electron-positron is a n process if the matrix S is proportional to α^n. In this way, a n process is described by the matrix $S_n(t, t_0)$. Here $\hat{A}(\boldsymbol{x}) = \gamma^{\mu}A_{\mu}(\boldsymbol{x})$ and $\overline{\psi} = \psi^*\beta$.

Since the operators $\hat{A}$, ψ and $\overline{\psi}$ are given as an expansion on creation and annihilation operators for each single particle, each term in Eq. (3.26) can be rewritten as products of electron-positron and photons creation and annihilation in different states. For example, in a transition that an electron decay

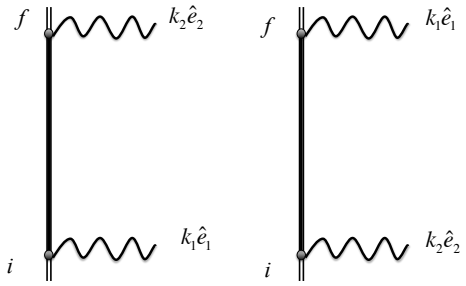

Figure 3.2: Two-photon transition Feynman diagrams - Representation of the Feynman diagrams for an emission of two photons with polarities $\hat{\boldsymbol{e}}_1$ and $\hat{\boldsymbol{e}}_2$, and wavenumber $\boldsymbol{k}_1$ and $\boldsymbol{k}_2$. The two diagrams corresponds to the two permutations of the two photon creation operators.

from an initial state to a final state by spontaneous emission of two photons, one of the annihilation operators must annihilate the electron in the initial state and three creation operators creates one electron and two photons in the final state. All the other operators must join in creation-annihilation pairs of the same particle (electron, positron or a photon). A Feynman diagram of this process is illustrated in Fig. 3.2. The thin lines that goes from infinite to a vertex, are operators that create or destroy an electron. The thick line corresponds to compacting all the creation-annihilation pairs of the same particle. The oscillatory line is a destruction or a creation of a photon.

3.2.3 S Matrix for two-photon transition

The n order matrix S of a process $i \to f$ is defined by

$$S^{(n)}_{i\to f} = \left\langle \Phi_f \left| S_n \right| \Phi_i \right\rangle = \sum_k S^{(n)}_k \,, \tag{3.28}$$

where Φ is a state vector in the Fock space or particle number space. Thus, all the unitary operators are removed. Each $S^{(n)}_k$ term differs by the order of the creation and annihilation operators in the same process. In the case illustrated in Fig. 3.2, the number is two due to the possible number of permutations between the two photon creation operators.

The matrix elements involved in a second order interaction between the electromagnetic field and the electron-positron field is described by the matrix S given by

$$S_2 = \int\int T\left[N\left(\overline{\psi}(\boldsymbol{x}_1)\hat{A}(\boldsymbol{x}_1)\psi(\boldsymbol{x}_1)\right)N\left(\overline{\psi}(\boldsymbol{x}_2)\hat{A}(\boldsymbol{x}_2)\psi(\boldsymbol{x}_2)\right)\right]d^4\boldsymbol{x}_1 d^4\boldsymbol{x}_2 \,. \tag{3.29}$$

The two-photon transition as showed in Fig. 3.2 is one of the various processes of interaction

associated to S_2. The matrix S for the diagram in Fig. 3.2 is given by

$$\begin{aligned} S^{(2)}_{i\to f} &= \int \Big[\overline{\psi}_f(\boldsymbol{x}_2)\hat{A}^*_2(\boldsymbol{x}_2)S^{(e)}_{\mathrm{G}}(\boldsymbol{x}_1,\boldsymbol{x}_2)\hat{A}^*_1(\boldsymbol{x}_1)\psi_i(\boldsymbol{x}_1) \\ &\quad + \overline{\psi}_f(\boldsymbol{x}_2)\hat{A}^*_1(\boldsymbol{x}_1)S^{(e)}_{\mathrm{G}}(\boldsymbol{x}_1,\boldsymbol{x}_2)\hat{A}^*_2(\boldsymbol{x}_2)\psi_i(\boldsymbol{x}_1)\Big]\, d^4\boldsymbol{x}_1 d^4\boldsymbol{x}_2 \\ &= S^{(2)}_a + S^{(2)}_b \,. \end{aligned} \tag{3.30}$$

The states $\psi_i(\boldsymbol{x})$ and $\psi_f(\boldsymbol{x})$ are the wavefunctions of the electron in the initial and final states, and $\hat{A}_1$ and $\hat{A}_2$ are the wavefunctions of the photon with polarity $\hat{\boldsymbol{e}}_{1(2)}$ and wavenumber $\boldsymbol{k}_{1(2)}$.

The function $S^{(e)}_{\mathrm{G}}(\boldsymbol{x}_1,\boldsymbol{x}_2)$ is the mean value of the various creation-annihilation pairs of the same particle (in this case electron and positron) resulting from the Dyson operator along with the Normal operator. It is given by [85]

$$S^{(e)}_{\mathrm{G}}(\boldsymbol{x}_1,\boldsymbol{x}_2) = \begin{cases} \displaystyle\sum_n \psi^{(+)}_n(\boldsymbol{x}_1)\psi^{(+)}_n(\boldsymbol{x}_2) & \text{if} \quad t_1 \geq t_2 \\ \\ \displaystyle -\sum_n \psi^{(-)}_n(\boldsymbol{x}_1)\psi^{(-)}_n(\boldsymbol{x}_2) & \text{if} \quad t_1 < t_2 \end{cases} , \tag{3.31}$$

where

$$\psi^{(\pm)}_n(\boldsymbol{x}_1) = \psi^{(\pm)}_{n0}(\boldsymbol{r_1})e^{-iE^{(\pm)}_n t} \,, \tag{3.32}$$

are the solutions of the Dirac equation (3.7) for an electron in external field given by the nuclear potential. The sum covers all the energies of the Dirac spectrum, both positive (+) and negative (−) states. In the case of a continuous energy band, such as the positive or the negative continuum, this sum is interpreted as an integral.

Considering the following identity [85]

$$\frac{1}{2\pi i}\int_{-\infty}^{\infty} \frac{e^{i\omega t}}{E(1-i0)+\omega} d\omega = \begin{cases} 0 & E<0 \\ e^{-iEt} & E>0 \quad t>0 \\ -e^{-iEt} & E<0 \quad t<0 \end{cases} , \tag{3.33}$$

$S^{(e)}_{\mathrm{G}}(\boldsymbol{x}_1,\boldsymbol{x}_2)$, known as the Green's function, can be given in a more compact expression given by

$$S^{(e)}_c(\boldsymbol{x}_1,\boldsymbol{x}_2) = \frac{1}{2\pi i}\int_{-\infty}^{\infty} e^{i\omega(t_1-t_2)} \sum_n \frac{\psi_{n0}(\mathbf{r}_2)\overline{\psi}_{n0}(\mathbf{r}_1)}{E_n(1-i0)+\omega} d\omega \,. \tag{3.34}$$

Replacing Eq. (3.34) in Eq. (3.30), we obtain

$$\begin{aligned} S_a^{(2)} &= \frac{1}{2\pi i}\int\int \overline{\psi}_f(\boldsymbol{x}_2)\hat{A}(\boldsymbol{x}_2)\int_{-\infty}^{\infty}\exp(i\omega\,(t_1-t_2)) \\ &\quad\times\sum_n \frac{\psi_{n0}(\boldsymbol{r}_2)\overline{\psi}_{n0}(\boldsymbol{r}_1)}{E_n(1-i0)+\omega}d\omega\hat{A}(\boldsymbol{x}_1)\psi_i(\boldsymbol{x}_1)d^4\boldsymbol{x}_1 d^4\boldsymbol{x}_2\,, \end{aligned} \tag{3.35}$$

Further simplifications can be done using plane waves to describe the photon and a *gauge* transformation (Eq. (3.6)) with an arbitrary function having a time dependence given by

$$\vartheta(\mathbf{r},t) = G\frac{ic}{\omega}\exp(-i\,(\mathbf{k}\cdot\mathbf{r}+\omega t))\,, \tag{3.36}$$

where G is an arbitrary number associated with *gauge* invariance. The result of these considerations in the case of two-photon emission is given by

$$S_a^{(2)} = \frac{2\pi}{\sqrt{\omega_1\omega_2}c}\sum_n \frac{\left\langle f\left|A_2^*\right|n\right\rangle\left\langle n\left|A_1^*\right|i\right\rangle}{E_n-E_i+\omega_1}\delta(E_f-E_i-\omega_1-\omega_2)\,. \tag{3.37}$$

The matrix elements are given in space coordinates by

$$\left\langle f\left|A_j^*\right|i\right\rangle = \int \psi_{f0}^*(\mathbf{r})A_j^*(\mathbf{r})\psi_{i0}(\mathbf{r})d\mathbf{r}\,, \tag{3.38}$$

where the operator A_j^* is given by

$$A_j^* = \boldsymbol{\alpha}\cdot(\hat{\boldsymbol{e}}_j + G\hat{\boldsymbol{k}}_j)\exp(-i\boldsymbol{k}_j\cdot\mathbf{r}) - G\exp(-i\boldsymbol{k}_j\cdot\mathbf{r})\,. \tag{3.39}$$

If the operator A_j is used instead of it's conjugate, then Eq. (3.37) describes the absorption of two-photons. If the conjugates are mixed, then the process in Eq. (3.37) describes the Rayleigh scattering or the Raman scattering if both frequencies are the same [85]. The delta Dirac in Eq. (3.37) means that the frequencies of the photons are restricted by energy conservation, i.e., $E_f - E_i = \omega_1 + \omega_2$.

Finally, the probability of a given process is given by

$$P_{i\to f} = 2\pi\left|\left\langle\Phi_f\left|S_{i\to f}^{(n)}\right|\Phi_i\right\rangle\right|^2\,. \tag{3.40}$$

3.3 Two-photon emission

When the initial and final states of the process lie in the continuum, as in the present case since the frequency of the emitted photon is continuous, the probability is differential. The differential

probability, dw, is obtained by multiplying P by the number of photons with wavenumber $\boldsymbol{k}$ in the range $d\boldsymbol{k}$,

$$dw = 2\pi \left| S_a^{(2)} + S_b^{(2)} \right|^2 \frac{dk_1}{(2\pi)^3} \frac{dk_2}{(2\pi)^3} \, . \tag{3.41}$$

The integration in order to ω_2 leads to the equation that describes the two-photon emission decay,

$$\frac{dw}{d\omega_1} = \frac{\omega_1 \omega_2}{(2\pi)^3 c^2} \left| M(2,1) + M(1,2) \right|^2 d\Omega_1 d\Omega_2 \, , \tag{3.42}$$

where $d\Omega_j$ is the solid angle of the photon emission j and the matrix element $M(2,1)$ is defined by

$$M(2,1) = \sum_n \frac{\left\langle f \left| A_2^* \right| n \right\rangle \left\langle n \left| A_1^* \right| i \right\rangle}{E_n - E_i + \omega_2} \, . \tag{3.43}$$

3.3.1 Multipole expansion for the total decay rate

A multipole expansion consist of an expansion of the electromagnetic field in components of the angular momentum L and its projection along the z axis, M_L, i.e., in functions that are eigenfunctions of an quantum angular momentum operator. In classical electrodynamics, the radiation field has an angular momentum defined by $\boldsymbol{r} \cdot \boldsymbol{E} \times \boldsymbol{B}$ [91], where $\boldsymbol{E}$ and $\boldsymbol{B}$ are the electric and magnetic fields. The respective quantum operator has properties of an angular momentum operator for a boson with one spin value, i.e., $\boldsymbol{M} = -i\boldsymbol{r} \times \boldsymbol{\nabla} + \boldsymbol{s}$ [85]. Such spin has three components (eigenvalues of s_z): two associated with transverse components of the radiation, $\lambda = 0, 1$, and one associated with the longitudinal component $\lambda = -1$, i.e., with same direction of the radiation wave. The two transverse components are mutually perpendicular to each other and are identified as the electric $\lambda = 1$ and magnetic $\lambda = 0$ components of the radiation. As expected from classical electrodynamics, the mean value of longitudinal terms vanish since the radiation classically has only transverse components.

An electric component of a multipole with an angular momentum L and $\lambda = 1$ is called electric 2^L pole or EL, while a component $\lambda = 0$ is called a magnetic 2^L pole or ML. For example, a component with $\lambda = 1$ and $L = 1$ is an electric dipole ($E1$) and a component with $\lambda = 0$ and $L = 3$ is a magnetic octopole ($M3$).

If we pretend to evaluate the total decay rate, the integration over the solid angles in Eq. (3.42) could be simplified using the following multipole expansions [60, 92]

$$\hat{\boldsymbol{e}} \exp(-i\boldsymbol{k} \cdot \mathbf{r}) = \sum_{L,M,\lambda} \left[\hat{\boldsymbol{e}} \cdot \mathbf{Y}_{L,M}^{(\lambda)}(\hat{\boldsymbol{k}}) \right] \mathbf{a}_{L,M}^{(\lambda)} \, , \tag{3.44}$$

$$\exp(-i\boldsymbol{k} \cdot \mathbf{r}) = \sum_{L,M,\lambda} Y_{L,M}(\hat{\boldsymbol{k}}) \Phi_{L,M} \, . \tag{3.45}$$

The index λ have values $-1, 0, 1$. $\mathbf{Y}^{(\lambda)}_{L,M}$ is related with the vector spherical harmonics according to

$$\mathbf{Y}^{(0)}_{L,M}(\hat{\boldsymbol{k}}) = \mathbf{Y}_{L,L,M}(\hat{\boldsymbol{k}}) , \tag{3.46}$$

$$\mathbf{Y}^{(1)}_{L,M}(\hat{\boldsymbol{k}}) = -i\hat{\mathbf{k}} \times \mathbf{Y}^{(0)}_{L,M}(\hat{\mathbf{k}}) , \tag{3.47}$$

$$\mathbf{Y}^{(-1)}_{L,M}(\hat{\boldsymbol{k}}) = \hat{\boldsymbol{k}} Y_{L,M}(\hat{\boldsymbol{k}}) . \tag{3.48}$$

The coefficients $\mathbf{a}^{(\lambda)}_{L,M}$ and $\Phi_{L,M}$ are given by

$$\mathbf{a}^{(0)}_{L,M} = g_L(kr)\mathbf{Y}_{L,L,M}(\hat{\mathbf{r}}) , \tag{3.49}$$

$$\mathbf{a}^{(1)}_{L,M} = \left(\frac{L}{2L+1}\right)^{1/2} g_{L+1}(kr)\mathbf{Y}_{L,L+1,M}(\hat{\mathbf{r}}) + \left(\frac{L+1}{2L+1}\right)^{1/2} g_{L-1}(kr)\mathbf{Y}_{L,L-1,M}(\hat{\mathbf{r}}) , \tag{3.50}$$

$$\mathbf{a}^{(-1)}_{L,M} = -\left(\frac{L+1}{2L+1}\right)^{1/2} g_{L+1}(kr)\mathbf{Y}_{L,L+1,M}(\hat{\mathbf{r}}) + \left(\frac{L}{2L+1}\right)^{1/2} g_{L-1}(kr)\mathbf{Y}_{L,L-1,M}(\hat{\mathbf{r}}) , \tag{3.51}$$

and

$$\Phi_{L,M} = g_L(kr) Y_{L,M}(\hat{\mathbf{r}}) , \tag{3.52}$$

with

$$g_L(kr) = 4\pi i^L j_L(kr) . \tag{3.53}$$

The function $j_L(kr)$ is the spherical Bessel function given by

$$j_L(x) = (-1)^L \frac{d^L}{dx^L}\left(\frac{\sin(x)}{x}\right) . \tag{3.54}$$

This function is the radial part of the Helmholtz equation ($(\nabla^2 + k^2) f(r) = 0$) solution and appears in physical problems related with oscillating waves.

Following the same procedure used to construct the spherical spinors (Eq. (3.10)), one combines spherical harmonics with the spherical basis set vectors given by

$$\boldsymbol{\zeta_1} = -\frac{1}{\sqrt{2}}\begin{pmatrix} 1 \\ i \\ 0 \end{pmatrix} , \quad \boldsymbol{\zeta_0} = \begin{pmatrix} 0 \\ 0 \\ 1 \end{pmatrix} , \quad \boldsymbol{\zeta_{-1}} = \frac{1}{\sqrt{2}}\begin{pmatrix} 1 \\ -i \\ 0 \end{pmatrix} , \tag{3.55}$$

to obtain the vector spherical harmonics,

$$\boldsymbol{Y_{J,L,M}} = \sum_{\sigma=-1}^{\sigma=1} \left\langle L\ M-\sigma, 1\ \sigma \middle| J\ M \right\rangle Y_{L,M-\sigma}(\hat{\boldsymbol{r}})\boldsymbol{\zeta_\sigma} . \tag{3.56}$$

Replacing the expansion (3.44) in the Eq. (3.39) results in

$$A_j^* = \sum_{L,M,\lambda} \left[\hat{e}_j \cdot \mathbf{Y}_{L,M}^{(\lambda)}(\hat{\boldsymbol{k}}_j)\right] \tilde{a}_{L,M}^{(\lambda)} \,, \tag{3.57}$$

by noticing that $\hat{\boldsymbol{k}} \cdot \mathbf{Y}_{L,M}^{(-1)}(\hat{\boldsymbol{k}}) = Y_{L,M}(\hat{\boldsymbol{k}})$, and

$$\tilde{a}_{L,M}^{(\lambda)} = \begin{cases} \boldsymbol{\alpha} \cdot \mathbf{a}_{L,M}^{(\lambda)} & \lambda = 1, 0 \\ G(\boldsymbol{\alpha} \cdot \mathbf{a}_{L,M}^{(-1)} - \Phi_{L,M}) & \lambda = -1 \end{cases} \,. \tag{3.58}$$

Replacing Eqs. (3.57) and (3.58) in Eq. (3.42), integrating over the solid angles $d\Omega_1 d\Omega_2$ and performing a sum over the possible polarizations, we obtain

$$\begin{aligned} \frac{dW}{d\omega_1} &= \int\int \sum_{\hat{e}_1,\hat{e}_2} \frac{dw}{d\omega_1} d\Omega_1 d\Omega_2 = \\ &= \frac{\omega_1 \omega_2}{(2\pi)^3 c^2} \sum_{L_1,M_1,\lambda_1,L_2,M_2,\lambda_2} \left| B_{L_1,M_1,\lambda_1}^{L_2,M_2,\lambda_2} + B_{L_2,M_2,\lambda_2}^{L_1,M_1,\lambda_1} \right|^2 \,, \end{aligned} \tag{3.59}$$

where

$$B_{L_1,M_1,\lambda_1}^{L_2,M_2,\lambda_2} = \sum_n \frac{\left\langle f \left| \tilde{a}_{L_2,M_2}^{(\lambda_2)} \right| n \right\rangle \left\langle n \left| \tilde{a}_{L_1,M_1}^{(\lambda_1)} \right| i \right\rangle}{E_n - E_i + \omega_1} \,. \tag{3.60}$$

The reduction of the matrix elements in the above equation to radial integrals is described in Ref. [113], where it is shown that

$$\begin{aligned} \left\langle f \left| \tilde{a}_{L,M}^{(\lambda)} \right| i \right\rangle &= (-1)^{j_f - m_f} \begin{pmatrix} j_f & L & j_i \\ -m_f & M & -m_i \end{pmatrix} (-1)^{L+\lambda-1} (-1)^{j_f - 1/2} \left(\frac{4\pi}{2L+1} \right)^{1/2} \\ &\quad \times \left[j_f, j_i \right]^{1/2} \begin{pmatrix} j_f & L & j_i \\ 1/2 & 0 & -1/2 \end{pmatrix} \bar{M}_{f,i}^{(\lambda,L)} \Pi(l_i, l_f, L, \lambda) \,, \end{aligned} \tag{3.61}$$

where the radial components are

$$\begin{aligned} \bar{M}_{f,i}^{(1,L)} &= \left(\frac{L}{L+1} \right)^{1/2} \left[\left(\kappa_f - \kappa_i \right) I_{L+1}^+ + (L+1) I_{L+1}^- \right] \\ &\quad - \left(\frac{L+1}{L} \right)^{1/2} \left[\left(\kappa_f - \kappa_i \right) I_{L-1}^+ - L I_{L-1}^- \right] \,, \end{aligned} \tag{3.62}$$

$$\bar{M}_{f,i}^{(0,L)} = \frac{2L+1}{\left(L\,(L+1) \right)^{1/2}} \left(\kappa_f + \kappa_i \right) I_L^+ \,, \tag{3.63}$$

$$\bar{M}_{f,i}^{(-1,L)} = G \left[(2L+1) J^{(L)} + \left(\kappa_f - \kappa_i \right) \left(I_{L+1}^+ + I_{L-1}^+ \right) - L I_{L-1}^- + (L+1) I_{L+1}^- \right] \,, \tag{3.64}$$

with

$$I_L^{\pm} = \int_0^{\infty} \left(P_f Q_i \pm P_i Q_f\right) j_L\left(\frac{\omega r}{c}\right) dr \,, \tag{3.65}$$

$$J_L = \int_0^{\infty} \left(P_f P_i + Q_f Q_i\right) j_L\left(\frac{\omega r}{c}\right) dr \,. \tag{3.66}$$

P and Q are the large and small components of radial Dirac equation (Eq. (3.15)), ω is the photon frequency and the notation $[j, k, ..]$ means $(2j + 1)(2k + 1)...$

The one-photon transition rate associated with electric or magnetic multipole of order L is proportional to the square modulus of the matrix element given by Eq. (3.61) [85]. These transition rates scale approximately with L as [85]

$$W_{EL} \sim \frac{\omega}{c}\left(\frac{\omega}{c}a\right)^{2L} \,, \tag{3.67}$$

$$W_{ML} \sim \begin{cases} c\left(\frac{Z}{c}\right)^{10} & \text{if} \quad L = 1 \,, \\ \frac{W_{EL}}{(ca)^2} & \text{if} \quad L \neq 1 \,, \end{cases} \tag{3.68}$$

where ω is the frequency of the emitted radiation and a is a length related to the atom size. For example, the first term of the multipole expansion with the highest value has $L = 1$ and $\lambda = 1$, which is the electric dipole, $E1$. Since ω and a scales as Z^2 and $1/Z$ respectively along an isoelectronic sequence, for lower charged ions, the wavelength of the emitted radiation, or photon is much less than the size of the atom, therefore, the $E1$ is the highest multipole, i.e., with higher transition rate. In contrast, the emitted wavelength from HCI is a fraction of the atom size. Therefore, the effect of higher multipoles is crucial in such atomic systems.

The selection rules expressed by the three-j symbol in Eq. (3.61) are a consequence of the angular momentum conservation. This requires that the initial atomic angular momentum j_i, the final angular momentum j_f and the emitted multipole term L satisfy the following triangular inequality

$$\left|J_i - J_f\right| \leq L \leq J_i + J_f \,, \tag{3.69}$$

and the respective z components satisfy the relation

$$M_i = M_f + M_L \,, \tag{3.70}$$

in order to the multipole term being possible to be emitted. Another selection rule results from the parity conservation. This results in the parity selection rule that states that the parity of the initial state

is the product of the final parity by $(-1)^{L+\lambda+1}$, i.e.,

$$P_i = P_f(-1)^{L+\lambda+1} \, . \tag{3.71}$$

The parity of an atomic state is given by the well-known relation $(-1)^{L_{i(f)}}$, where $L_{i(f)}$ is the orbital angular momentum of the initial (final) state. The term $\Pi(l_i, l_f, L, \lambda)$ in Eq. (3.61) is one if Eq. (3.71) holds true and is zero otherwise. For instance, in the $2s_{1/2} \rightarrow 1s_{1/2}$ transition of H-like ions, the $E1$ emission of a photon is forbidden by parity selection rule, which makes this transition a forbidden one.

Among the large variety of possible *gauges*, *Grant* [113] showed that there are two values of G which are of particular utility because they lead to well–known non-relativistic operators. If $G = 0$, one has the so-called Coulomb, or velocity *gauge*, which leads to the dipole velocity form in the non-relativistic limit. If $G = [(L+1)/L]^{1/2}$, for example, $G = \sqrt{2}$ for $E1$ transitions ($L = 1$), one obtains a non-relativistic expression which reduces to the dipole length, Lorentz or Babushkin *gauge* of the transition operator. The two-photon transitions *gauge* invariance was studied by *Goldman* and *Drake* [60].

Equation (3.59) can be further simplify by defining the following functions

$$S^j(2,1) = \sum_{n_l} \frac{\bar{M}^{(\lambda_2,L_2)}_{f,n_l}(\omega_2)\bar{M}^{(\lambda_1,L_1)}_{n_l,i}(\omega_1)}{E_{n_l} - E_i + \omega_1} \Delta^j(2,1)\Pi^l(2,1) \, , \tag{3.72}$$

and

$$\theta^j(2,1) = [j]^{1/2} \sum_{m_j} (-1)^{m_j+m_f+1} \begin{pmatrix} j_f & L_2 & j \\ -m_f & M_2 & m_j \end{pmatrix} \begin{pmatrix} j & L_1 & j_i \\ -m_j & M_1 & m_i \end{pmatrix} , \tag{3.73}$$

where

$$\Delta^j(2,1) = \frac{4\pi[j_i, j, j_f]^{1/2}}{[L_1, L_2]^{1/2}} \begin{pmatrix} j_f & L_2 & j \\ 1/2 & 0 & -1/2 \end{pmatrix} \begin{pmatrix} j & L_1 & j_i \\ 1/2 & 0 & -1/2 \end{pmatrix} , \tag{3.74}$$

$$\Pi^l(2,1) = \pi^l_i(1)\pi^l_f(2) \, , \tag{3.75}$$

with

$$\pi^l_k(t) = \begin{cases} 1 & \text{if } l_k + l + L_t + \lambda_t = \text{odd} \\ 0 & \text{if } l_k + l + L_t + \lambda_t = \text{even} \end{cases} \, . \tag{3.76}$$

The parity selection rules (3.76) follow from the calculation of the reduced matrix elements expressed in Eq. (3.61). It should be again emphasized that the summation in Eq. (3.72) is over a complete spectrum of the Dirac equation, both bound states and *positive* and *negative* continuum, which is not a trivial task. We delegate the evaluation of the function (3.72), which we define as the reduced two-photon amplitude, to the Sec. (3.4).

By performing the sum over m_f and averaging over m_i, i.e.,

$$\frac{d\overline{W}}{d\omega_1} = \frac{\omega_1\omega_2}{(2\pi)^3 c^2 [j_i]} \sum_{L_1,M_1,\lambda_1,L_2,M_2,\lambda_2,m_f,m_i} \left| \sum_j \left[\theta^j(2,1) S^j(2,1) + \theta^j(1,2) S^j(1,2) \right] \right|^2 . \tag{3.77}$$

and using the sum rules,

$$\sum_{M_1,M_2,m_f,m_i} \theta^j(2,1)\theta^{j'}(2,1) = \delta_{jj'} , \tag{3.78}$$

$$\sum_{M_1,M_2,m_f,m_i} \theta^j(2,1)\theta^{j'}(1,2) = [j,j']^{1/2} (-1)^{2j'+L_1+L_2} \left\{ \begin{array}{ccc} j_f & j' & L_1 \\ j_i & j & L_2 \end{array} \right\} , \tag{3.79}$$

one obtains the following expression of the decay rate

$$\begin{aligned} \frac{d\overline{W}}{d\omega_1} &= \frac{\omega_1\omega_2}{(2\pi)^3 c^2 (2j_i+1)} \sum_{L_1,\lambda_1,L_2,\lambda_2,j} \left[\left[S^j(2,1) \right]^2 + \left[S^j(1,2) \right]^2 + 2 \sum_{j'} d(j,j') S^j(2,1) S^{j'}(1,2) \right] \\ &= \sum_{L_1,\lambda_1,L_2,\lambda_2} \frac{d\overline{W}^{\lambda_1 L_1 \lambda_2 L_2}}{d\omega_1} , \end{aligned} \tag{3.80}$$

where

$$d(j,j') = (-1)^{2j'+L_1+L_2} [j,j']^{1/2} \left\{ \begin{array}{ccc} j_f & j' & L_1 \\ j_i & j & L_2 \end{array} \right\} . \tag{3.81}$$

Equation (3.80) can also be given in terms of the individual electric and/or magnetic multipoles,

$$\frac{d\overline{W}^{\Theta_1 L_1 \Theta_2 L_2}}{d\omega_1} = \sum_{\lambda_{\Theta_1}\lambda_{\Theta_2}} \frac{d\overline{W}^{\lambda_1 L_1 \lambda_2 L_2}}{d\omega_1} , \tag{3.82}$$

where

$$\left\{ \begin{array}{ll} \lambda_\Theta = -1, 1 & \text{if } \Theta = \text{E} \\ \lambda_\Theta = 0 & \text{if } \Theta = \text{M} \end{array} \right. . \tag{3.83}$$

One criterion that checks the precision of the calculation, is the agreement between the values obtained by using different *gauges G*, as already refereed. This agreement is verified when $d\overline{W}^{\lambda_1 L_1 \lambda_2 L_2}/d\omega_1$ is zero when λ_1 or λ_2 has a value equal to -1 in Coulomb *gauge*. Ideally, this agreement is accomplished when the summation in Eq. (3.72) is performed with a complete set of exact wavefunctions and energies. Since the summation in Eq. (3.72) has to be evaluated numerically, the relative difference between two *gauges* gives an indication of the numerical quality of the Dirac spectrum used for the evaluation. In conclusion, the *gauge* invariance can be used not only for checking the implemented final expression, but also to numerically assess the Dirac solutions used in the evaluation.

The differential total decay rate is given by the sum over all multipole contributions

$$\frac{dW}{d\omega_1} = \frac{1}{2} \sum_{\Theta_1 L_1 \Theta_2 L_2} \frac{d\overline{W}^{\Theta_1 L_1 \Theta_2 L_2}}{d\omega_1} \,. \tag{3.84}$$

The factor $1/2$ is included in order to avoid counting each pair twice when both photons have the same characteristics, e.g., the $2E1$ contribution.

Finally, the total decay rate of two-photon emission is given by

$$W^{\mathrm{TE}} = \sum_{\substack{\Theta_1 L_1 \Theta_2 L_2 \\ \text{unless} \\ \text{symmetric terms}}} \int_0^{\omega_t} t_{\Theta_1 L_1 \Theta_2 L_2} \frac{d\overline{W}^{\Theta_2 L_2 \Theta_1 L_1}}{d\omega_1} d\omega_1 \,, \tag{3.85}$$

where

$$t_{\Theta_1 L_1 \Theta_2 L_2} = \begin{cases} 1 & \text{if } \Theta_1 \mathrm{L}_1 \neq \Theta_2 \mathrm{L}_2 \\ 1/2 & \text{if } \Theta_1 \mathrm{L}_1 = \Theta_2 \mathrm{L}_2 \end{cases} \,, \tag{3.86}$$

is included to avoid calculating the same term twice. The superscript is refereed to two-photon emission.

3.4 Evaluation methods of the reduced two-photon amplitude

In this section we describe the numerical methods necessary for the evaluation of the reduced matrix elements defined by Eq. (3.72). The evaluation of such function is an example of an high–order perturbation calculation, which in atomic physics generally requires summations over the *complete* spectrum of the system under consideration. Within the relativistic framework, such a "summation" is not a simple task since it includes a summation over the discrete part of the Dirac spectrum, as well as the integration over the positive– and negative–energy continua. A number of methods have been developed over the past decades to perform this summation consistently. Apart from the various Green's function approaches [52, 58, 114, 115], the *finite basis set* method is widely employed nowadays in (relativistic and non–relativistic) high–order calculations [12, 116, 117]. In this method, a *finite* set of discrete pseudo-states is constructed from some basis functions and used to carrying out the summation. The particular choice of suitable basis functions is crucial for the practical implementation of the method. Usually, the discrete (pseudo–) solutions are built up from *piecewise polynomial* sets. The piecewise polynomials are precisely defined, calculated rapidly on modern computer systems, can represent a great variety of functions, and can be differentiated and integrated easily [118].

3.4.1 Finite basis set approach to the Dirac equation

In the finite basis set approach, the summation of the intermediate states that includes integration over the positive– and negative–energy continua, can be performed very efficiently if one considers the (atomic or molecular) system to be enclosed in a finite cavity with a radius R. This leads to a discretization of the continua and, hence, to a representation of the entire Dirac spectrum in terms of the pseudo-state basis functions. A (quasi–complete) finite set of these functions are determined subsequently by making use of the variational Galerkin method [119]. In this method, we assume the ion (or atom) is enclosed in a finite cavity with a radius R large enough to get a good approximation of the wavefunctions with some suitable set of boundary conditions. In order to construct these functions, we shall turn to the principle of least action [120]

$$\delta S_\kappa = 0 \ , \tag{3.87}$$

from which the Dirac equation (Eq. (3.15)) can be derived. In this expression, the action S_κ is defined as

$$\begin{aligned} S_\kappa &= \frac{1}{2}\int_0^R \{cP_{n\kappa}(r)O_-^\kappa Q_{n\kappa}(r) - cQ_{n\kappa}(r)O_+^\kappa P_{n\kappa}(r) \\ &\quad + V(r)\left[P_{n\kappa}(r)^2 + Q_{n\kappa}(r)^2\right] - 2m_e c^2 Q_{n\kappa}(r)^2\Big\}\, dr \\ &\quad - \frac{1}{2}\,\epsilon \int_0^R \left[P_{n\kappa}(r)^2 + Q_{n\kappa}(r)^2\right] dr + S_\kappa^{\text{bond}} \ , \end{aligned} \tag{3.88}$$

where the upper integration limit R is the radius of the confining cavity. The variational principle applied to S_κ leads to solutions of the Dirac equation. For the sake of shortness, we introduced here the operator

$$O_\pm^\kappa = \frac{d}{dr} \pm \frac{\kappa}{r} \ . \tag{3.89}$$

The term S_κ^{bond} that will be specified below, stands for the boundary conditions and the parameter ϵ is a Lagrange multiplier introduced to ensure the normalization constraint (Eq. (3.17)), Here, the large, $P_{n\kappa}(r)$, and small, $Q_{n\kappa}(r)$, radial components of the electron wavefunctions can be written as a finite expansion

$$\begin{aligned} P(r) &= \sum_{i=1}^{N} p_i B_i(r) \ , \\ Q(r) &= \sum_{i=1}^{N} q_i B_i(r) \ , \end{aligned} \tag{3.90}$$

over some basis functions $B_i(r)$. The explicit form of these functions is not crucial for the following discussion and will be specified later in Subsecs. 3.4.3 and 3.4.4. Moreover, in Eq. (3.90), the

subscripts n and κ have been omitted from the functions $P_{n\kappa}(r)$ and $Q_{n\kappa}(r)$ for the sake of notation simplicity.

Inserting the radial components (3.90) into the least action principle (3.87) and evaluating the variation S_κ with respect to change of expansion coefficients p_i and q_i, we obtain the matrix equation

$$Av = \epsilon Bv \,, \tag{3.91}$$

where $v = (p_1, p_2, \ldots, p_N, q_1, q_2, \ldots, q_N)$ and A and B are symmetric $2N \times 2N$ matrices given, respectively by

$$A = \begin{bmatrix} (V) & c\left[(D) - \left(\frac{\kappa}{r}\right)\right] \\ -c\left[(D) + \left(\frac{\kappa}{r}\right)\right] & -2c^2(C) + (V) \end{bmatrix} + A^{\text{bond}} \,, \tag{3.92}$$

and

$$B = \begin{bmatrix} (C) & 0 \\ 0 & (C) \end{bmatrix}. \tag{3.93}$$

The matrix A^{bond} reflects the boundary conditions, and the $N \times N$ matrices (C), (D), (V) and (κ/r) are given by

$$(C)_{ij} = \int B_i(r) B_j(r) dr \,, \tag{3.94}$$

$$(D)_{ij} = \int B_i(r) \frac{d}{dr} B_j(r) dr, \tag{3.95}$$

$$\left(\frac{\kappa}{r}\right)_{ij} = \int B_i(r) \frac{\kappa}{r} B_j(r) dr. \tag{3.96}$$

$$(V)_{ij} = \int B_i(r) V(r) B_j(r) dr \,. \tag{3.97}$$

Equation (3.91) is known as a generalized eigenvalue problem that can be solved by employing the standard techniques from the linear algebra. In the present work, we have used the well-established Linear Algebra PACKage 3.3.1 (LAPACK) [121], which provides fast and effective routines for solving problems involving matrices. This library package consist of Fortran 90 routines for solving systems of simultaneous linear equations, least-squares solutions of linear systems of equations, eigenvalue problems, and singular value problems, as well as matrix operations, such as LU (Lower Upper triangles), Cholesky and Schur factorizations. In our case, we use the subroutine *DSYGVX* (Double precision, SYmmetric, Generalized eigenValues in eXpert mode), which solves a generalized eigenvalue problem.

By using this package, we obtain $2N$ real eigenvalues ϵ_λ and $2N$ orthogonal eigenvectors v^λ that span both positive and negative energy solutions. Solutions labeled by $i = 1, \ldots, N$ describe the negative continuum $\varepsilon_n^i < -2mc^2$ and solutions labeled by $i = N+1, \ldots, 2N$ describe bound states and the positive continuum $\varepsilon_n^i > 0$.

The finite basis set method allows to study the effect of the negative continuum since the index i can be restricted to the bound and positive continuum states $i = N + 1, ..., 2N$.

By making use of a finite piecewise polynomials basis set to describe the large and small radial components of the Dirac wavefunctions (Eq. (3.90)), both, $I_L^{\pm}(\omega)$ and $J_L(\omega)$ can be reduced to a linear combination of the integrals

$$\int_0^{\infty} F^{L,S}(r)F^{L,S}(r)j_L\left(\frac{\omega r}{c}\right)dr = \sum_{i=1}^{n}\sum_{j=1}^{n} f_i^{L,S} f_j^{L,S} (j_L)_{ij} \,. \tag{3.98}$$

Here, for the sake of shortness, we denote $F^L(r) = P(r)$ and $F^S(r) = Q(r)$, as well as $f_i^L = p_i$ and $f_i^S = q_i$, and the matrix elements $(j_L)_{ij}$ are defined by

$$(j_L)_{ij} = \int_0^{\infty} B_i(r)B_j(r)j_L\left(\frac{\omega r}{c}\right)dr \,. \tag{3.99}$$

In fact, these radial matrix elements are the "building blocks" of the two–photon decay rate evaluation.

3.4.2 Spurious states and boundary conditions

The practical implementation of the finite basis set approaches is usually "complicated" by the well–known spurious states problem. These non–physical states appear as solutions of the single–particle radial Dirac equation for $\kappa > 0$ ($p_{1/2}, d_{3/2}, \ldots$ orbitals) [122]. Although the spurious solutions "spoil" the spectrum of the ion (or atom) under consideration, they are required for providing completeness of the basis set. The problem of spurious states has been discussed in detail in the literature, and several solutions were proposed [122, 123, 124, 125, 126]. *Johnson et al.* [120], in their pioneering applications of the B–splines to the relativistic many–body problem, have proposed that the function S_κ^{Bond} in Eq. (3.88) could be given by

$$S_\kappa^{\text{Bond}} = \begin{cases} \frac{c}{4}\left[P^2(R) - Q^2(R)\right] + \frac{c}{2}P(0)\left[P(0) - Q(0)\right] & \text{for } \kappa < 0 \\ \frac{c}{4}\left[P^2(R) - Q^2(R)\right] + \frac{c}{2}P(0)\left[2cP(0) - Q(0)\right] & \text{for } \kappa > 0 \end{cases} , \tag{3.100}$$

in order to *lift* the spurious states to higher energies (to the negative continuum), thus restoring the low–energy mapping of the physical solutions. For variations of $P(r)$ and $Q(r)$, the boundary terms vanish if

$$P(0) = 0 \quad \text{and} \quad P(R) = Q(R) \,. \tag{3.101}$$

The boundary condition at the outer boundary $r = R$ is the *MIT–bag-model* condition [127], and was included to avoid the Klein's paradox, which arises when one attempts to confine a particle to a cavity, essentially by forcing the radial current crossing the boundary to vanish [83].

With this boundary condition, the matrix A^{bond} is given by

$$A_{ij}^{\text{bond}} = \begin{cases} c\delta_{i,1}\delta_{j,1} - \frac{c}{2}\delta_{i,1}\delta_{j,n+1} - \frac{c}{2}\delta_{i,n+1}\delta_{j,1} + \frac{c}{2}\delta_{i,n}\delta_{j,n} - \frac{c}{2}\delta_{i,2n}\delta_{j,2n} & \text{if } \kappa \leq 0\,, \\ 2c^2\delta_{i,1}\delta_{j,1} - \frac{c}{2}\delta_{i,1}\delta_{j,n+1} - \frac{c}{2}\delta_{i,n+1}\delta_{j,1} + \frac{c}{2}\delta_{i,n}\delta_{j,n} - \frac{c}{2}\delta_{i,2n}\delta_{j,2n} & \text{if } \kappa > 0\,. \end{cases} \tag{3.102}$$

Shabaev et al. proposed another method for dealing with the spurious states, the so-called *dual kinetical balanced* approach [126]. This method takes advantage of the kinetically balanced relation between the small and large components in the non-relativistic limit (Eq. (3.16)) and a similar kinetically relation that considers $V(r) \to -V(r)$, $\kappa \to -\kappa$ and $E \to -E$. In detail, this method does not consider any bound matrix A^{bond} and instead of using the expansion given by Eq. (3.90), it defines another expansion given by

$$\begin{aligned} P(r) &= \sum_{i=1}^{N} p_i \begin{bmatrix} B_i(r) \\ \frac{1}{2c}\left(\frac{d}{dr} + \frac{\kappa}{r}\right) B_i(r) \end{bmatrix}, \\ Q(r) &= \sum_{i=1}^{N} q_i \begin{bmatrix} \frac{1}{2c}\left(\frac{d}{dr} - \frac{\kappa}{r}\right) B_i(r) \\ B_i(r) \end{bmatrix}. \end{aligned} \tag{3.103}$$

The spurious state are avoided since both P and Q functions have the proper behavior at zero and ∞.

While the former approach has been used in all the present calculations, the last approach can implemented in future calculations to assess the precision of the obtained results.

3.4.3 B-splines

The basis splines [128], also called *B–splines*, are one of the most commonly used family of piecewise polynomials. These polynomials, which are well adapted to numerical tasks, have been successfully used in many atomic–physics studies. For example, *Johnson et al*. have applied the B–splines to the many–body perturbation theory [120, 129]. *Froese Fischer et al*. used them in (variational) Hartree–Fock calculations and continuum problems [130, 131]. *Qiu* and *Froese Fischer* introduced the integration by cell algorithm for Slater integrals in a B–spline basis obtaining an improved efficiency and accuracy over traditional methods [132]. *Bhatti et al*. [133] used similar techniques to find an approximate solution of a set of the non–homogeneous second–order differential equations and to obtain static polarizabilities of the hydrogenic states. *Indelicato et al*. employed B–splines in the multi–configuration Dirac–Fock (MCDF) relativistic atomic structure calculations [19, 134] and in relativistic two–photon decay calculations [12, 78, 79]. Although B–spline basis sets were proven to be an important tool for studying the variety of atomic structure and dynamics problems (see Ref. [116] for further details and examples), one might adopt other piecewise polynomial sets to speed up relativistic high–order calculations, such as two-photon decay rates, especially for many–electron systems.

Following the de Boor [128] textbook, we divide the interval of interest $[0, R]$ into segments whose endpoints define a knot sequence $\{t_i\} = 1, 2, \ldots, n + k$. The B–splines of the order k, $B_{i,k}(r)$, are defined on this knot sequence by the recurrence relation

$$B_{i,k}(r) = \frac{r - t_i}{t_{i+k-1} - t_i} B_{i,k-1}(r) + \frac{t_{i+k} - r}{t_{i+k} - t_{i+1}} B_{i+1,k-1}(r) \,, \tag{3.104}$$

where the B–splines of the first order read as

$$B_{i,1}(r) = \begin{cases} 1, & t_i \leq r \leq t_{i+1} \\ 0, & \text{otherwise} \end{cases} \,. \tag{3.105}$$

The first 1, 2... k and the last $n+1$, $n+2$... $n+k$ knots must be equal and are defined as: $t_1 = t_2 = \ldots = t_k = 0$ and $t_{n+1} = t_{n+2} = \ldots = t_{n+k} = R$. Otherwise, the t_i knots with $k < i < n$ follow an exponential grind.

3.4.4 B-polynomials

In this work, we argue that the Bernstein polynomials, or *B–polynomials* [135], are a good alternative to the B–splines since they enable *analytical* finite basis set calculations. They are polynomial functions of n^{th} degree that have been recently used to obtain the solution of some linear and non-linear differential equations [136, 137, 138]. *Bhatti and Perger* developed an algorithm for constructing accurate solutions to the radial Dirac equation in a B-polynomial basis set [139].

We employed the finite (discrete) solutions constructed from the B–polynomial sets in order to compute two–photon decay of H–like ions. Theoretical analysis of this process requires evaluation of the second–order transition amplitudes and, hence, can be used as a "testing ground" for the high–order B–polynomial calculations.

Results of the relativistic calculations for these rates obtained for the $2s_{1/2} \to 1s_{1/2}$ transition in neutral hydrogen and H–like ions will be presented in Sec. 4.2 of the next Chapter. We compare it with the "standard" B–spline calculations, as well as the predictions by *Labzowsky et al.* [59]. Detailed comparison with these predictions will allow us to justify the application of the B–polynomial approach in second–order calculations and to underline its advantages.

3.4.4.1 Description of B-polynomials

The B–polynomials of kth–order are defined by [135, 136, 137]

$$B_{i,k}(r) = \begin{pmatrix} k \\ i \end{pmatrix} \frac{(r-a)^i \, (b-r)^{k-i}}{(b-a)^k} \quad , \quad i = 0, 1, \ldots, k \,, \tag{3.106}$$

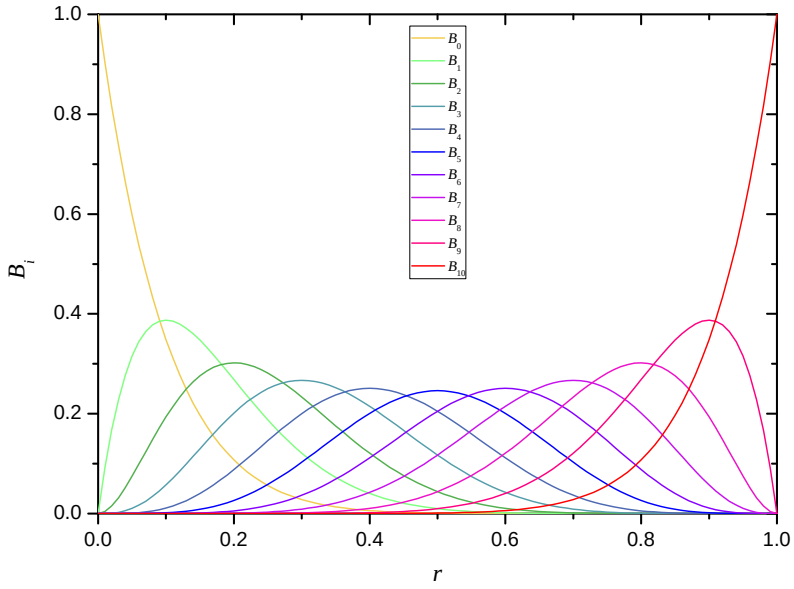

Figure 3.3: Eleven B–polynomials of degree ten - All the B-polynomial are positive and define between zero and R. The sum of all polynomials is unity.

where the standard form of the binomial coefficients is used

$$\begin{pmatrix} k \\ i \end{pmatrix} = \frac{k!}{i!(k-i)!} \,. \tag{3.107}$$

Here, a and b denote the limits of the interval $[a, b]$ over which the polynomials are defined to form a complete basis. Since the atomic system is defined in a finite cavity of radius R, we take $a = 0$ and $b = R$.

As seen from definition (Eq. (3.106)), there are $(k+1)$ polynomials of degree k. By definition, we set $B_{i,k}(r) = 0$ if $i < 0$ and $i > k$. As an example, a set of eleven B–polynomials of degree ten is plotted in Fig. 3.3, where is showed that each B-polynomial is positive and the sum of all B-polynomials at all points is unitary.

The great advantage of B–polynomials is that they allow for an analytical evaluation of the matrices (C), (D) and (κ/r) in the generalized eigenvalue problem (3.91). That is, by inserting $B_i = B_{i,k}(r)$

into Eqs. (3.94)-(3.96), we obtain

$$(C)_{ij} = R\binom{k}{i}\binom{k}{j}\frac{1}{(2k+1)\binom{2k}{i+j}}\,, \tag{3.108}$$

$$(D)_{ij} = \binom{k}{i}\binom{k}{j}\frac{(j-i)}{2(i+j)\binom{2k-1}{i+j}}\,, \tag{3.109}$$

$$\left(\frac{\kappa}{r}\right)_{ij} = \kappa\binom{k}{i}\binom{k}{j}\frac{1}{(i+j)\binom{2k}{i+j}}\,. \tag{3.110}$$

Apart from the basis functions $B_{i,k}(r)$, the knowledge of the nuclear charge distribution is also required for an evaluation of the matrix (V) whose elements are defined by Eq. (3.97). For example, for the point–like nucleus model, $V^{\rm p}(r) = -Z/r$, these matrix elements read as

$$(V^{\rm p})_{ij} = -Z\binom{k}{i}\binom{k}{j}\frac{1}{(i+j)\binom{2k}{i+j}}\,. \tag{3.111}$$

A more complicated expression for the matrix (V) is obtained by taking into account for the finite nuclear size effects. To address these effects, we employed the potential of Eq. (3.8) due to a uniform spherical nuclear charge distribution with radius $R_{\rm N}$. By employing this potential in Eq. (3.97), we obtain

$$\begin{aligned}(V^{\rm U})_{ij} = (V^{\rm p})_{ij} + Z\binom{k}{i}\binom{k}{j}\Bigg\{&B\left(\frac{R_{\rm N}}{R};i+j,1-i-j+2k\right)\\ &-\frac{1}{2}\left(\frac{R_{\rm N}}{R}\right)^{i+j}\frac{3_2F_1\left[\{1+i+j,i+j-2k\},\{2+i+j\},\frac{R_{\rm N}}{R}\right]}{1+i+j}\\ &+\frac{1}{2}\left(\frac{R_{\rm N}}{R}\right)^{i+j}\frac{{}_2F_1\left[\{3+i+j,i+j-2k\},\{4+i+j\},\frac{R_{\rm N}}{R}\right]}{3+i+j}\Bigg\}\,,\end{aligned} \tag{3.112}$$

where $B(x;h,k)$ and ${}_pF_q$ are the incomplete beta function and the generalized hypergeometric function respectively. These mathematical functions are defined by

$$B(x;h,k) = \int_0^x t^{h-1}(1-t)^{k-1}dt\,, \tag{3.113}$$

n	E^{Exact}	$\Delta E_{\text{TW}}^{\text{B-Pol}}$	$\Delta E_{\text{TW}}^{\text{B-splines}}$	$\Delta E_{\text{BP}}^{\text{B-Pol}}$
1	-0.5000066565953603	1.6(−12)	3.8(−10)	2.7(−12)
2	-0.12500208018900594	1.4(−12)	1.4(−10)	1.5(−8)
3	-0.05555629517766647	1.7(−7)	3.4(−9)	1.8(−3)
4	-0.03125033803007682	1.4(−3)	5.9(−5)	2.3(−1)

Table 3.2: Energies obtained from finite basis set method - Relative differences between the computed energy eigenvalues of hydrogen (s states) using B-polynomials and B-splines and the exact results of the Dirac equation, E^{Exact}, given by Eq. (3.18). $\Delta E_{\text{TW}}^{\text{B-Pol}}$ and $\Delta E_{\text{TW}}^{\text{B-splines}}$ represent, respectively, the relative differences calculated in this work (TW) with the B-polynomials and with the B-splines. $\Delta E_{\text{BP}}^{\text{B-Pol}}$ denote the relative difference obtained with the B-polynomials values by *Bhatti and Perger* [137]. Powers of ten are given in parentheses.

and

$$ {}_pF_q\left[\left\{a_1,...,a_p\right\},\left\{b_1,...,b_q\right\},x\right] \;=\; \sum_{s=0}^{\infty}\frac{(a_1)_s\,..\left(a_p\right)_s}{(b_1)_s\,..\left(b_q\right)_s}\frac{x^s}{s!}\,, \tag{3.114} $$

with $(q)_s$ being the Pochhammer symbol or descending factorial given by

$$ (q)_s = q(q-1)(q-2)...(q-s+1)\,. \tag{3.115} $$

3.4.4.2 Energies obtained with B-polynomials basis set

Having made a description of the B-polynomilas basis set, we now present some Dirac energies obtained with this basis set, as well as with B-splines. In Table 3.2 is the relative differences between the computed energies of the $ns_{1/2}$ states of neutral hydrogen and the corresponding "exact" values, $\varepsilon_n^{\text{Exact}}$, defined by Eq. (3.18). Here, $\Delta E_{\text{TW}}^{\text{B-Pol}}$ and $\Delta E_{\text{TW}}^{\text{B-splines}}$ represent the differences obtained by employing the B–polynomial and B–spline sets, correspondingly. Moreover, $\Delta E_{\text{BP}}^{\text{B-Pol}}$ denote the relative difference calculated with the B–polynomial values by *Bhatti and Perger* [137]. The B-polynomial relative differences are very similar each to the B–Spline relative differences, for $n > 1$. For $n = 1$, the latter case achieved an excellent 12 digits agreement with the exact result, two orders of magnitude better than the B-splines.

3.4.4.3 Analytical expression for the radial matrix elements

Inserting Eq. (3.106) into Eq. (3.99) we find that $(j_L)_{ij}$ matrix elements are given *analytically* by

$$\begin{aligned}(j_L)_{ij} &= R\left(\frac{\omega R}{c}\right)^L \begin{pmatrix} k \\ i \end{pmatrix}\begin{pmatrix} k \\ j \end{pmatrix} \frac{\pi\,(i+j+L)!\,(2k-i-j)!}{2^{2(L+k+1)}} \\ &\times\ {}_2\widetilde{F}_3\left[\left\{\frac{i+j+L+1}{2}, \frac{i+j+L+2}{2}\right\}\ , \right. \\ &\left. \left\{\frac{2L+3}{2}, \frac{2k+L+2}{2}, \frac{2k+L+3}{2}\right\}, -\left(\frac{\omega R}{2c}\right)^2\right]\ , \end{aligned} \tag{3.116}$$

where ${}_p\widetilde{F}_q$ is the regularized generalized hypergeometric function,

$${}_p\widetilde{F}_q\left[\left\{a_1,...,a_p\right\},\left\{b_1,...,b_q\right\},x\right] = \frac{1}{\Gamma\left(b_1\right)...\Gamma\left(b_q\right)}\,{}_pF_q\left[\left\{a_1,...,a_p\right\},\left\{b_1,...,b_q\right\},x\right]\ , \tag{3.117}$$

and $\Gamma(x)$ is the gamma function given by

$$\Gamma(x) = \int_o^{-\infty} t^{x-1}e^{-t}dt\ . \tag{3.118}$$

3.5 Negative contribution to the two-photon emission

Since the energy release in two-photon transitions (Eq. (2.1)) is much less than the energy required for the electron-positron pair production ($2c^2$), the contribution from the negative part of Dirac's spectrum in Eq. (3.72) can be expected to be negligible, even for the decay in HCI. This is equivalent to restrict the summation in Eq. (3.72) only over positive energy states. From a practical view point, such exclusion can also simplify calculations, in particular, ones that involves many electrons.

Despite this restriction, it was argued that second-order evaluations such as Thomson scattering [140], interaction of ions with intense electromagnetic pulses [141, 142] in the under-critical regime, as well as magnetic transitions in two-electron ions [18, 19, 143], have to take into account the contribution of the negative continuum. The contribution of the negative energy states in two-photon properties has been done by *Labzowsky et al.* [59] who focused on the $E1M1$ and $E1E2$ $2p_{1/2} \rightarrow 1s_{1/2}$ total decay rates. In that work, the relativistic calculations have indicated the importance of negative energy contributions in H-like ions not only for high-Z but also for low-Z domain.

For the low-Z ions it is useful to estimate the negative-energy contributions within the semi-relativistic approach as proposed by *Labzowsky et al.* [59]. According to this approach, the sum in Eq. (3.42) is restricted to the negatives states. The corresponding energy denominator in Eq. (3.42) can be written as $E_n - E_i + \omega_j \sim E_n \sim -2c^2$ since the negative energy states have energies of the order

$-2c^2$, which is much lower compared with bound energies. The corresponding expression is given by

$$\frac{dw^{(-)}}{d\omega_1} = \frac{\omega_1\omega_2}{(2\pi)^3 4c^6}\left|\sum_{n^{(-)}}\left(\left\langle f\left|A_2^*\right|n\right\rangle\left\langle n\left|A_1^*\right|i\right\rangle + \left\langle f\left|A_1^*\right|n\right\rangle\left\langle n\left|A_2^*\right|i\right\rangle\right)\right|^2 d\Omega_1 d\Omega_2 \,. \tag{3.119}$$

For the sake of simplicity, we restrict to the case of Coulomb *gauge*, i.e., $G = 0$. So far, the states $n^{(-)}$ were considered as solutions of the Dirac equation. However, these states can also be approximately obtained from a Schrödinger equation with a repulsive nuclear potential and a $2c^2$ energy shift. In fact, these states are the solutions of the Schrödinger equation for positrons. Therefore, the $n^{(-)}$ form a *complete* set of solutions [83], and Eq. (3.119) can be further simplified using the closure relation.

$$\frac{dw^{(-)}}{d\omega_1} = \frac{\omega_1\omega_2}{(2\pi)^3 c^6}\left|\hat{\boldsymbol{e}}_{\boldsymbol{1}}\cdot\hat{\boldsymbol{e}}_{\boldsymbol{2}}\left\langle f\left|e^{-i(\boldsymbol{k_1}+\boldsymbol{k_2})\cdot\boldsymbol{r}}\right|i\right\rangle\right|^2 d\Omega_1 d\Omega_2 \,. \tag{3.120}$$

The exponential term in Eq. (3.120) can be written as a Taylor series expansion, i.e.,

$$e^{-i(\boldsymbol{k_1}+\boldsymbol{k_2})\cdot\boldsymbol{r}} = 1 - i(\boldsymbol{k_1}+\boldsymbol{k_2})\cdot\boldsymbol{r} + \frac{\boldsymbol{k_1}\cdot\boldsymbol{r}(\boldsymbol{k_2}\cdot\boldsymbol{r})}{2} \ldots \tag{3.121}$$

We retained only the first three terms of this expansion since they provide the main multipole groups. In contrast to the standard multipole expansion, such as in Eq. (3.44), the series (3.121) usually does not allow one to make a clear distinction between the different multipole components of the emitted radiation. However, one can relate each term of the expansion with groups of different multipoles. The first term of the expansion, which is the one value term, is related to the long wavelength approximation. It corresponds to the electric dipole term $2E1$ in the non-relativistic approximation. The contribution of this term for the decay rate is zero due to the orthogonality of the wavefunctions ($\langle f|i\rangle = \delta_{if}$). Therefore, in the non-relativistic limit the negative continuum does not contribute for the $2E1$ multipole. The second term contains the $\boldsymbol{k_1}\cdot\boldsymbol{r}$ and $\boldsymbol{k_2}\cdot\boldsymbol{r}$ terms and is related to the multipoles $E1E2$ and $E1M1$. The contribution of these terms is zero in the $2s_{1/2} \to 1s_{1/2}$ transition due to parity selection rule, and in the $2p_{1/2} \to 1s_{1/2}$ transition the contribution is given by

$$\begin{aligned}\frac{d\overline{W}^{(-)}_{E1E2,\,E1M1}}{d\omega_1} &= \frac{\omega_1\omega_2}{(2\pi)^3 c^6}\left|\hat{\boldsymbol{e}}_{\boldsymbol{1}}\cdot\hat{\boldsymbol{e}}_{\boldsymbol{2}}\left\langle 1s\left|(\boldsymbol{k_1}+\boldsymbol{k_2})\cdot\boldsymbol{r}\right|2p\right\rangle\right|^2 d\Omega_1 d\Omega_2 \\ &= \frac{2^{17}}{3^{12}}\frac{1}{\pi Z^2 c^8}\omega_1\omega_2(\omega_1^2+\omega_2^2)\,,\end{aligned} \tag{3.122}$$

if one performs an integration over the photon emission angles as well as a summation over the polarization states (further details in Ref. [59]).

The third term of the expansion in Eq. (3.121) is related to the multipoles $M1M1$, $M1E2$ and

$E2E2$. For the $2s_{1/2} \to 1s_{1/2}$ transition the contribution is equal to

$$\begin{aligned} \frac{d\overline{W}^{(-)}_{M1M1,\, M1E2,\, E2E2}}{d\omega_1} &= \frac{\omega_1\omega_2}{(2\pi)^3 c^6} \left|\hat{\boldsymbol{e}}_{\boldsymbol{1}} \cdot \hat{\boldsymbol{e}}_{\boldsymbol{2}} \left\langle 1s \left| \boldsymbol{k_1} \cdot \boldsymbol{r} (\boldsymbol{k_2} \cdot \boldsymbol{r}) \right| 2s \right\rangle\right|^2 d\Omega_1 d\Omega_2 \\ &= \frac{2^{22}}{3^{13}} \frac{1}{5\pi Z^4 c^1 0} \omega_1^3 \omega_2^3 \,. \end{aligned} \tag{3.123}$$

Equations (3.122) and (3.123) provide the differential rates for the main multipole two-photon decay channels in $2s_{1/2} \to 1s_{1/2}$ and $2p_{1/2} \to 1s_{1/2}$, as obtained within the non-relativistic framework, by restricting the summation over the intermediate spectrum to the negative energy states only. Being valid for low-Z ions, these expressions allow the analysis of the negative-energy contribution to the total decay rate. In detail, the total decay rate for the $2s_{1/2} \to 1s_{1/2}$ and $2p_{1/2} \to 1s_{1/2}$ transitions, taking into account the main multipoles contributions, are

$$\overline{W}^{(-)}_{M1M1,\, M1E2,\, E2E2} = 1.247 \times 10^{-6} (\alpha Z)^{10} \,, \tag{3.124}$$

$$\overline{W}^{(-)}_{E1M1,\, E1E2} = 5.822 \times 10^{-5} (\alpha Z)^{8} \,. \tag{3.125}$$

These equations, together with Eqs. (3.122) and (3.123), can be used later in order to check the validity of our numerical calculations in the low-Z domain.

3.6 Two-photon emission angular and polarization correlations

The two-photon differential decay rate in case of the excited ions being initially unpolarized and the polarization of the emitted photons remain unobserved during the measurement, can be obtained using Eq. (3.42). Since no particular direction is preferred for the decay of an unpolarized ion, it is most convenient to adopt the quantization ($\hat{z}$) axis along the momentum of the first photon: $\boldsymbol{k_1} \| \hat{z}$. Such a choice of the quantization axis leads to the definition of the angular correlation function as

$$W^{\mathrm{C}}(\theta) = \frac{8\pi^2 (E_i - E_f)}{[j_i]} \sum_{m_i, m_f} \sum_{e_1, e_2} \frac{dw}{d\omega_1\, d\Omega_1\, d\Omega_2} (\theta_1 = 0, \phi_1 = 0, \phi_2 = 0) \,, \tag{3.126}$$

where the polar angle of the second photon (θ_2) is defined as the opening angle (θ). In the above equation, moreover, the factor $8\pi^2$ arises from the integration over the solid angle of the first photon ($d\Omega_1$), as well as the integration over the azimuthal angle of the second photon ($d\phi_2$). The variable $W^{\mathrm{C}}(\theta)$ represents the (density) number of photon pair emitted per second with a given opening angle θ, irrespectively of their polarizations.

Due to the total photon-photon permutation symmetry that characterizes the amplitude in Eq. (3.42), the analytic expression for $W^{\mathrm{C}}(\theta)$ can only contain terms which are θ–even, since the exchange of the

emitted photons corresponds to the algebraic replacement $\theta \to -\theta$. By virtue of this, we are allowed to decompose $W^{\mathrm{C}}(\theta)$ in terms of a polynomial expansion in $\cos\theta$

$$W^{\mathrm{C}}(\theta) = a_0(1 + a_1\cos\theta + a_2\cos^2\theta + a_3\cos^3\theta + a_4\cos^4\theta + ...)\,, \tag{3.127}$$

where the parameters a_i depend on the atomic number of the ion, the energy sharing parameter y and the states involved in the decay. Such parametrization in $\cos\theta$ polynomials can be compared with other theoretical calculations and provides an accurate fit model for future experiments which involves two-photon transitions.

For the $2s_{1/2} \to 1s_{1/2}$ transition, it might be of interest writing the coefficients a_i directly in terms of the general reduced matrix elements defined in Eq. (3.72), in order to study the effects of higher terms of the electron-photon interaction expansion other than electric dipolar term. We restrict to electric and magnetic multipoles less than third order, i.e., multipoles $\Theta_1 L_1 \Theta_2 L_2$ (Θ = E, M) with L_1 and L_2 less than three. By doing so, Eq. (3.127) is given by

$$\begin{aligned} W^{\mathrm{C}}(\theta) \quad \propto \quad & |S_{E1}|^2 \Bigg(1 + \cos^2\theta - 2\frac{S_{M2}}{S_{E1}} + 4\frac{S_{M1}}{S_{E1}}\cos\theta + \\ & 6\frac{S_{M2}}{S_{E1}}\cos^2\theta + 4\frac{S_{E2}}{S_{E1}}\cos^3\theta + ...\Bigg)\,, \end{aligned} \tag{3.128}$$

where, for the sake of brevity, we have introduced the notation

$$S_{L\lambda} = (-1)^{j-1/2}\sqrt{[j]}\left[S(2,1)^{j}_{L\lambda L\lambda} + S(1,2)^{j}_{L\lambda L\lambda}\right] - (-1)^{j+1/2}\sqrt{[j+1]}\left[S(2,1)^{j+1}_{L\lambda L\lambda} + S(1,2)^{j+1}_{L\lambda L\lambda}\right]. \tag{3.129}$$

The dependencies on y (energy sharing) and Z (atomic number) are included in the $S(2,1)$ elements (3.72). The energy sharing is given by $y = \omega_1/\omega_t$, i.e., is the energy of the first photon divided by the transition energy or the sum of both photons.

If only the electric dipolar term of the multipole expansion was taking into account, the angular correlation reduces to a term proportional to $(1 + \cos^2\theta)$. As can be seen in Eqs. (3.128) and (3.128), the coefficient of the θ-asymmetric terms (a_1) is brought into existence by the next leading order term, $M1$, in the multipole expansion. After the term $M1$, the next leading terms, $E2$ and $M2$, introduces even more asymmetry to the angular distribution. This result is similar to the one expressed in Eq. (18) of Ref. [80] where the multipole contributions were evaluated for the case of two-photon absorption with $\theta = 0$.

We used the spin-polarization density matrix to perform the analysis of the polarization properties of the emitted radiation, Such formalism have been applied several times [58, 144, 145] to the two-photon decay rate. We restrict here to refer the relation between the first degree polarization and the

second order amplitudes (3.43), which is given by

$$P_L(\theta) = \frac{2}{[j_i]}\mathrm{Re}\left[\sum_{m_i,m_f,e_2} M(2,1)M(2,1)^*\right], \tag{3.130}$$

and further details can be traced to the previous references. The derivation of Eq. (3.130) follows from the assumption that the polarization of only one of the photons is observed. The degree of linear polarization of the second photon can also be defined as [145]

$$P_L(\theta) = \frac{P_{L\parallel}(\theta) - P_{L\perp}(\theta)}{P_{L\parallel}(\theta) + P_{L\perp}(\theta)}, \tag{3.131}$$

where $P_{\parallel(\perp)}$ denotes the two-photon decay rate, for the case the first photon polarization remains unobserved and the linear polarization of the second photon is detected parallel (perpendicular) to the reaction plane. It can be noticed that the denominator in the right term of Eq. (3.131) is nothing but the angular correlation $W^{\mathrm{C}}(\theta)$ defined in Eq. (3.126). Therefore, by employing Eq. (3.127) into Eq. (3.131) and using the symmetry properties of $M(2,1)$, we can parametrize P_L as

$$P_L(\theta) = \frac{b_0(1 + b_1\cos\theta + b_2\cos^2\theta + b_3\cos^3\theta + ...)}{a_0(1 + a_1\cos\theta + a_2\cos^2\theta + a_3\cos^3\theta + ...)}. \tag{3.132}$$

Analogously to Eq. (3.128), we write the first degree polarization in terms of the reduced matrix elements. By doing so, Eq. (3.132) is given by

$$P_L(\theta) = \frac{-\sin^2\theta\left(1 - 2\frac{S_{M2}}{S_{E1}} - 4\frac{S_{M1}}{S_{E1}}\cos\theta\right)}{1 + \cos^2\theta - 2\frac{S_{M2}}{S_{E1}} + 4\frac{S_{M1}}{S_{E1}}\cos\theta + 6\frac{S_{M2}}{S_{E1}}\cos^2\theta + 4\frac{S_{E2}}{S_{E1}}\cos^3\theta}, \tag{3.133}$$

In case of just considering the electric dipole component of the multipole expansion, then $P_L(\theta)$ is given by $-\sin^2\theta/(1+\cos^2\theta)$. Therefore, the degree of polarization of the photon is zero for lower charged H-like ions and for values of θ equal to zero or π. For $\theta = \pi/2$ the degree of polarization is minimum corresponding to minus one. The photon is vertically polarized.

In Sec. 4.3 we shall proceed with the numerical evaluation of the coefficients a_i and b_i.

3.7 Resonant transitions

If the energy of an intermediate state E_n is equal to the energy $(E_i - \omega_r)$ in the denominators of Eq. (3.42) (with $r = 1, 2$), the differential emission rate has a pole or a resonant behavior at the energy E_n. Physically, this occurs when an intermediate virtual state, between the initial and final states, coincides with a real state so that the two-photon transition coincides with the cascade de-excitation process.

For example, in the $2E1\ 3s \rightarrow 1s_{1/2}$ transition, the shape of the frequency distribution presents narrow resonances at energies corresponding to the $3s \rightarrow 2p_{3/2,1/2} \rightarrow 1s_{1/2}$ cascades. This effect has been confirmed both experimentally [146] and theoretically [147].

In this work, we refer to initial states that have intermediate bound states as resonant states and non-resonant states otherwise. While resonant states have cascade transitions as a possible decay channel, in non-resonant states the cascade process is absent. As refereed in previous chapter, the two-photon decay from the non-resonant state $2s$ gives a great contribution to the hydrogen recombination. The $ns \rightarrow 1s_{1/2}$ ($n > 2$) and $nd \rightarrow 1s_{1/2}$ two-photon transitions can also give a sizable contribution to the process of hydrogen recombination for the CMB as argued in Refs. [148, 149]. Since in resonant states the cascade photons can be reabsorbed, the problem of separation of the pure two-photon contribution from the cascade contribution arises in the process of hydrogen recombination. An interference term between the two decay channels should also be taken into account on the balance equations of hydrogen recombination.

The cascade problem also arises in connection with HFI in He-like HCI. In Fig. 1.1 it is represented the decay of the metastable $1s2p\ ^3\mathrm{P}_0$ level. As refereed in previous chapter, for isotopes with nuclear spin $I = 0$, the HFI dominates the $^3\mathrm{P}_0$ decay, while for isotopes with $I \neq 0$, where the $2^3\mathrm{P}_0$ decay is unquenched, the two cascade processes, $1s2p\ ^3\mathrm{P}_0 \rightarrow 1\mathrm{s2s}\ ^3\mathrm{S}_1 + E1 \rightarrow 1s^2\ ^1\mathrm{S}_0 + M1$ and $1s2p\ ^3\mathrm{P}_0 \rightarrow 1\mathrm{s2p}\ ^3\mathrm{P}_1 + \mathrm{M1} \rightarrow 1s^2\ ^1\mathrm{S}_0 + E1$ are the main dominant channels. The corresponding decay rate was first evaluated by *Drake* [150] and later by *Savukov* and *Johnson* [151] by subtracting the resonant peaks at the two-photon distribution with fitted Lorentzian profile (details not relevant for this discussion of this shape are give further on in Eq. (7.42)). The Lorentzians profiles were identified as the cascade terms, and the result of the subtraction associated with both "pure" two-photon and interference term between the two processes.

Closely related with the calculation of the $E1M1$ decay of the $^3\mathrm{P}_0$ to the $^1\mathrm{S}_0$ is the PNC testing in He-like HCI, which was already mentioned. Therefore, the calculation method for resonant states is crucial for accurate evaluation of the $E1M1$ total rate.

The divergent behavior of the resonant denominator in the Eq. (3.72) is related to the Green function used in that expression, which does not take into account the interaction between the electron and the vacuum fluctuations of the electromagnetic field. Similar approach concerning double Compton scattering have recently been discussed in Ref. [152]

In this section, which uses the techniques described in Sec. 3.3, is studied the two–photon decay of several excited states using two approaches to deal with resonances and the problem of the cascade separation, the Line Profile Approach (LPA) [153] and QED approach based on the analysis of the relativistic two-loop self-energy Approach (TLA) [154, 155], to regularize the resonant contribution to the decay rate. We present calculated values for two-photon decay rates obtained with both approaches for one-electron ions with a nuclear charge of up to 92 in the next chapter.

3.7.1 Line profile approach

To deal with singularities present in resonant states, the LPA approach is based in the summation of an infinite series of the electron self-energy insertions into the electron propagator as performed in [153, 156]. This sum is equivalent to a geometric progression and in this way the electron self-energy matrix element (and the level width as its imaginary part) enters in the energy denominator and shifts the pole from the real axis into the complex energy plane, thus making the transition rate finite. An expression for the differential emission that takes partially into account this contribution, using the LPA, is [153, 156]

$$\frac{dw^{\mathrm{LPA}}}{d\omega_1} = \frac{\omega_1\omega_2}{(2\pi)^3c^2}\left|\sum_n\left(\frac{\left\langle f\left|A_2^*\right|n\right\rangle\left\langle n\left|A_1^*\right|i\right\rangle}{V_n - V_i + \omega_1} + \frac{\left\langle f\left|A_1^*\right|n\right\rangle\left\langle n\left|A_2^*\right|i\right\rangle}{E_n - E_i + \omega_2}\right)\right|^2 d\Omega_1 d\Omega_2 \,, \tag{3.134}$$

where

$$V_n = E_n + \eta_{n,r}\left\{\left\langle n\left|\sum{}_e\right|n\right\rangle + \left\langle n\left|\prod{}_e\right|n\right\rangle\right\} \,, \tag{3.135}$$

with

$$\eta_{n,r} = \begin{cases} 1 & \text{if } n \text{ is a resonant intermediate state} \\ 0 & \text{otherwise} \end{cases} \,, \tag{3.136}$$

and $\left\langle n\left|\sum_e\right|n\right\rangle$ and $\left\langle n\left|\prod_e\right|n\right\rangle$ are the electron mean value of the self-energy and vacuum polarization operators in lowest order for the state n, respectively. Both the mean value of the self-energy and vacuum polarization operator have a real part, ΔE_n, that is a correction to the energy E_n. On the other hand, only the self–energy operator has an imaginary part, $\Gamma_n/2$, which is the width of the state n.

A reasoning similar to the one followed to obtain (3.80) leads to

$$\frac{d\overline{W}^{\mathrm{LPA}}}{d\omega_1} = \sum_{L_1,\lambda_1,L_2,\lambda_2}\frac{d\overline{W}^{\mathrm{LPA}}_{L_1,\lambda_1,L_2,\lambda_2}}{d\omega_1} \,, \tag{3.137}$$

where

$$\begin{aligned}\frac{d\overline{W}^{\mathrm{LPA}}_{L_1,\lambda_1,L_2,\lambda_2}}{d\omega_1} &= \frac{\omega_1\omega_2}{(2\pi)^3c^2(2j_i+1)}\sum_j\left[\left|\overline{S}^j(2,1)\right|^2 + \left|\overline{S}^j(1,2)\right|^2 + \right. \\ &\left. +2\sum_{j'}d(j,j')\left\{\mathrm{Re}\left[\overline{S}^j(2,1)\right]\mathrm{Re}\left[\overline{S}^{j'}(1,2)\right] + \mathrm{Im}\left[\overline{S}^j(2,1)\right]\mathrm{Im}\left[\overline{S}^{j'}(1,2)\right]\right\}\right] \,,\end{aligned} \tag{3.138}$$

and $d(j,j')$ is defined by Eq. (3.81). $\overline{S}^j(2,1)$ is given by Eq. (3.72) with E_{n_l} and E_i replaced by V_{n_l}

and V_i, respectively, if n_l is a resonant state, i.e.,

$$\overline{S}^j(2,1) = \sum_{n_l} \frac{\overline{M}^{(\lambda_2,L_2)}_{f,n_l}(\omega_2)\,\overline{M}^{(\lambda_1,L_1)}_{n_l,i}(\omega_1)}{V_{n_l} - V_i + \omega_1} \Delta^j(2,1)\Pi^l(2,1)\,. \tag{3.139}$$

The differential decay rate for a transition $\Theta_1 L_1 \Theta_2 L_2$, and the decay rate for the resonant processes are given by Eqs. (3.84) and (3.85), respectively, with $d\overline{W}_{L_1,\lambda_1,L_2,\lambda_2}/d\omega_1$ replaced by $d\overline{W}^{\mathrm{LPA}}_{L_1,\lambda_1,L_2,\lambda_2}/d\omega_1$.

3.7.2 Two-loop self-energy

Another method for dealing with resonances was developed by *Jentschura* and *Surzhykov* [154, 155], which uses a procedure based on two-loop self-energy. They obtained an expression similar to Eq. (3.80) for evaluating a non-resonant component of the two–photon decay rate,

$$w^{\mathrm{TLA}} = \lim_{\epsilon\to 0} \mathrm{Re} \int_0^{\omega_t} d\omega_1 \frac{\omega_1\omega_2}{(2\pi)^3 c^2} S_{if}\, d\Omega_1 d\Omega_2\,. \tag{3.140}$$

The function S_{if} is given, as in Ref. [155], by

$$S_{if} = \left(\sum_n \left\{ \frac{\left\langle f \left| A_2^* \right| n \right\rangle \left\langle n \left| A_1^* \right| i \right\rangle}{E_n - E_i + \omega_1 - i\epsilon} + \frac{\left\langle f \left| A_1^* \right| n \right\rangle \left\langle n \left| A_2^* \right| i \right\rangle}{E_n - E_i + \omega_2 - i\epsilon} \right\} \right)^2 . \tag{3.141}$$

In this way, one obtains finite results since the integration over the frequency ω_1 is displaced by an infinitesimal quantity, ϵ, from the resonant poles, provided that the limit is not permuted with the integration. If one considers a non-resonant transition such as $2s \to 1s_{1/2}$, then the limit can be permuted with the integration and Eq. (3.140) reduces to Eq. (3.80). For non-resonant transition both approaches gives the same result.

3.7.3 Integration method for resonant intermediate states

For resonant transitions, Eq. (3.138) produces sharp peaks near the resonant frequencies, which requires special attention in the integral evaluation to avoid meaningless results. Near a resonant frequency ω_r^j, Eq. (3.138) can be written as

$$\frac{d\overline{W}^{\mathrm{LPA}}_{L_1,\lambda_1,L_2,\lambda_2}}{d\omega_1} = \sum_j g^j(\omega_1) = \sum_j \frac{f^j(\omega_1)}{\left(\omega_1 - \omega_r^j\right)^2 + \left(\frac{\Gamma_r^j}{2}\right)^2}\,, \tag{3.142}$$

where $f^j(\omega_1)$ is a smooth function; the resonant behavior is given by the denominator. Consequently, the function $f^j(\omega_1)$ can be expanded in a Taylor series around the resonant frequency. It should be

emphasize that the shape in the right side of Eq. (3.142) is not a Lorentz profile since $f^j(\omega_1)$ depends on ω_1, thus, the peak profile can be asymmetric. Subtracting the first two terms of the expansion on $g^j(\omega_1)$, we obtain a smooth function, $h(\omega_1)$, which does not contain the resonant behavior and, consequently, can be integrated using standard methods, such as the Gauss-Legendre method,

$$h^{\mathrm{LPA}}(\omega_1) = \sum_j g^j(\omega_1) - \frac{a_0^j}{\left(\omega_1 - \omega_r^j\right)^2 + \left(\frac{\Gamma_r^j}{2}\right)^2} - \frac{a_1^j\left(\omega_1 - \omega_r^j\right)}{\left(\omega_1 - \omega_r^j\right)^2 + \left(\frac{\Gamma_r^j}{2}\right)^2} . \tag{3.143}$$

The coefficients a_0^j and a_1^j are derived from the Taylor expansion of $f^j(\omega_1)$ around ω_r^j:

$$a_0^j = f^j(\omega_r) = g^j(\omega_r)\left(\frac{\Gamma_r^j}{2}\right)^2 , \tag{3.144}$$

$$a_1^j = \left\{\frac{d}{d\omega_1} f^j(\omega_1)\right\}_{\omega_r} = \left\{\frac{d}{d\omega_1} g^j(\omega_1)\right\}_{\omega_r}\left(\frac{\Gamma_r^j}{2}\right)^2 . \tag{3.145}$$

Further simplifications can be done in the matrix elements (Eqs. (3.62) and (3.64)) by noticing that the longitudinal part of the operator $\widetilde{a}_{L,M}^{(\lambda)}$,

$$\left(\widetilde{a}_{L,M}^{(-1)}\right)_{\parallel} = \frac{c}{i\omega}\boldsymbol{\alpha}\cdot\boldsymbol{\nabla}\Phi_{L,M} , \tag{3.146}$$

can be written using a commutation relation as [92]

$$\left(\widetilde{a}_{L,M}^{(-1)}\right)_{\parallel} = \frac{c}{i\omega}\left[H_D, \Phi_{L,M}\right] , \tag{3.147}$$

where H_D stands for the Dirac Hamiltonian and $\Phi_{L,M}$ are the components resulting from the multipole expansion of the potential A_j^* in Eq. (3.44). The reduction of Eq. (3.147) to radial integrals along with the scalar term of the potential A_j^* leads to the following expression for the radial element matrix $\overline{M}_{f,i}^{(-1,L)}$

$$\overline{M}_{f,i}^{(-1,L)} = G(2L+1)\left(\frac{\omega+\omega_{fi}}{\omega}\right)J^{(L)} , \tag{3.148}$$

where ω_{fi} is the energy of the one-photon transition. This term is *gauge* independent for one-photon, as demonstrated by *Grant* [113], since $\omega_{fi} = -\omega$. Considering Eq. (3.147), the radial matrix element $\overline{M}_{f,i}^{(1,L)}$ can also be rewritten as

$$\overline{M}_{f,i}^{(1,L)} = \frac{(2L+1)}{\sqrt{L(L+1)}}\left[-(\kappa_f - \kappa_i)I_{L-1}^{+} + LI_{L-1}^{-} + L\frac{\omega_{fi}}{\omega}J^L\right] . \tag{3.149}$$

The explicit expressions of the derivatives of the matrix elements (Eqs. (3.149), (3.63) and

	$Z = 1$	$Z = 40$	$Z = 92$
$a_0^{1/2}$	5.081524(−3)	3.554138(10)	3.793201(13)
$a_1^{1/2}$	−3.468385(−1)	−1.425932(9)	−2.066515(11)
$a_0^{3/2}$	1.016398(−2)	8.148532(10)	1.250476(14)
$a_1^{3/2}$	−6.936930(−1)	−2.929768(9)	−3.488010(11)

Table 3.3: Coefficients a_0^j and a_1^j - Values of the coefficients a_0^j (s^{-2}) and a_1^j (s^{-1}) for the transition $3s \rightarrow 1s_{1/2}$, and for several values of Z. Powers of ten are given in parentheses.

(3.148)) are given by

$$\begin{aligned}\frac{d}{d\omega}\left[\overline{M}_{f,i}^{(1,L)}(\omega)\right] &= \frac{2L+1}{\sqrt{L(L+1)}}\left[(\kappa_f-\kappa_i)\left(I_L^r+\frac{I_{L-1}^+}{\omega}\right)\right. \\ &- \left. L\frac{I_{L-1}^-}{\omega}-\frac{\omega_{fi}}{\omega^2}L\,(L+2)\,J^{(L)}\right], \end{aligned} \tag{3.150}$$

$$\frac{d}{d\omega}\left[\overline{M}_{f,i}^{(0,L)}(\omega)\right] = \frac{2L+1}{\sqrt{L(L+1)}}\left(\kappa_f+\kappa_i\right)\left[I_{L-1}^r-\frac{(L+1)}{\omega}I_L^+\right], \tag{3.151}$$

and

$$\begin{aligned}\frac{d}{d\omega}\left[\overline{M}_{f,i}^{(-1,L)}(\omega)\right] &= G(2L+1)\left\{\left(\frac{\omega+\omega_{fi}}{\omega}\right)J_r^{(L-1)}\right. \\ &- \left.\frac{1}{\omega^2}\left[(L+1)\,\omega+(L+2)\,\omega_{fi}\right]J^{(L)}\right\}, \end{aligned} \tag{3.152}$$

where the integrals $J_r^{(L)}$ and I_L^r are defined by

$$I_L^r = \frac{1}{c}\int_0^\infty \left(P_fQ_i+P_iQ_f\right)r\,j_L\left(\frac{\omega r}{c}\right)dr\,, \tag{3.153}$$

$$J_r^{(L)} = \frac{1}{c}\int_0^\infty \left(P_fP_i+Q_fQ_i\right)r\,j_L\left(\frac{\omega r}{c}\right)dr\,. \tag{3.154}$$

As an example, the coefficients a_0^j and a_1^j evaluated for the $3s_{1/2} \rightarrow 1s_{1/2}$ transition for ions with $Z = 1$, 40, and 92 are listed in Table 3.3.

The integration of Eq. (3.142) is carry out by adding to the integral of the smooth function h the two terms $\mathfrak{h}_0$ and $\mathfrak{h}_1$ evaluated analytically, i.e.,

$$\overline{W}_{L_1,\lambda_1,L_2,\lambda_2}^{\rm LPA} = \mathfrak{h}^{\rm LPA}+\mathfrak{h}_0^{\rm LPA}+\mathfrak{h}_1^{\rm LPA}\,, \tag{3.155}$$

where

$$\mathfrak{h}^{\rm LPA} = \int_0^{\omega_t} h^{\rm LPA}\,d\omega_1\,, \tag{3.156}$$

$$\begin{aligned}\mathfrak{h}_0^{\mathrm{LPA}} &= \sum_j a_0^j \int_0^{\omega_t} \frac{1}{\left|\omega_1 - \omega_r^j - i\frac{\Gamma_r^j}{2}\right|^2} d\omega_1 \\ &= \sum_j \frac{2a_0^j}{\Gamma_r^j}\left[\arctan\left(\frac{2\left(\omega_1-\omega_r^j\right)}{\Gamma_r^j}\right)\right]_0^{\omega_t} , \end{aligned} \tag{3.157}$$

$$\begin{aligned}\mathfrak{h}_1^{\mathrm{LPA}} &= \sum_j a_1^j \int_0^{\omega_t} \frac{\left(\omega_1 - \omega_r^j\right)}{\left|\omega_1 - \omega_r^j - i\frac{\Gamma_r^j}{2}\right|^2} d\omega_1 \\ &= \sum_j \frac{a_1^j}{2} \ln\left[\frac{\left(\omega_t-\omega_r^j\right)^2 + \left(\Gamma_r^j/2\right)^2}{\left(\omega_r^j\right)^2 + \left(\Gamma_r^j/2\right)^2}\right] . \end{aligned} \tag{3.158}$$

We note that a_0^j is given approximately (unless we consider the limit $\Gamma \to 0$, in which case it is given exactly) by

$$a_0^j \approx \frac{w_{i\to r}^{\lambda_2,L_2} w_{r\to f}^{\lambda_1,L_1}}{2\pi} , \tag{3.159}$$

where the term $w_{i\to f}^{\lambda_k,L_k}(\omega)$ is the decay rate from an initial i to a final state f by the emission of one photon, given by [113]

$$w_{i\to f}^{\lambda L}(\omega) = \frac{2\omega[j_f]}{c[L]} \begin{pmatrix} j_f & L & j_i \\ \frac{1}{2} & 0 & -\frac{1}{2} \end{pmatrix}^2 \left|\overline{M}_{f,i}^{\lambda L}\right|^2 . \tag{3.160}$$

Using this result we get

$$\frac{d\mathfrak{h}_0^{\mathrm{LPA}}}{d\omega_1} \approx \sum_j \frac{1}{2\pi} \frac{w_{i\to r} w_{r\to f}}{\left(\omega_1 - \omega_r^j\right)^2 + \left(\frac{\Gamma_r^j}{2}\right)^2} , \tag{3.161}$$

and identify $\mathfrak{h}_0^{\mathrm{LPA}}$ as a cascade emission decay rate term.

Applying this method to obtain w^{TLA} given by Eq. (3.140), we end up with a smooth function h^{TLA} as in the LPA. One difference between the two approaches is in the term of order $\sim (\Gamma_r/2)^2$. That difference results from considering the infinitesimal quantity, ϵ, finite, i.e., taking the role of a level width ($\epsilon \to \Gamma$). In the present evaluation, we obtain the function h^{TLA} by replacing $\Gamma_r \to \Gamma_r q$, where q is a parameter than can be made arbitrarily small. It is thus obtained convergence since the difference in h^{TLA} using $q = 1$ or $q = 10^{-2}$ is in the fifth digit. For $q = 10^{-2}$ and $q = 10^{-3}$ the difference in h^{TLA} is in the ninth digit. So, we may conclude that using h^{LPA} defined in Eq. (3.143) with $q = 10^{-2}$, is a good approximation for the function h^{TLA}. Another difference between the TLA and LPA is the inclusion of radiative corrections Re [SE] and VP, which for values of Z as high as 92 changes the value of h from one approach to another in the second digit.

The major difference between the two approaches lies in the integral $\mathfrak{h}_0$, which in the TLA is given by

$$\mathfrak{h}_0^{\mathrm{TLA}} = \sum_j a_0^j \frac{1}{\omega_r^j \left(\omega_r^j - \omega_t\right)} , \tag{3.162}$$

which comes from the different ways the pole regularization is done.

Notice that the terms $\mathfrak{h}_0^{\mathrm{LPA}}$ and $\mathfrak{h}_0^{\mathrm{TLA}}$ are related by

$$\mathfrak{h}_0^{\mathrm{LPA}} = \mathfrak{h}_0^{\mathrm{TLA}} + \sum_j \frac{2\pi a_0^j}{\Gamma_r^j} + O\left(\Gamma_r^j\right) , \tag{3.163}$$

which shows that the difference between $\mathfrak{h}_0^{\mathrm{LPA}}$ and $\mathfrak{h}_0^{\mathrm{TLA}}$ is mainly due to the second term on the left side of Eq. (3.163) (since $\Gamma_r^j \ll 1$), or by the product of one-photon transitions (cascade process).

On the other hand, the integral $\mathfrak{h}_1$ is given in the TLA approach by

$$\mathfrak{h}_1^{\mathrm{TLA}} = \sum_j a_1^j \ln\left[\frac{\omega_t - \omega_r^j}{\omega_r^j}\right] . \tag{3.164}$$

We notice that this expression could be obtained from Eq. (3.158) taking $\Gamma_r \to 0$.

Considering that

$$\mathfrak{h}^{\mathrm{TLA}} = \int_0^{\omega_t} h^{\mathrm{TLA}}\, d\omega_1 , \tag{3.165}$$

the decay rate in the TLA, $\overline{W}^{\mathrm{TLA}}_{L_1,\lambda_1,L_2,\lambda_2}$, is given by an expression similar to Eq. (3.155), in which the LPA contributions are replaced by the correspondent TLA contributions.

As we will see in Chapter 4, these differences on the sum of $\mathfrak{h}$ and $\mathfrak{h}_1$ will result basically no deviation between the LPA and TLA methods for low-Z ions but bring a slight discrepancy for heavier systems.

3.8 Two-photon excitation

Two-photon excitation or two-photon absorption is the time reversal process of two-photon decay. While the previous happens spontaneously, the former process occurs by means of an external radiation. The calculation of the two-photon excitation follows similar steps compared with the decay. Following the QED formalism of quantifying the electromagnetic field, the only difference between the electron-photon potential expressed in Eq. (3.39) is considering its complex conjugate, i.e., A_j. Another crucial difference is that since the two-photon excitation is performed by means of coherent light, i.e., with one or two discrete frequencies, there is no multiplication by the number of photons with wavenumber $\hat{\boldsymbol{k}}$ and subsequent integration over the wavenumbers solid angles. We restrict here

to the case of excitation with a single laser, thus, restricting the photon energy to equal energy sharing ($y = 0.5$).

Experimental results on the two-photon absorption are often presented in terms of the parameter α_0 that can be calculated as

$$\begin{aligned} \alpha_0 &= \frac{(2\pi)^3 c^2}{4\omega^3 [j_i]} \sum_{m_i, m_f} |M(2,1) + M(1,2))|^2 \\ &= \frac{(2\pi)^3 c^2}{4\omega^3 [j_i]} \sum_{kq} \left| U_{kq}(j_f, j_i) \right|^2 . \end{aligned} \tag{3.166}$$

This parameter, which in Système International (SI) units is expressed in $(\mathrm{cm}^2/\mathrm{s})/(\mathrm{W}/\mathrm{cm}^2)$, is directly related to the effective excitation cross-section (given in cm^4/W),

$$\sigma^{2\mathrm{exc}} = \alpha_0 g(\omega) G^{(2)} , \tag{3.167}$$

and to the two-photon rate (in s^{-1}) by

$$W^{2\mathrm{exc}} = \frac{I^2}{\omega} \alpha_0 g(\omega) G^{(2)} . \tag{3.168}$$

In these expressions, I is the intensity of the incident light, $G^{(2)}$ is the two-photon statistical factor, which takes the value $G^{(2)} = 1$ for a single-mode laser and $G^{(2)} = 2$ for an incoherent source [157, 158], and $g(\omega)$ is the line shape function of the laser. By considering the resonant condition associate to energy conservation (similar to Eq. (2.2) for excitation) and the Gaussian profile (explicit function in Eq. (7.44)) of the laser beam, we can write this function as

$$g(\omega) = \sqrt{\frac{4\ln(2)}{\pi}} \frac{1}{\sqrt{\Delta\omega_D^2 + 2\Delta\omega_L^2}} , \tag{3.169}$$

where $\Delta\omega_D$ and $\Delta\omega_L$ are the Doppler width and laser linewidth, respectively. Here, both these widths are assumed to be larger than the natural width of the excited ionic state. This assumption might not always be true for the two-photon absorption of high-Z ions. For such ions, one should use the generalization of Eq. (3.169) as given, for example, in Ref. [159].

The function U_{kq} follows the multipole expansion (similar to Eq. (3.44)) and subsequent angular reduction [92]. The explicit form is given by

$$
\begin{aligned}
U_{kq}(j_f, j_i) &= \sum_{L_1,\lambda_1,L_2,\lambda_2} i^{L_1+L_2-|\lambda_1|-|\lambda_2|}(-1)^{j_f+j_i+\lambda_1+\lambda_2} T_{kq}^{L_1\lambda_1 L_2\lambda_2} \\
&\times \sum_j (-1)^{j-1/2}\sqrt{[j]}\left(\begin{Bmatrix} L_2 & L_1 & k \\ j_i & j_f & j \end{Bmatrix} S^j(2,1) + (-1)^{L_1+L_2+k} \begin{Bmatrix} L_2 & L_1 & k \\ j_i & j_f & j \end{Bmatrix} S^j(1,2) \right) ,
\end{aligned}
\tag{3.170}
$$

where the term $T_{kq}^{L_1\lambda_1 L_2\lambda_2}$ defines the polarization as well as the angular dependence of the two-photon absorption process. The most general form of this function has been derived by *Manakov et al*. in Refs. [160, 161]. In the present work, we restrict ourselves to the particular case of linearly polarized photons whose polarization vectors $\hat{\boldsymbol{e}}_{1,2}$ are described by the tilt angles χ_1 and χ_2 with respect to the reaction plane, which is spanned by the momenta $\hat{\boldsymbol{k}}_{\boldsymbol{1}}$ and $\hat{\boldsymbol{k}}_{\boldsymbol{2}}$, respectively. Since there was no direction initially preferred for the excitation of unpolarized, as well as unaligned ions or atoms, we adopted $\hat{\boldsymbol{z}}$ as the quantization axis along the momentum of the first photon, i.e., $\hat{\boldsymbol{k}}_{\boldsymbol{1}} \| \hat{\boldsymbol{z}}$. The angular polarization function reads

$$
T_{kq}^{L_1\lambda_1 L_2\lambda_2}(\theta) = \frac{\sqrt{[L_1, L_2]}}{16\pi} \sum_{q_1,q_2} e^{-i(q_1\chi_1+q_2\chi_2)}(-q_1)^{\lambda_1}(-q_2)^{\lambda_2} \langle L_1\lambda_1 L_2 M_2 | kq \rangle D_{M_2 q_2}^{L_2}(0,\theta,0) , \tag{3.171}
$$

where like in previous Sec. 3.6, θ is the angle between the two photons and D_{Mq}^{L} is the Wigner rotation matrix [92].

The results obtained with the theory presented in this section is presented in Sec. 4.5 of the next chapter.

Chapter 4

Results for Two-photon Transitions

4.1 Optimization of the numerical evaluation

The evaluations of two-photon transitions done for non-resonant states serves the purpose of obtaining the *optimal* set parameters for all the results of this chapter. While the calculations done with B-splines basis set were performed in order to compare with previous calculations and other theoretical calculations, the B-Polynomial basis set were employed in an higher-order evaluation for the first time. Therefore, a detailed description of the *optimal* set parameter optimization and results for that basis set are presented in this chapter.

4.1.1 B-splines

The decay rates of the non-resonant $2s_{1/2} \rightarrow 1s_{1/2}$ and $2p_{1/2} \rightarrow 1s_{1/2}$ transitions were obtained using Eq. (3.80).

The parameters of the B-splines used to obtain of the results presented in this work are $k = 9$, $ns = 60$ and $R = 60$ a.u.. They were obtained by a convergency criterion.

The most significant multipole combinations included in the calculation of the two-photon decay rates of the $2p_{1/2} \rightarrow 1s_{1/2}$ transition are listed in Table 4.1. The magnitude of the multipole combinations not listed in this table are, at least, four orders of magnitude smaller than the most significant $E1M1$ and $E1E2$ decay channels.

The values given by *Labzowsky et al.* in [59] were obtained using expressions similar to the ones used by *Goldman* and *Drake* [60]. The results published in Ref. [162] were obtained using the non-relativistic Coulomb Green's function which, for high values of Z such as 92 leads to inaccurate values. The relative difference between our results and the results in Ref. [59] is $0.1 - 0.4\%$. We observe that, for the three studied Z values, more than 99% of the total decay rate is due to the

Multipoles	Contribution (s^{-1})		
	$Z = 1$	$Z = 40$	$Z = 92$
$E1M1$	9.676654(−6)	6.027323(7)	3.863302(10)
	9.667(−6) [1]	6.020(7) [1]	3.859(10) [1]
	9.677(−6) [2]	6.341(7) [2]	4.966(10) [2]
$E1E2$	6.61179(−6)	4.092020(7)	2.358404(10)
	6.605(−6) [1]	4.088(7) [1]	2.357(10) [1]
	6.673(−6) [2]	4.374(7) [2]	3.425(10) [2]
$M1M2$	3.827877(−17)	5.602320(2)	7.689142(6)
$E2M2$	9.385470(−17)	1.521687(3)	2.834065(7)
$E2E3$	4.095985(−18)	6.608612(1)	1.177403(6)
Total	1.628845(−5)	1.01195(8)	6.225309(10)

[1] *Labzowsky et al.* [59]
[2] *Labzowsky et al.* [162]

Table 4.1: Multipole contributions for the $2p_{1/2} \rightarrow 1s_{1/2}$ transition - Multipole contributions included in the present calculation of the total two-photon rate for the $2p_{1/2} \rightarrow 1s_{1/2}$ transition. Comparison between the values obtained in this work and other theoretical values. Powers of ten are given in parentheses.

multipole contributions $E1M1$ (about 60%) and $E1E2$ (about 40%). The fact that the two multipole combinations $E1M1$ and $E1E2$ give almost the same contribution is somewhat expected since $M1$ and $E2$ have the same order of magnitude in the multipole expansion of the photon field [85]. On the other hand, a comparison between the listed most ($E1M1$) and less ($E2E3$) significant contributions reveals that the relative importance of the latter increases with Z, being 12, 5 and 4 orders of magnitude smaller than the former for $Z = 1$, $Z = 40$, and $Z = 92$, respectively.

In Table 4.2 we report the two-photon total decay rates for $2p_{1/2} \rightarrow 1s_{1/2}$ and $2s_{1/2} \rightarrow 1s_{1/2}$ transitions. Enough multipoles have been included in the calculation of the total two-photon decay rates to reach an accuracy of six digits. The values for the $2s_{1/2} \rightarrow 1s_{1/2}$ transition differ slightly from the ones published in Ref. [12] due to the most recent values of physical constants [81, 90], such as the fine-structure constant. We refer here that for all H-like ions, this transition is dominated by the $2E1$ decay channel while all the higher multipoles contribute by less than 0.5% to the decay rate.

It should be mentioned that the interest in the transition $2p_{1/2} \rightarrow 1s_{1/2}$ is only academic since not only the transition is suppressed by the selection rules but also this channel is in direct competition with the allowed one-photon transition ($E1$). However, detailed investigation on this decay channel is highly required for future experiments on the parity violation in simple atomic systems [42]. A number of calculations [153, 162] have been performed, therefore, for the transition probabilities of the dominant $E1M1$ and $E1E2$ multipole components.

To present the spectral (or frequency) distribution for a specific value of Z is convenient to express

		Total decay rate (s^{-1})	
$Z = 1$	$f\backslash i$	$2s_{1/2}$	$2p_{1/2}$
	$1s_{1/2}$	8.229059 8.2202 [1]	1.628845(-5) 1.6272(-5) [1] 1.6350(-5) [2]
$Z = 40$	$f\backslash i$	$2s_{1/2}$	$2p_{1/2}$
	$1s_{1/2}$	3.198851(10) 3.1954(10) [1]	1.01195(8) 1.010(8) [1] 1.071(8) [2]
$Z = 92$	$f\backslash i$	$2s_{1/2}$	$2p_{1/2}$
	$1s_{1/2}$	3.835978(12) 3.8216(12) [1]	6.225309(10) 6.216(10) [1] 8.391(10) [2]

[1] *Labzowsky et al.* [59]
[2] *Labzowsky et al.* [162]

Table 4.2: Two-photon decay rate of non-resonant states - Total two-photon decay rates (s^{-1}) for the transitions $2s_{1/2} \rightarrow 1s_{1/2}$ and $2p_{1/2} \rightarrow 1s_{1/2}$. Comparison between the values obtained in this work and other theoretical values. Powers of ten are given in parentheses.

the results in the form suggested by Spitzer and Greenstein [28]

$$\psi(y, Z) = \left(\frac{2^{10}}{9}\right)(Z\alpha)^{-n}\,\frac{dW}{dy} \quad \text{Ry}\,, \tag{4.1}$$

where $y = \omega/\omega_t$ is the fraction of the photon energy carried by one of the two-photons, ω_t is the energy of the transition and $\frac{dW}{dy}$ is given by Eq. (3.138) in Ry. In the case of an even→even (or odd→odd) transition, the major multipole contribution $2E1$ scales as Z^6 and, consequently, $n = 6$. For an even→ odd (or odd→even) transition, both $E1M1$ and $E1E2$ scale as Z^8.

In Fig. 4.1 are presented the frequency distribution of the multipole contributions $E1M1$, $M1E1$, $E1E2$ and $E2E1$ for the transition $2p_{1/2} \rightarrow 1s_{1/2}$. Although each one of these four most significant contributions is asymmetric, the sum of each pair ($E1M1$, $M1E1$) and ($E1E2$, $E2E1$) is symmetric around $y = 0.5$. Therefore, the total frequency distribution is also symmetric around the $y = 0.5$ value, as can be seen in Fig. 4.2.

4.1.2 B-polynomials

The B-polynomials basis set was also used in the evaluation of the $2s_{1/2} \rightarrow 1s_{1/2}$ two-photon decay rate in order to assess the efficiency of this basis–set. To determine the optimal parameters set for the B–polynomial approach, it was first studied the energy transition ω_t, which is related with the initial state ($2s_{1/2}$) and final state ($1s_{1/2}$) from Eq. (2.2). Whose accurate value is required since the total

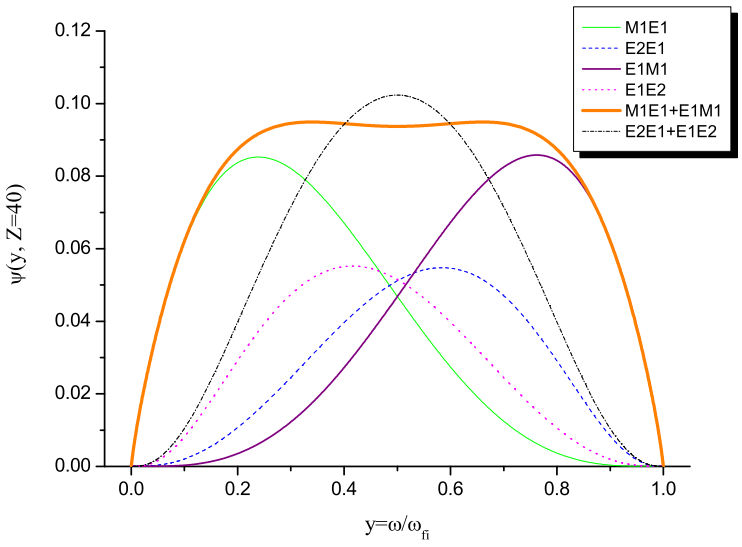

Figure 4.1: Spectral distribution of the $E1M1$ and $E1E2$ - Spectral distribution function $\psi(y)$ of the $E1M1$ and $E1E2$ contributions for the transition $2p_{1/2} \rightarrow 1s_{1/2}$ at Z=40. The variable $y = \omega_1/\omega_{fi}$ is the fraction of the photon energy carried by one of the two-photons.

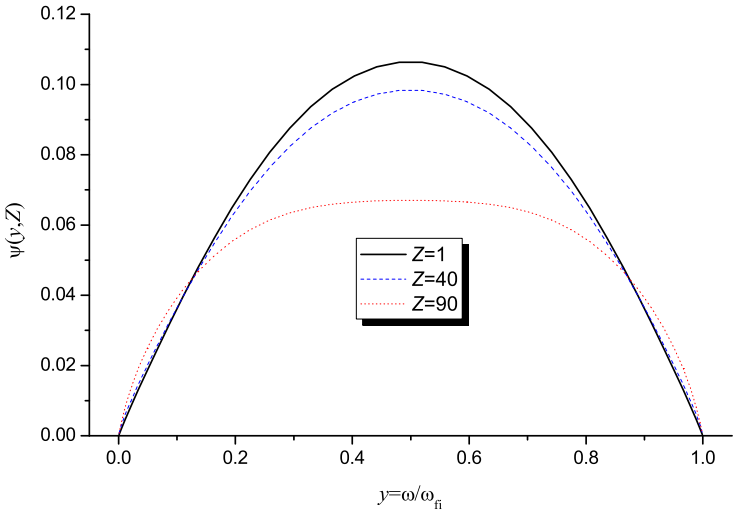

Figure 4.2: Spectral distribution of the $2p_{1/2} \rightarrow 1s_{1/2}$ - Spectral distribution function $\psi(y, Z)$ for the transition $2p_{1/2} \rightarrow 1s_{1/2}$ at Z=1, 40, and 92. The variable $y = \omega_1/\omega_{fi}$ is the fraction of the photon energy carried by one of the two-photons.

decay rate (3.80) and (3.85) depends on it quadratically. Detailed calculations of this energy value were carried out by making use of B–polynomial basis sets for various numbers of polynomials, n_{BP}, and of the cavity radius (R). The relative difference $\Delta = |(\omega_t^{\mathrm{Exact}} - \omega_t^{\mathrm{BP}})/\omega_t^{\mathrm{Exact}}|$ between the exact $\omega_t^{\mathrm{Exact}}$ solution and the basis set value ω_t^{BP}, or accuracy is presented in Fig. 4.3 as a function of the number of polynomials, n_{BP}, for Z equal to 1, 40 and 92.

Apart from the energy values, evaluation of two–photon transition rates in Eqs. (3.80) and (3.85) requires also detailed knowledge of the atomic wavefunctions. As usual in atomic structure calculations, an indication of the completeness and quality of the basis set can be obtained from the comparison of the results obtained within two different *gauges* (Eq. (3.39)). In this way, detailed calculations of the total decay rates for the leading two-photon $2E1\ 2s_{1/2} \rightarrow 1s_{1/2}$ channel have been performed, in both length and velocity *gauges*. The accuracy in *gauge* invariance, together with the accuracy in the energy ω_t determine the optimal set of parameters. In Fig. 4.4, we display the relative difference between the length and velocity *gauge* decay rate values of the $2E1$, $\Delta_{\mathrm{l-v}}$, a function of n_{BP} for the same values of the atomic number Z.

As seen from Figs. 4.3 and 4.4, the optimal n_{BP} value for the case of $Z = 1$ is above 34 and the optimal R is 50. We emphasize that even a lower number n_{BP} such as 25 provides a *gauge* invariance in the two-photon rate less then 10^{-16}. For the case of $Z = 40$, the optimal parameters are $n_{\mathrm{BP}} > 40$ and $R = 1$, and for $Z = 92$, they are $n_{\mathrm{BP}} > 40$ and $R = 0.25$.

Working in double precision, we noticed a loss of numerical significance in the results for $n_{\mathrm{BP}} > 23$ due to the LAPACK routines used for the solution of the generalized eigenvalue problem. We detected that this is due to the difficulty of these routines, namely the *DSYGVX* routine, to deal with diagonally dominant matrices that have very large diagonal elements and very small off-diagonal elements. This problem was overcome by using quadruple precision for the evaluation of the matrix elements and compiling the LAPACK subroutine in quadruple precision as well, using the compiler auto-doubling option. This situation is illustrated in Fig. 4.5, where the relative difference $\Delta_{\mathrm{l-v}}$ is plotted for $Z = 1$ and $R = 40$, obtained in double and quadruple precision. Nevertheless, we should emphasize that even with a low n_{BP} value, such as 20, and working in double precision, we get a *gauge* invariance in the two-photon rate less than 10^{-15}. In double precision, 10^{-16} is the lowest computational accuracy.

In Table 4.3 we display the most significant multipole contributions to the $2s_{1/2} \rightarrow 1s_{1/2}$ two-photon total decay rate (3.85) of neutral hydrogen. Again, calculations have been performed within two different gauges and by employing B–polynomial, as well as B–spline basis sets. Multipoles with only magnetic components such as $2M1$ are only given in velocity *gauge*. As seen from the Table 4.3, both approaches yield almost identical results (with the relative difference of less than 2×10^{-7}) for all multipole decay channels. Moreover, one may observe a remarkable agreement (smaller

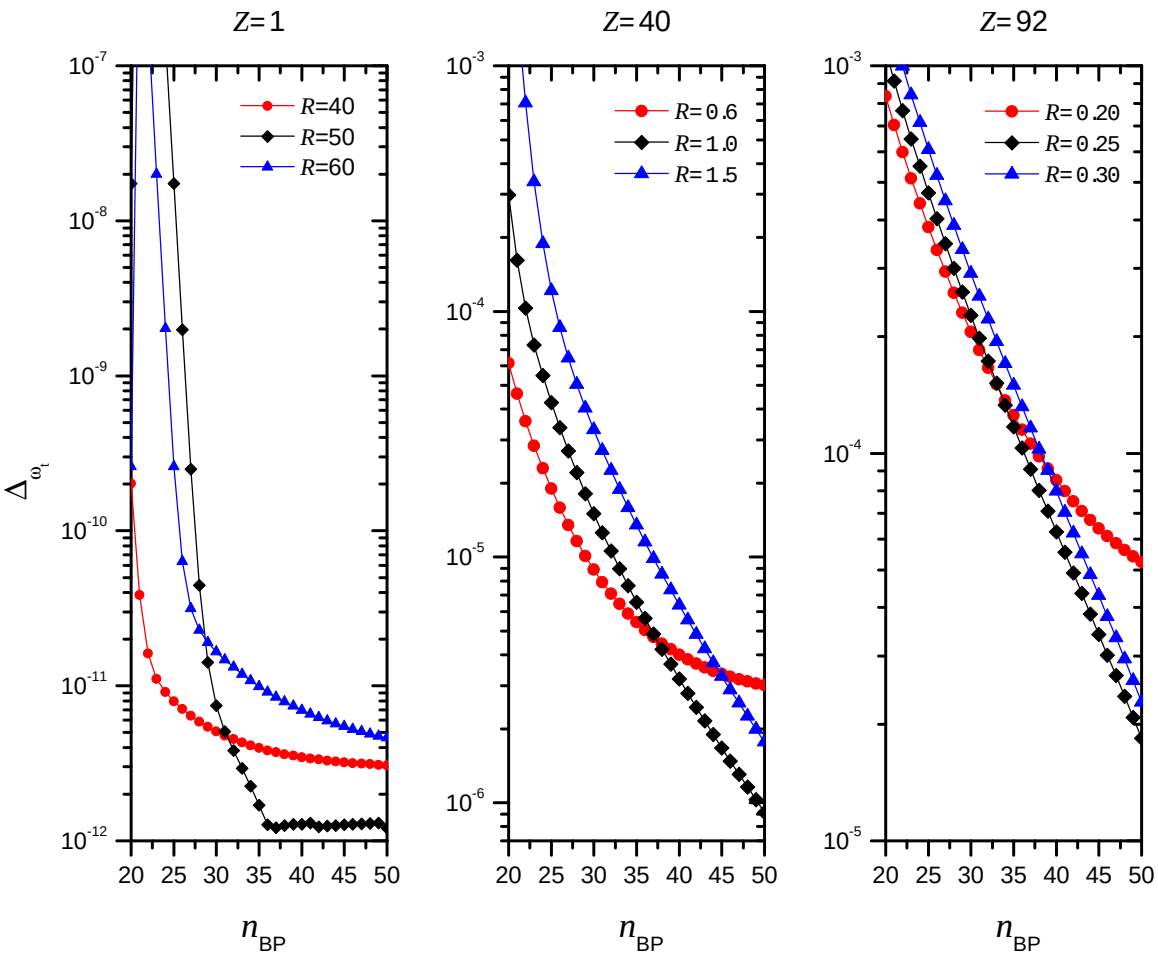

Figure 4.3: Δ_{ω_t} **as function of** n_{BP} - Relative difference between the computed ω_t energy and the value $\omega_t^{\mathrm{Exact}} = E_{2s}^{\mathrm{Exact}} - E_{1s}^{\mathrm{Exact}}$ as function of the number of B-Polynomials, n_{BP}, for Z equal to 1, 40 and 92. Here, E_n^{Exact} are the exact solutions of the Dirac equation with a point-like model given by Eq. (3.18).

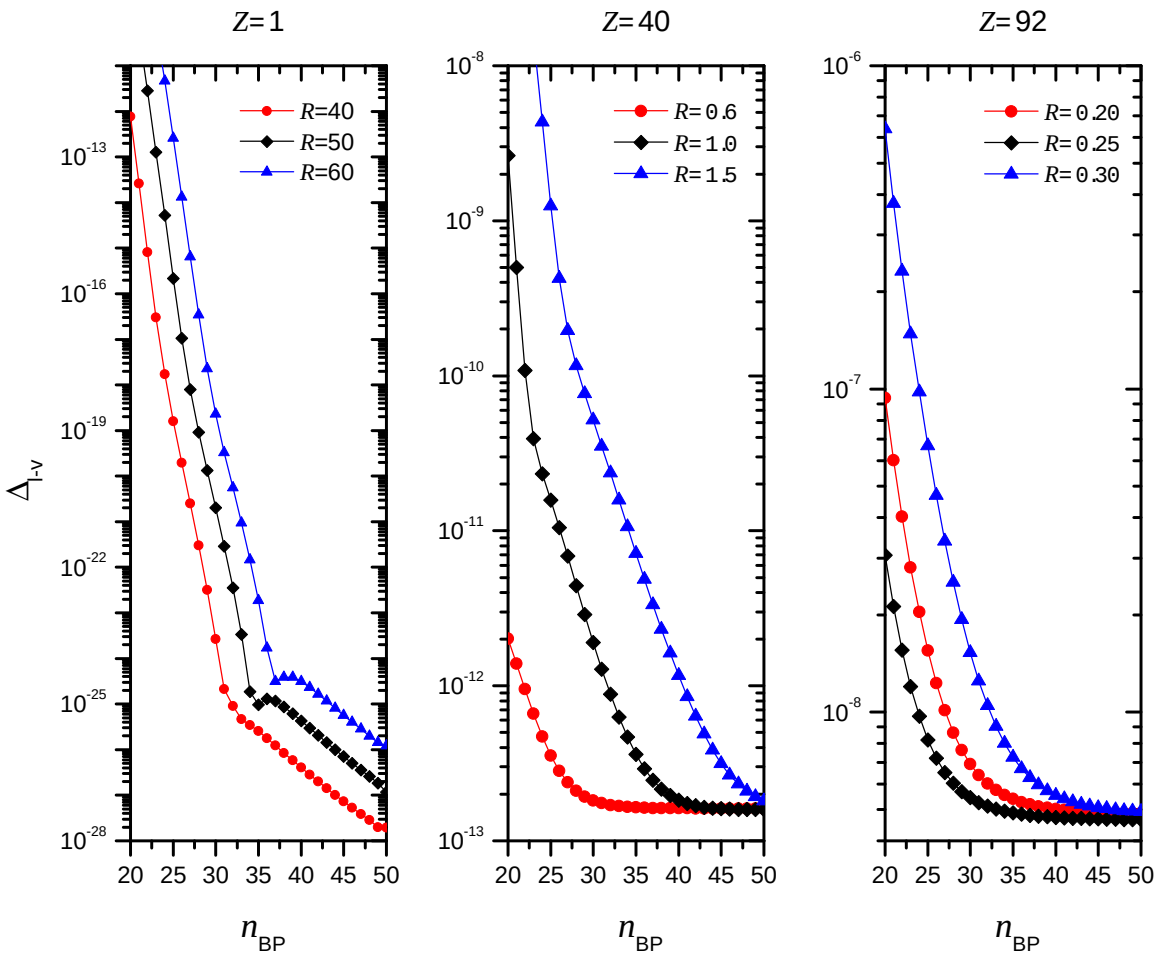

Figure 4.4: Δ_{l-v}**, as function of** n_{BP} - Relative difference between the length and velocity *gauge* decay rate values of the $2E1\ 2s_{1/2} \rightarrow 1s_{1/2}$, Δ_{l-v}, as function of the number of B-Polynomials, n_{BP}, for Z equal to 1, 40 and 92.

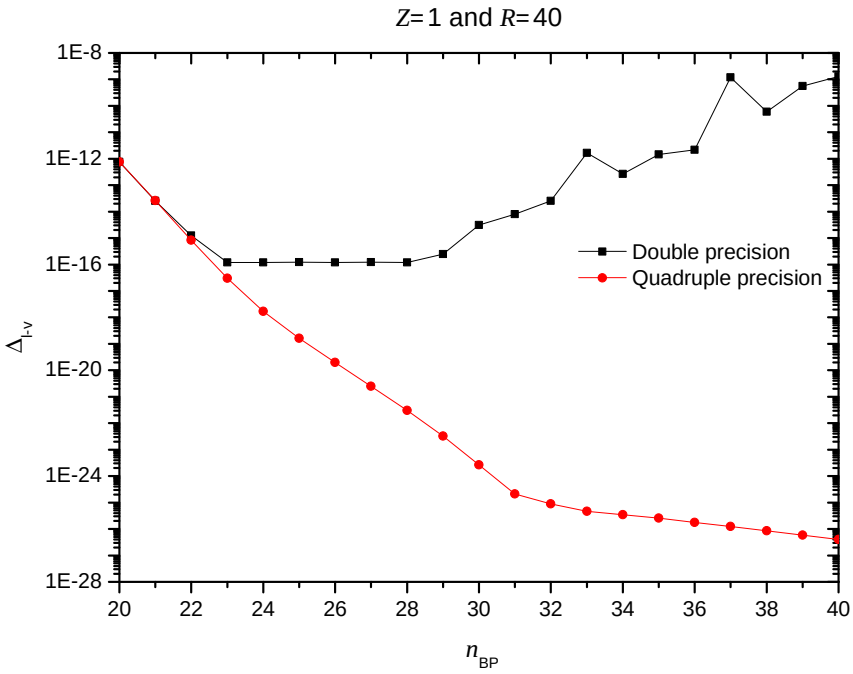

Figure 4.5: Δ_{l-v} **in double and quadruple precision** - Relative difference between the length and velocity *gauge* decay rate of the $2E1\ 2s_{1/2} \rightarrow 1s_{1/2}$, Δ_{l-v}, for $Z = 1$ and $R = 40$, obtained in double and quadruple precision.

than 10^{-25}) between the values obtained in the length and velocity *gauges* with a B-polynomials basis set.

These results clearly indicate that the finite basis set approach based on B–polynomial solutions provides an alternative tool for studying the two–photon transitions. Moreover, with such an approach, that employs *analytical* evaluation of the second–order matrix elements (Eqs. (3.98) and (3.99)) and smaller optimal $n_{\rm BP}$, the computation time required for the determination of each multipole contribution in real double precision, is about *two and half* times smaller than the time required using the B–Splines basis set. With such improvement, the evaluation was done in quadruple precision.

The integration over the photon frequency has been performed using a 15 points Gauss-Legendre algorithm for the non-resonant transitions [163].

4.2 Negative continuum contribution in two-photon emission

In order to investigate the contribution of negative continuum, we performed detailed calculations for the $2s_{1/2} \rightarrow 1s_{1/2}$ and $2p_{1/2} \rightarrow 1s_{1/2}$ transitions in neutral hydrogen H, as well as for H-like xenon ($Z = 54$) and H-like uranium ($Z = 92$) ions.

	Contribution (s^{-1})			
	B-Polynomials		B-Splines	
Multipoles	length gauge	Δ_{l-v}	length gauge	Δ_{l-v}
$2E1$	8.2290591586	< 1.0(−26)	8.2290591509	< 1.0(−15)
$E1M2$	2.5371807735(−10)	< 1.0(−25)	2.5371807635(−10)	< 1.0(−15)
$2M1$	1.3803580496(−11)	–	1.3803580473(−11)	–
$2E2$	4.9072289232(−12)	< 1.0(−34)	4.9072289165(−12)	< 1.0(−14)
$2M2$	3.0693510074(−22)	–	3.0693509833(−22)	–
$E2M1$	1.6393565197(−23)	< 1.0(−36)	1.6397413530(−23)	< 1.0(−4)
Total	8.2290591589		8.2290591512	

Table 4.3: Multipole contributions for B-Polynomials and B-splines - Multipole contributions (in s^{-1}) of the $2s_{1/2} \to 1s_{1/2}$ two-photon decay for $Z = 1$. The relativistic calculations have been performed within the velocity and length *gauges*, using the B-polynomials and B-splines basis sets. Δ_{l-v} stands for the relative difference between the length and velocity gauge values. Powers of ten are given in parentheses.

The differential decay rate given by Eq. (3.82) for the emission of two electric dipole photons is displayed in Fig. 4.6 for the decay of neutral hydrogen as well as H-like xenon Xe^{53+} and uranium U^{91+} ions.

For these ions, relativistic second-order calculations have been done within the Coulomb *gauge* and by performing intermediate-state summation over the complete Dirac spectrum (solid black line) as well as over the positive- (dashed blue line) and negative-energy (dotted green line) solutions only. As seen in this figure, the negative-energy contribution to the differential decay rate is negligible for low-Z ions but becomes rather pronounced as the atomic number Z is increased. For the $2E1$ decay of hydrogen-like uranium, for example, exclusion of the negative solutions from the intermediate-state summation in Eq. (3.72) leads to about 20% reduction of the decay rate when compared with the *exact* result.

While for the leading $2E1$ $2s_{1/2} \to 1s_{1/2}$ transition the negative continuum effects arise only for rather heavy ions, they might strongly affect properties of the higher multipole decay channels in low-Z domain. In Fig. 4.7, for example, we display the energy distributions of photons emitted in $2M1$ and $2E2$ transitions. As seen in the upper panel of the figure corresponding to the decay of neutral hydrogen, the negative energy part of the Dirac's spectrum gives the dominant contribution to the sum of the differential rates for these decay channels. With the increasing atomic number Z, the role of positive energy solutions also becomes more pronounced. However, these solutions allow one to describe reasonably well the differential rates (Eq. (3.80)) only if one of the photons is much more energetic than the second one, i.e., when either $y < 0.1$ or $y > 0.9$. For a nearly equal energy sharing ($y \sim 0.5$), in contrast, accurate relativistic calculations of the $2M1$ and $2E2$ rates obviously require

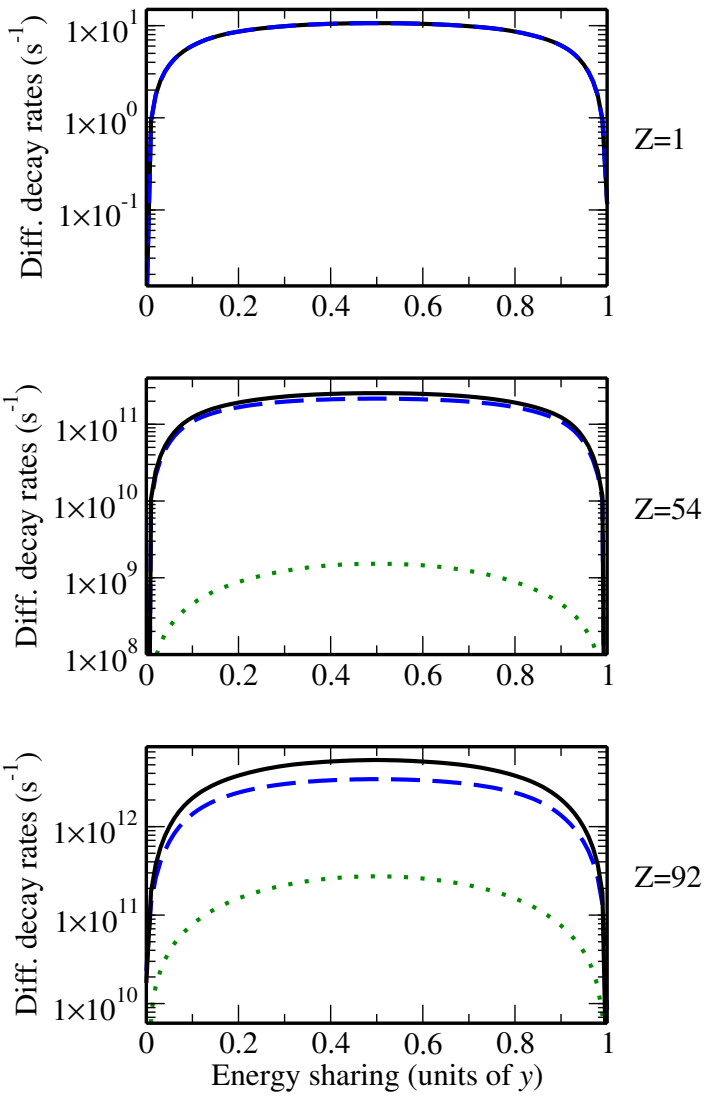

Figure 4.6: Negative contribution to the $2E1\ 2s_{1/2} \to 1s_{1/2}$ **two–photon decay** - Differential transition rates for the $2E1\ 2s_{1/2} \to 1s_{1/2}$ two–photon decay of hydrogen and H–like ions. Relativistic calculations have been carried out by performing intermediate–state summation over complete Dirac's spectrum (solid black line), as well as by restricting this summation to the positive– (dashed blue line) and negative–energy (dotted green line) states only.

summation over both, the negative and the positive energy states.

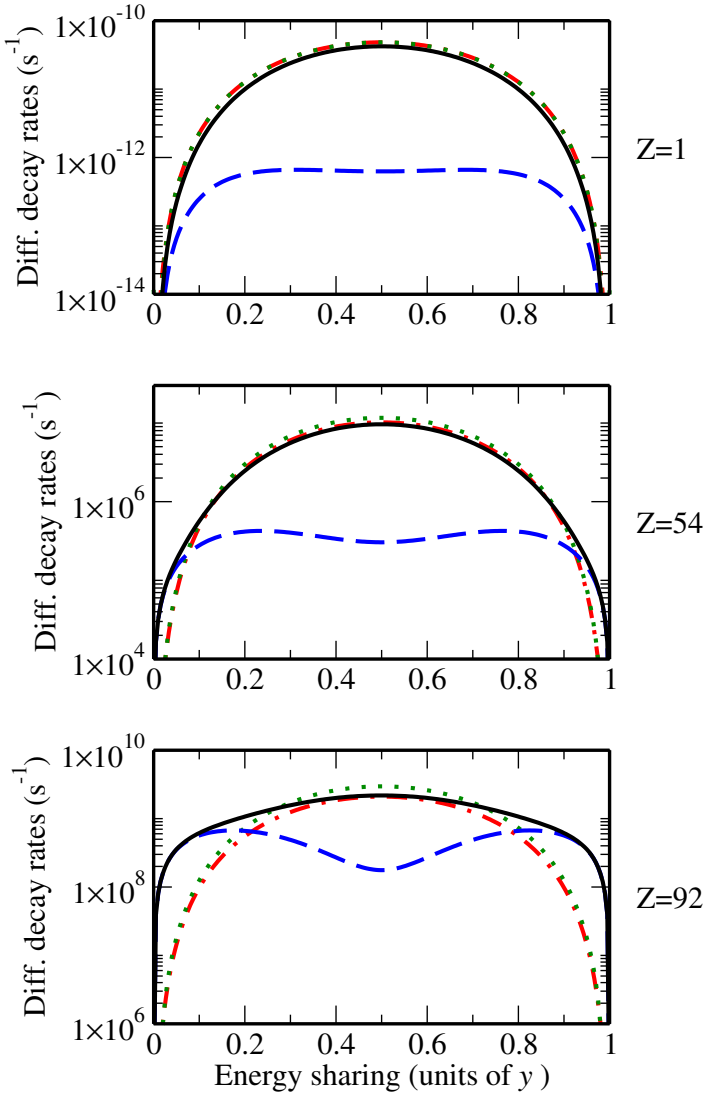

Figure 4.7: Negative contribution to the $2M1$, $2E2$ and $E2M1$ $2s_{1/2} \to 1s_{1/2}$ two–photon decay - Differential decay rates for the (sum of the) $2M1$, $2E2$ and $E2M1$ $2s_{1/2} \to 1s_{1/2}$ multipole two–photon transitions in hydrogen and hydrogen–like ions. Relativistic calculations have been carried out by performing intermediate–state summation over complete Dirac's spectrum (solid black line) as well as by restricting this summation to the positive– (dashed blue line) and negative–energy (dotted green line) states only. Results of relativistic calculations are compared also with the semi–relativistic prediction (dot–dashed red line) as given by Eq. (3.123).

Apart from the results of relativistic calculations, we also display in Fig. 4.7 the sum of the negative-energy contributions to the $2M1$, $2E2$, $M1E2$, and $E2M1$ $2s_{1/2} \to 1s_{1/2}$ transition probabilities as obtained within the semi-relativistic approach (Eq. (3.123)). As expected, for low-Z ions both the relativistic (dotted green line) and semi-relativistic (dot-dashed red line) results basically coincide and are well described by Eq. (3.123). As the atomic number Z is increased, however, semi-relativistic treatment leads to a slight underestimation of the negative-energy contribution to the two-photon differential transition probabilities. For the $2s_{1/2} \to 1s_{1/2}$ decay of H-like uranium ion, for example,

results obtained from Eq. (3.123) is about 30% smaller than the corresponding relativistic predictions.

In order to discuss the role of Dirac's negative continuum in the two-photon transition $2p_{1/2} \to 1s_{1/2}$, we display in Fig. 4.8 the differential rate for the sum of the $E1M1$ and $E1E2$ multipoles. Again, the calculations have been carried out within the Coulomb *gauge* for the electron-photon coupling and for three atomic numbers $Z = 1$, 54, and 92. As seen in this figure, negative-energy summation in the second-order transition amplitude (3.72) is of great importance for accurate evaluation of $2p_{1/2} \to 1s_{1/2}$ transition probabilities both for low-Z and high-Z ions. That is, restriction of the intermediate-state summation to positive part of Dirac's spectrum results in an overestimation of the $E1M1$ and $E1E2$ differential decay rates by factors of about 2 and 2.5 for the neutral hydrogen and H-like uranium, respectively.

Similar to the $2s_{1/2} \to 1s_{1/2}$ multipole transitions, we make use of the semi-relativistic Eq. (3.123) to cross-check our relativistic computations for the negative-energy contribution to the $E1M1$ and $E1E2$ $2p_{1/2} \to 1s_{1/2}$ decay rates in low-Z domain. Again, while for neutral hydrogen both, semi-relativistic and relativistic approaches produce virtually identical results, they start to differ as the atomic number Z is increased.

In Table 4.4 we display decay rates for the various multipole channels of $2s_{1/2} \to 1s_{1/2}$ two-photon decay. In contrast to the photon energy distributions from above, here relativistic calculations have been performed in Coulomb (velocity), as well as Lorentz (length) *gauges*. In both *gauges*, negative-energy contribution to the total probability of the leading $2E1$ transition is about eight orders of magnitude smaller than the positive-energy term if decay of low-Z ions is considered, but is significantly increased for higher values of atomic number.

For the H-like uranium, for example, the total $2E1$ decay rate is enhanced from 2.9041×10^{12} s^{-1} in the velocity gauge and 2.3939×10^{12} s^{-1} in the length *gauge* to the *nearly gauge* independent value of 3.8256×10^{12} s^{-1} if, apart from the positive-energy states, the Dirac's states with negative energy are taken into account in the transition amplitude given in Eq. (3.72).

These results clearly indicate the importance of the negative-state summation for the accurate evaluation of $2E1$ $2s_{1/2} \to 1s_{1/2}$ total rates in both, velocity and length *gauges*.

In Table 4.4, besides the leading $2E1$ decay channel, we present the results of relativistic calculations for the higher multipole contributions to the $2s_{1/2} \to 1s_{1/2}$ two-photon transition. The influence of Dirac's negative continuum is obviously different for various multipole combinations. While, for example, the negative-energy contribution to the intermediate-state summation in low-Z domain is negligible for the $E1M2$ decay it becomes important for the $2E2$ and $2M1$ decay channels. Moreover, $2s_{1/2} \to 1s_{1/2}$ transition with emission of two magnetic dipole $2M1$ photons in light ions seems to happen almost exclusively via the negative energy intermediate states.

One may observe in Table 4.4 that the total rates for the leading $2E1$ transition, as well as for

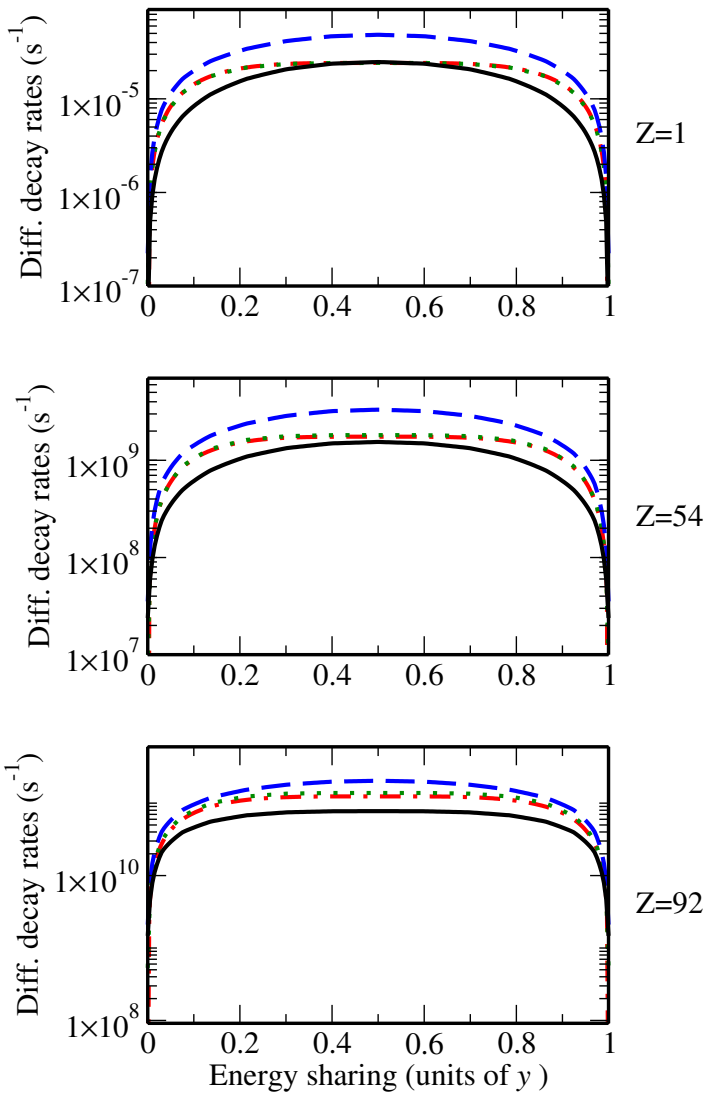

Figure 4.8: Negative contribution to the $E1M1$ and $E1E2$ $2p_{1/2} \to 1s_{1/2}$ two–photon decay - Differential decay rates for the sum of the $E1M1$, $M1E1$, $E1E2$, and $E2E1$ $2p_{1/2} \to 1s_{1/2}$ multipole two-photon transitions in hydrogen and H-like ions. Relativistic calculations have been carried out by performing intermediate-state summation over complete Dirac's spectrum (solid black line) as well as by restricting this summation to the positive- (dashed blue line) and negative-energy (dotted green line) states only. Results of relativistic calculations are compared also with the semi-relativistic prediction (dot-dashed red line) as given by Eq. (3.122).

		Z=1		Z=54		Z=92	
		length	velocity	length	velocity	length	velocity
$2E1$	W^+	8.2291 (+00)	8.2291 (+00)	1.6311 (+11)	1.6023 (+11)	2.9041 (+12)	2.3939 (+12)
	W^-	2.4949 (−08)	6.2372 (−09)	3.8442 (+09)	9.6290 (+08)	6.8066 (+11)	1.7044 (+11)
	W^{T}	8.2291 (+00)	8.2291 (+00)	1.8592 (+11)	1.8592 (+11)	3.8256 (+12)	3.8256 (+12)
$E1M2$	W^+	2.5372 (−10)	2.5372 (−10)	4.7949 (+07)	4.7940 (+07)	8.2955 (+09)	8.2714 (+09)
	W^-	9.1743 (−21)	4.5871 (−21)	1.9521 (+04)	9.7905 (+03)	4.8084 (+07)	2.4070 (+07)
	W^{T}	2.5372 (−10)	2.5372 (−10)	4.9278 (+07)	4.9278 (+07)	9.1387 (+09)	9.1387 (+09)
$2E2$	W^+	3.7296 (−11)	4.8617 (−13)	9.1765 (+06)	1.9624 (+05)	2.4730 (+09)	9.7383 (+07)
	W^-	4.5092 (−11)	8.2822 (−12)	1.1000 (+07)	2.0202 (+06)	2.9087 (+09)	5.3305 (+08)
	W^{T}	4.9072 (−12)	4.9072 (−12)	9.8177 (+05)	9.8177 (+05)	1.7859 (+08)	1.7859 (+08)
$2M1$	W^+	5.9021 (−20)		1.2691 (+05)		3.3321 (+08)	
	W^-	1.3804 (−11)		3.2695 (+06)		7.9720 (+08)	
	W^{T}	1.3804 (−11)		3.4027 (+06)		1.1093 (+09)	

Table 4.4: Contributions of the positive and negative energy to several multipoles - Rates (in s^{-1}) for the several multipole combinations of $2s_{1/2} \rightarrow 1s_{1/2}$ two–photon decay. Relativistic calculations have been performed within the velocity and length *gauges* and by carrying out intermediate–state summation over the complete Dirac's spectrum (W^{T}) as well as over the positive– (W^+) and negative–energy (W^-) solutions only.

higher multipole decay channels in medium- and high-Z ions, are not just sums of the corresponding rates W^+ and W^-. As seen from Eq. (3.72), this comes from the fact that the two-photon transition probabilities contain also terms that arise due to interference between the positive- and negative-energy Dirac solutions. For the $2E1$ and $E1M2$ transitions in the high-Z reagion, the interference terms lead to an enhancement of the total decay rates by 10–30% when compared with incoherent sum of W^+ and W^- contributions. In contrast, strong reduction of the total rates can be observed for the emission of two electric quadrupole photons $2E2$. This effect is most pronounced in the length *gauge* where the negative interference term is as large as -5.21×10^9 s^{-1} for the decay of H-like uranium ion.

It worth mentioning, however, that while for velocity *gauge* our findings are in agreement with results reported in Ref. [59], some discrepancy was found for calculations performed in length gauge, in particular for the contribution of the negative continuum. In detail, the comparison between the values calculated by *Labzowsky et al*. and the ones performed in this work with both basis set is showed in Table 4.5. We notice in this table a good agreement between the predictions obtained within the B-polynomial and B-spline approaches can be found for the ions along the entire isoelectronic sequence. Moreover, both our calculations show almost perfect agreement between gauges, which is better than the one reported in Ref. [153].

Labzowsky et al. argue that the contribution from the Dirac's negative continuum is negligible

		Decay rates (s^{-1})					
		B-Polynomials		B-Splines		LSS	
Z		length gauge	Δ_{l-v}	length gauge	Δ_{l-v}	length gauge	Δ_{l-v}
1	W^+	8.22906		8.22906		8.2206	
	W^-	2.49477(−8)		2.49481(−8)		3.9975(−22)	
	W^T	8.22906	< 1.0(−26)	8.22906	< 1.0(−15)	8.2207	< 1.0(−4)
40	W^+	2.96130(+10)		2.96124(+10)		3.1953(+10)	
	W^-	2.10270(+8)		2.10250(+8)		5.8284	
	W^T	3.19862(+10)	< 1.0(−13)	3.19858(+10)	< 1.0(−15)	3.1953(+10)	< 1.0(−4)
92	W^+	2.90482(+12)		2.90409(+12)		3.8230(+12)	
	W^-	6.85553(+11)		6.80648(+11)		1.2851(+5)	
	W^T	3.825839(+12)	< 1.0(−9)	3.82555(+12)	< 1.0(−15)	3.8216(+12)	< 1.0(−5)

Table 4.5: Two-photon with B-polynomials and B-splines - Total two-photon $2E1\ 2s_{1/2} \to 1s_{1/2}$ decay rates (in s^{-1}) for selected values of the nuclear charge Z. The relativistic calculations have been performed within the velocity and length *gauges*, using the B-polynomials and B-splines basis sets, and by carrying out intermediate-state summation over the complete Dirac's spectrum (W^T) as well as over the positive- (W^+) and negative-energy (W^-) solutions only. Δ_{l-v} stands for the relative difference between the length and velocity gauge values, and LSS denotes the values calculated by *Labzowsky et al.* [59]. Powers of ten are given in parentheses.

even for heaviest ions. Based on our theoretical analysis, we argue that such a discrepancy is caused by the incorrect summation performed in Ref. [153] over the electric $\lambda = 1$ and longitudinal $\lambda = -1$ components in Eq. (3.80). In detail, these terms were added terms *coherently*, i.e., using the following substitutions, $\bar{M}^{(1,L)}_{f,i} \to \bar{M}^{(1,L)}_{f,i} + \bar{M}^{(-1,L)}_{f,i}$ and $\bar{M}^{(-1,L)}_{f,i} \to 0$, in the reduced radial matrix elements (3.63). This interpretation is confirmed by our numerical calculations, which reproduce the results from Ref. [153] when we sum matrix elements *coherently*. However, it was proven by *Drake et al.* [60] that the terms have to be added *incoherently* if neither the polarization states nor the emission angles of photons are observed. As seen from Eq. (3.80), such an *incoherent* summation was performed in this work in order to investigate the differential in energy as well as the total two-photon decay rates.

4.3 Angular correlations and polarization in two-photon emission

In Fig. 4.9, we display the obtained values of the coefficients a_i and b_i, given by Eqs. (3.127), as a function of Z, for the two-photon transition $2s_{1/2} \to 1s_{1/2}$. We considered only the multipole terms that show a visible contribution to the figure. With such multipole contributions the coefficients a_4 have non-vanishing values. Several different energy shares ($y = 0.1,\ 0.25,\ 0.5$) are displayed. A B-spline basis set is used in all the evaluations.

For small atomic numbers, the coefficients $a_{i>2,\,i=1}$ nearly vanish, while a_2 tends to one. We notice

that the angular correlation function is well described in the low-Z regime by $W^y(\theta) \propto (1 + \cos^2\theta)$, corresponding to the dipole approximation [28]. This is in agreement with the more general result by *Yang* [164], which predicts an angular correlation of the form $(1 + \beta\cos^2(\theta))$ for dipole-dipole transitions. In detail, if the particles of some two-body scattering process could be given in plane waves, and, additionally, retained only the electric dipolar term of the multipole expansion, then, the dependence of the scattering cross-section on the angular between the two particles is given by the later general result. Such phenomena can be observed in molecules [165], photoelectrons [166] and Auger transitions [167]. The deviation to this expression along the isoelectronic sequence is due to the inclusion of higher multipoles in the coefficients a_i, which brings an asymmetric contribution (with respect to $\theta = \pi/2$) of the type $\sim \cos(\theta)$ and $\sim \cos^3(\theta)$. Because of this contribution, the angular correlation function results *tilted*, so that the two-photon emission in backward direction occurs (slightly) in preference to the emission in collinear direction. This behavior was first studied theoretically by Au [168], who used a non-relativistic approach with an inclusion of higher order multipoles. The results calculated in this work, and presented in Fig. 4.9, are in good agreement with a previous work by *Surzhykov et al.* [58], which compares the calculations of Au [168] with a full relativistic calculation.

Overall, we notice that deviations from the formula $W^y(\theta) = a_0(1 + \cos^2\theta)$ start playing the role of some percent from H-like Tin ion onwards ($Z \gtrsim 50$) and they grow generally fast with Z.

Likewise, the numerator of the degree of linear polarization (3.132) in $2s_{1/2} \to 1s_{1/2}$ transitions can be well described by $-a_0\sin^2(\theta)$, so that $P_L(\theta) \sim -\sin^2(\theta)/(1 + \cos^2(\theta))$, as long as the atomic number is relatively small ($Z \lesssim 50$). We point out that the relations $b_1 = -b_3$ and $b_2 = 1 + b_4$ stand for the all the isoelectronic sequence. The degree of polarization $P_L(\theta)$ is multiplied by a $\sin^2(\theta)$ function, for all the Z values. Therefore, for values of θ equal to 0 or π the degree of polarization is zero, since in those conditions there is no unique plane of reaction defined by the path of the photons. The value of maximum degree of polarization corresponds to $\theta = \pi/2$ with the explicit value of $P_L(\pi/2) = b_0/a_0$. For equal energy sharing, this value ranges from -1.0 (linearly vertical polarized) for $Z = 1$ to -0.88 for $Z = 100$. The deviations to both the angular correlation and the degree of linear polarization present a non-trivial dependence on the energy sharing that characterizes the decay: $a_{1,3,4}$ and $b_{1,3}$ are bigger in magnitude for higher energy shares, while a_2 deviates faster from 1 for lower energy shares. The energy sharing determines even the sign of some coefficients ($b_{1,3,4}$ and $a_{3,4}$), in case the atomic number being sufficiently large.

In Figs. 4.10, 4.11, we display the coefficients a_i and b_i obtained for the two-photon transitions $3d_{3/2} \to 1s_{1/2}$ and $3d_{5/2} \to 1s_{1/2}$, respectively. Similarly to Fig. 4.9, we notice that deviations from the non-relativistic formula $W^y(\theta) \approx a_0(1 + \cos^2\theta/13)$ are of the order of some percent from $Z \approx 50$ onwards. Also, in that lower Z regime, the degree of linear polarization is given by $P_L(\theta) \sim -\sin^2(\theta)/(13 + \cos^2(\theta))$. As in the previous case, the behavior of the curves is not linear but rather characterized by a non-trivial interplay between the dependence on the atomic number and on the

Z	a_0/Z^6	a_1/a_0	a_2/a_0	a_3/a_0	a_4/a_0
1	1.21411(−15)	−6.73510(−6)	1.00000	−5.48252(−6)	−1.30854(−11)
4	1.21388(−15)	−1.07867(−4)	1.00000	−8.76841(−5)	−3.35546(−9)
8	1.21317(−15)	−4.32805(−4)	1.00000	−3.50269(−4)	−5.39747(−8)
12	1.21197(−15)	−9.78853(−4)	0.99998	−7.86336(−4)	−2.75683(−7)
16	1.21031(−15)	−1.75278(−3)	0.99994	−1.39346(−3)	−8.82159(−7)
20	1.20819(−15)	−2.76417(−3)	0.99985	−2.16812(−3)	−2.18816(−6)
30	1.20102(−15)	−6.42095(−3)	0.99924	−4.80309(−3)	−1.16990(−5)
40	1.19150(−15)	−1.19292(−2)	0.99752	−8.33394(−3)	−3.98600(−5)
50	1.18023(−15)	−1.97041(−2)	0.99364	−1.25586(−2)	−1.06968(−4)
60	1.16817(−15)	−3.03114(−2)	0.98596	−1.71431(−2)	−2.48292(−4)
70	1.15685(−15)	−4.44730(−2)	0.97193	−2.15434(−2)	−5.23662(−4)
80	1.14876(−15)	−6.30296(−2)	0.94758	−2.48791(−2)	−1.03267(−3)
90	1.14820(−15)	−8.67780(−2)	0.90665	−2.57344(−2)	−1.93760(−3)
100	1.16319(−15)	−1.15969(−1)	0.83924	−2.18634(−2)	−3.49407(−3)

Table 4.6: Paramter a_i for $2s_{1/2} \to 1s_{1/2}$ - Values of the parameters a_i defined in Eq. (3.127), for the transition $2s_{1/2} \to 1s_{1/2}$ and several values of atomic number. The energy sharing is fixed at $y = 0.5$. Powers of ten are given in parentheses.

energy sharing. We see that the relations $b_1 = -b_3$ and $b_2 = 1 + b_4$ hold true also in these cases. Contrary to the $2s_{1/2} \to 1s_{1/2}$ transition, the minimum polarization at $\theta = \pi/2$ varies slowly with Z, being -0.0769 for $Z = 1$ and -0.0770 for $Z = 100$. We tabulate in Tables 4.6 – 4.11 the values of the coefficients for some atomic numbers, and for case of equal energy sharing.

The angular correlation and the degree of linear polarization given by Eqs. (3.127) and (3.132), together with parameters in Figs. 4.9-4.11 provide a accurate fit model for future experiments which involves two-photon polarization, for example, the PNC mixing coefficient measurement [64].

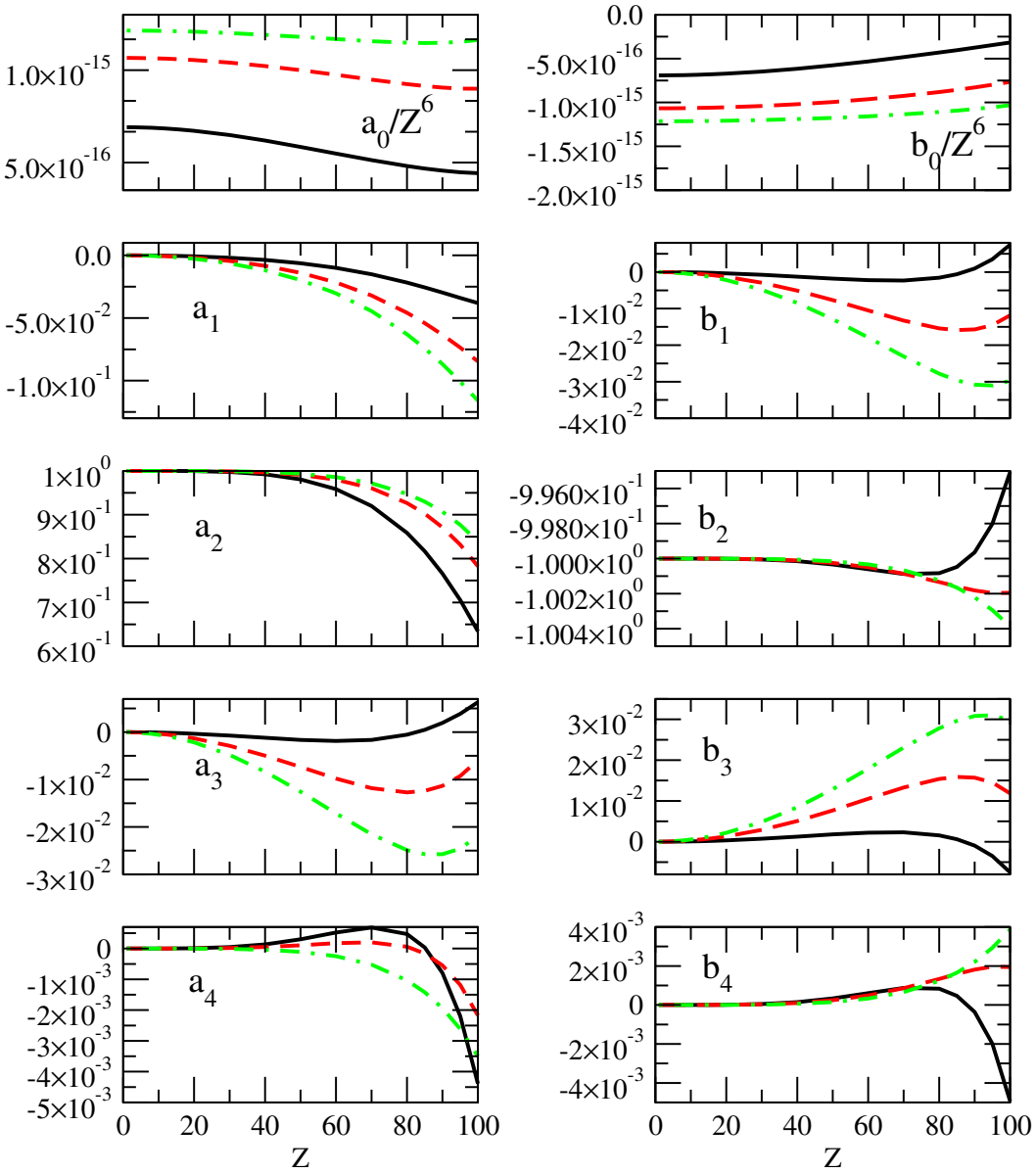

Figure 4.9: Parameters a_i and b_i for $2s_{1/2} \rightarrow 1s_{1/2}$ - Values of the parameters a_i and b_i defined in Eqs. (3.127) and (3.132), for the $2s_{1/2} \rightarrow 1s_{1/2}$ transition as function of Z. The values, which correspond to different energy shares $y = 0.1, 0.25, 0.5$, are represented by a black-solid, red-dashed and green-dot-dashed curve, respectively. Atomic units are used.

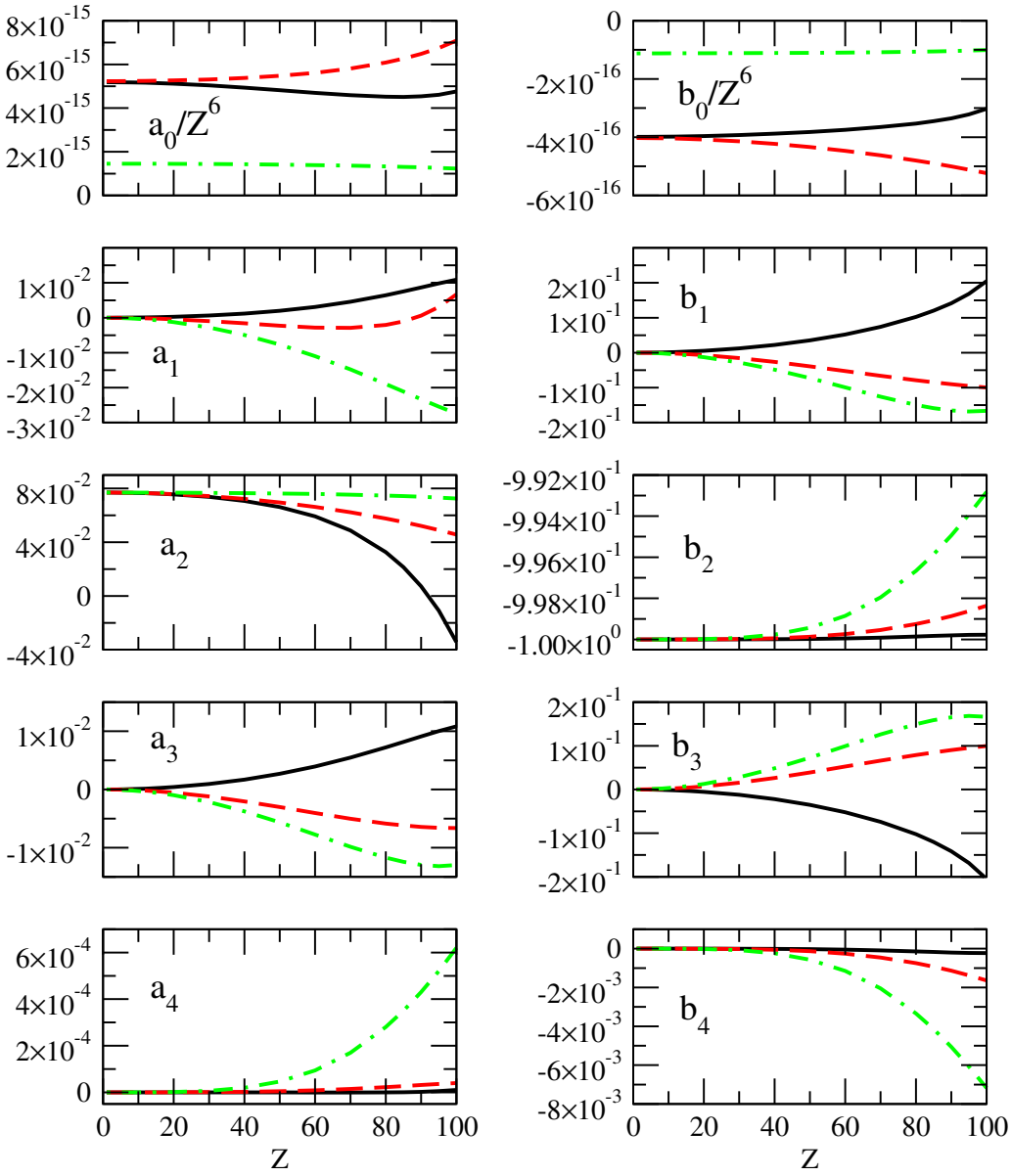

Figure 4.10: Parameters a_i and b_i for $3d_{3/2} \rightarrow 1s_{1/2}$ - As in Fig. 4.9, but for $3d_{5/2} \rightarrow 1s_{1/2}$ transition.

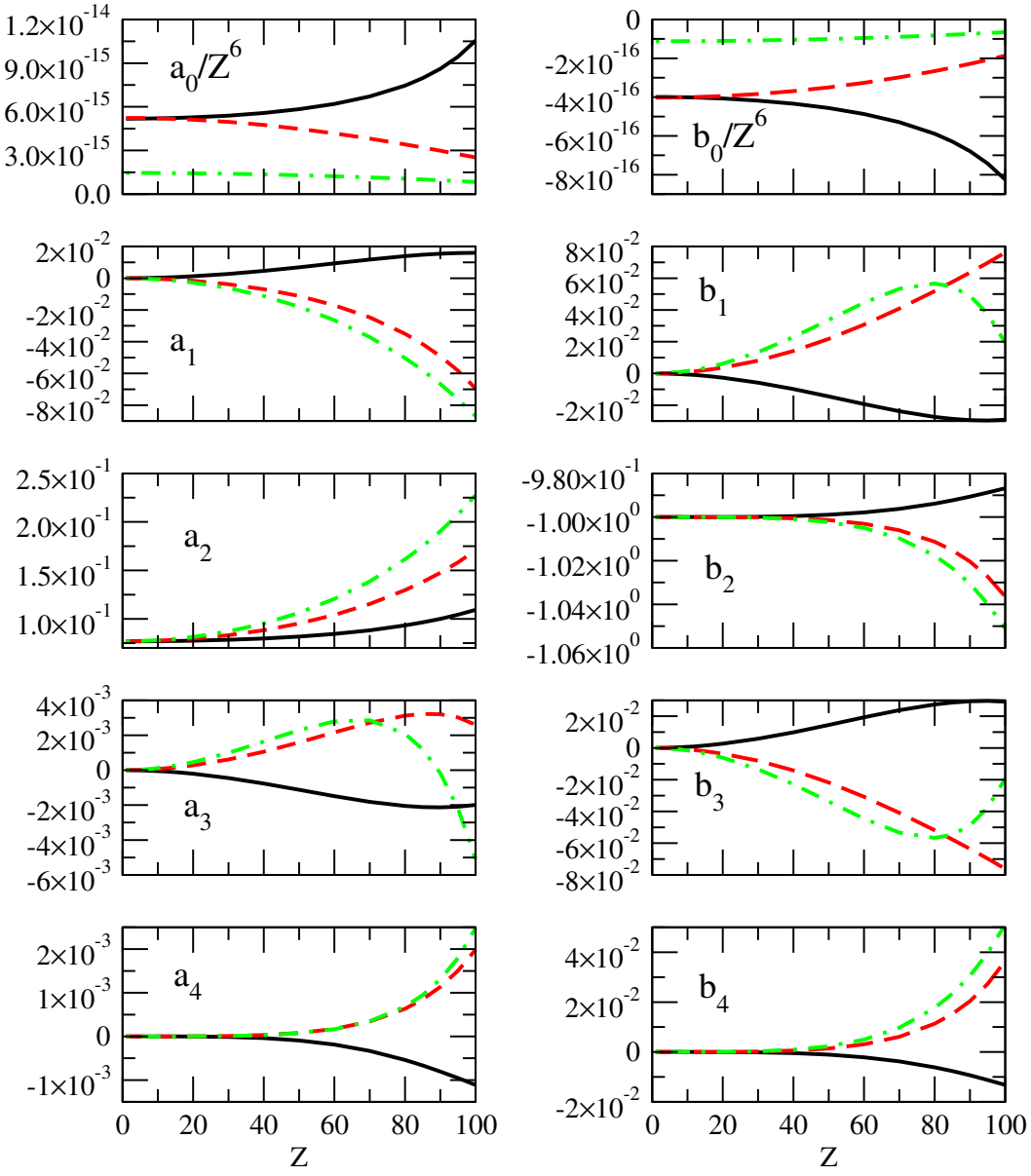

Figure 4.11: Parameters a_i and b_i for $3d_{5/2} \rightarrow 1s_{1/2}$ - As in Fig. 4.9, but for $3d_{5/2} \rightarrow 1s_{1/2}$ transition.

Z	a_0/Z^6	a_1/a_0	a_2/a_0	a_3/a_0	a_4/a_0
1	1.45454(−15)	−3.10016(−6)	7.69228(−2)	−2.48527(−6)	7.72423(−12)
4	1.45429(−15)	−4.96010(−5)	7.69193(−2)	−3.97438(−5)	1.97694(−9)
8	1.45349(−15)	−1.98384(−4)	7.69078(−2)	−1.58714(−4)	3.16076(−8)
12	1.45216(−15)	−4.46286(−4)	7.68885(−2)	−3.56121(−4)	1.59814(−7)
16	1.45028(−15)	−7.93195(−4)	7.68612(−2)	−6.30642(−4)	5.04208(−7)
20	1.44785(−15)	−1.23893(−3)	7.68256(−2)	−9.80398(−4)	1.22819(−6)
30	1.43932(−15)	−2.78367(−3)	7.66978(−2)	−2.16635(−3)	6.16807(−6)
40	1.42706(−15)	−4.93636(−3)	7.65071(−2)	−3.74968(−3)	1.92693(−5)
50	1.41072(−15)	−7.68045(−3)	7.62404(−2)	−5.64560(−3)	4.63149(−5)
60	1.38973(−15)	−1.09833(−2)	7.58780(−2)	−7.73187(−3)	9.41095(−5)
70	1.36321(−15)	−1.47830(−2)	7.53900(−2)	−9.83430(−3)	1.69889(−4)
80	1.32978(−15)	−1.89644(−2)	7.47285(−2)	−1.17008(−2)	2.80405(−4)
90	1.28723(−15)	−2.33125(−2)	7.38107(−2)	−1.29513(−2)	4.30433(−4)
100	1.23178(−15)	−2.74113(−2)	7.24782(−2)	−1.29719(−2)	6.20005(−4)

Table 4.7: Parameter a_i for $3d_{3/2} \to 1s_{1/2}$ - Same as Table 4.6 but for $3d_{3/2} \to 1s_{1/2}$ transition.

Z	a_0/Z^6	a_1/a_0	a_2/a_0	a_3/a_0	a_4/a_0
1	1.45450(−15)	−6.78618(−6)	7.69341(−2)	1.20042(−6)	9.61684(−12)
4	1.45354(−15)	−1.08613(−4)	7.70995(−2)	1.91827(−5)	2.46476(−9)
8	1.45049(−15)	−4.34890(−4)	7.76297(−2)	7.64220(−5)	3.95825(−8)
12	1.44542(−15)	−9.80149(−4)	7.85160(−2)	1.70786(−4)	2.01630(−7)
16	1.43831(−15)	−1.74660(−3)	7.97629(−2)	3.00700(−4)	6.42808(−7)
20	1.42918(−15)	−2.73739(−3)	8.13762(−2)	4.63913(−4)	1.58705(−6)
30	1.39756(−15)	−6.22516(−3)	8.70696(−2)	9.96154(−4)	8.35655(−6)
40	1.35344(−15)	−1.12362(−2)	9.52897(−2)	1.64591(−3)	2.79348(−5)
50	1.29698(−15)	−1.79106(−2)	1.06316(−1)	2.30175(−3)	7.34460(−5)
60	1.22834(−15)	−2.64482(−2)	1.20561(−1)	2.79288(−3)	1.67295(−4)
70	1.14763(−15)	−3.71286(−2)	1.38626(−1)	2.85811(−3)	3.48200(−4)
80	1.05490(−15)	−5.03456(−2)	1.61407(−1)	2.08979(−3)	6.85277(−4)
90	9.50027(−16)	−6.66663(−2)	1.90297(−1)	−1.74248(−4)	1.30843(−3)
100	8.32500(−16)	−8.69456(−2)	2.27615(−1)	−5.08017(−3)	2.48119(−3)

Table 4.8: Parameter a_i for $3d_{5/2} \to 1s_{1/2}$ - Same as Table 4.6 but for $3d_{5/2} \to 1s_{1/2}$ transition.

Z	b_0/Z^6	b_1	b_2
1	−1.21411(−15)	−5.48256(−6)	−1.00000
4	−1.21389(−15)	−8.76942(−5)	−1.00000
8	−1.21316(−15)	−3.50432(−4)	−1.00000
12	−1.21196(−15)	−7.87170(−4)	−1.00000
16	−1.21026(−15)	−1.39613(−3)	−1.00000
20	−1.20808(−15)	−2.17476(−3)	−1.00000
30	−1.20046(−15)	−4.83863(−3)	−1.00002
40	−1.18964(−15)	−8.45514(−3)	−1.00006
50	−1.17545(−15)	−1.28830(−2)	−1.00015
60	−1.15760(−15)	−1.78893(−2)	−1.00033
70	−1.13557(−15)	−2.30857(−2)	−1.00066
80	−1.10851(−15)	−2.78031(−2)	−1.00123
90	−1.07488(−15)	−3.08231(−2)	−1.00221
100	−1.03175(−15)	−2.97366(−2)	−1.00387

Table 4.9: Parameter b_i for $2s_{1/2} \to 1s_{1/2}$ - Values of the parameters b_i defined in Eq. (3.132), for the transition $2s_{1/2} \to 1s_{1/2}$ and several values of atomic number Z. The energy sharing is fixed at $y = 0.5$. Powers of ten are given in parentheses.

Z	b_0/Z^6	b_1	b_2
1	−1.11889(−16)	−3.23083(−5)	−1.00000
4	−1.11880(−16)	−5.16640(−4)	−1.00000
8	−1.11852(−16)	−2.06280(−3)	−1.00000
12	−1.11805(−16)	−4.62715(−3)	−9.99998(−1)
16	−1.11739(−16)	−8.19075(−3)	−9.99994(−1)
20	−1.11652(−16)	−1.27268(−2)	−9.99985(−1)
30	−1.11340(−16)	−2.80726(−2)	−9.99924(−1)
40	−1.10874(−16)	−4.84756(−2)	−9.99762(−1)
50	−1.10217(−16)	−7.27773(−2)	−9.99433(−1)
60	−1.09315(−16)	−9.93555(−2)	−9.98857(−1)
70	−1.08084(−16)	−1.25971(−1)	−9.97956(−1)
80	−1.06389(−16)	−1.49493(−1)	−9.96664(−1)
90	−1.04010(−16)	−1.65345(−1)	−9.94944(−1)
100	−1.00557(−16)	−1.66306(−1)	−9.92819(−1)

Table 4.10: Parameter b_i for $3d_{3/2} \to 1s_{1/2}$ - Same as Table 4.9 but for $3d_{3/2} \to 1s_{1/2}$ transition.

Z	b_0/Z^6	b_1	b_2
1	−1.11885(−16)	1.56060(−5)	−1.00000
4	−1.11817(−16)	2.49515(−4)	−1.00000
8	−1.11599(−16)	9.95739(−4)	−1.00000
12	−1.11236(−16)	2.23166(−3)	−1.00000
16	−1.10727(−16)	3.94542(−3)	−1.00002
20	−1.10072(−16)	6.12007(−3)	−1.00005
30	−1.07795(−16)	1.34110(−2)	−1.00028
40	−1.04592(−16)	2.28963(−2)	−1.00091
50	−1.00451(−16)	3.37235(−2)	−1.00230
60	−9.53527(−17)	4.45643(−2)	−1.00498
70	−8.92709(−17)	5.33363(−2)	−1.00972
80	−8.21712(−17)	5.66721(−2)	−1.01767
90	−7.40053(−17)	4.88362(−2)	−1.03056
100	−6.47002(−17)	1.92873(−2)	−1.05109

Table 4.11: Parameter b_i for $3d_{5/2} \rightarrow 1s_{1/2}$ - Same as Table 4.9 but for $3d_{5/2} \rightarrow 1s_{1/2}$ transition.

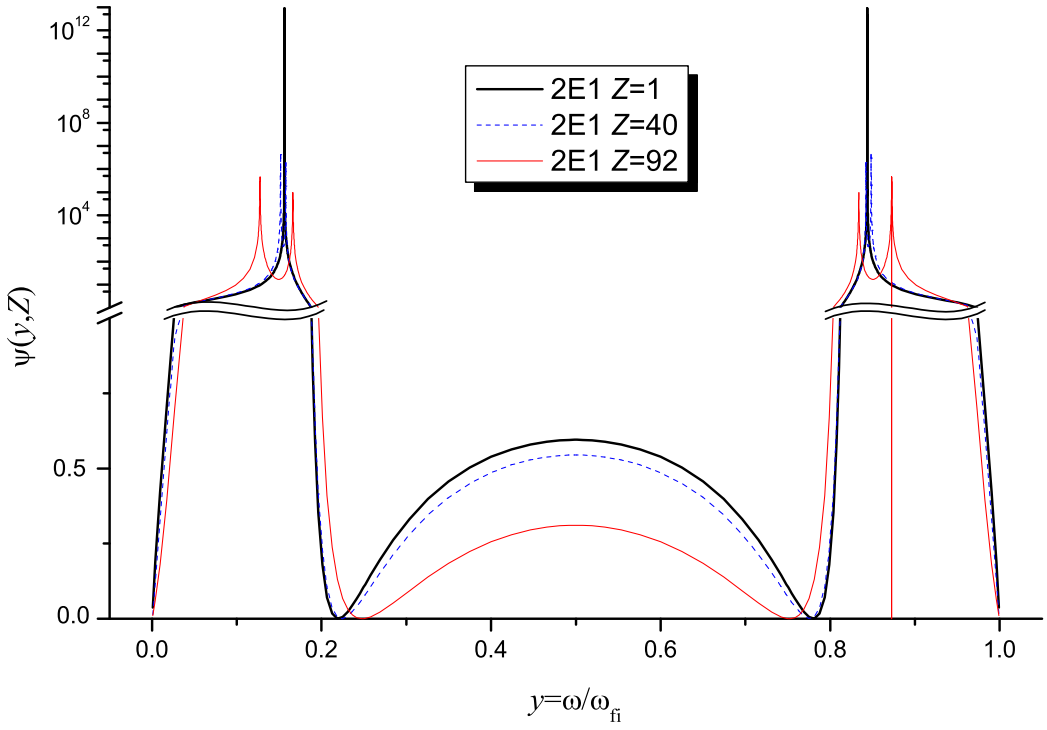

Figure 4.12: Spectral distribution of $3s_{1/2} \rightarrow 1s_{1/2}$ $2E1$ - Spectral distribution function $\psi(y)$ defined by Eq. 4.1, of the $2E1$ contribution for the transition $3s_{1/2} \rightarrow 1s_{1/2}$ at Z=1, 40, and 92. The variable $y = \omega_1/\omega_{fi}$ is the fraction of the photon energy carried by one of the two-photons.

4.4 Resonance states

After the discussion of the non-resonant $2s_{1/2} \rightarrow 1s_{1/2}$ and $2p_{1/2} \rightarrow 1s_{1/2}$ two-photon transitions, we now turn to the evaluation of the differential total decay rates from the higher excited states.

In the spectral distribution for the $3s_{1/2} \rightarrow 1s_{1/2}$ transition, plotted in Fig. 4.12, we notice several features that are not found in the corresponding plot for the $2p_{1/2} \rightarrow 1s_{1/2}$ transition (Fig. 4.2). In particular, the $\psi_{3s\rightarrow 1s}(y, Z)$ function exhibits sharp peaks and, as mentioned in Sec.3.7, this behavior is due to a resonance between the transition $E_{3s} - E_{2p}$ and the transition $E_{2p} - E_{1s}$. As expected, both peaks splits into two with increasing values of Z as consequence of fine-structure splitting.

In addition, besides the zeroes at the endpoints, there are two more zeroes at $y = 0.2197$ and 0.7803. Such minima were observed in two-photon spectra by *Tung et al.* [53, 169], and they were referred to as "transparencies". In Table 4.12 we list the transparencies for several two-photon transitions obtained in this work (from Eq. (3.138)) and by other authors. Their relative difference are less than 0.01% for $Z = 1$. To the best of our knowledge, there are no published data for other Z values.

In Fig. 4.13 we plot the transparency frequency y^{transp} of the transition $3s_{1/2} \rightarrow 1s_{1/2}$ as function

Transition	y ($Z = 1$)	y ($Z = 40$)	y ($Z = 92$)
$3s_{1/2} \rightarrow 1s_{1/2}$	0.780267	0.77628	0.7518
	0.7803 [1]		
	0.7802 [2]		
	0.7803 [3]		
$4s_{1/2} \rightarrow 1s_{1/2}$	0.737322	0.73273	0.7034
	0.7373 [1]		
	0.7373 [3]		
$6s_{1/2} \rightarrow 1s_{1/2}$	0.7032201	0.70497	0.6725
	0.7098 [1]		
	0.7079 [2]		
	0.7098 [3]		

[1] *Florescu et al.* [170]
[2] *Quattropani et al.* [171]
[3] *Tung et al.* [53]

Table 4.12: Transparencies for several two-photon transitions - The variable $y = \omega_1/\omega_{fi}$ is the fraction of the photon energy carried by one of the two-photons.

of Z. We notice that the transparency values scale with Z^2 as the transition energy.

The spectral distribution for the $3d_{3/2} \rightarrow 1s_{1/2}$ transition, plotted in Fig. 4.14, exhibits only the resonant behavior, and not the above zero behavior as mentioned in Ref. [53], which is due to the fine-structure splittings between $2p_{1/2}$ and $2p_{3/2}$ and $3p_{1/2}$ and $3d_{3/2}$. Using two-photon absorption with a two color laser it is possible to populate the $3d$ state without populating the $3s$ state by tuning the laser frequencies for the transparencies.

In Fig. 4.15 is plotted the frequency distribution of the multipole $E1M1$ contribution for the $2p_{3/2} \rightarrow 1s_{1/2}$ transition. Along with the resonances predicted in Sec. 3.7, the curve for each contribution is similar to the ones in Fig. 4.1 for the $2p_{1/2} \rightarrow 1s_{1/2}$ transition. In the $E1M1$ case, the resonance in the low-frequency side occurs when the energy of one of the photons is equal to the energy difference $E_{2p_{3/2}} - E_{2s_{1/2}}$, while the resonance in the high-frequency side occurs when the energy of one of the photons is equal to the energy difference $E_{2p_{3/2}} - E_{2p_{1/2}}$.

In Table 4.13 we list the radiative corrections terms for some states, which were included in Eq. (3.139) to achieve the accuracy of, at least, six digits. The values for the real part of self-energy and vacuum polarization were obtained from the MCDF code developed by J. P Desclaux, P. Indelicato and collaborators [8, 9, 172]. The level width, Γ_n, is equal (in a.u.) to the sum of the one–photon partial level widths, given by Eq. (3.160).

As seen from Eq. (3.85), by performing the integration of the differential transition probabilities over energy of the emitted photon, we may finally obtain the total two-photon decay rates. Eq. (3.155) shows that these rates can be traced back to $\mathfrak{h}$ functions.

In Table 4.14 we list the sum of the terms $\mathfrak{h}^{\mathrm{LPA}}$ and $\mathfrak{h}_1^{\mathrm{LPA}}$ given by Eqs. (3.156) and (3.158),

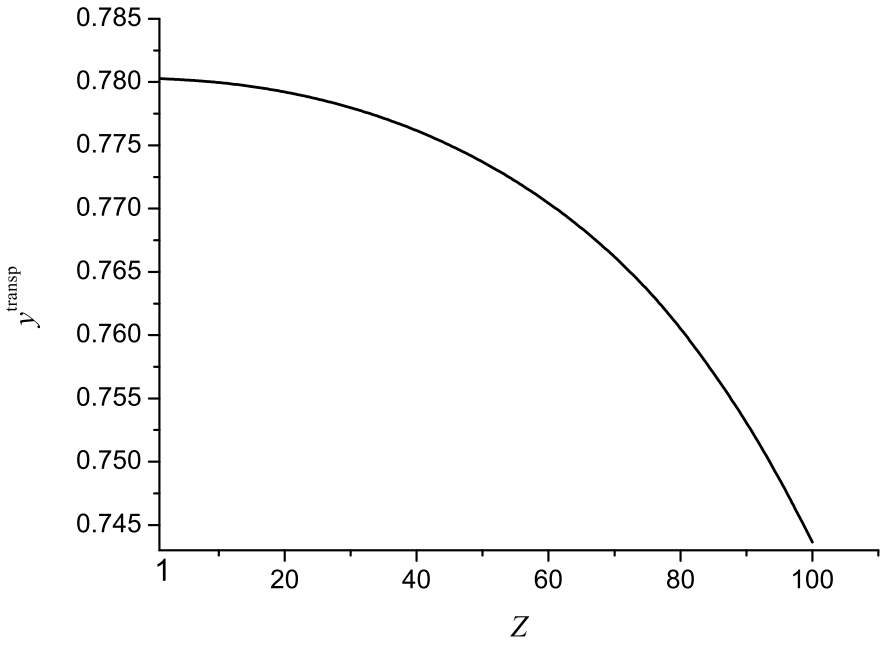

Figure 4.13: Transparencies of $3s_{1/2} \to 1s_{1/2}$ - Transparency frequency y^{transp} of the transition $3s_{1/2} \to 1s_{1/2}$ as function of the atomic number Z.

			$Z = 1$			
	$2s_{1/2}$	$2p_{1/2}$	$2p_{3/2}$	$3s_{1/2}$	$3p_{1/2}$	$3p_{3/2}$
Re [SE]+VP= ΔE_n	1.5867(−7)	−1.9542(−9)	1.9095(−9)	4.7376(−8)	−5.5003(−10)	6.4103(−10)
Im [SE]= $\Gamma_n/2$	1.9905(−16)	1.5162(−8)	1.5162(−8)	1.5281(−10)	4.5911(−9)	4.5911(−9)
			$Z = 40$			
	$2s_{1/2}$	$2p_{1/2}$	$2p_{3/2}$	$3s_{1/2}$	$3p_{1/2}$	$3p_{3/2}$
Re [SE]+VP= ΔE_n	8.6991(−2)	−1.4913(−3)	7.0905(−3)	2.6401(−2)	−1.3587(−4)	2.3058(−3)
Im [SE]= $\Gamma_n/2$	1.4690(−6)	3.9208(−2)	3.8037(−2)	4.6373(−4)	1.1689(−2)	1.1627(−2)
			$Z = 92$			
	$2s_{1/2}$	$2p_{1/2}$	$2p_{3/2}$	$3s_{1/2}$	$3p_{1/2}$	$3p_{3/2}$
Re [SE]+VP= ΔE_n	1.7995	2.4965(−1)	3.2252(−1)	5.7911(−1)	9.3654(−2)	1.102(−1)
Im [SE]= $\Gamma_n/2$	4.7468(−3)	1.1417	9.5531(−1)	2.7061(−2)	3.1125(−1)	3.044(−1)

Table 4.13: Radiative corrections - Values of Re [SE]+VP and Im [SE] for several states in a.u. Powers of ten are given in parentheses.

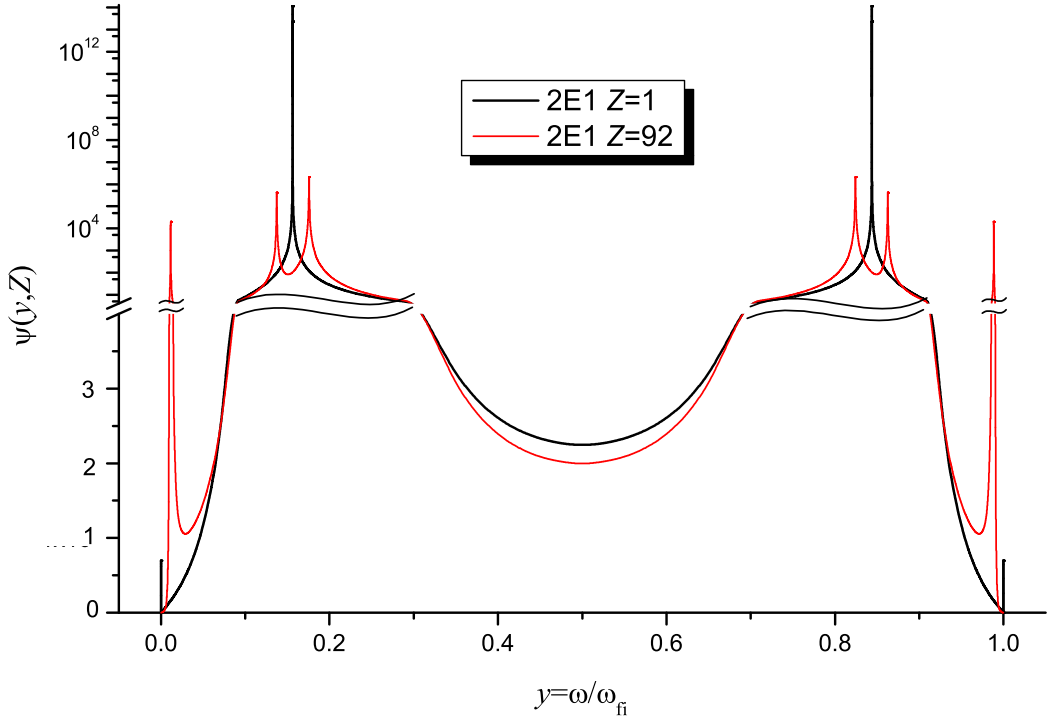

Figure 4.14: Spectral distribution of $3d_{3/2} \rightarrow 1s_{1/2}$ $2E1$ - Spectral distribution functions $\psi(y, Z)$ defined by Eq. 4.1, of the $2E1$ contribution for the transition $3d_{3/2} \rightarrow 1s_{1/2}$ at $Z = 1$ and 92. For the legend, see Fig. 4.12 caption.

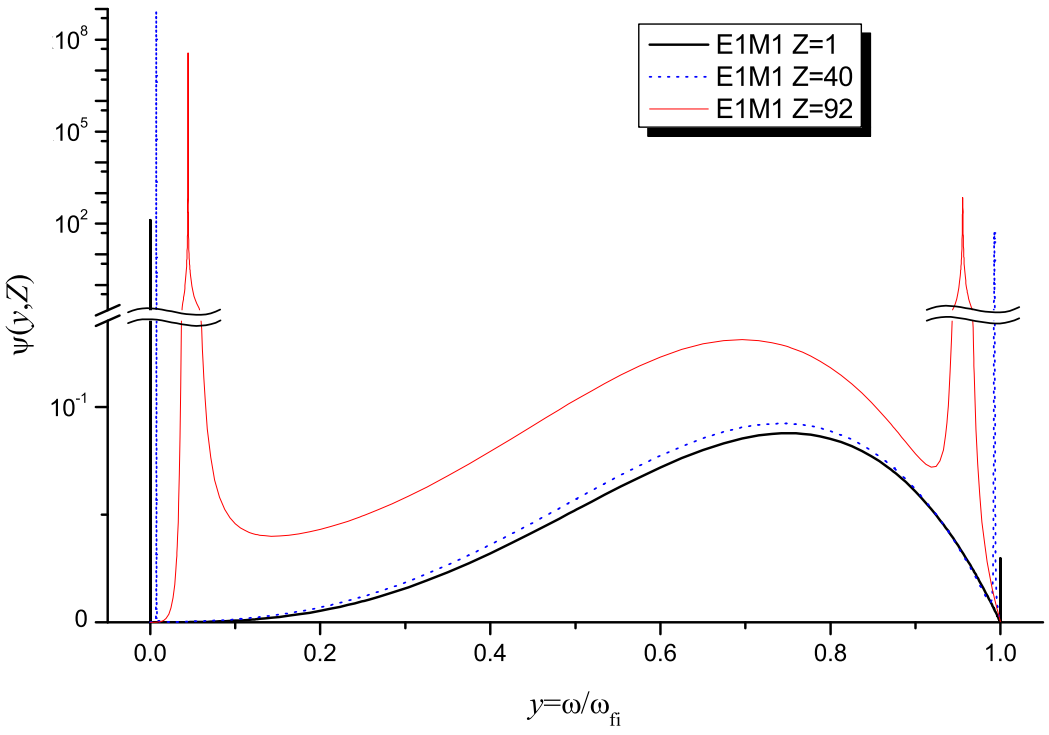

Figure 4.15: Spectral distribution of $2p_{3/2} \rightarrow 1s_{1/2}$ $E1M1$ - Spectral distribution functions $\psi(y,Z)$ defined by Eq. 4.1, of the $E1M1$ contribution for the transition $2p_{3/2} \rightarrow 1s_{1/2}$ at $Z = 1$, 40 and 92. For the legend, see Fig. 4.12 caption.

$Z = 1$	$f\backslash i$	$3s_{1/2}$	$3p_{1/2}$	$3p_{3/2}$	$3d_{3/2}$	$3d_{5/2}$
	$1s_{1/2}$	2.342758	3.966941(-6)	3.230044(-6)	3.706845	3.706854
	$2s_{1/2}$	6.452435(-2)	4.925801(-8)	4.926319(-8)	7.762447(-4)	7.750004(-4)
	$2p_{1/2}$	2.894796(-8)	4.660148(-2)	4.414498(-4)	3.890718(-8)	3.049476(-9)
	$2p_{3/2}$	5.789457(-8)	8.832671(-4)	4.704893(-2)	1.326766(-8)	4.912187(-8)
$Z = 40$	$f\backslash i$	$3s_{1/2}$	$3p_{1/2}$	$3p_{3/2}$	$3d_{3/2}$	$3d_{5/2}$
	$1s_{1/2}$	7.813052(9)	2.872804(7)	2.002016(7)	1.436349(10)	1.441446(10)
	$2s_{1/2}$	2.247363(8)	2.812583(5)	3.395829(5)	6.369235(6)	−1.183514(6)
	$2p_{1/2}$	1.756667(5)	1.797278(8)	3.117290(6)	3.012475(5)	2.478360(4)
	$2p_{3/2}$	3.370367(5)	8.545466(6)	2.168435(8)	8.878266(4)	3.231816(5)
$Z = 92$	$f\backslash i$	$3s_{1/2}$	$3p_{1/2}$	$3p_{3/2}$	$3d_{3/2}$	$3d_{5/2}$
	$1s_{1/2}$	−5.316586(10)	3.647738(10)	2.048248(11)	1.646524(12)	1.637676(12)
	$2s_{1/2}$	7.443297(9)	1.683735(8)	6.928218(8)	1.135193(10)	6.013487(9)
	$2p_{1/2}$	9.548939(7)	2.314262(10)	3.637390(9)	4.841719(8)	1.534768(7)
	$2p_{3/2}$	1.554405(8)	5.312377(9)	5.376493(10)	1.660640(8)	3.122434(8)

Table 4.14: Sum of the terms $\mathfrak{h}^{\mathbf{LPA}}$ and $\mathfrak{h}_{\mathbf{1}}^{\mathbf{LPA}}$ - Sum of the terms $\mathfrak{h}^{\mathrm{LPA}}$ and $\mathfrak{h}_1^{\mathrm{LPA}}$ given by Eq. (3.156) and Eq. (3.158), respectively, for transitions from bound states with $n_i = 3$. This values were obtained using the radiative corrections of Table 4.13 and $q = 1$. Powers of ten are given in parentheses.

respectively, required for the evaluation of the decay rates for transitions from bound states with $n_i = 3$ in the LPA, i.e., including the most relevant multipoles, radiative corrections and using $q = 1$. The correspondent values obtained in TLA are listed in Table 4.15. By comparing the values of these two tables we conclude that they differ less than 0.001 % for $Z = 1$, 2.3 % for $Z = 40$ and 10 % for $Z = 92$, which shows the importance of the radiative effects.

In Tables 4.16 and 4.17 we list all multipole combinations included in the calculation of the two-photon decay rate for the $2p_{3/2} \to 1s_{1/2}$ and $3s_{1/2} \to 2s_{1/2}$ transitions. We notice that for $Z = 1$ the decay rate values of some multipole contributions, such as the $E1M1$ and the $E1E2$, listed in Table 4.16, are similar to the correspondent ones for the transition $2p_{1/2} \to 1s_{1/2}$. Nevertheless, this is not the case for $Z = 40$ and $Z = 92$. This is due to fact the that the energy separation between $2p_{3/2}$ and $2s$ increases with Z and, consequently, the decay rate contribution from the cascade process also increases. This aspect is also evident in Fig. 4.16, where the multipole combination E1M1 decay rate W_{E1M1}, obtained in the LPA and TLA, is plotted as a function of the atomic number Z for the $2p_{1/2,3/2} \to 1s_{1/2}$ transitions.

The resonant behavior of the $2p_{3/2} \to 1s_{1/2}$ transition is strongly suppressed for low Z values. We notice that for lower Z values both solid LPA and dotted TLA lines have similar values, which is a consequence of the fact that non-resonant contribution related to integral of background in both transitions $M1E1$ in Figs. 4.1 and 4.15 is much higher than the cascade term dashed line. For higher values of Z, the solid line follows the dashed line. This could be explained by the different Z scalings of the two contributions. The background scales as Z^8 and the cascade term, $2p_{3/2} \to 2s_{1/2} \to 1s_{1/2}$,

$Z = 1$	$f\backslash i$	$3s_{1/2}$	$3p_{1/2}$	$3p_{3/2}$	$3d_{3/2}$	$3d_{5/2}$
	$1s_{1/2}$	2.342751	3.966941(-6)	3.230044(-6)	3.706845	3.706854
	$2s_{1/2}$	6.452428(-2)	4.925765(-8)	4.926337(-8)	7.762447(-4)	7.750004(-4)
	$2p_{1/2}$	2.894793(-8)	4.660148(-2)	4.414498(-4)	3.890718(-8)	3.049476(-9)
	$2p_{3/2}$	5.789453(-8)	8.832670(-4)	4.704892(-2)	1.326766(-8)	4.912188(-8)
$Z = 40$	$f\backslash i$	$3s_{1/2}$	$3p_{1/2}$	$3p_{3/2}$	$3d_{3/2}$	$3d_{5/2}$
	$1s_{1/2}$	7.799875(9)	2.872822(7)	2.000453(7)	1.436350(10)	1.441394(10)
	$2s_{1/2}$	2.246945(8)	2.802618(5)	3.400453(5)	6.369529(6)	−1.180529(6)
	$2p_{1/2}$	1.756241(5)	1.797280(8)	3.116223(6)	3.080467(5)	2.477876(4)
	$2p_{3/2}$	3.369973(5)	8.514049(6)	2.167575(8)	8.872957(4)	3.233897(5)
$Z = 92$	$f\backslash i$	$3s_{1/2}$	$3p_{1/2}$	$3p_{3/2}$	$3d_{3/2}$	$3d_{5/2}$
	$1s_{1/2}$	−5.843073(10)	3.632557(10)	2.037502 (11)	1.648325(12)	1.637187(12)
	$2s_{1/2}$	7.703355(9)	1.624996(8)	7.340967(8)	1.135843(10)	6.400342(9)
	$2p_{1/2}$	9.552389(7)	2.313307(10)	3.630875(9)	4.857978(8)	1.5282890(7)
	$2p_{3/2}$	1.556356(8)	5.270175(9)	5.351656(10)	1.655470(8)	3.134378(8)

Table 4.15: Sum of $\mathfrak{h}^{\mathbf{TLA}}$ and $\mathfrak{h}_{\mathbf{1}}^{\mathbf{TLA}}$ - Sum of the terms $\mathfrak{h}^{\mathrm{TLA}}$ and $\mathfrak{h}_1^{\mathrm{TLA}}$ given by Eq. (3.165) and Eq. (3.164), respectively, for transitions from bound states with $n_i = 3$. This values were obtained without radiative corrections, using $q = 10^{-2}$ and following and using TLA. Powers of ten are given in parentheses.

scales as Z^{10}. The dash-dotted decay rate of $2p_{1/2} \to 1s_{1/2}$ and dotted lines are almost coincident in low-Z region and diverge from about $Z = 40$, which is evidence of the relativistic effects in the $np_{1/2}$ and $np_{3/2}$ states.

In Table 4.18 we report two-photon decay rates for transitions from the initial level $n = 3$ obtained with Eq. (3.138) (LPA). The results of *Tung et al.* presented in this table were obtained using the analytical formulas described in Ref. [53], which were obtained through the so called implicit technique that describes the intermediate states by a differential equation.

We restrict ourselves to list the two-photon decay rates obtained in the LPA because in some cases they are very different from the TLA ones, which is essentially due to the cascade term in Eq. (3.163).

One important aspect concerning total decay rates of resonant transitions is the calculation of the non-resonant decay rate without interference of the resonant intermediate states. *Cresser et al.* [173], using a fourth-order perturbation term development, obtained an expression similar to Eq. (35.21) in [85] where the sum over the intermediate states considers only the states above the initial one, avoiding in this way the resonant denominators, and found the value 8.2197 s^{-1} for the $3s_{1/2} \to 1s_{1/2}$ transition rate. *Florescu* [174], using the same procedure, obtained the value 8.22581 s^{-1}. The non-relativistic limit of Eq. (3.80) in the Coulomb gauge gives the same expression as the one reported by *Cresser et al.* [173] and, consequently, the same result.

Jentschura [175] pointed out that *Cresser et al.*'s procedure is not *gauge* invariant since in a second order evaluation the sum over the complete spectrum of intermediate states is required to have

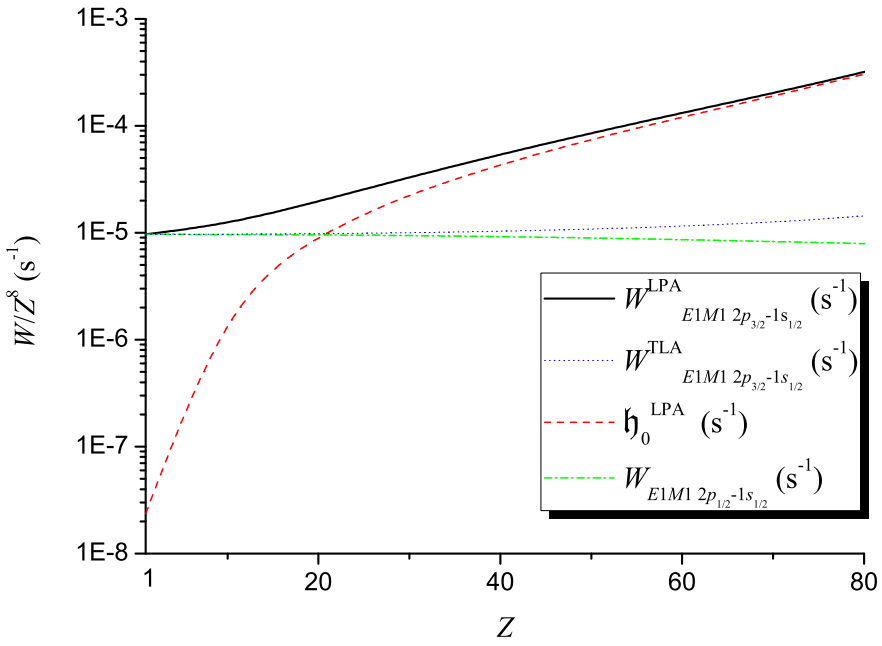

Figure 4.16: E1M1 Multipole contribution of $2p_{3/2} \rightarrow 1s_{1/2}$ - Multipole combination $E1M1$ decay rate values W_{E1M1}, obtained in the LPA and TLA, as functions of the atomic number Z for the transitions $2p_{1/2} \rightarrow 1s_{1/2}$ (dot-dashed green line) and $2p_{3/2} \rightarrow 1s_{1/2}$ (solid black and dotted blue lines). The cascade term in LPA is represented by the dashed red line.

Multipoles	Contribution (s^{-1})		
	$Z = 1$	$Z = 40$	$Z = 92$
$E1M1$	9.700994(−6)	3.547078 (8)	2.93820 (12)
$E1E2$	6.612242(−6)	4.597372(7)	1.113120 (11)
$E1M3$	1.761532(−16)	3.264236(3)	1.216566 (8)
$M1M2$	2.450145(−15)	4.265433(4)	1.129082 (9)
$E2M2$	7.227055(−17)	1.337970(3)	4.923824 (7)
$E2E3$	4.096369(−18)	7.718214(1)	1.216566 (8)
Total	1.631323(−5)	4.007255 (8)	3.050699(12)

Table 4.16: Multipole contributions for the $2p_{3/2} \rightarrow 1s_{1/2}$ - Same as Table 4.1 for the transition $2p_{3/2} \rightarrow 1s_{1/2}$. Powers of ten are given in parentheses.

Multipoles	Contribution (s^{-1})		
	$Z = 1$	$Z = 40$	$Z = 92$
$2E1$	6.452436(−2)	3.167606(8)	1.850546 (12)
$E1M2$	6.725935(−14)	1.150220(3)	3.359725 (8)
$2M1$	1.038556(−14)	1.241685(2)	1.031596 (6)
$2E2$	1.456030(−14)	1.584123(2)	8.482772 (5)
$2M2$	1.901242(−27)	6.068107(−5)	4.479357 (3)
Total	6.452436(−2)	3.167620(8)	1.850884 (12)

Table 4.17: Multipole contributions for the $3s_{1/2} \rightarrow 2s_{1/2}$ - Same as Table 4.1 for the transition $3s_{1/2} \rightarrow 2s_{1/2}$. Powers of ten are given in parentheses.

		Total decay rate (s^{-1})				
$Z = 1$	$f\backslash i$	$3s_{1/2}$	$3p_{1/2}$	$3p_{3/2}$	$3d_{3/2}$	$3d_{5/2}$
	$1s_{1/2}$	6.382020(6)	3.431055(1)	3.431043(1)	7.213121(7)	7.212970(7)
	$2s_{1/2}$	6.452436(−2) 6.4527(-2) [1]	4.925806(-8)	4.965339(-8)	7.762774(-4) 7.7589(-4) [1]	7.751032(-4)
	$2p_{1/2}$	2.894796(-8)	4.6601485(-2) 4.7484(-2) [1]	4.414514(-4)	3.890719(-8)	3.070354(-9)
	$2p_{3/2}$	5.789457(-8)	8.832671(-4)	4.704893(-2)	1.326768(-8)	4.912603(-8)
$Z = 40$	$f\backslash i$	$3s_{1/2}$	$3p_{1/2}$	$3p_{3/2}$	$3d_{3/2}$	$3d_{5/2}$
	$1s_{1/2}$	1.940069(13)	1.465902(11)	1.459393(13)	1.909365(14)	1.846466(14)
	$2s_{1/2}$	3.167620(8)	1.249212(6)	6.204266(6)	4.239616(8)	1.256275(9)
	$2p_{1/2}$	2.488771(5)	1.797286(8)	2.342989(7)	4.767668(5)	1.268419(6)
	$2p_{3/2}$	3.370367(5)	8.545466(6)	2.648671(8)	4.278490(5)	3.734221(5)
$Z = 92$	$f\backslash i$	$3s_{1/2}$	$3p_{1/2}$	$3p_{3/2}$	$3d_{3/2}$	$3d_{5/2}$
	$1s_{1/2}$	1.067206(15)	5.649957(13)	4.187334(13)	6.170663(15)	5.175621(15)
	$2s_{1/2}$	1.850884(12)	4.581582(10)	1.219838(11)	5.062691(12)	1.123469(13)
	$2p_{1/2}$	8.893987(9)	2.336202(10)	2.576780(11)	9.697069(9)	5.543826(10)
	$2p_{3/2}$	1.554405(8)	5.312377(9)	1.059702(12)	1.959473(10)	1.239531(9)

[1] *Tung et al.* [53]

Table 4.18: Two-photon decay rate in LPA - Total two-photon decay rates, and the most relevant multipoles, in the Line Profile approach (s^{-1}) for transitions from bound states with $n_i = 3$. Powers of ten are given in parentheses.

equivalence between two different *gauges* (more details in appendix of Ref. [60]).

The values listed in Table 4.15 were used to calculate the non-resonant radiative corrections presented in Table 4.19 (setting $q = 10^{-3}$). We notice that for the $3s_{1/2} \rightarrow 1s_{1/2}$ transition the values calculated in this work differ from the values presented in Ref. [154] by 0.01 % for $Z = 1$ and 0.1 % for $Z = 40$.

The reason that some values in Table 4.19 are negative, such as the $3s_{1/2} \rightarrow 1s_{1/2}$ transition correction for $Z = 92$, is because they were obtained from the evaluation of the two–loop self-energy, which can be negative as any negative correction to the decay rates [154]. In Fig. 4.17 we represent the values of the non-resonant radiative correction for several values of atomic number. We notice that the last value of Z which the non-resonant correction has a positive sign is $Z = 80$.

After the publication of the results presented in this section in Ref. [79], good agreement was verified with afterwards Refs. [176, 177, 178].

		Total non-resonant correction (s^{-1})				
$Z = 1$	$f\backslash i$	$3s_{1/2}$	$3p_{1/2}$	$3p_{3/2}$	$3d_{3/2}$	$3d_{5/2}$
	$1s_{1/2}$	2.082562 2.082853 [1]	2.981766(−6)	2.98676(−6)	1.042768 1.042896 [2]	1.042835
	$2s_{1/2}$	6.452428(−2) 6.4530(-2) [1]	4.925721(−8)	4.926293(−8)	7.762407(−4)	7.749962(−4)
	$2p_{1/2}$	2.894793(−8)	4.660148(−2)	4.414498(−4)	3.890718(−8)	3.049476(−9)
	$2p_{3/2}$	5.789453(−8)	8.832670(−4)	4.704892(−2)	1.326767(−8)	4.912188(−8)
$Z = 40$	$f\backslash i$	$3s_{1/2}$	$3p_{1/2}$	$3p_{3/2}$	$3d_{3/2}$	$3d_{5/2}$
	$1s_{1/2}$	6.560351(9) 6.554(9) [3]	2.224659(7)	1.885681(7)	3.456276(9)	3.874677(9)
	$2s_{1/2}$	2.245669(8)	2.793230(5)	3.395425(5)	5.920457(6)	−2.764917(6)
	$2p_{1/2}$	1.755215(5)	1.797280(8)	3.088316(6)	3.078375(5)	2.349043(4)
	$2p_{3/2}$	3.369973(5)	8.514049(6)	2.166915(8)	8.842254(4)	3.233689(5)
$Z = 92$	$f\backslash i$	$3s_{1/2}$	$3p_{1/2}$	$3p_{3/2}$	$3d_{3/2}$	$3d_{5/2}$
	$1s_{1/2}$	−3.842113(11)	2.891626(10)	7.976296(10)	8.916260(10)	3.271857(11)
	$2s_{1/2}$	5.570205(9)	1.258571(8)	7.132981(8)	7.613467(9)	−5.085413(9)
	$2p_{1/2}$	8.535648(7)	2.313315(10)	3.386706(9)	4.767493(8)	−5.866950(7)
	$2p_{3/2}$	1.556356(8)	5.270175(9)	5.253150(10)	1.539227(8)	3.127867(8)

[1] *Jentschura* [154]
[2] *Jentschura* [179]
[3] *Jentschura et al.* [155]

Table 4.19: Two-photon non-resonant correction - Total non-resonant two-photon correction (s^{-1}) for transitions from bound states with $n_i = 3$. Comparison between the values obtained in this work and other theoretical values. Powers of ten are given in parentheses.

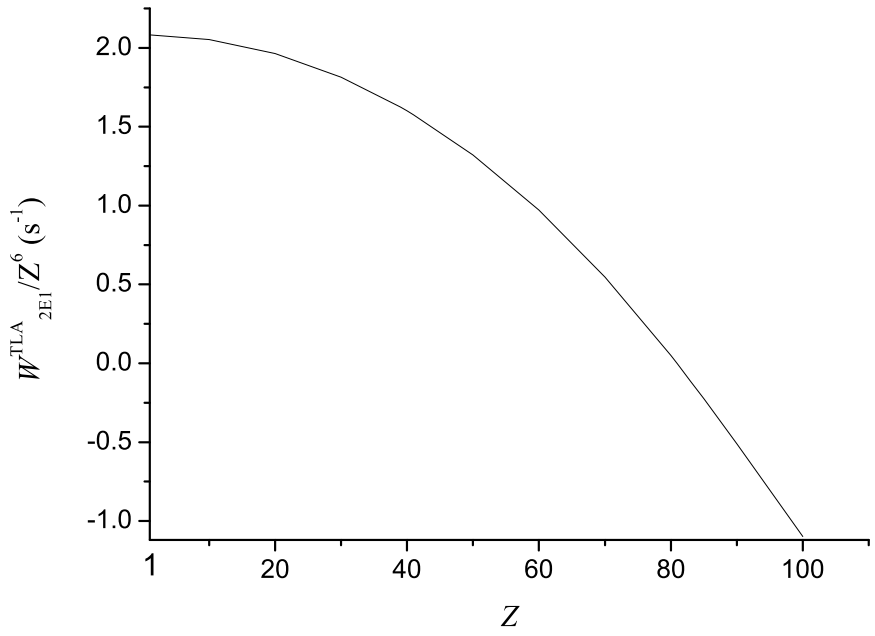

Figure 4.17: Non-resonant correction to $2E1$ in $3s_{1/2} \rightarrow 1s_{1/2}$ - Non-resonant correction of the multipole combination $2E1$ in the $3s_{1/2} \rightarrow 1s_{1/2}$ transition divided by Z^6 as function of the atomic number Z.

4.5 Two-photon excitation

The results presented in this section were obtained using Eqs. (3.166), (3.170) and (3.171) by considering a linear polarized laser laser, i.e., with $\omega_1 = \omega_2 = (E_f - E_i)/2$, $\hat{\boldsymbol{k}}_{\mathbf{1}} = \hat{\boldsymbol{k}}_{\mathbf{2}}$, and $\chi_1 = \chi_2$.

Tables 4.20, 4.21, and 4.22 display the parameter α_0 values for various $ns \rightarrow n's$ transitions in neutral hydrogen, as well as H-like xenon Xe^{53+} and uranium U^{91+} ions. The calculations have been performed in velocity and length *gauges* for the coupling of the radiation field. Although an agreement between these two *gauges* does not prove the correctness of the predicted data directly, it is usually used as an indicator for the accuracy of the atomic-structure calculations (both energies and wavefunctions), as already mentioned. Predictions of the exact relativistic theory that account for all allowed multipole components ($\Theta_1 L_1$, $\Theta_2 L_2$) are compared with those from the electric dipole approximation, i.e., if the multipole summation is restricted to the single term with $2E1$. As expected, like in the case of two-photon emission, both approaches yield almost identical results for neutral hydrogen, for which the relativistic and non-dipole effects are known to be negligible. For $Z = 1$, moreover, our calculations reproduce the non-relativistic dipole calculations by *Tung et al*. [169], as well as by *Gontier* and *Trahin* [180] very well, and they are in good agreement with the experimental measurement for the $1s_{1/2} \rightarrow 2s_{1/2}$ effective excitation cross-section σ from Ref. [181]. In that reference, a value of $\sigma_{\text{exp}} = 3.3 \pm 0.8 \times 10^{-28}$ cm^4/W was obtained, which can be compared directly

to our prediction of $\sigma_{\rm th} = 5.2 \pm 1.3 \times 10^{-28}$ cm^4/W. The latter value has been obtained using Eq. (3.167) for the two-photon statistical factor $G^{(2)} = 2$ and the line-shape function $g(\omega) = 9.6 \pm 2.5 \times 10^{12}$ s (as recommended in Ref. [181]). One may note that, despite the numerical accuracy of the α_0 parameters in Table 4.20, the theoretical value $\sigma_{\rm th}(1s \to 2s)$ has an uncertainty of about 25%. As seen from Eq. (3.169) for the line-shape function, this uncertainty accounts for the incomplete knowledge about the properties of the laser beam as well as of the ensemble of target atoms in a particular experiment. For example, in the work reported by *Bickel* and *McRae* in Ref. [181], a 243-nm XeCl dye laser was used for which the linewidth $\omega_L = 18.8$ GHz was known only within about 20% uncertainty. An almost equally large uncertainty was found for the Doppler width ω_D and was attributed to the wide velocity spread of the (target) hydrogen atoms, which were produced by the laser ablation of the zirconium alloys. Any improvement in the accuracy of the two-photon absorption studies, therefore, will require a better control of the temporal and spatial laser-beam characteristics and of the target properties. This can be achieved, for example, by using cold-atomic targets together with the single frequency high-power lasers (cf. Ref. [182]) or narrow cw single-mode lasers as well as by performing Doppler-free spectroscopy [32, 66, 183].

As seen from Tables 4.21 and 4.22, we observe a significant reduction in parameter α_0 as the atomic number Z increases. This Z behavior can easily be understood, at least, within the framework of the non-relativistic dipole approximation, if we consider the individual trends of the matrix elements and energy denominator in Eq. (3.166): while the two-photon matrix element (3.72) is weakly dependent on Z (cf. Ref. [52]), the transition energy $2\omega = E_f - E_i$ follows a Z^2 law (cf. Eq. (3.19)). That yields a simple estimate $\alpha_0 \sim Z^{-6}$ which, however, takes neither the relativistic contraction of the wave functions toward the nucleus nor the nondipole effects in the electron-photon interaction into account. The relativistic contraction further reduce the two-photon cross-sections by a factor of about two for high-Z ions (cf. Ref. [52]). In contrast, the influence of the higher-multipole contributions is not so significant. As seen from Tables 4.21 and 4.22, for example, the probability of the $1s_{1/2} \to 2s_{1/2}$ two-photon absorption is decreased only by about 2% for Xe^{53+} and by 6% for U^{91+} if, apart from the leading $2E1$ channel, the nondipole terms are taken into account.

We have discussed the $ns \to n's$ two-photon excitations of H-like ions. Besides this case, we also consider the $ns \to n'p$ induced transitions. Although these transitions are rather weak, they can provide a route for studying PNC phenomena in H-like ions as already mentioned. For the two-photon excitation to the p states, moreover, one expects that nondipole terms in the electron-photon interaction play a more significant role than for the $ns \to n's$ excitations since the $2E1$ channel is forbidden. In order to investigate the role of these (and higher-order) multipole terms, we list in Table 4.23 the α_0 parameter for the excitation of neutral hydrogen as well as H-like xenon and uranium ions by a single linearly polarized laser. The summation runs over all allowed multipole combinations for the total values, and the $E1M1$ plus $E1E2$ approximation includes only the leading channels.

	α_0 (cm^2/s)/(W/cm^2)		
	Multipolarity	velocity	length
$1s_{1/2} \rightarrow 2s_{1/2}$	$2E1$	2.747952(−17)	2.747952(−17)
		2.75(−17) [1]	
	Total	2.747935(−17)	2.747935(−17)
$1s_{1/2} \rightarrow 3s_{1/2}$	$2E1$	2.419411(−18)	2.419411(−18)
		2.42(-18) [1]	
	Total	2.419404(-18)	2.419404 (−18)
$1s_{1/2} \rightarrow 4s_{1/2}$	$2E1$	6.687125(−19)	6.687125(−19)
		6.69(−19) [1]	
	Total	6.687113(−19)	6.687113(−19)
$2s_{1/2} \rightarrow 3s_{1/2}$	$2E1$	5.70941(−15)	5.709419(−15)
		5.72(−15) [1]	
	Total	5.709405(−15)	5.709405(−15)
$2s_{1/2} \rightarrow 4s_{1/2}$	$2E1$	3.079139(−17)	3.079139(−17)
		3.52(−17) [1]	
	Total	3.079124(−17)	3.079124(−17)

[1] *Tung et al.* [169]

Table 4.20: α_0 for transitions $ns \rightarrow n's$ and $Z = 1$ - Effective two-photon excitation cross-section (cm^2/s)/(W/cm^2) for several transitions $ns \rightarrow n's$ and atomic number $Z = 1$. For each transition, the first line refers to the result of Eq. (3.166) with only the $2E1$ contribution while the second line is for all contributions. Comparison between the values obtained in this work and other theoretical values. Calculations were performed in both velocity and length *gauges*. Powers of ten are given in parentheses.

As seen from Table 4.23, this approximation provides a good estimate of the parameter α_0 along the entire isoelectronic sequence. That is, the discrepancy between the $E1M1$ and $E1E2$ calculations and rigorous results does not exceed 5%–7% for the heaviest elements. The leading role of the $E1M1$ and $E1E2$ excitation channels also allows us to qualitatively understand the Z scaling of the α_0 parameter for the $ns \rightarrow n'p$ transitions. The matrix elements for these two channels scale approximately as Z, thus, leading to an $\alpha_0 \sim Z^{-4}$ dependence. In the relativistic case, again, this dependence has to be corrected for the relativistic contraction and higher-term effects.

	α_0 (cm^2/s)/(W/cm^2)		
	Multipolarity	velocity	length
$1s_{1/2} \rightarrow 2s_{1/2}$	$2E1$	8.495884(−28)	8.495884(−28)
	Total	8.338306(−28)	8.338306(−28)
$1s_{1/2} \rightarrow 3s_{1/2}$	$2E1$	6.421630(−29)	6.421630(−29)
	Total	6.369145(−29)	6.369145(−29)
$1s_{1/2} \rightarrow 4s_{1/2}$	$2E1$	1.650110(−29)	1.650117(−29)
	Total	1.643400(−29)	1.643405(−29)
$2s_{1/2} \rightarrow 3s_{1/2}$	$2E1$	1.311563(−25)	1.311563(−25)
	Total	1.299959(−25)	1.299959(−25)
$2s_{1/2} \rightarrow 4s_{1/2}$	$2E1$	1.471467(−28)	1.471465(−28)
	Total	1.529490(−28)	1.529488(−28)

Table 4.21: α_0 for transitions $ns \rightarrow n's$ and $Z = 54$ - Effective two-photon excitation cross-section (cm^2/s)/(W/cm^2) for several transitions $ns \rightarrow n's$ and atomic number $Z = 54$. For each transition, the first line refers to the result of Eq. (3.166) with only the $2E1$ contribution while the second line is for all contributions. Calculations were performed in both velocity and length *gauges*. Powers of ten are given in parentheses.

	α_0 (cm^2/s)/(W/cm^2)		
	Multipolarity	velocity	length
$1s_{1/2} \rightarrow 2s_{1/2}$	$2E1$	1.849824(−29)	1.849824(−29)
	Total	1.743653(−29)	1.743653(−29)
$1s_{1/2} \rightarrow 3s_{1/2}$	$2E1$	9.063289(−31)	9.063420(−31)
	Total	8.937087(−31)	8.937237(−31)
$1s_{1/2} \rightarrow 4s_{1/2}$	$2E1$	1.856756(−31)	1.856662(−31)
	Total	1.868169(−31)	1.867428(−31)
$2s_{1/2} \rightarrow 3s_{1/2}$	$2E1$	5.398854(−28)	5.398855(−28)
	Total	5.053379(−28)	5.053380(−28)
$2s_{1/2} \rightarrow 4s_{1/2}$	$2E1$	2.422525(−29)	2.422506(−29)
	Total	2.306343(−29)	2.306325(−29)

Table 4.22: α_0 for transitions $ns \rightarrow n's$ and $Z = 92$ - Effective two-photon excitation cross-section (cm^2/s)/(W/cm^2) for several transitions $ns \rightarrow n's$ and atomic number $Z = 92$. For each transition, the first line refers to the result of Eq. (3.166) with only the $2E1$ contribution while the second line is for all contributions. Calculations were performed in both velocity and length *gauges*. Powers of ten are given in parentheses.

		α_0 (cm^2/s)/(W/cm^2)		
Transition	Multipolarity	$Z = 1$	$Z = 54$	$Z = 92$
$1s_{1/2} \rightarrow 2p_{1/2}$	$E1M1 - E1E2$	1.277404(-22)	1.028584(−29)	4.753682(−31)
	Total	1.277407(-22)	1.035005(−29)	4.857008(−31)
$1s_{1/2} \rightarrow 3p_{1/2}$	$E1M1 - E1E2$	1.406394(-24)	5.340185(-32)	5.354621(-35)
	Total	1.406396(-24)	5.341826(-32)	7.417931(-35)
$1s_{1/2} \rightarrow 4p_{1/2}$	$E1M1 - E1E2$	3.289574(-26)	1.622427(-34)	1.171781(-33)
	Total	3.289564(-26)	1.814492(-34)	1.271929(-33)
$2s_{1/2} \rightarrow 3p_{1/2}$	$E1M1 - E1E2$	7.462732(−21)	6.096173(−28)	2.620305(−29)
	Total	7.462732(−21)	6.092971(−28)	2.596358(−29)
$2s_{1/2} \rightarrow 4p_{1/2}$	$E1M1 - E1E2$	1.728988(-22)	1.424077(−29)	5.300456(−31)
	Total	1.728992(-22)	1.435945(−29)	5.549392(−31)

Table 4.23: α_0 for transitions $ns \rightarrow n'p$ and several atomic numbers - Effective two-photon excitation cross-section (cm^2/s)/(W/cm^2) for several $ns \rightarrow n'p$ transitions and atomic numbers Z. For each transition, the first line refers to the result of Eq. (3.166) with only the $E1M1 + E1E2$ contribution while the second line is for all contributions. Values are for length *gauge*. Powers of ten are given in parentheses.

4.6 Preliminary results in He-like Ions

In this section we present preliminary results for two-photon emission in He-like ions obtained in this work following the theory presented in the paper by *Santos et al.* [184]. In this work, it was derived an expression of two-photon emission rate in He-like systems within a *independent particle* model, i.e., only one electron participating in the transition. Moreover, a single configuration state for defining the two-electron wave function was also considered. The expression of the decay rate is similar to Eq. (3.80) and is given by

$$\begin{aligned}\frac{d\overline{W}}{d\omega_1} &= \frac{\omega_1\omega_2}{(2\pi)^3 c^2 [J_i]} \sum_{L_1,\lambda_1,L_2,\lambda_2} \sum_{j_{1_n},j'_{1_n}} \sum_{J_n} S^{J_n j_{1_n}}(2,1) S^{J_n j'_{1_n}}(2,1) + S^{J_n j_{1_n}}(1,2) S^{J_n j'_{1_n}}(1,2) \\ &+ \sum_{J'_n} (-1)^{2J'_n + L_1 + L_2} [J_n, J'_n]^{1/2} \begin{Bmatrix} J_f & J'_n & L_1 \\ J_i & J_n & L_2 \end{Bmatrix} \\ &\times \left\{ S^{J_n j_{1_n}}(2,1) S^{J'_n j'_{1_n}}(1,2) + S^{J_n j_{1_n}}(1,2) S^{J'_n j'_{1_n}}(2,1) \right\} , \end{aligned} \tag{4.2}$$

where $S^{J_n j_{1_n}}(2,1)$ is defined in a similar way like Eq. (3.72),

$$S^{J_n j_{1_n}}(2,1) = \sum_{n_l} \frac{\bar{M}^{(\lambda_2,L_2)}_{f,n_l}(\omega_2) \cdot \bar{M}^{(\lambda_1,L_1)}_{n_l,i}(\omega_1)}{E_{n_l} - E_i + \omega_1} \Delta^{J_n j_{1_n}}(2,1) \Pi^l(2,1) , \tag{4.3}$$

with $\Delta^{J_n j_{1_n}}(2,1)$ given by

$$\Delta^{J_n j_{1_n}}(2,1) = \frac{4\pi[j_{1_i}, j_{1_n}, j_{1_f}]^{1/2}}{[L_1, L_2]^{1/2}} \begin{pmatrix} j_{1_f} & L_2 & j_{1_n} \\ 1/2 & 0 & -1/2 \end{pmatrix} \begin{pmatrix} j_{1_n} & L_1 & j_{1_i} \\ 1/2 & 0 & -1/2 \end{pmatrix} \times [j_{1_n}]^{1/2} [J_i, J_n, J_f]^{1/2} \begin{Bmatrix} J_f & L_2 & J_n \\ j_{1_n} & j_2 & j_{1_f} \end{Bmatrix} \begin{Bmatrix} J_n & L_1 & J_i \\ j_{1_i} & j_2 & j_{1_n} \end{Bmatrix} . \quad (4.4)$$

The various total angular momentums with uppercase letter, J_i, J_n and J_f refer to the two-electron system, while with lowercase latter, j_{1_f}, j_{1_i} and j_{1_n} refer to the active electron. j'_{1_n} is the angular momentum of the non-active electron.

The matrix elements $\bar{M}^{(\lambda,L)}_{f,i}$ are given as in the one electron case with P and Q obtained from a evaluation of the Dirac-Coulomb equation with a Coulomb and Breit interaction between the two electrons. In this work we use two wavefunctions: hidrogenic wave functions and Dirac-fock wavefunctions [84] with a nuclear Coulomb potential and a Coulomb interaction between the two electrons. Since the non-active electron is in the $1s$ state, the corresponding Dirac-fock equation is the Dirac equation with an effective potential given by

$$V'(r) = V(r) + v_0\,(1s, r) = V(r) + \int_0^\infty dr' \left(P^2_{1s}(r') + Q^2_{1s}(r')\right) \frac{1}{r_>} . \quad (4.5)$$

The finite basis set was employed with that potential in order to obtain the complete set of states of the active electron.

It should be noticed that Eq. (4.2) differs from Eq. (32) in Ref. [184]. This is due to an accidental addition of a term $\delta(j_{1_n}, j'_{1_n})$ in Eq. (30) of Ref. [184] that restricts the summation over j'_{1_n} and j'_{1_n}.

In Table 4.24 we list the decay rates values evaluated using this procedure for the transition $1s2s\,^1\mathrm{S}_0 \rightarrow 1\mathrm{s}^2\ ^1\mathrm{S}_0\ 2E1$, for several atomic numbers. We also obtained the two-photon decay rate using hydrogen-like wavefunctions and a potential with $(Z-1)$ for comparison purposes. In all calculation, good *gauge* agreement was obtained. For higher values of the atomic number the three approaches tend to produce similar values as expected since the attractive nuclear potential tends to overwhelm the repulsive Coulomb interaction between the two electrons. We notice that the values obtained with Dirac-Fock wavefunctions are in better agreement with the *ab initio* evaluation by *Derevianko* and *Johnson* [14]. In that work, the total decay rate was obtained only for the leading multipole $2E1$ using multiple configuration state functions in initial, final and intermediate states. Moreover, the interaction between the electrons was calculated with the Breit interaction.

The evaluation of Eq. (4.2) was carried on with a single state configuration. However, it takes into account all multipole configuration in both velocity and length *gauges*. Moreover, the energies and wavefunctions used in the evaluation of the $\bar{M}^{(\lambda,L)}_{f,i}$ functions can be further improved with including the Breit term in the electron-electron interaction. An ansatz potential can be chosen in order to

	Decay rate, (s^{-1})		
	Hydrogenic	$Z-1$	Dirac-Fock
$Z = 2$	1.005320(3)	1.645811(2)	5.691436(1) 5.102(1)[1]
$Z = 40$	6.393182(10)	5.506058(10)	5.689526(10) 5.692(10)[1]
$Z = 92$	7.58160(12)	7.144164(12)	7.24155(12) 7.27(12)[1]

[1] *Derenvienko et al*. [14]

Table 4.24: Two-photon decay rate for the transition $1s2s\,^1S_0 \rightarrow 1s^2\,^1S_0\ 2E1$ - Total two-photon decay rate (s^{-1}) for the transition $1s2s\,^1S_0 \rightarrow 1s^2\,^1S_0\ 2E1$. The second column is refereed to radial matrix elements constructed with hydrogenic wavefunctions. The third column is using a potential with uniform nuclear distribution (Eq. (3.8)) for a charge of $Z-1$. The last column contains the values obtained with the potential of Eq. (4.5). .

obtain, within the finite basis set approach, energies and wave-functions of the $1s$ and $2s$ orbitals in good agreement with a MCDF calculation with radiative corrections [8, 9, 172]. On the other hand, the MCDF calculation cannot be applied directly in the two-photon calculation without losing the *gauge* invariance, since in a self-consistent process there is no local potential used to define all the single-electron wave functions. In detail, the self-consisting process can be used to obtain the initial and final states $1s2s\ ^1S_0$ and $1s^2\ ^1S_0$ with good accuracy. However, there is no criterion according to which self-consistent process can be used for the intermediate states. Thus, to overcome this problem, one can use a set of configuration state functions (Configuration Interaction), or a local effective potential for all orbitals that emulates accurately the initial and final states energies and wavefunctions of a MCDF calculation. The same local potential can, thus, be used for the p orbitals of the intermediate states.

Once the evaluation is improved, the resonance study of the H-like ions in Sec. 4.4 can be applied to He-like systems, thus, it would be possible to discuss the role of resonances in two-photon transitions related with PNC in heavy He-like ions.

Chapter 5

Conclusion

In this part, we performed a theoretical study of two-photon transitions in H-like ions.

Special attention has been paid to the summation over the intermediate states, which occurs in such a two-photon evaluation and runs over complete one-particle Dirac spectrum, including a summation over discrete bound states as well as over the positive and negative continuum. In particular, we discussed the role of the negative energy continuum in an accurate evaluation of the second-order transition amplitudes and, hence, the energy differential as well as total decay rates. Detailed calculations of these rates have been presented for the $2s_{1/2} \rightarrow 1s_{1/2}$ and $2p_{1/2} \rightarrow 1s_{1/2}$ two-photon transitions in neutral hydrogen, as well as for H-like xenon and uranium ions. As seen from the results obtained, both the total decay probabilities and the energy distributions of the simultaneously emitted photons can be strongly affected by the negative-state summation not only for heavy ions but also for low-Z ones. We demonstrated, however, that the role of Dirac's negative continuum becomes most pronounced for the higher multipoles.

We calculate the decay rates in the line profile and the QED two-loop self-energy approaches for all two-photon transitions from initial states with $n = 2, 3$ for a set of H-like ions with nuclear charge ranging from $Z = 1$ to $Z = 92$. In these calculations the most significant multipoles contributions were considered, such as the $2E1$, $E1M1$, and $2M1$. We have also studied the spectral distributions of several transitions, which exhibit specific structures, such as resonances and transparencies. The latter reveals that two-photon emission is not possible at certain frequencies.

The numerical results obtained in this work are in good agreement with other non-relativistic and relativistic theoretical results. The QED approach gives a better contribution for a pure coherent non-resonant two-photon emission than the methods of *Cresser et al*. [173] and *Chluba* and *Sunyaev* [185], not only because it is derived from physical arguments, but also due to the fact that it can be obtained from the LPA by removing the cascade process and setting the radiative corrections to zero. Therefore, it is a useful technique in theoretical evaluations that require a coherent two-photon decay

rate rather than the sum of this term along with the sequential one-photon decay rate cascade process.

We conclude that the line profile approach is the most suitable for comparison with experimental results since it includes the terms associated with cascade process as well as radiative corrections.

We emphasize that the integration method used to obtain one-electron decay rates in both approaches, and for both non-resonant and resonant transitions can be adapted to ions with two or three electrons.

A parametrization of the angular correlation and the degree of linear polarization was performed for the radiation emitted in two-photon decay of H-like ions. These two physical quantities have been expanded in $\cos\theta$-polynomials and the coefficients have been plotted for the entire isoelectronic sequence ($0 \leq Z \leq 100$). By restricting to the first two multipoles of the photon field expansions, such coefficients have been analytically written in terms of the reduced amplitude of the process. Overall, we have seen that the coefficients which bring deviations from non-relativistic formulae start being of some percent from approximately H-like Tin ion onwards ($Z \gtrsim 50$).

The presented parametrization of the angular correlation and the degree of linear polarization, can be profitably used in future experiments that aim to measure the angular and polarization properties of the radiation emitted in two-photon decay of atoms or ions.

We investigate the excitation of few-electron ions under the simultaneous absorption of two photons. For that matter, detailed calculations have been carried out for the $ns \rightarrow n's$ and $ns \rightarrow n'p$ two-photon-induced transitions in neutral hydrogen as well as H-like xenon Xe^{53+} and uranium U^{91+} ions. These calculations, which made use of the finite basis set approach, demonstrated the importance of the relativistic contraction of the wave functions as well as the non-dipole excitation channels for the accurate analysis of the absorption rates.

It was investigated, for the first time, the efficiency and accuracy of the B-polynomial basis set for studying the two-photon transitions in hydrogen-like systems. Based on the finite basis set approach, the generalized eigenproblem (Eq. (3.91)) was solved in order to provide the eigenvalues and eigenfunctions, which were successfully used for the calculations of the two-photon decay rates. We took advantage of the B-polynomial properties and derived fully relativistic analytical expressions for the two-photon rates within both the point-like and finite nucleus models, instead of employing numerical methods. In order to illustrate the application of the B-polynomial method and to verify its accuracy, we have performed detailed calculations of the total rates for the $2s_{1/2} \rightarrow 1s_{1/2}$ two-photon transition in neutral hydrogen and hydrogen-like ions. Results of these calculations have been compared with the predictions of the well-established B-spline approach. While the perfect agreement between the results of both B-spline and B-polynomial approximations was observed along the entire isoelectronic sequence, the B-polynomial calculations were found to be much less computationally demanding. It was noticed that if we consider a basis set with more than 23 B-polynomials, we need to work in quadruple precision due to the LAPACK routines limitation to deal with matrices that have very large

diagonal matrix elements and very small off-diagonal values. We conclude that the B-polynomial basis sets are suitable for the investigation of the two-photon transitions with the great advantage of enabling analytical expressions for the involved integrals, which speed up the calculations. The presented procedure may be easily extended to calculate two-photon transitions in many-electron ions or atoms, as well as to the QED calculations that usually require the summation over the complete Dirac spectrum. In the future all calculations can be checked by comparing the results of both basis sets.

Part II

Measurement of Forbidden Transitions with a Double Crystal Spectrometer

Chapter 6

Introduction to the Experimental Work

In the experimental part of this work, we used a double crystal spectrometer (DCS) and an electron cyclotron resonance ion source (ECRIS) to perform a 2.3 ppm measurement of the forbidden $1s2s\,^3\mathrm{S}_1 \rightarrow 1\mathrm{s}^2\,^1\mathrm{S}_0$ relativistic $M1$ transition in He-like argon, without reference to any theoretical or experimental energy, using the known lattice spacing of a Si crystal, tied to the definition of the meter, as a transfer standard. For that purpose, a vacuum DCS, working in reflection, has been built during the last ten years at an ECRIS source located at Source d'Ions Multichargés de Paris (SIMPA).

Measurement of X-ray transitions energies is one of the main methods to test QED corrections. The case of He atom has been studied and agreement between experiment [186, 187] and theory [188] is very good. However, a recent measurement of the Lamb shift in muonic hydrogen (μp) [189] provides a proton charge radius 6.9 standard deviations away from the latest 2010 CODATA value obtained by combining results from hydrogen spectroscopy and electron-proton scattering [90]. The cause of this discrepancy can be investigated with measures in atomic ions with different different field strengths ($Z\alpha$) or finite nuclear corrections. Compared to simple neutral systems like hydrogen or helium, one- and two-electron ions are more sensitive to QED corrections.

In the last years, a number of accurate experiments have been performed on the allowed $1s^2 2p \rightarrow 1s^2 2s$ transition in Li-like ions with $Z = 1$ to 92 at storage ring [190] or EBIT facilities [191]. These measurements have accuracies of the order of the size of two-loop QED corrections to the lower level energy. Such $\Delta n = 0$ transitions have also been measured in two-electron Si^{12+} with laser spectroscopy to 0.8 ppm [192] and in U^{90+} [193]. Measurements of $n = 2 \rightarrow n = 1$ transitions, even at high-Z, are not yet sufficiently accurate to test two-loop QED corrections [194]. Very high-Z systems are also very sensitive to nuclear size corrections (see, e.g., [74]) and nuclear polarization [195], which ultimately limits the accuracy of the comparison. Recently, the allowed $1s2p\,^1\mathrm{P}_1 \rightarrow 1\mathrm{s}^2$ transition in He-like Ar has been measured to 1.9 ppm accuracy, relative to the theoretical value of the $2p \rightarrow 1s$ transition in H-like Ar [196]. In the same work, the $2p \rightarrow 1s$ transition in H-like chlorine

was measured to 10 ppm accuracy, without external reference. Earlier absolute measurements on both the $M1$ and $1s2p \rightarrow 1s^2$ transitions of He-like V [197], were calibrated against a series of X-ray standards [198, 199], reaching an accuracy of $\approx$ 30 ppm. Half of this uncertainty is related to the difficulties associated with broad, asymmetric X-ray standards from core-excited neutral elements, sensitive to excitation conditions and chemical effects [198, 199].

We have used a DCS and an ECRIS to perform a 2.3 ppm measurement of the $1s2s\,^3S_1 \rightarrow 1s^2\,^1S_0$ transition. This method allows to avoid the difficulty associated with existing X-ray standards since provides absolute measurements.

Contrary to the case of x rays emitted by neutral elements with a K-hole, which were, up to now, the only transitions measured with a DCS, the $M1$ line is much narrower than the instrument response function. We can thus directly probe for the first time the shape of this response function. To analyze the experimental spectra, we developed a simulation code, that exactly contains the geometry of the instrument and of the X-ray source, the X-ray beam vertical divergence and the shape of the crystal reflectivity profile, as well as the line width and gaussian Doppler broadening.

This part is organized as follows: after making an historical overview of the DCS, as well as providing the importance of the DCS in atomic physics, the rest of this chapter will be devoted to the technical features of the ECRIS (Sec. 6.2.1) and the DCS (Sec. 6.2.2), as well as their alignment (Sec. 6.2.2).

On Chapter 7 will be given a theoretical description of the DCS and the model used for the DCS Monte-Carlo simulation developed in the present work. In detail, the dynamical diffraction theory necessary for the description of the crystal reflectivity will be presented in Sec. 7.1 and the DCS theory in Sec. 7.2. The description of the DCS simulation and data analysis will be given in Secs. 7.3 and 7.4 respectively. In Sec. 7.5 several systematic errors will be simulated with the current DCS simulation.

We present and discuss measurements done with the present experimental setup in Chapter 8. In Sec. 8.1, we present several experimental spectrums done during the present work and discuss possible systematic errors. The precise analysis of the latest measurements for $1s2s\,^3S_1 \rightarrow 1s^2\,^1S_0$ is given in Sec. 8.2, where the results are compared with other theoretical and experimental results.

The conclusions of this part will be given in Chapter 9.

6.1 Double Crystal Spectrometer

The discovery of x rays by *Röntgen* [200] in 1895 led to the development of the field of X-ray spectroscopy. *Röntgen* made an experimental setup in which an electric discharge, passing trough an

highly evacuated tube, emits a radiation that was able to passe through heavy objects. Due to it unknown nature, this radiation was named x-ray. The importance of this discovery was acknowledged in 1901 with the first Nobel Prize in Physics.

The subject of x rays gave a major contribution to the early understanding of matter. In detail, *Sommerfeld* observed that a beam of x rays passing through a narrow slit suffered a small broadening leading to a wavelength estimation of 10^{-8} cm [201]. This value was only slightly smaller than the estimative of interatomic distances in solids from density, molecular weight and Avogadro's number [202]. This fact indicates the possibility of using crystals as natural diffracting gratings for x rays, as suggested by *von Laue* in 1912 [203, 204]. This suggestion was confirmed in the same year by the results of experiments with x rays and crystals performed by *W.H. Bragg* and *W.L. Bragg* [205]. Those experiments revealed a distinct diffraction pattern that could be easily explained: the crystal is made of a periodic arrangement of atoms and the x rays are electromagnetic waves with a wavelength of the same order of the interatomic distance that are scattered by the atoms. This diffraction patterns led to the Bragg law, which states that an incident monochromatic X-ray on a crystal will be reflected only at certain specific incident angles. This so-called Bragg angles (θ_B) are related to the wavelength, λ, by the Bragg law equation given by [206]

$$n\lambda = 2d\sin(\theta_B)\,, \tag{6.1}$$

where d is the inter-planar distance and n is the order of the diffraction.

By the mid-30's of the 20th century most of the pioneering work on this subject was developed, so that *Compton* and *Allison* presented a complete description of X-ray spectroscopy in the seminal book *X-Rays in theory and experiment* [207]. One of the spectroscopic technics described in this textbook, is the use of a *Double-Crystal Spectrometer* (DCS).

Precision spectroscopy with a DCS has a long history. It was first conceived by *Compton* in 1917 [208] and independently by *Davis* and *Stempel* [209] with the purpose of characterize experimentally the reflectivity profiles of crystals. The first technical details were described by *Compton*, as well as by *William* and *Allison* [210, 211]. Later, *Davis* and *Purks* studied the properties of the dispersive mode [212, 213]. The DCS geometry was given in detail by *Schwarzschild* [214] and a discussion of the alignment errors was given by *Bearden* and *Thomsen* [215]. This spectrometer gained further accuracy with the introduction of high-resolution angular encoders [216]. During the last years, the DCS spectrometer had been applied in several studies, as for example, the measurement of the lattice difference between the epitaxic layer and its substrate [217, 218], the study of elastic properties of Si [219], absolute lattice determination [220, 221], measurement of the temperature dependence of the lattice parameter [222], absolute wavelength determination of capture gamma-ray energies [223], determination of crystal structure factors [224] and the measurement of X-ray emission lines [225, 226, 227], X-ray fluorescence of Si [228] and widths of Cu Kα transitions [229].

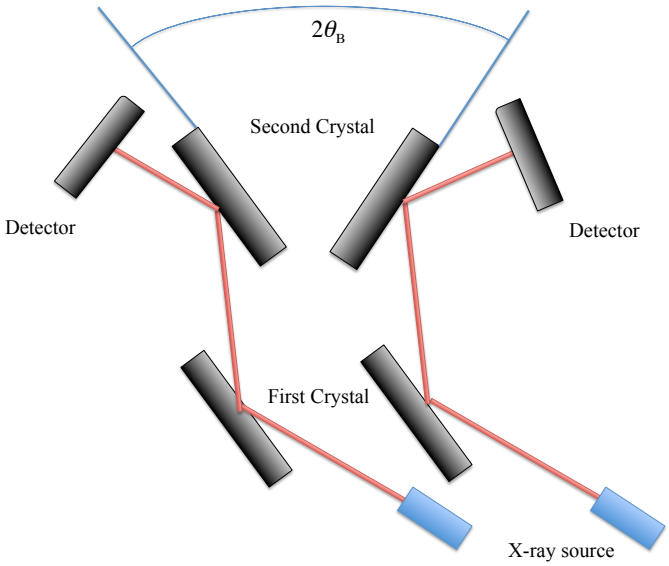

Figure 6.1: Simple DCS representation - The first crystal selects and collimates the reflected x rays into parallel monochromatic bundles. The second crystal makes two types of angle scan and the angular difference between the peak positions gives an absolute value of the θ_B.

Indeed, the development of such spectrometer has provided an invaluable tool for precision measurements of X-ray transitions, since it provides an high resolving power [$(\Delta\lambda/\lambda) < 10^{-5}$] compared to single crystal instruments, which is due to the increased dispersion of two crystals utilized in series. The first crystal, being at a fixed angle, separates the reflected x rays according to the Bragg law (Eq. (6.1)) into monochromatic parallel bundles when leaving the crystal. Therefore, the first crystal can be considered as a collimator and a wavelength filter. Then, the second crystal makes an angular scan in a similar way compared with a simple Bragg spectrometer and a spectrum with a peak is obtained in the process.

Along with an high resolving power, this instrument provides absolute measurements, i.e., without the need of calibration energies or wavelengths. This is due to the two types of scans that the second crystal makes with respect to the first crystal, as showed in Fig. 6.1. The angular difference between the two peak positions obtained from both angular scans provide an absolute measurement of the Bragg angle that can be traced back to an energy or wavelength if the lattice distance is known. With the obtention of Si and Ge high-purity single crystals needed for the fabrication of transistors and with interferometric methods, the lattice spacing can be measured with accuracies below 10^{-8} [230, 231, 232, 233, 234].

The double dispersion of the DCS imposes a limitation in detection efficiency. To overcome this fact, the DCS requires stable sources with high continuous X-ray intensity, which has been limiting the usage of these instruments to high intensity laboratory X-ray tubes with variable fluorescence targets.

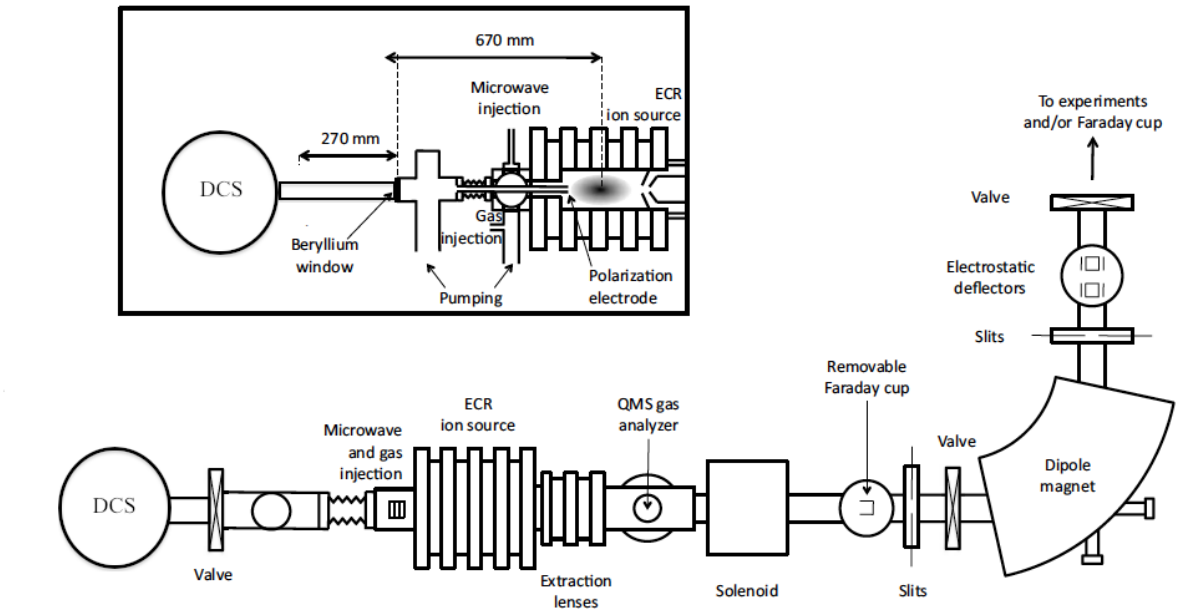

Figure 6.2: SIMPA's ECRIS representation - On the ECRIS right side, plasma is extracted for spectroscopy at an electrostatic trap and surface experiments. On the left side, the emitted x rays are measured with high-resolution spectrometers. Picture taken from Ref. [237] with a different X-ray detector (DCS).

Until nowadays, the DCS had never been used for measuring X-ray energies from transitions in HCI. Neither, for measuring X-ray energies from forbidden transitions, such as the $2s \rightarrow 1s$ $M1$ in H-like ions or the $1s2s\ ^3\mathrm{S}_1 \rightarrow 1s^2\ ^1\mathrm{S}_0$ $M1$ in He-like ions. In the present work, we used an ECRIS [235] as the X-ray source for precision spectroscopy with a DCS. The ECRIS plasma provides x rays from inner-shell transitions in HCI up to H-like and He-like ions. We also demonstrated that the ECRIS, as an X-ray source, is capable of providing the necessary intensity for doing accurate and absolute measurements with a DCS, even for forbidden transitions. The level of precision reached in this work was a few parts per million (ppm), which enables the test of QED corrections, such as two-loop self-energy corrections and provide new and more reliable X-ray standards in the few keV energy region [198, 236]. Much emphasis will be done on the description of this spectrometer. In this work, we perform accurate and absolute measurements, so it is necessary that the systematic errors of this spectrometer are understood and quantified. For that matter, a simulation was developed not only for studying those systematic errors but also to assist in the search of the spectrum peaks. Furthermore, the measurement of a forbidden transition, such as $1s2s\ ^3\mathrm{S}_1 \rightarrow 1s^2\ ^1\mathrm{S}_0$ $M1$, with a DCS provides the opportunity to test the DCS theory due the transition natural width, or lifetime, being very low ($\sim 10^{-7}$ eV) compared with the DCS FWHM (Full Width at Half Maximum) of the instrumental response function (0.6 eV obtained in Sec. 7.5.3).

Due to the $M1$ transition negligible natural width, measurements of the Doppler broadening and, hence, plasma temperatures can be performed in the current plasma of the ECRIS.

6.2 Experimental setup

6.2.1 ECRIS

The SIMPA, a full permanent magnet "supernanogan" type [238] ECRIS, with a microwave line of 14.5 GHz attached into the plasma chamber, has been jointly operated by Laboratoire Kastler Brossel (LKB) and the Institut des NanoSciences de Paris (INSP) since 2004. Numerous projects that use the extracted beam and the X-ray radiation of the ECRIS plasma have been started in atomic, plasma and surface physics [237, 239].

The operation principle of the ECRIS is the following: electrons are emitted from a polarization electrode and immerse in a strong magnetic field produced by a permanent magnet (Agenda Tesla). This magnetic field has a configuration of a magnetic bottle with a hexapole that traps electrons in the beam axis (minimum-B structure) and along the perpendicular direction. The electrons are excited and heated with a high-frequency electromagnetic wave (microwave) corresponding to their cyclotron movement in the magnetic field (resonance zone). This microwave field of frequency of 14.5 GHz is created by a 2 KW klystron. Thus, the electrons gain sufficient energy to ionize, by inelastic collisions, a gas (Ar, Kr, Xe) inside the chamber and the electrons gained in the ionization process are also excited in a cascade way when passing through the resonance zone. This mechanism allows the creation of ions with high charge state up to, e.g. 18^+ in a plasma with ionic temperatures of a few eV and electron temperatures that can reach several dozens of keV. A good way to understand the specific mechanisms that lead to the different charge state production and level populations in different ions is by the observation of the X-ray lines emitted by the ECRIS plasma [240], under different conditions, with very high resolution.

A 400 W microwave line and a 1.3 T magnetic confinement enables the formation of highly charge states in the plasma up to e.g. 17^+ in Ar and Kr. The ECRIS at SIMPA is illustrated in Fig. 6.2. On the right side of the ECRIS, a portion of plasma can be extracted with the use of electrostatic lenses and focused with a solenoid. Then, a single charge state from the extracted plasma can be selected with a dipole magnet for experiments, such as spectroscopy inside an electrostatic trap and surface interaction with HCI. On the left side of the ECRIS, there is a beryllium window that is resistant to the vacuum pressure ($\simeq$100 N/m^2) and semi-transparent to low energy x rays (reduction of a factor of two at 3 keV). This enables the observation and measurement of x rays with spectrometers, such as the mosaic-crystal spectrometer [237] or the DCS.

6.2.2 DCS

The most characteristic aspect of the DCS at SIMPA, compared to other double crystal instruments, such as the one located at NIST (National Institute of Standard and Technology) [216], is that both

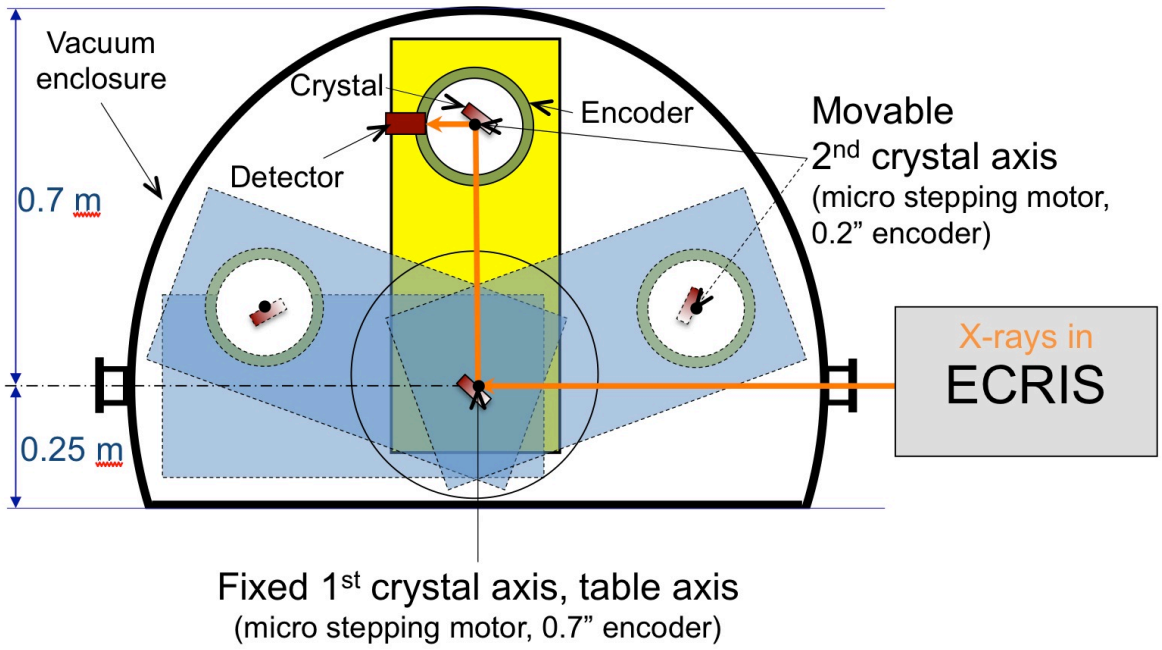

Figure 6.3: Concept of the rotating table - The rotating axes of both crystals are mounted in a single table with a rotating axis concentric with first crystal axis. The detector is also mounted in the table with a rotating path concentric with the second crystal axis.

crystals axis are mounted in a single optical table that rotates around the first crystal axis. In others DCS's, the crystals are fixed on a steady platform with the X-ray source having a rotation concentric with the first crystal. Rotating the X-ray source to a given position, assures that the diffracted rays that are leaving the first crystal will reach the centre of the second crystal.

In SIMPA, the X-ray source is a massive and complicated device with several Tons of fixed components (vacuum system, magnets, beam line), which makes the rotation of the source impossible. Figure 6.3 shows a scheme of the DCS with the concept of the rotating table around the axis of the first crystal and the second crystal axis sitting on the other end of this table.

An overall view of the spectrometer with all the major components is showed in Fig. 6.4. Both crystals are mounted on a single horizontal table and are rotatable around their vertical axis located in the center of the surface of both crystals. The table and the axis of the table are made of a special steel (nitrated stainless steel LK3) that was thermally treated at 900 °C after machining to avoid residual constraints in the material.

The rotation of the crystals is performed with precision stepping motors powered by micro-stepping controllers with steps of 0.017". An Huber Goniometer 410/410A motor is used for the first crystal, a Newport RV80 for the second crystal and a RV240 for the rotation of the detector. The angle of the first crystal is measured with an Heidenhain ROD800 encoder installed in the vertical axis to a precision of 0.07", while the second crystal angle is measured up to a precision of 0.2" with an Heindenhain RON905 encoder, controlled by an Heidenhain AWE1024 box. The operation principle

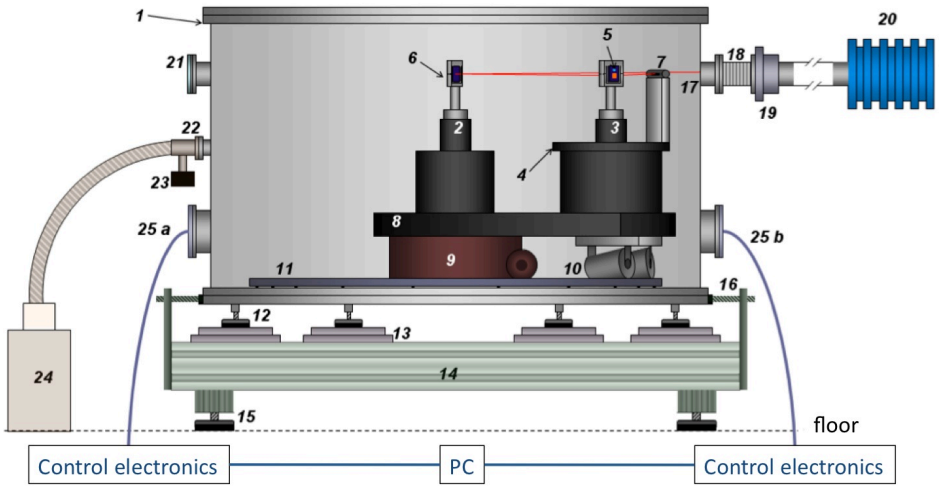

Figure 6.4: Spectrometer setup - 1) vacuum enclosure; 2) axis #1 (crystal 1 and table); 3) axis #2 (crystal 2 and detector); 4) detector rotation support; 5) crystal; 6) crystal holder; 7) detector; 8) table; 9) table rotation support; 10) rotating cones; 11) tracks for cones; 12) enclosure support; 13) translation stages; 14) support; 15) legs; 16) translating screws; 17) X-ray entrance; 18) bellows; 19) Be window; 20) ECRIS-SIMPA; 21) window; 22) connection to pumping; 23) pressure gauge; 24) rotary vacuum pump; 25) a and b feed-through for cables. Figure obtained from Ref. [241].

of the encoders is based on projected-light from LED (Light Emitted Diodes) into two high-quality transparent rotating glasses, both with precision grading scales. On the other side of the two scales, photocells measures the intensity of the transmitted light. The relative position between the two grading scales makes the transmitted light intensity changing according to the relative phase between the grading scales. Therefore, the signal of the photocells of the relative motion between the two grading scales is sinusoidal and the period indicates the angle deviation. As the period of the grating structures becomes smaller, the smaller is the angle deviation. A full circle between the two grading scales have $\sim 3.6 \times 10^4$ sinusoidal periods with values of 36". The deviations from a pure sinusoidal function due imperfections on the grading scales are ~ 1 % that makes an overall accuracy of ~ 0.36" for the angle measurement. Absolute measurement of the angle is possible with a single reference mark on the grading scale. Therefore, when the encoders are restarted, a full circle rotation of the crystals is necessary for finding the reference mark.

A xenon (90 %) and methane (10 %) gas filled proportional counter detector is mounted on the table with an axis of rotation concentric with the second crystal vertical axis. The detector has a 50 μm thick Be window and an active area of about 12 mm by 25 mm. The detector is charged to its operating high voltage of about 2000 V by an external power supply. The detector signal is processed by a preamp, a 142AH ORTEC amplifier and a gated signal adopted for the approximate X-ray energy to be measured and counted by a computer card controlled by Labview. The motors of both crystals, the detector and both encoders are controlled by a Labview interface. The same interface also allows to start scans of the second crystal while the first crystal is steady and record spectra.

The table rotates inside a metallic chamber around the same vertical axis as the first crystal ro-

tating axis. The metallic surface, where the table rotates on cone shaped wheels inside the chamber, was prepared to be horizontally flat to a 2 μm accuracy. The chamber can be pumped down with a rotatory pump to primary vacuum of 10^{-2} mbar that reduces the absorption of the low energy x rays (around 3 keV).

The crystals used in this experiment were cut from a single bundle of Silicon to ensure a perfect crystal without defects. Two different pairs of crystals were cut with Miller indices (111) and (220) (Fig. A.3 and details in Appendix A), being the first pair used in the present work. The crystals were polished and etched at NIST with a symmetry of the cut (angle between crystal planes and crystal surface) controlled to 11" at a temperature of 22.5 °C. The lattice spacing of the two orientations in the same Si boodle was also measured at NIST, using the crystal of the Avogadro Project [242] as the standard reference. The measured lattice spacing of the Si(220) crystal is $d_{\mathrm{Si(220)}} = 1.92015569(50)$ Å that corresponds to a lattice spacing of the Si(111) crystal equal to $d_{\mathrm{Si(111)}} = 3.13560111$ Å. The uncertainty of these values varies according to the crystal and energy. For the Si(220) the uncertainty ranges from 0.45 to 3.6 ppm for the energy range from 3.6 to 12.0 KeV, while for the Si(111), the range is 0.45 to 3.6 ppm for the energy range 2.2 to 7.5 KeV.

The linear thermal coefficient $\alpha(T)$ was also measured, and was found to be $\alpha(T) = 2.56 \times 10^{-6}\ ^{\circ}\mathrm{C}^{-1}$.

To remove the mechanical stresses and strains caused by the cutting procedures of the crystals and to avoid any mosaic effect, the crystals were etched in a bath of hydrofluoric acid, then polished and etched again.

In all measurements, the temperatures of both crystals are kept stable with a copper heater plate pressed against the back of the crystals, a calibrated Pt100 thermistor sensor and a PID (proporcional-integral-derivative) feedback loop. The maximum fluctuation of 0.2 °C was observed. The temperature of both crystals is also recorded during the scans, being each data point registered in the data files. Other technical aspects about the DCS not mentioned here can be found in *Schlesser*'s Thesis [241].

6.2.3 Alignment

The DCS was aligned with respect to the SIMPA axis. The cylindrical components of the ion source and the beam line define an axis to which the spectrometers horizontal plane on the platform of the center of both crystals and the detector was adjusted. This assures the capture of most x rays (better statistics) and avoid geometrical systematic errors. The steps of the alignment procedure follows similar steps presented in the *Schlesser*'s Thesis [241]. The alignment procedure is described bellow. The angles presented in the alignment follows the mathematical convention of a clockwise rotation being negative.

1. The table position was aligned with the X-ray source with the use of a theodolite telescope. In order to do so, the crystals were removed from the supports and replaced with targets. In addition, targets were included at the source, at the tube of dipole magnet and at the beryllium window (Fig. 6.2). This corresponds to the angle zero of the table.

2. A laser was placed at the dipole magnet end and was aligned with those targets at the source and crystals.

3. The target of the first crystal was replaced by an optical mirror. The laser was reflected from the mirror and makes a light spot near the laser aperture. The zero offset of the encoder was set by tuning the reflected laser spot precisely at the laser entrance. Therefore, an angle 0° of the encoder corresponds to the crystal being perpendicular to the table. The crystal supporters (point 6) of Fig. 6.4) have micrometer screws that can adjust the verticality of the mirror, in order to the laser spot being vertically aligned with the laser aperture. Since the micrometer screws adjust the sub-supporter that supports the mirror with nylon screws, the mirror can be replaced by the crystal without losing the verticality. The laser total path distance is $\sim$ 10 m and the uncertainty of the reflected laser spot at the entrance is 5 mm, which corresponds to angle uncertainty of $\sim$1.8".

4. The first crystal was rotated by $-2\theta_C$, which makes the laser spot disappear from laser aperture. This was restored by precisely rotating the table by $\theta_T = 2\theta_C$. The θ_C is a value in the neighborhood of the Bragg angle (Eq. (6.1)). An image of the DCS at SIMPA taken at this point is displayed in Fig. 6.5. In the first crystal support is visible the laser incident at the optical mirror. Attached to the support is a target that enables the alignment of the crystal center with the laser.

5. The first crystal was rotated again by $\theta_F = -90 - \theta_C$ that makes the laser going to the center of the second crystal. At this point the mirror has a glancing angle of θ_C with respect to the laser.

6. Similar to point (3), the target at the second crystal was replaced by a second optical mirror. The verticality and the zero offset were adjust for the second mirror by tuning the reflected laser spot at the laser aperture.

7. The verticality of the second crystal axis of rotation was measured (precision of few seconds of arc) with a Wyler zerotronic sensor. In Fig. 6.6 is plotted a measurementent of the verticality at the second axis using the zerotronic sensor at the two different positions of the table (0 and θ_T). The dependence of the vertical tilt with the horizontal angle, showed in Fig. 6.6, has a sine-like shape. This is due to the vertical axis having some amount of tilt. The offset of the sine function is not relevant because the zerotronic sensor was not fully perpendicular to the rotation axis since the attachment surfaces were not totally parallel. This offset is calibrated by noticing that at a zero horizontal angle the vertical tilt is also zero according to point (6). At the

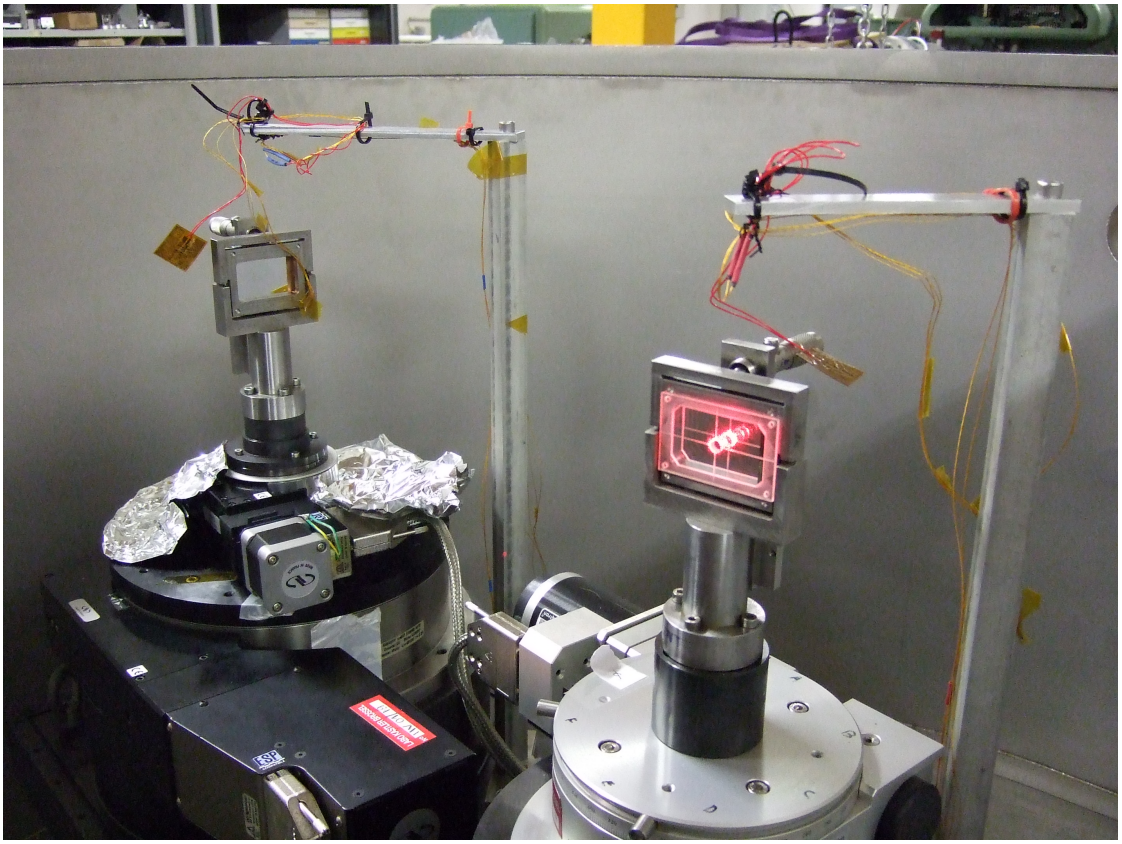

Figure 6.5: Image of the DCS at SIMPA. - Both crystal supports are visible in this figure. The first crystal was rotated by $-2\theta_C$ and a target is attach to it. Since the table was rotated by $\theta_T = 2\theta_C$, the laser reflects at the optical mirror and makes a spot near the laser entrance. It is also visible at the first crystal support back one of the micrometers screws, which enables the vertical adjustment of the crystal.

table position θ_T, where the measurements were done, the value of the sine function amplitude is 0.05 °.

8. The second crystal was rotated by $\theta_P = 90 - \theta_C$ and the detector by $\theta_{DP} = -2\theta_C$. This corresponds to the parallel mode of measurement (details not relevant in this alignment description can be found in the next Chapter 7). With this setting, the laser spot hits the detector. The detector was vertically and horizontally adjusted so that the laser spot was at the detector aperture center. The angle θ_P is 50.434 °, which in Fig. 6.6 corresponds to a vertical angle difference (δ) from the value with θ equal to zero of 10^{-4} °.

9. The second crystal was rotated to the angle $\theta_{AP} = -90 + \theta_C$ and the detector by $\theta_{DP} = 2\theta_C$, which is the antiparallel mode of measurement. The laser spot was at the center of the detector aperture, which confirms the efficiency of the alignment. In this case, the angle θ_{AP} is -50.434 ° and the vertical angle difference is 0.013 °.

10. Finally, the mirrors were replaced with the crystals along with the heater and temperature sensor. A nylon screws at the back were adjusted gently so that the crystals surface has the same position as the mirror surface without bending.

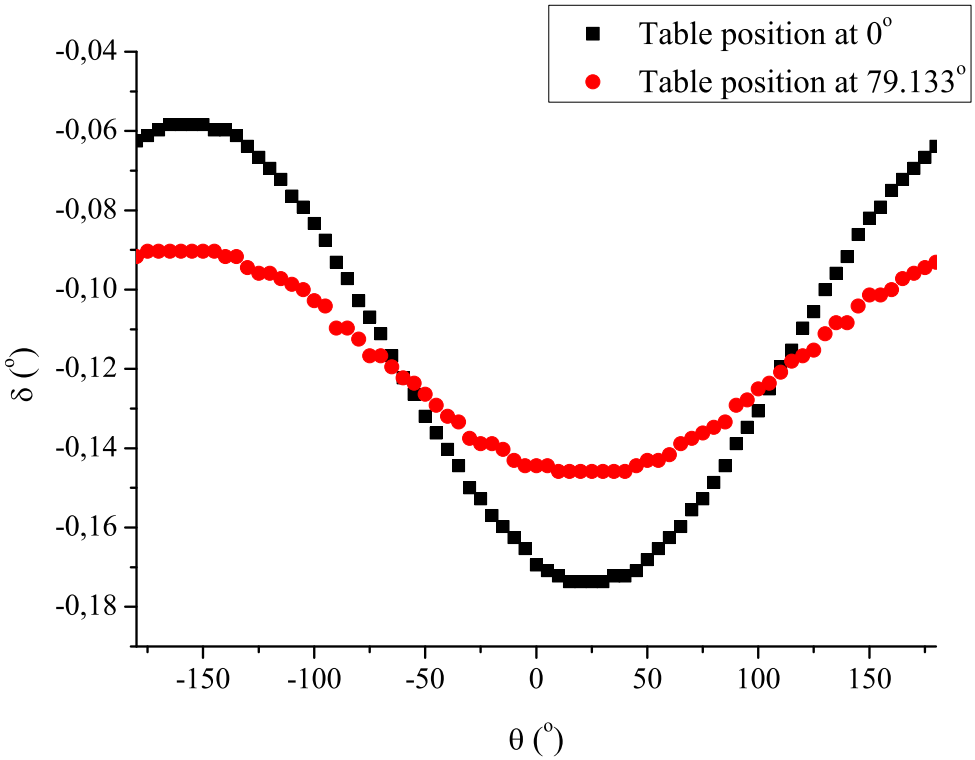

Figure 6.6: Measurement of the vertical tilt with zerotronic sensor for several horizontal angles. - The measurement was made for two table positions: at 0 ° and 79.133°.

Overall, the vertical alignment of the spectrometer components was done to a precision of 0.013°. The horizontality of the different components of the DCS was checked to a few seconds of arc using a Wyler clino 2000 tiltmeter.

Chapter 7

Theory and Simulation of the Double Crystal Spectrometer

Before making a description of the DCS theory and the simulation necessary for the analysis of experimental results, it is necessary to characterize the reflectivity of a single crystal. For that matter, we give a theoretical overview of the dynamical theory of X-ray diffraction in crystals. Some basic concepts of crystallography are described in Appendix A .

7.1 Dynamical theory of X-ray diffraction

The dynamical theory of X-ray diffraction establishes the theoretical foundations for the determination of the crystal structure from experimentally measured diffraction patterns. In general, a X-ray diffraction pattern of a crystal is produced by the x rays scattering by each atom in the crystal structure and the subsequent destructive and constructive interference of the scattered x rays. There are two types of geometry depending on the orientation of observation of the scattered x rays with respect to the incident x rays. The direction of the incident and scattered x rays, as well as the crystal surface and the crystallographic plane (111), are shown in Fig. 7.1. The Bragg type geometry consists of the diffraction pattern of the reflected scattered x rays, while the Laue type consists of the transmitted diffraction pattern.

The dynamical theory of X-ray diffraction was first studied by *Darwin* [243] and later independently by *Ewald* [244]. Both models consider the use of an infinite amount of plane layers and also the interference between transmitted and reflected waves inside the crystals. From this method, a series of finite difference equations are solved in order to obtain the reflectivity. Later, *Prins* [245] propose the introduction of a complex refractive index in order to taken into account X-ray absorption in the

previous models. A more complete model, which is the one used in the present work, was developed by *von Laue* [246]. This model, described in detail in the textbook of *Zachariasen* [247], is based on the solution of the Maxwell equations for a medium with a periodic electric susceptibility along the crystal structure. The von Laue model also considers the crystal as a periodic array of oscillating dipoles excited by the incident radiation. The electromagnetic radiation produced by these dipoles, or the scattered elastic radiation, will constructively or destructively interfere with each other, thus, making a diffraction profile. In the present work, i.e. at the DCS, the crystals reflectivity is just for the Bragg type geometry case, so we restrict to its description. However, the Laue type geometry follows a similar description.

A perfect flat crystal is assumed without any defects in the crystal structure. The diffraction pattern, profile or the reflectivity of a single perfect crystal of thickness t, obtained from the von Laue model, is given by

$$R(\alpha - \theta_{\mathrm{B}}) = \frac{|x_1 x_2|^2}{|b|} \left| \frac{e^{-i\phi_0} - 1}{x_1 e^{-i\phi_0} - x_2} \right|^2 , \tag{7.1}$$

where α is the glancing incident angle, θ_{B} is the Bragg angle (Eq. (6.1)) and the various variables are defined by

$$x_j = \frac{-z + (-1)^{j-1}\sqrt{qP^2 + z^2}}{P\chi_m} , \quad b = \frac{\gamma_0}{\gamma_r} , \quad \phi_0 = k\frac{\sqrt{qP^2 + z^2}}{\gamma_0} t , \quad z = \frac{1-b}{2}\chi + b(\alpha - \theta_{\mathrm{B}})\sin(2\theta_{\mathrm{B}}) , \tag{7.2}$$

with $k = 2\pi/\lambda$ being the wavenumber of the incident radiation with wavelength λ. The quantity b is the asymmetry term defined by the direction cosines $\gamma_0 = \boldsymbol{n} \cdot \boldsymbol{u_i}$ and $\gamma_r = \boldsymbol{n} \cdot \boldsymbol{u_r}$, where $\boldsymbol{n}$ is an unitary vector normal to the crystal surface pointing to the crystal medium and $\boldsymbol{u_{i,r}}$ are unitary vectors with the same direction as the wavenumber of the incident/diffracted radiation. For the Bragg case represented in Fig. 7.1, and with an ideal cut on the surface along a Miller plane, b is equal to -1. P is the polarization factor having values $\cos(2\theta_{\mathrm{B}})$ for the π-radiation (parallel to the crystal surface), and 1 for σ-radiation (perpendicular to the crystal surface). $q = b\chi_m\chi_{-m}$, with χ_m being the Fourier component of χ, is given by

$$\chi = \textstyle\sum_m \chi_m e^{-i2\pi m \bar{\boldsymbol{B}}_{\boldsymbol{hkl}} \cdot \boldsymbol{r}} , \quad \chi_m = \frac{1}{V}\int_V \chi e^{i2\pi m \bar{\boldsymbol{B}}_{\boldsymbol{hkl}} \cdot \boldsymbol{r}} dV , \tag{7.3}$$

where χ is the electric susceptibility divided by two, $\bar{\boldsymbol{B}}_{\boldsymbol{hkl}}$ is the reciprocal-lattice vector (details in Appendix A) and $\boldsymbol{r}$ the position vector. The imaginary part of the electric susceptibility is related with the absorption of the medium and with other physical processes besides the elastic scattering, such as inelastic Compton scattering and photoelectric ionization. Setting $\chi_m = \chi^*_{-m}$ is equivalent to neglect the absorption of the medium. If a thick crystal is also considered, i.e, t is large compared with d_{hkl}, then Eq. (7.1) for the σ-component reduces to

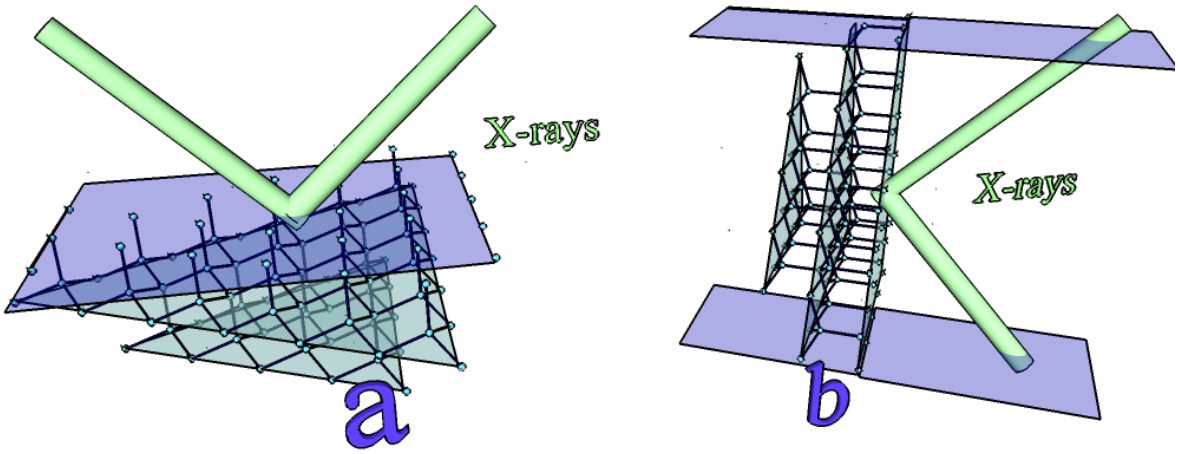

Figure 7.1: Bragg and Laue diffraction types - The green line represents the incident and diffracted x rays. The crystal surface is showed in purple. a) is the Bragg diffraction type and b) the Laue diffraction type.

$$R^{\text{Darwin}}(\alpha-\theta_{\text{B}}) = \begin{cases} 1 & \text{if} \quad |y|<1 \\ \dfrac{1}{y^2+\dfrac{y^2-1}{\tan^2(\sqrt{y^2-1})}} & \text{if} \quad y\geq 1 \end{cases}, \tag{7.4}$$

where $y = z/\chi$. This is a symmetrical function around $y = 0$, that in terms of $\alpha - \theta_{\text{B}}$ is symmetric around

$$\alpha^r - \theta_{\text{B}} = \Delta_r = \frac{\delta}{\sin(\theta_{\text{B}})\cos(\theta_{\text{B}})}, \tag{7.5}$$

with δ being the real part of the electric susceptibility, which is related with the index of refraction by $n = 1 - \delta$. Eq. (7.5) shows that the maximum diffraction does not occur at θ_{B}, but at a value slightly higher with given by $\delta\sec(\theta_{\text{B}})\csc(\theta_{\text{B}})$. This function has a "top-hat" shape, where the top region is unitary and values outside this region suddenly drops to a zero value. This function may be also obtained from Darwin theory [243]. The exact implementation of the reflectivity expressed as in Eq. (7.1) is not a trivial task and numerical methods, such as finite difference methods, must be used. In the present work, the program *XCRYSTAL*, included in the X-ray oriented programs 2.3 package (XOP) [248], was used to obtain the reflectivity according to Eq. (7.1). This package provides models of X-ray sources, like a synchrotron source, characteristics of X-ray optical devices, such as filters and crystals, data visualization and data analysis. In Fig. 7.2, is shown a plot of the reflectivity (Eq. (7.1)) as a function of $\alpha - \theta_B$ for the σ and π polarizations of the radiation, as well as their sum for the energy of 3104 eV. Here, π σ and refer to the polarization vector parallel and perpendicular to the surface, respectively. The main difference between the function in Fig. 7.2 , and the result of Eq. (7.4) is the inclusion of absorption, which causes a different shape in the σ-component. In detail, the introduction of these corrections results in a relatively small decrease of the reflectivity and an

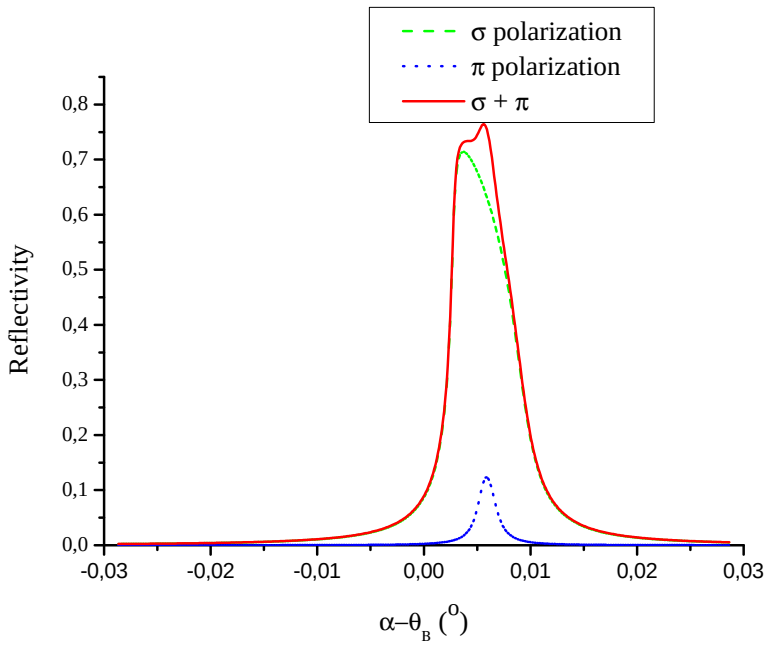

Figure 7.2: Reflectivity obtained from XOP - The green dashed line, s, refers to the σ-component while the blue dot line, p, to the π-component. The sum of both components is represented by the solid red line.

asymmetric distortion.

If an asymmetric crystal is considered, i.e., the surface is not at a Miller plane, then b in Eq. (7.2) is different from minus one and consequently, the shape of reflectivity in Fig. 7.2 changes with b. The main changes are a shift of the center position and an higher width compared with the case of $b = -1$. In this case, the position shift is given by [249]

$$\Delta_r = \frac{\delta}{\sin(\theta_B)\cos(\theta_B)}\frac{|b|+1}{|b|} \approx \delta\left(\frac{1}{\sin(\theta_B)\cos(\theta_B)} + \frac{\theta_A}{\sin(\theta_B)^2}\right), \tag{7.6}$$

where θ_A is the angle between the surface and the Miller plane in radians. Notice that the Bragg angle is towards the Miller plane and not to the surface. For the case of the reflectivity width, the change is inversely proportional to $\sqrt{|b|}$, i.e.,

$$W = \frac{W_0}{\sqrt{|b|}} \approx W_0\left(1 + \frac{\theta_A}{\tan(\theta_B)^2}\right), \tag{7.7}$$

with W_0 being a width for the case of θ_A equal to zero. The definition of the width is arbitrary and can be the FWHM (Full Width at Half Maximum).

7.2 Theory of the DCS

The various angles and notations necessary for the simulation are defined in this section, and several properties of the rocking curves will be obtained for comparison with simulation. In Figs. 7.3 and 7.4 is showed the DCS geometry in both horizontal and vertical planes with all the relevant angles necessary for the respective description.

The first crystal selects an energy, or wavelength, of the polychromatic X-ray beam that will go to the second crystal. A diffraction profile, that is refereed as "rocking curve", is defined by the counts on the detector versus the second crystal angle position while performing a rotation on its own vertical axis.

There are two different rocking curves depending on the orientation of second crystal glazing angle with respect to the first crystal. The rocking curve called parallel, nondispersive or $(n_1, -n_2)$ in Allisson notation [250] (n_i is the order of the diffraction in Eq. (6.1)), is obtained by rotating the second crystal in a setup in which both crystals are parallel, as can be observed in Fig. 7.3 a). This is called nondispersive since each angle in the rocking curve has contributions from all wavelengths accepted by the first crystal and a more detailed discussion can be found in Sec. 7.2.1.1. In this case, a peak obtained from the scan indicates the angle that the crystallographic planes are parallel. On the other hand, the rocking curve called antiparallel, dispersive or $(n_1, +n_2)$, represented in Fig. 7.3 b), gives information about the X-ray's wavelength profile of the source since each angle contains wavelengths within a narrow region (more details in Sec. 7.2.1.2). Due to being dispersive, the antiparallel rocking curve have much less counts comparing with the parallel rocking curve. This instrument enables absolute measurements since the parallel peak is used to calibrate the antiparallel X-ray's wavelength profile. For the sake of clarity, and since all the measurements where done considering first order diffraction, we restrict our analysis to the $(1, -1)$ and $(1, +1)$ cases.

The red dot line in Figs. 7.3 and 7.4 defines the optical axis. It connects the center axis of the source with the center of the various geometrical components (source, first/second crystal and detector) in an ideal aligned instrument and defines the horizontal plane and the vertical axis. The variable θ_C is the angle between the optical axis and the crystallographic plane of the first crystal. This angle is related with the experimental table angle, θ_T, and the experimental first crystal angle, θ_F defined at the points 4 and 5 of the experimental alignment. In case of a misalignment, or the encoder having a offset θ_{offset}, then θ_C is related with the previous angles by

$$\theta_C = -\theta_T - \theta_F + \theta_{offset} \, . \tag{7.8}$$

The rotation of the second crystal is given by the variable β, which represents the angle difference between a given position of the second crystal and the position for which the second crystal have the same glazing angle as the first crystal (θ_C) towards the optical axis.

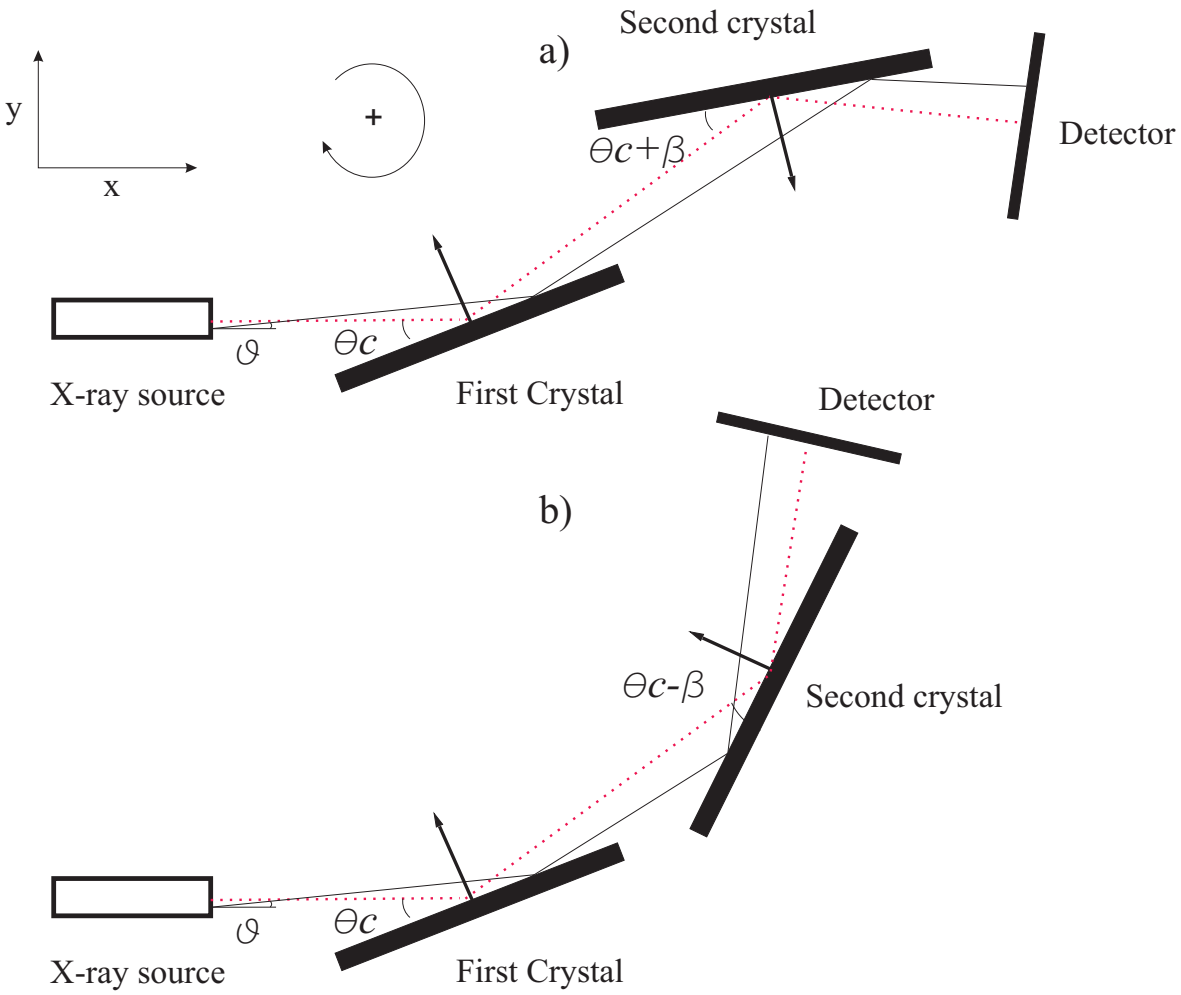

Figure 7.3: Geometry of the DCS in an horizontal plane - a) and b) refers to the parallel and antiparallel setups respectively. A positive rotation is clockwise. The optical axis is the red dot line and connects the geometrical center of all components (detector, first/second crystal and detector) in an ideal DCS. A single random ray is the solid black line and is related horizontally with the optical axis by the angle, ϑ, and some horizontal shift. ϑ is the horizontal angle that the single ray does with the direction of the optical axis. θ_C is the angle between the first crystal and the optical axis. The angle β is a positive rotation of the second crystal around a position having an angle of θ_C with the optical axis. In this case, the angle that the optical axis makes with the second crystal surface is $\theta_C + \beta$ for the parallel case, while for the antiparallel case is $\theta_C - \beta$. The vectors on the first and second crystal surfaces are normal to the respective crystallographic planes.

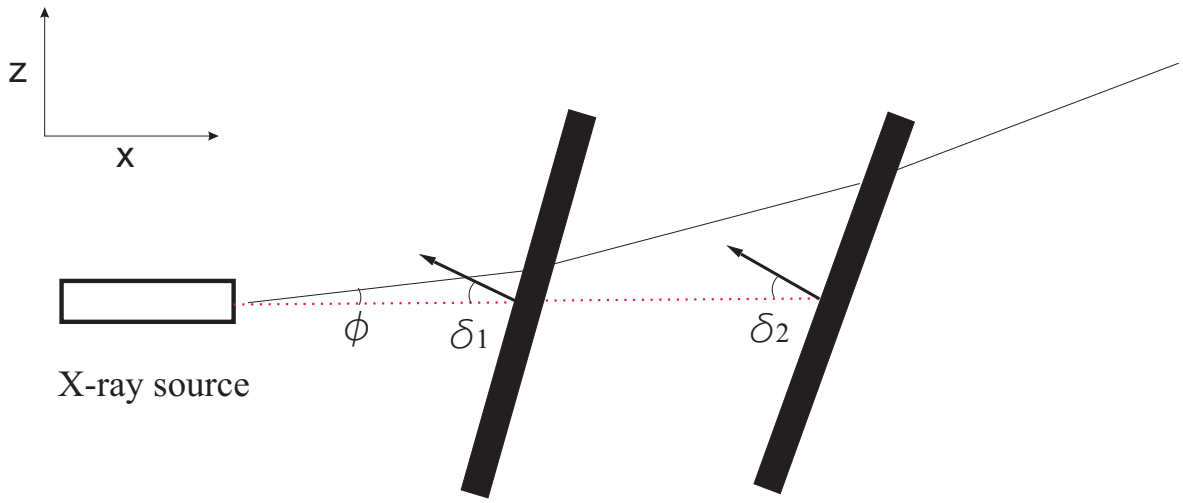

Figure 7.4: Geometry of the DCS in a vertical plane. - The optical axis is represented by the red dot line while a single ray is showed as the solid black line. The angle ϕ is the vertical angle between a single ray and the horizontal plane defined by the optical axis. The crystallographic planes are defined by their normal vector. The angles δ_1 and δ_2 are angles between the plane vector and the horizontal plane of the first and second crystal respectively. $\delta_2 = \delta_2^{\pm}$ where "+/−" refers to antiparallel/parallel.

The black solid line represents a single random ray that can start at any position of the source aperture and follows a direction described by the angles (ϑ, ϕ) towards the optical axis. In Fig. 7.3, ϑ is the angle between the projection of the single ray on the horizontal plane and the optical axis. The variable ϕ describes the angle between a single ray, represented in Fig. 7.4 by the black solid line, and the horizontal plane. In the same figure, the angles between the crystallographic planes of the first and second crystal, and their vertical axis of rotation are δ_1 and $\delta_2^{\pm}$, respectively.

As already mentioned in point (7) of Sec. 6.2.3 , if the second crystal axis is not perpendicular to the horizontal plane, the normal plane vector of the crystal will not be horizontal. The angle difference, δ_2, between the normal plane vector and the horizontal plane, will depend on the angle of rotation β as a sine function. The analytical expression of this function is given by

$$\delta_2^{\pm} = \delta_2^{\pm}(\beta) = \begin{cases} \arccos\left[\cos(\delta_{\text{axis}})\cos(\theta_{\text{axis}}^{\pm})^2 + \sin(\theta_{\text{axis}}^{\pm})^2\right] + \delta_{\text{offset}} & \text{if } \cos(\theta_{\text{axis}}^{\pm}) \geq 0 \\ -\arccos\left[\cos(\delta_{\text{axis}})\cos(\theta_{\text{axis}}^{\pm})^2 + \sin(\theta_{\text{axis}}^{\pm})^2\right] + \delta_{\text{offset}} & \text{if } \cos(\theta_{\text{axis}}^{\pm}) < 0 \end{cases} , \tag{7.9}$$

where δ_{axis} is the angle that the rotation axis makes with the vertical axis and $\theta_{\text{axis}}^{\pm} = \mp 90 \pm \theta_{\text{C}} + \beta + \theta_{\text{phase}}$. The angle between the horizontal projection of the surface normal vector and the horizontal projection of the tilted axis is θ_{phase}. The angle δ_{offset} takes account the surface of crystal not being collinear with the axis of rotation. Since the angle δ_{axis} is low in an aligned DCS, it is reasonable to make a first order approximation on this angle. The result is given by

$$\delta_2^{\pm} \approx -\delta_{\text{axis}} \sin(\theta_{\text{axis}}^{\pm}) + \delta_{\text{offset}} , \tag{7.10}$$

which has the same sine shape as Fig. 6.6. All angles in Eq. (7.10) are given in radians. The various

parameters, θ_{phase} , δ_{axis} and δ_{offset}, can be obtained by fitting (further details on the fitting process can be found in Sec. 7.4.1) a sine type function, like Eq. (7.9), with experimental data. Later, these parameters can be included in a DCS simulation.

A differential element of the incident beam on the first crystal consists of radiation with wavelength between λ and $\lambda + d\lambda$, and will have horizontal and vertical angular spread $d\vartheta$ and $d\phi$ in the neighborhood of the values ϑ and ϕ. The differential intensity of such differential element is written as [207].

$$dI = G(\vartheta, \phi)J(\lambda)d\vartheta d\lambda d\phi \, . \tag{7.11}$$

The function $G(\vartheta, \phi)$ describes the rays distribution for each angle and depends on the shape of the geometrical slit apertures and the distribution of intensity on the focal spot.

An example of $G(\vartheta, \phi)$ can be given for the case of two vertical slits of unequal height and sufficient long length to be considered infinite. In this case, $G(\vartheta, \phi)$ will not depend on ϑ and will be a function of ϕ only. Let us define ϕ_C as the angle for which a ray just glancing the lower edge of the first slit, also glances the lower edge of the second and ϕ_m as the angle for which a ray just glancing the upper of the first slit, also glances the lower edge of the second. Both variables are given by

$$\phi_c = \frac{b-a}{2L} \, , \quad \phi_m = \frac{b+a}{2L} \, , \tag{7.12}$$

where b and a are the height of the second and first slits, respectively, and L the distance between them. Obviously, no ray can pass through the slit system if $|\phi| > \phi_m$. If the source have an uniform intensity along the entrance, then the function $G(\vartheta, \phi)$ is given by

$$G(\vartheta, \phi) = \begin{cases} A(\phi_m - \phi_c) & \text{if } |\phi| < \phi_c \\ A(\phi_m - |\phi|) & \text{if } \phi_c \leq |\phi| \leq \phi_m \end{cases} \, . \tag{7.13}$$

A is a constant dependent on the intensity of the source or on number of rays. In the current DCS, the connection between the spectrometer and the source is trough a long cylindrical tube, which acts as a collimator. In this case, the function $G(\vartheta, \phi)$ with normalized maximum, is showed in Fig. 7.5 , where it was used an uniform focal distribution. The shape of the function in Fig. 7.5 is similar to the one of Eq. (7.13) with $a = b$ but for circular slits.

The function J in Eq. (7.11) gives the wavelength distribution of the incident beam. There are several physical processes responsible for the wavelength distribution, such as the Compton scattering, the Bremsstrahlung (as discussed in Ref. [237]), the Doppler broadening and the atomic radiative decay process. The last two processes influences for the shape of the peaks, while the first ones contributes to a constant distribution offset.

When the differential element of incident beam is diffracted from the first crystal, the intensity of the diffracted beam depends on the glancing angle α_1. This dependence is given by the crystal

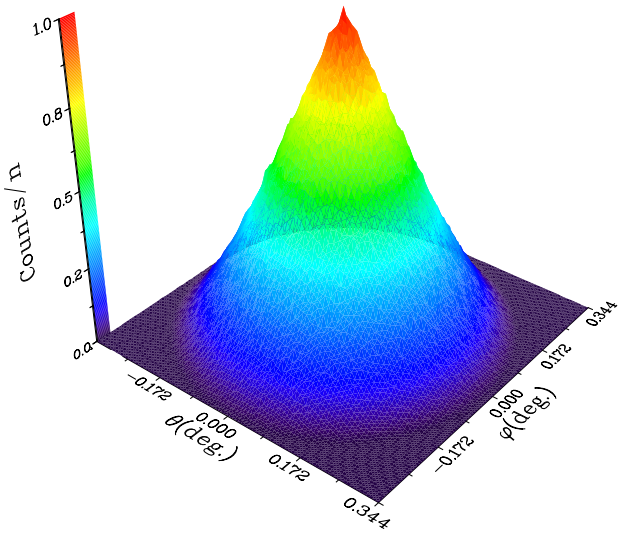

Figure 7.5: Function $G(\vartheta, \phi)$. - Histogram of the number of rays for values of ϑ and ϕ for an uniform focal distribution and a cylindrical geometry as collimator.

reflectivity R, and it is given by Eq. (7.1) if the crystal is perfect and flat. Thus, the intensity of the differential element upon diffraction of the first crystal and after by the second crystal is

$$G(\vartheta, \phi)J(\lambda)R_1(\alpha_1 - \theta_\mathrm{B})R_2(\alpha_2^{\pm} - \theta_\mathrm{B})d\vartheta d\lambda d\phi \,, \tag{7.14}$$

where R_1 and R_2 are the reflectivity of the first and second crystal, which are not necessarily the same. $\alpha_2^{\pm}$ is the second crystal glancing angle, where the plus and minus sign refer to the antiparallel and parallel modes, respectively. The total intensity is given after integration of the differential element in Eq. (7.14), i.e.,

$$\begin{aligned} P_{\pm}(\beta) &= \int_{\lambda_\mathrm{min}}^{\lambda_\mathrm{max}} \int_{\phi_\mathrm{min}}^{\phi_\mathrm{max}} \int_{\vartheta_\mathrm{min}}^{\vartheta_\mathrm{max}} J(\lambda - \lambda_0)\, G(\vartheta, \phi) \\ &\times R_1(\alpha_1(\vartheta, \phi, \delta_1) - \theta_B(\lambda))\, R_2\left(\alpha_2^{\pm}\left(\vartheta, \phi, \beta, \delta_1, \delta_2^{\pm}\right) - \theta_B(\lambda)\right) d\lambda d\vartheta d\phi \,. \end{aligned} \tag{7.15}$$

The maximum and minimum angles ϕ_max, ϕ_min, ϑ_max and ϑ_min, depend on the geometry of the experimental setup. Since there is an integration in λ, the dependency of θ_B on this variable due to the Bragg law (Eq. (6.1)) is written explicitly.

7.2.1 Study of the rocking curves

Using Eq. (7.15), it can be deduced approximate values of the parallel and antiparallel peaks, which can be implemented in a DCS simulation as a check for the angle ranges. Moreover, some properties

of the parallel and antiparallel rocking curves can also be deduced. Such properties includes, being (or not) dispersive, or the rocking curve changes with geometry.

In order to make the study of the rocking curves easier, further simplifications and assumptions can be done in Eq. (7.15).The first assumption is that the reflectivity is the same in both crystals. This assumption is reasonable in the current experiment since, not only both crystals were cut from the same Si wafer, but also they were given the same chemical and mechanical treatment in order to be perfect crystals (Sec. 6.2.2).Another assumption consists in using the following approximation for the single ray first and second crystal glazing angles [251],

$$\alpha_1(\vartheta,\phi,\delta_1) \approx \theta_C + \vartheta + \varepsilon_1(\phi,\delta_1)\ , \tag{7.16}$$

$$\alpha_2^{\pm}(\vartheta,\phi,\beta,\delta_1,\delta_2) \approx \theta_C \mp \vartheta + \varepsilon_2^{\pm}\left(\phi,\delta_1,\delta_2^{\pm}\right) \pm \beta\ , \tag{7.17}$$

where $\varepsilon_1(\phi,\delta_1)$ and $\varepsilon_2^{\pm}\left(\phi,\delta_2^{\pm}\right)$ are the angle deviation angles due to the ray having a vertical projection, ϕ or the crystals being tilted (δ_1 and $\delta_2^{\pm}$). Using the definitions

$$\begin{aligned}
\omega(\phi,\lambda) &= \theta_C + \vartheta + \varepsilon_1(\phi,\delta_1) - \theta_B(\lambda)\ ,\\
\gamma^{\pm}(\lambda) &= \pm\beta + 2\left(\theta_C - \theta_B(\lambda)\right)\delta^{\pm}\ ,\\
\varepsilon^{\pm}(\phi) &= \varepsilon_2^{\pm}\left(\phi,\delta_1,\delta_2^{\pm}\right) \pm \varepsilon_1(\phi,\delta_1)\ ,
\end{aligned} \tag{7.18}$$

The Eq. (7.15) can be written as

$$P_{\pm}(\beta) = \int_{\lambda_{\min}}^{\lambda_{\max}}\int_{\phi_{\min}}^{\phi_{\max}}\int_{\omega_{\min}}^{\omega_{\max}} J(\lambda-\lambda_0)\,G(\omega,\phi)\,R(\omega)\,R\left(\mp\omega+\varepsilon^{\pm}+\gamma^{\pm}\right)d\lambda d\omega d\phi\ . \tag{7.19}$$

The function $\delta^{\pm}$ assumes values one and zero for the antiparallel and parallel modes. In the case of a perfect aligned spectrometer with an ideal vertically narrow infinite apart slits, the terms $\varepsilon_2^{\pm}\left(\phi,\delta_1,\delta_2^{\pm}\right)$ and $\varepsilon_1(\phi,\delta_1)$ are equal to zero. They are given in second order of ϕ, δ_1 and $\delta_2^{\pm}$ by

$$\begin{aligned}
\varepsilon_1(\phi,\delta_1) &\approx -\frac{1}{2}\left(\phi^2+\delta_1^2\right)\tan(\theta_C) + \frac{\delta_1\phi}{\cos(\theta_C)}\\
\varepsilon_2^{\pm}\left(\phi,\delta_1,\delta_2^{\pm}\right) &\approx -\frac{1}{2}\left(\phi^2 + (\delta_2^{\pm})^2 \mp 4\delta_1^2\cos(\theta_C\pm\theta_C) + 4\delta_2^{\pm}\delta_1\right)\tan(\theta_C)\\
&\quad + \frac{\phi}{\cos(\theta_C)}\left(\mp 2\delta_1\cos(\theta_C\pm\theta_C) + \delta_2^{\pm}\right)\ .
\end{aligned} \tag{7.20}$$

Let us consider the integration in ω keeping λ and ϕ constants in Eq. (7.19). The width of the function G (Fig. 7.5) is much higher then the crystal reflectivity, so the only angles that are pertinent

to the integration in Eq. (7.19), are the ones in the narrow angular region of the function R (Fig. 7.2). In detail, the width of G is $\sim 0.15°$, while for R is 6×10^{-3} °. For these values, the dependence of the function G in ω for the region of integration can be neglected, i.e., the value ϑ in G is approximately constant. Thus, the function $G(\omega, \phi)$ is replaced by $Gg(\phi)$ in Eq. (7.19). Another consideration is that the horizontal aperture of the spectrometer is very wide compared with narrow angular region of the reflectivity R so that $\omega_{\min} = -\infty$ and $\omega_{\max} = \infty$. The angles $\varepsilon_1(\phi, \delta_1)$ and $\varepsilon_2^{\pm}(\phi, \delta_1, \delta_2)$ can be isolated in Eq. (7.19) by making a first order expansion. The result is given by

$$P_{\pm}(\beta) = h_0(\varepsilon^{\pm}) H^{\pm}(\beta) \mp h_1(\varepsilon^{\pm}) \frac{dH^{\pm}(\beta)}{d\beta} + O^{(2)} , \tag{7.21}$$

where

$$\begin{aligned} H^{\pm}(\beta) &= \int_{\lambda_{\min}}^{\lambda_{\max}} J(\lambda - \lambda_0) \int_{-\infty}^{\infty} R(\omega) R(\mp\omega + \gamma^{\pm}) \, d\lambda d\omega , \\ h_n(\varepsilon) &= G \int_{\phi_{\min}}^{\phi_{\max}} \varepsilon^n g(\phi) \, d\phi . \end{aligned} \tag{7.22}$$

The parameters $h_{n>0}[\varepsilon]$ are related with vertical misalignment errors. We define vertical misalignment as the mean value between ϕ_{min} and ϕ_{max},

$$\xi = \frac{\phi_{max} + \phi_{min}}{2} . \tag{7.23}$$

If ϕ_{min} is different from $-\phi_{max}$ due to some misplaced slit, there is a vertical misalignment. If the values of vertical tilts δ_1 and $\delta_2^{\pm}$ are zero and the rays are moving in parallel horizontal planes ($\phi = 0$), then the parameters $h_{n>0}[\varepsilon^{\pm}]$ will also be zero. Therefore, the function $H^{\pm}(\beta)$ has the physical meaning of being the ideal rocking curve without vertical misalignment and both crystals having ideal vertical axis (no tilt). The situation of the rays moving in parallel horizontal planes can be nearly obtained by using long Soller slits, which are just a great number of compact parallel plates. From Eq. (7.21), it is clear that the vertical misalignment and crystal tilts changes the shape of $P_{\pm}(\beta)$. By noticing the definition of a derivative, Eq. (7.21) is given approximately by

$$P_{\pm}(\beta) \approx h_0(\varepsilon^{\pm}) H^{\pm}(\beta \mp \xi_1) , \quad \xi_1^{\pm} = \frac{h_1(\varepsilon^{\pm})}{h_0(\varepsilon^{\pm})} , \tag{7.24}$$

which indicates that, in first approximation, the effect of vertical misalignment and crystal tilts is producing a shift in the function $H^{\pm}(\beta)$ with value $\xi_1^{\pm} = h_1(\varepsilon^{\pm})/h_0(\varepsilon^{\pm})$.

7.2.1.1 Parallel rocking curve

Using the previous approximations, the ideal parallel rocking curve is given by

$$H^{-}(\beta) = \int_{\lambda_{\min}}^{\lambda_{\max}} J(\lambda - \lambda_0) \int_{-\infty}^{\infty} R(\omega) R(\omega + \beta) \, d\lambda d\omega \, . \tag{7.25}$$

In a improper integral, if a constant value is added to the independent variable, the value of the integral remains invariant. Therefore, the variable $\theta_B(\lambda)$ included in ω (Eq. (7.18)), can be subtracted in Eq. (7.25). Thus, the double integral in Eq. (7.25) can be given as a product of two independent integrals, one in λ and the other in ω,

$$H^{-}(\beta) = j \int_{-\infty}^{\infty} R(\omega) R(\omega + \beta) \, d\omega \, . \tag{7.26}$$

This integral over ω corresponds to the autocorrelation of the reflectivity [252]. The constant j is the value of the integration over the wavelength distribution, J, and has the physical meaning that the shape of the parallel rocking curve is independent of the wavelength distribution. Different wavelength distributions only changes the value of j.This property is independent of vertical misalignments since the derivatives of $H^{-}(\beta)$ in Eq. (7.21) also contains the product of two integrals.

From Eq. (7.21) it is clear that vertical misalignment and crystal tilts changes the shape of the rocking curve in terms of the parameters $h_n[\varepsilon]$. However, if the value of the crystal tilts is considered to be zero, then $h_{n>0}[\varepsilon]$ have also a zero value independent of vertical misalignment, i.e., in the case of the crystals axis being ideally vertical, the parallel rocking curve does not depend on vertical misalignment.

By considering the condition of a ray being reflected at the neighborhood of the reflectivity maximum of both crystals ($\omega = \Delta_r \ \wedge \ \omega + \beta + \xi_1^{-} = \Delta_r$), an estimative of the parallel maximum peak is given by

$$\beta_{\text{para}} = -\xi_1^{-} = \frac{1}{2}\left((\delta_2^{-})^2 + 3\delta_1^2 + 4\delta_2^{-}\delta_1\right)\tan(\theta_C) - \frac{\xi(\delta_2^{-} + \delta_1)}{\cos(\theta_C)} \, , \tag{7.27}$$

where ξ is the vertical misalignment, $\xi = (\phi_{min} + \phi_{max})/2$. If the second crystal angle is measured according to the zero reference of point (6) of the alignment procedure described in Sec. 6.2.3, the position of the peak is given by

$$\theta_{\text{para}} = 90^{\circ} - \theta_C + \frac{1}{2}\left((\delta_2^{-})^2 + 3\delta_1^2 + 4\delta_2^{-}\delta_1\right)\tan(\theta_C) - \frac{\xi(\delta_2^{-} + \delta_1)}{\cos(\theta_C)} \, . \tag{7.28}$$

The autocorrelation function (Eq. (7.26)) have two properties [252]. First, it has the maximum at $\beta = 0$, and second $H^{-}(\beta) = H^{-}(-\beta)$. Therefore, the shape of $H^{-}(\beta)$ is a peak function symmetric around the maximum at $\beta = 0$, independent of the reflectivity shape or position (Eq. (7.1)).

7.2.1.2 Antiparallel rocking curve

The same properties of parallel rocking curve will be considered here. As in the parallel case, the ideal antiparallel rocking curve is given by

$$H^{+}(\beta) = \int_{\lambda_{\min}}^{\lambda_{\max}} J(\lambda - \lambda_0) \int_{-\infty}^{\infty} R(\omega)\, R(-\omega + \beta + 2(\theta_C - \theta_B(\lambda)))\, d\lambda d\omega \,. \tag{7.29}$$

This integral represents the convolution of the function R with itself with another convolution with the wavelength distribution J. Unlike the parallel rocking curve, this rocking curve depends on the wavelength, so it is dispersive. In detail, a spectrum can be obtained by the rotation of the second crystal in antiparallel mode. In case of a monochromatic source, the ideal rocking curve, $H^{+}(\beta)$, have the same shape as $H^{-}(\beta)$. The antiparallel rocking curve depends on vertical misalignment even without crystal tilts. The parameter ξ_1^{+} is given by

$$\xi_1^{+} = -\xi^2 \tan(\theta_C) - \frac{\int_{-\phi_t}^{\phi_t} \phi^2 g(\phi)\, d\phi}{\int_{-\phi_t}^{\phi_t} g(\phi)\, d\phi} \tan(\theta_C) = -(\xi^2 + \xi_{\mathrm{VD}}) \tan(\theta_C) \,, \tag{7.30}$$

where $\phi_t = \phi_{max} - \xi$. If the DCS has a rectangular entrance, then $g(\phi)$ is given by Eq. (7.13) and ξ_1 by

$$\xi_1^{\mathrm{rect}} = -\xi^2 \tan(\theta_C) - \frac{a^2 + b^2}{12L^2} \tan(\theta_C) \,, \tag{7.31}$$

with a and b defined as in Eq. (7.13). The antiparallel rocking curve is shifted by the second term of Eqs. (7.30) or (7.31), even without vertical misalignment. This last term in Eq. (7.31) is known as the vertical divergency correction [215, 225].

Similar to the parallel case, the estimative of the antiparallel maximum position peak is given by

$$\beta_{\mathrm{anti}} = 2\Delta_r - 2(\theta_C - \theta_{\mathrm{B}}) + \xi_1^{+} \,, \tag{7.32}$$

with ξ_1^{+} given, in the general case, by

$$\begin{aligned} \xi_1^{+} = \; & - \; (\xi^2 + \xi_{\mathrm{VD}}) \tan(\theta_C) \\ & - \; \frac{1}{2}\left[(\delta_2^{+})^2 - 4\delta_1^2 \cos(2\theta_C) + \delta_1^2 + 4\delta_2^{+}\delta_1\right] \tan(\theta_C) \\ & + \; \frac{\xi\{\delta_2^{+} + \delta_1\,[1 - 2\cos(2\theta_C)]\}}{\cos(\theta_C)} \,. \end{aligned} \tag{7.33}$$

Unlike the parallel case, in the antiparallel case the second crystal rotation depends on the wavelength through the Bragg angle. Again, if the second crystal rotation is measured with respect to the zero reference of point (6) of Sec. 6.2.3, the estimative of the antiparallel peak is

$$\theta_{\text{anti}} = -90^\circ + \theta_C + 2\Delta_r - 2(\theta_C - \theta_{\text{B}}) + \xi_1^+ \,. \tag{7.34}$$

Both ξ_1^+ and ξ_1^- represent the angle deviations due to vertical misalignment and crystal tilts in the angles θ_{anti} and θ_{para}, respectively. In the case of a perfectly aligned DCS, the last term of Eq. (7.34) is the vertical divergency correction, $-(\xi_{\text{VD}})\tan(\theta_C)$.

The DCS enables absolute measurements since the parallel peak can be used to calibrate the antiparallel one, i.e., without the knowledge of the first crystal angle and the use of other calibrating energy. It is clear that a value of θ_{B} can be obtained from the difference between Eqs. (7.28) and (7.34), along with the correction Δ_r and the vertical divergency correction.

7.3 Simulation of the DCS

In the present work, it was developed and used a ray trace program to obtain simulated parallel and antiparallel rocking curves (Eq. (7.15)), necessary in the analysis of the experimental data. It consists of a Monte-Carlo simulation code that takes into account all relevant geometrical parts of the experimental DCS with the crystal reflectivity given by the dynamical diffraction theory presented in Sec. 7.1 [247]. The horizontal and vertical views of the DCS geometry are shown in Figs. 7.3 and 7.4, respectively. As refereed in the previous Sec. 7.2, the red dot line defines the optical axis, which is crucial for the simulation model. It connects the axis of the source with the center of the various geometrical components in an ideal aligned instrument. The tri-orthogonal *xyz* axis follows the optical axis, as represented in Fig. 7.6.

Any misaligned component is taking into account in the simulation with respect to the tri-orthogonal *xyz* axes defined by the optical axis. Since the optical axis connects the axis of rotation of both crystals, the angle between the x direction before and after the first crystal is not necessarily $2 \times \theta_{\text{C}}$, but a value that is defined as θ_{T}. It is the angle that the table where the crystals are mounted does with the axis of the source.

An additional axis attached to the crystallographic plane of the crystals (cf. Fig. 7.6) is considered to define the position along the plane of the crystals. Considering the axis presented in Fig. 7.6, a single ray is described by its position, (y, z), and direction, (ϑ, ϕ). The description of the ray along the x axis corresponds to transformations, such as translations and rotations of the position and direction vectors. The optical axis is a special ray with a position (0, 0) and direction (0, 0) along all the x axis. The ray is also characterized by its wavelength.

In order to obtain simulated rocking curves, the simulation generates N rays in the source with random distributions, for several angles β, and counts the ones that reaches the detector. In Fig. 7.7

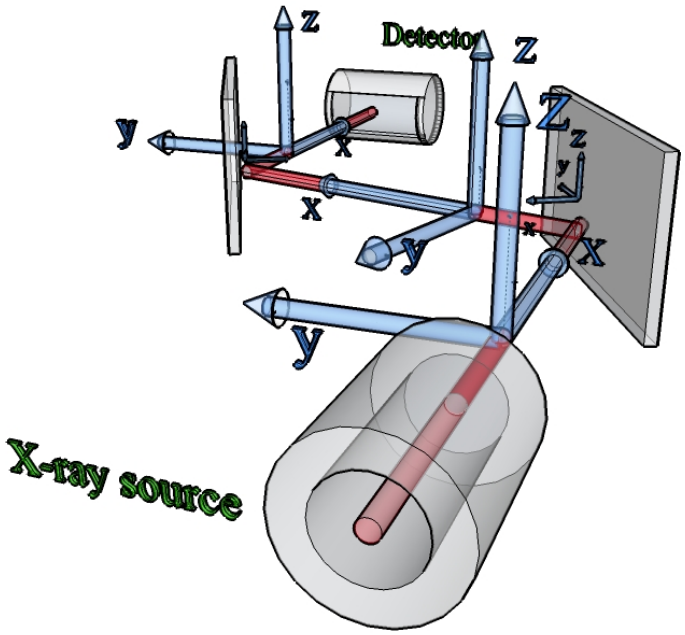

Figure 7.6: Optical axis - Geometry of the DCS in a parallel setup with the optical axis and the tri-orthogonal *xyz* axis along the optical axis.

is presented a flowchart of the simulation, where the contents of each box are described in the next subsections.

7.3.1 Path between the source and first crystal

The path of a single ray along the DCS starts at the source with a random uniform distribution for the direction (U[$\vartheta_{\min}, \vartheta_{\max}$], U[$\phi_{\min}, \phi_{\max}$]), where the several angles, $\vartheta_{\min}$, $\vartheta_{\max}$, $\phi_{\min}$ and $\phi_{\max}$ are given by the collimators between the source and the first crystal. In the present experiment, as shown in Fig. 6.4, it corresponds to a 1.5 m long tube with a diameter of 12 mm between the components #17 and #20. The ray direction is expressed by the cartesian components of the unitary vector, $\boldsymbol{r}$,

$$\begin{aligned} r_x &= \cos(\phi)\cos(\vartheta)\,, \\ r_y &= \cos(\phi)\sin(\vartheta)\,, \\ r_z &= \sin(\phi) \qquad\quad . \end{aligned} \tag{7.35}$$

Furthermore, the initial position of the rays at the source may be generated by several distributions according to the user choice. Can be given as a fixed point, in the case of a point-like source. Can follow an uniform random distribution (U[$-D_c, D_c$], U[$-D_c, D_c$]), where D_c is the source tube diameter, or even following a radial Gaussian distribution. In detail, the last case follows a Gaussian distribution for the radius with σ_{R} and an uniform distribution for the angle (U[$0, 2\pi$]). If a position is generated outside the region $y^2 + z^2 < (D_c/2)^2$, it is discarded and another point is generated. The

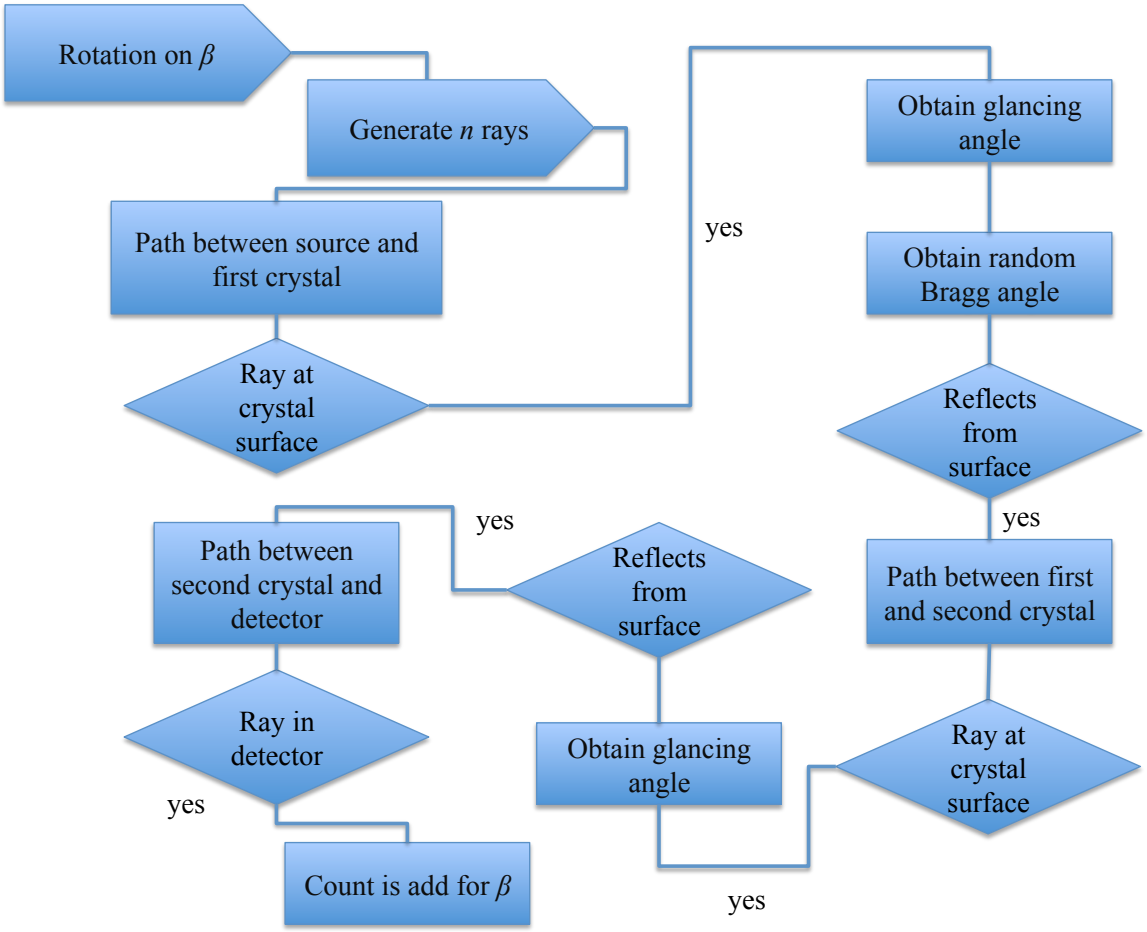

Figure 7.7: Flowchart of the simulation - The boxes refereed to the second crystal and detector part simulates for both parallel and antiparallel settings, i.e., with a single rotation of β, both parallel and antiparallel rocking curves can be obtained.

simulations presented in this work were done with an uniform source distribution. An histogram of the number of rays done for this geometry is showed in Fig. 7.5. It was found that both point-like and uniform distribution approaches provided almost the same results, which is due to the relative long distance between the source and the detector. Obviously, a Gaussian distribution is an intermediate situation between the point-like source and an uniform distribution. Both cases can be emulated with a Gaussian distribution using $\sigma_{\mathrm{R}} << D_c$ and $\sigma_{\mathrm{R}} >> D_c$.

The pseudo-random uniform sampling was obtained from the routine *ran*1 in Ref. [163], which is based on the linear congruential algorithm. The description of how much "random" the linear congruential algorithm is, can be found in Ref. [163]. Nevertheless, in the present work we checked the simulations done with a more complex, accurate, time-consuming routine (*ran*2 from [163]) and was not observed difference between the two routines.

After an iteration, the new position of the ray in the plane *yz*, perpendicular to the source axis, that includes also the first crystal axis of rotation, is given by

$$\begin{aligned} y' &= y + L\tan(\vartheta)\,, \\ z' &= z + L\tan(\phi)\,, \end{aligned} \tag{7.36}$$

where L is the translation distance, i.e., the distance between the source and the first crystal. Finally, the position at the surface of the crystal is given by the projection of the position vector over the surface axis,

$$\begin{aligned} y' &= y\frac{\cos(\vartheta)}{\cos(\vartheta + \frac{\pi}{2} - \theta_{\mathrm{C}})}\,, \\ z' &= z\frac{\cos(\phi)}{\cos(\phi + \delta_1)}\,. \end{aligned} \tag{7.37}$$

The angle that the ray makes with the crystallographic plane of first crystal is given by

$$\alpha_1 = \arcsin(-\boldsymbol{r}\cdot\boldsymbol{n_1})\,, \tag{7.38}$$

where $\boldsymbol{r}$ is the ray vector position (Eq. (7.35)) and $\boldsymbol{n_1}$ is an unitary vector perpendicular to the first crystal crystallographic plane expressed by

$$\begin{aligned} n_{1x} &= -\cos(\delta_1)\cos(\theta_{\mathrm{C}})\,, \\ n_{1y} &= \cos(\delta_1)\sin(\theta_{\mathrm{C}})\,, \\ n_{1z} &= \sin(\delta_1)\,. \end{aligned} \tag{7.39}$$

Therefore, the direction of the reflected ray is given by

$$\boldsymbol{r'} = \boldsymbol{r} - 2(\boldsymbol{r} \cdot \boldsymbol{n_1})\boldsymbol{n_1} \ . \tag{7.40}$$

7.3.2 Generation of a random wavelength and a Bragg angle

If happens that the ray position is inside the crystal, it is generated randomly a wavelength, λ_i, with probability p_i, related to the emission of a photon in the decay process, i, of an ion with a definite charge state. It is generated at the first crystal plane, and not in the source, due to minimization of computation.

This randomly obtained wavelength, for instance λ_1, is used as center position of a Lorentzian random number generator, $L(\lambda_1, \Gamma_1)$, where Γ_1 is the natural line width associated with the decay life time. The method used for Lorentzian random number generator is the inverse method [163]. This is a method for generating pseudo-random numbers from a probability distribution in case of the cumulative distribution function being possible to invert, i.e., it has an inverse function. The cumulative distribution function of a continuous random variable is defined by

$$F(x) = \int_{-\infty}^{x} f(x')dx' \ , \tag{7.41}$$

where $f(x')$ is the probability density function. Since the cumulative distribution function gives the probability of a variable X taking a value less than x, $F(\infty) = 1$. By defining $u = F(x)$ and if u is obtained from an uniform distribution (U[0, 1]), then, with the use of the inverse function, $x = F^{-1}(u)$, x will be a number that follows the $f(x')$ probability density function. In case of a Lorentzian distribution

$$f(\lambda_1', \lambda_1, \Gamma_1) = \frac{1}{2\pi} \frac{\Gamma_1}{(\lambda_1' - \lambda_1)^2 + \left(\frac{\Gamma_1}{2}^2\right)} \ , \tag{7.42}$$

the Lorentzian random number generator, $L(\lambda_1, \Gamma_1)$, that follows that distribution (Eq. (7.42)), is given by

$$\lambda_1' = \lambda_1 + \frac{\Gamma_1}{2} \tan(\mathrm{U}[0, 1]) \ . \tag{7.43}$$

The obtained wavelength from the process, λ_1', then is used as a center position of a Gaussian random number generator $G(\lambda_1', \sigma)$, where σ takes account a Doppler broadening due to a velocity distribution of the ions. The Gaussian random number generator was implemented with a method based on the two-dimension generalization of the inverse method, so-called *Box-Muller* method [163]. This method generates two random numbers with a Gaussian probability density function given by

$$f(\lambda_1'', \lambda_1', \sigma) = \frac{e^{-\frac{(\lambda_1' - \lambda_1'')^2}{2\sigma^2}}}{\sigma\sqrt{2\pi}} \ , \tag{7.44}$$

from two calls of an uniform distribution (U[0, 1]). In detail, the Gaussian random number generator $G(\lambda_1', \sigma)$ of those two numbers, is given by

$$\begin{aligned} \lambda_1'' &= \lambda_1' + \sigma\sqrt{-2\ln v_1}\frac{v_1}{R}\,, \\ \lambda_{1'}'' &= \lambda_1' + \sigma\sqrt{-2\ln v_1}\frac{v_2}{R}\,, \end{aligned} \tag{7.45}$$

where $R = \sqrt{v_1^2 + v_2^2} \wedge R \leq 1$ with v_1 and v_2 following two independent uniform distributions U[0, 1]. One other variable that is convenient to define is the FWHM, which for a Lorentzian distribution (Eq. (7.42)) is Γ_1, while for a Gaussian distribution (Eq. (7.44)) it is related with σ by

$$\mathrm{FWHM_G} = 2\sqrt{2\ln 2}\sigma\,. \tag{7.46}$$

Finally, the wavelength λ_1'' obtained from the Lorentzian random number generator (Eq. (7.43)) in series with a Gaussian random number generator follows another distribution so-called Voigt function, $V(\lambda_1, \Gamma_1, \sigma)$, where the density probability function is given by

$$f(\lambda_1'', \lambda_1, \Gamma_1, \sigma) = \int_{-\infty}^{\infty} \frac{e^{-\frac{\lambda_1'^2}{2\sigma^2}}}{\sigma\sqrt{2\pi}} \frac{1}{2\pi} \frac{\Gamma_1}{(\lambda_1'' - \lambda_1 - \lambda_1')^2 + \left(\frac{\Gamma_1}{2}^2\right)} d\lambda_1'\,. \tag{7.47}$$

The derivation of this result can be found in Ref. [253]. This function consists in the convolution of two physical mechanisms, one associate with Doppler broadening, and the other associate with the natural width of the initial state decay. The FWHM of a Voigt function (Eq. (7.47)) is given approximately (accuracy 0.02%) in terms of the Lorentzian and Gaussian $\mathrm{FWHM_{L,G}}$ by [254]

$$\mathrm{FWHM_V} = 0.5346\,\mathrm{FWHM_L} + \sqrt{0.2166\,\mathrm{FWHM_L^2} + \mathrm{FWHM_G^2}}\,. \tag{7.48}$$

In the present simulation, the temperature dependence is described by the linear thermal coefficient, $\alpha(T)$. The lattice distance, $d(T)$, in the crystallographic plane for a given temperature, is related to the lattice distance at 22.5 °C by

$$d(T) = d_{22.5}\left(\int_{22.5}^{T} \alpha(T)\,dt + 1\right), \tag{7.49}$$

where the temperature is given in °C, and $d_{22.5}$ is the lattice distance at 22.5 C°. If α is assumed to be constant and given by the manufacture (see Sec. 6.2.2), then $d(T)$ is given by

$$d(T) = d_{22.5}(1 + (T - 22.5)(2.56 \times 10^{-6}))\,. \tag{7.50}$$

The quantity $d_{22.5}$ is provide by the manufacturer (see Sec. 6.2.2). The other option considers the linear thermal coefficient given by Ref. [255]

$$\alpha(T) = \left(3.725\left\{1 - e^{-5.88\times10^{-3}(T-22.5)}\right\} + 5.548\times10^{-4}T\right)\times10^{-6}\,, \tag{7.51}$$

with T in Kelvin. For $T = 295.65$ K (22.5 °C), the linear thermal coefficient, $\alpha(T)$, is 2.53×10^{-6} °C^{-1}. The difference between the two approaches is less than 0.2 ppm.

The Bragg angle, θ_B, is related to the generated wavelength, λ_1'', and the lattice distance, $d(T)$, by Eq. (6.1). Furthermore, the energy of the photon is related the wavelength according to

$$E = \frac{C}{\lambda}\,, \tag{7.52}$$

where the constant $C = hc$ (Planck constant times the speed of light), is the conversion factor and according to the CODATA [90], is equal to 1.239841875×10^4 ÅeV.

7.3.3 X-ray Reflection in first crystal

The rays reflection is described according to the dynamical diffraction theory (see Sec. 7.1). The reflectivity was obtained from the XOP 2.3 code [248] taking into account both σ and π components of the radiation. In Fig. 7.2, is represented the reflectivity as a function of $\alpha_1 - \theta_B$ used in the simulation. The reflectivity is interpolated with cubic splines. A random number U[0, 1] is generated and is compared with the reflectivity at a position $\alpha_1 - \theta_B$ with Eq. (7.50 and λ_1'' and α_1 from Eq. (7.38). If the value is lower, then the ray is considered to be reflected from the crystal, otherwise, is considered to be absorbed.

By writing the reflectivity as a function of $\alpha_1 - \theta_B$, we have assumed that the range of energies covered in any rocking curve is small, and consequently, the variation of the reflectivity with energy can be neglected. For example, in the current region of measurements (3096 to 3114 eV), the relative difference between the FWHM's reflectivity and the maximum reflectivity change 0.08 %/eV and 0.1 %/eV, respectively.

In this simulation it is assumed a perfect crystal , i.e., it was neglected the degree of mosaic, defects on the crystal and the uncertainty in the crystal lattice, since the manufacturer guaranties an uncertainty of 0.03 ppm (see Sec. 6.2.2), which is much less than the goal of a few ppm accuracy in the measured energy.

7.3.4 Path from first crystal to detector

Once the ray is reflected, the y position along the new axis is given by $y' = -y\sin(\theta_\mathrm{T} - \theta_\mathrm{C})$. The position vector at the second crystal in the parallel or antiparallel setup is obtained in a similar way to the first crystal with a translation (Eq. (7.36) with the appropriate L, and a projection over the surface of the second crystal. The position at the second crystal crystallographic plane is given by

$$\begin{aligned} y' &= y\frac{\cos(\theta)}{\cos(\pm\theta + \theta_\mathrm{C} \mp \beta)} , \\ z' &= z\frac{\cos(\phi)}{\cos(\phi + \delta_2^\pm)} . \end{aligned} \tag{7.53}$$

The reflection process by the first crystal is repeated for the second one. Furthermore, as in the first crystal, the glazing angle is obtained from Eq. (7.38) with $\boldsymbol{r}$ defined after the first crystal reflection (Eq. (7.40)) and the normal vector of the second crystal given by

$$\begin{aligned} n_{2x}^\pm &= \mp\cos(\delta_2^\pm)\sin(\theta_\mathrm{T} \pm \theta_C + \beta) , \\ n_{2y}^\pm &= \pm\cos(\delta_2^\pm)\cos(\theta_\mathrm{T} \pm \theta_C + \beta) , \\ n_{2z}^\pm &= \sin(\delta_2^\pm) . \end{aligned} \tag{7.54}$$

In order to describe the reflected ray from the second crystal in terms of the xyz axis between the second crystal and the detector, it is necessary to multiply its direction vector by a rotation matrix along the z axis with angle, $\theta_\mathrm{T} + \theta_D^\pm$, where $\theta_D^\pm$ is the angle between the detector in antiparallel or parallel position and the axis of the source.

If the ray reaches the detector, in either parallel or antiparallel modes, then a count is added to the simulated spectrum for the β value. With a scan of β, both types of rocking curves are obtained.

The resolution of detector was not taken into account, since the dispersion on the wavelength is given by the rotation of the second crystal. In detail, the detector just have to detect photon counts no matter of its energy, because the energy was already selected by the position of the second crystal.

Since the zero position of the experimental second crystal scan is at a position perpendicular to the table axis, and not at θ_C, a value of β corresponds experimentally to $\beta + 90 - \theta_\mathrm{C}$ and $\beta - 90 + \theta_\mathrm{C}$ for parallel and antiparallel, respectively.

In Figs. 7.8 and 7.9 are shown examples of simulated parallel and antiparallel rocking curves, respectively. The wavelength or energy distribution used in those simulations consists of an energy of 3104.1 eV with zero natural width and a Gaussian distribution with σ equal to 0, 100 and 180 eV. The parallel curve does not depend on the wavelength or energy distribution as mentioned in Sec. 7.2.1.1. That's why is showed only the 0 eV case in Fig. 7.8. On the other hand, since the antiparallel curve is dispersive (Sec. 7.2.1.2), it is visible in Fig. 7.9 the increase of the FWHM with increasingly larger

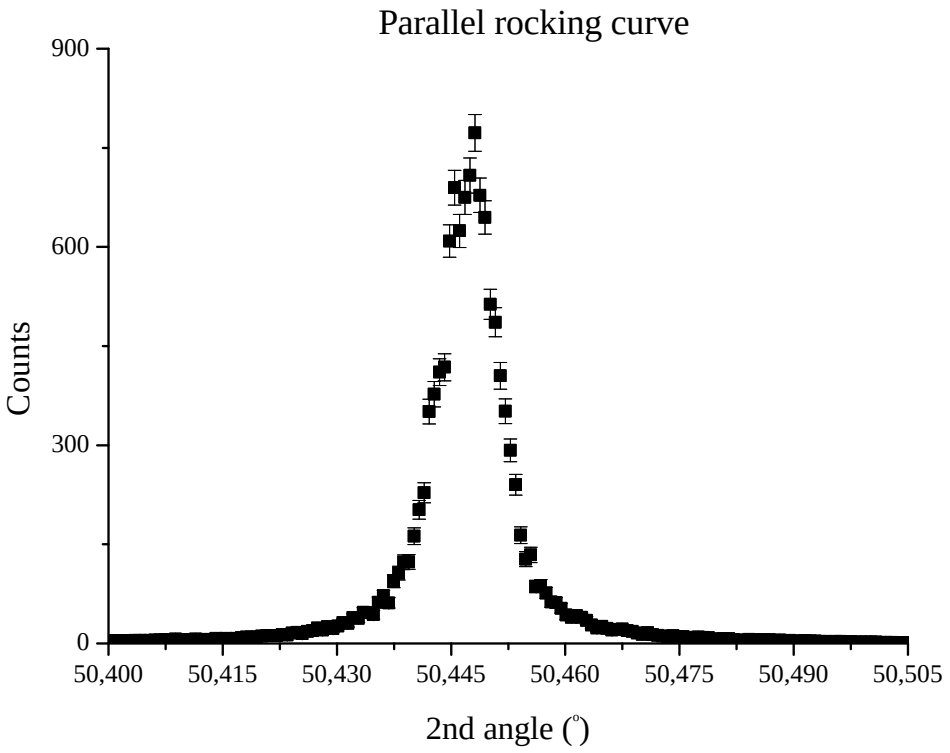

Figure 7.8: Simulated parallel rocking curve - Spectrum of counts for each second crystal angle in a parallel setting.

values of σ. The error bars in those figures corresponds to $\sqrt{n_i}$, where n_i is the number of counts in a bin i.

A technical description of the necessary input data for the simulation, as well as the output data provided by the simulation is presented in the Appendix B.

7.4 Data analysis

Having made a description of the Monte-Carlo simulation, we now proceed with a description of the analytical method used to retrieving an estimates the energy from raw data.

Generally, data consists of numbers created by some experiment without any processing or computation. These numbers follow some function model, which is related to the complexity of the physical process or experiment specifications (e.g. the detector response function). In addition, it is considered that these numbers have some degree of random fluctuation around a value.These random fluctuations can be from the instrument measurement uncertainties or statistical fluctuations.

In the current DCS, raw experimental data consists of both parallel and antiparallel rocking curves, i.e., of the counts given by the detector for a given angle of the second crystal. The angle is a

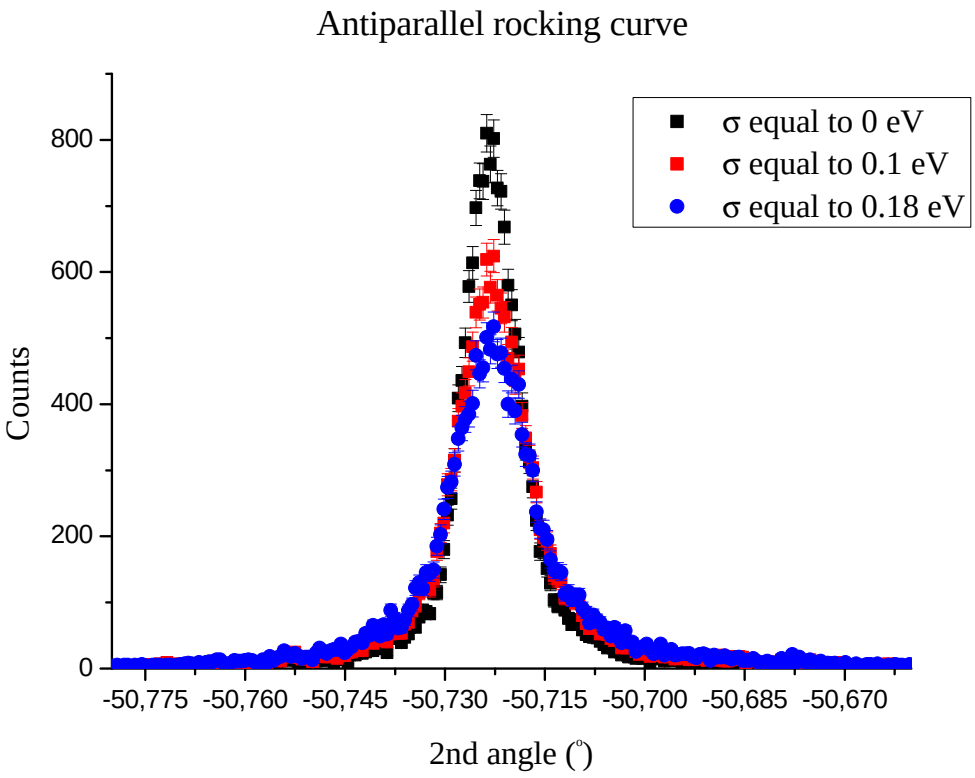

Figure 7.9: Simulated antiparallel rocking curve - Spectrum of counts for each second crystal angle in an antiparallel setting.

continuum variable, therefore, needs to be discretized in bins in order to fit in a file. Thus, in the current experiment, a data set consists of the number of counts for each angular bin.

7.4.1 χ^2 fitting

In order to compare data (simulated or experimental) with a given model, the usual method is the Maximum likelihood estimator. Given a particular data set with (x_i, y_i), this method retrieves the optimal set of parameters a_1, ..., a_m , which minimizes some difference function between y_i and $y(x_i; a_1, ..., a_m)$, If the measured y_i follow a Gaussian distribution (Eq. (7.44)), then this method reduces to a least-square minimization. In detail, it reduces to the minimization of the function χ^2 defined by

$$\chi^2 = \sum_{i=1}^{N} \left[\frac{n_i - y(x_i; a_1, ...a_m)}{\sigma_i} \right]^2 , \tag{7.55}$$

where in the present case N is the number of bins, σ_i is the standard deviation and m the number of parameters. This minimization process corresponds to fitting the data with the model. In an experiment, where there are counting events, the measurement error of the counts in each bin is distributed as Poisson statistics [256]. However, for large number of counts, this distribution converges to a Gaussian distribution [256]. The minimal value χ^2 obtained from two different models gives an indication of which model the data set follows better.

In theDCS case, the models for the parallel and antiparallel data set are given by Eq. (7.19), or by the approximations Eqs. (7.26) and (7.29). In fact, the rocking curves are peak functions (Figs. 7.8 and 7.9), so any peak function can be used as a fit model for a preliminary estimation. All these models have a non-linear dependence on the model parameters. In the present work, we use a standard method for non-linear least-square minimization, known as the Levenberg-Marquardt method [163]. This method combines two methods depending on each how far the minimum is. For points far away from the minimum, this method is approximately given by the steepest descend method (steps proportional to the negative of the gradient), otherwise, it reduces to the inverse-Hessian method (based on the analytical first order expansion of Eq. (7.55)). This algorithm requires a value of the model function at a given point and parameters, as well as the derivatives with respect to the parameters.

By performing this fit, the standard deviation of the obtained parameter i is $\sqrt{C_{ii}v}$, where C_{ii} is the inverse of the curvature matrix and v is the number of bins minus the number of parameters [163]. The standard deviation was obtained assuming that the probability distribution of the parameter is Gaussian. With the last assumption, the confidence intervals are 68 % for one and 95 % for two standard deviations, respectively. A more rigorous treatment of confidence intervals can be found in Ref. [163]. In the present work, since we use this analysis to compare systematic errors, rather

than to retrieve precise physical values with rigorous confidence, we restrict to those confident values. Moreover, the rigorous analysis of the experimental data is given in Ref. [257].

7.4.2 Voigt functions

Due to its adaptability, the Voigt function (Eq. (7.47)) can be used to fit any symmetric peak. The values of the Gaussian σ and the Lorentzian Γ can be adjusted, so that the Voigt function follows not only the tails of a given peak, but also the behavior on top.

Using this function, both parallel and antiparallel data can fitted with a model given by

$$y\,(x; x_0, \sigma, \Gamma, A, B) = A\; V\,(x, x_0, \sigma, \Gamma) + B\,, \tag{7.56}$$

where x_0, σ, Γ, A and B are the fit parameters and V the Voigt function given by Eq. (7.47). This function is symmetric and has its maximum at $x = x_0$. As discussed in Sec. 7.3.2, the emission of a X-ray follows a Voigt distribution. However, the parallel peak (Eq. (7.19) or Fig. 7.8) is independent of this distribution (Sec. 7.2.1.1). Since the parallel peak is symmetric about the maximum (Sec. 7.2.1.1), by performing a fit with a Voigt function, the parameter x_0 tends to the value of Eqs. (7.27) or (7.28). On the other hand, by performing a fit of the antiparallel peak, the x_0 is approximately given by Eq. (7.34). As mentioned before, the antiparallel curve is the convolution of the wavelength distribution with the convolution of the reflectivity, so it is not given by the model in Eq. (7.56). However, if the reflectivity had no absorption as given in Eq. (7.4), which is a symmetric function around Δ_r, then the convolution in Eq. (7.29) reduces to a correlation function around $\beta + 2\Delta_r - 2(\theta_C - \theta_B) + \xi_1^+$, and the latter approximation becomes exact.

In order to perform the Levenberg-Marquardt minimization, it is required the knowledge of the function value in several points, as well as the derivatives with respect to the parameters. These values were obtained with a procedure based in the calculation of the error function using Cauchy-Riemann equations (routine *CW*) [258].

Using the fit parameter x_0 of the parallel and antiparallel peaks, an approximate Bragg angle is given by

$$\theta'_B = \frac{[180 - (x_0^{anti} - x_0^{para}) - 2\Delta_r - (\xi_1^+ - \xi_1^-)]}{2}\,, \tag{7.57}$$

$$E' = \frac{C}{2d\sin(\theta'_B)}\,, \tag{7.58}$$

where E' is the energy obtained from the method, Δ_r is a correction due to the index of refraction and Δ_v is a correction due to vertical divergency [215]. x_0^{anti} and x_0^{para} are the antiparallel and antiparallel fitted peak positions with Voigt functions, respectively. The constant $C = hc$ is the conversion factor.

The last two terms of Eq. (7.58) are related to the vertical geometric systematic errors. They are given by

$$\begin{aligned} \xi_1^+ - \xi_1^- = & - (\xi^2 + \xi_{\mathrm{VD}}) \tan(\theta_C) \\ & - \{\delta_2^2 - 2\delta_1^2 [1 - \cos(2\theta_C)] + 4\delta_2\delta_1\} \tan(\theta_C) \\ & + \frac{2\xi\{\delta_2 + \delta_1 [1 - \cos(2\theta_C)]\}}{\cos(\theta_C)} , \end{aligned} \tag{7.59}$$

for the case of the tilt in second crystal being the same as in parallel and antiparallel modes. These errors will be discussed in detail in the next Section.

7.5 Study of systematic errors

The notion of systematic errors are related to the accuracy of an experiment, rather than to the precision. While the latter gives the information of how well the experimental results have been determine, without reference to its true value, the former is a measure of how close the result is to the right value. Furthermore, the precision is also a measure of the result's reproducibility and is related with result's statistics. A good accuracy is obtained by minimizing systematic errors. An economic approach to study the effect of systematic errors is using a Monte-Carlo simulation and compare the results with and without a particular systematic error.

In order to perform this comparison, both types of rocking curves were fitted using the Levenberg-Marquardt method with a Voigt function (Sec. 7.4.2). The output fit parameters, like position (x_0), width (FWHM), amplitude (A), or energy (E) (Eq. (7.58)), can then be compared in order to study the possible systematic errors.

In all simulations were used a monochromatic source, i. e, a single wavelength without any Lorentzian or Gaussian broadening. A few cases were checked with a Lorentzian broadening in order to confirm that results presented in this section are independent of the wavelength distribution.

7.5.1 Vertical misalignment

The first systematic error considered is the vertical misalignment, which is defined by Eq. (7.23). The vertical misalignment could be identified by using a mask, which absorbs x rays, in the second crystal covering the upper or lower vertical half part. The comparison of the energy obtained from Eq. (7.58) in the upper and lower cases gives an indication of the amount of vertical misalignment. In Fig. 7.10 is plotted the simulated energy difference for several values of vertical shifts in the tube entrance (between #17 and #20 in Fig. 6.4), that connects the source to the spectrometer. Along with

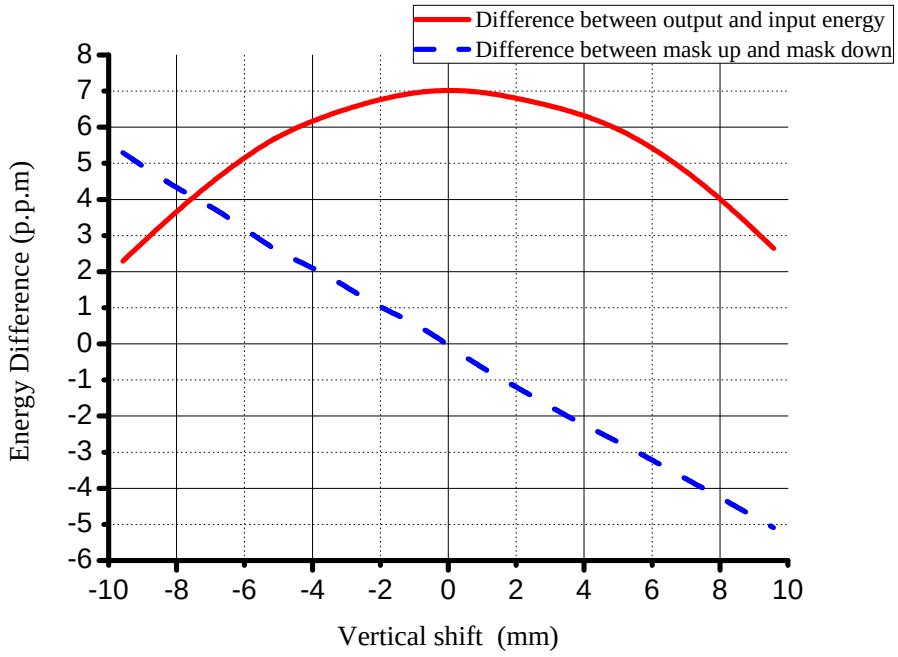

Figure 7.10: Energy obtained for several values of vertical misalignment - The red solid line is the difference between the energy obtained (Eq. (7.58)) from simulation and the input energy. The blue dashed line is the difference between the energy obtained (Eq. (7.58)) with upper and lower masks.

this function, in Fig. 7.10 is also plotted the energy difference between the input energy in simulation and the output energy (Eq. (7.58)). We notice that the last mentioned function varies according to an inverted parabola with the minimum not at zero, but at approximately 7 ppm. As mentioned before, using Voigt function gives an approximate value of the Bragg angle, since it is not the right model to fit. The parabolic shape is due to the term ξ^2 (square of vertical misalignment) in the antiparallel curve (ξ_1^+ of Eq. (7.59)). Therefore, in case of δ_1 and $\delta_2^\pm$ being equal to zero, the parabolic shift on the energy is due exclusively to a shift in the antiparallel peak (parameter x_0^{para}), i.e., the parallel curve is independent of vertical misalignment. This systematic error always produces an energy negative systematic error. This result can be generalized for any component of the DCS that makes this effect. As for the difference between lower and upper cases, we obtain a linear dependence as function of the vertical misalignment according to -0.54 ppm/mm. This simulations were done without crystal tilts.

7.5.2 Crystal tilt

Along with the vertical misalignment, it was also considered the effect of the crystal tilts (δ_1 and $\delta_2^\pm$). The mask test can be also used for tracking this systematic error. The simulations were carried on assuming the same tilt in both parallel and antiparallel modes. Similar to Fig. 7.10, in Fig. 7.11 is plotted the energy differences between upper and lower masks for several values of crystal tilts, $\delta_{1,2}$. The mentioned energy differences is approximately given, in ppm, by

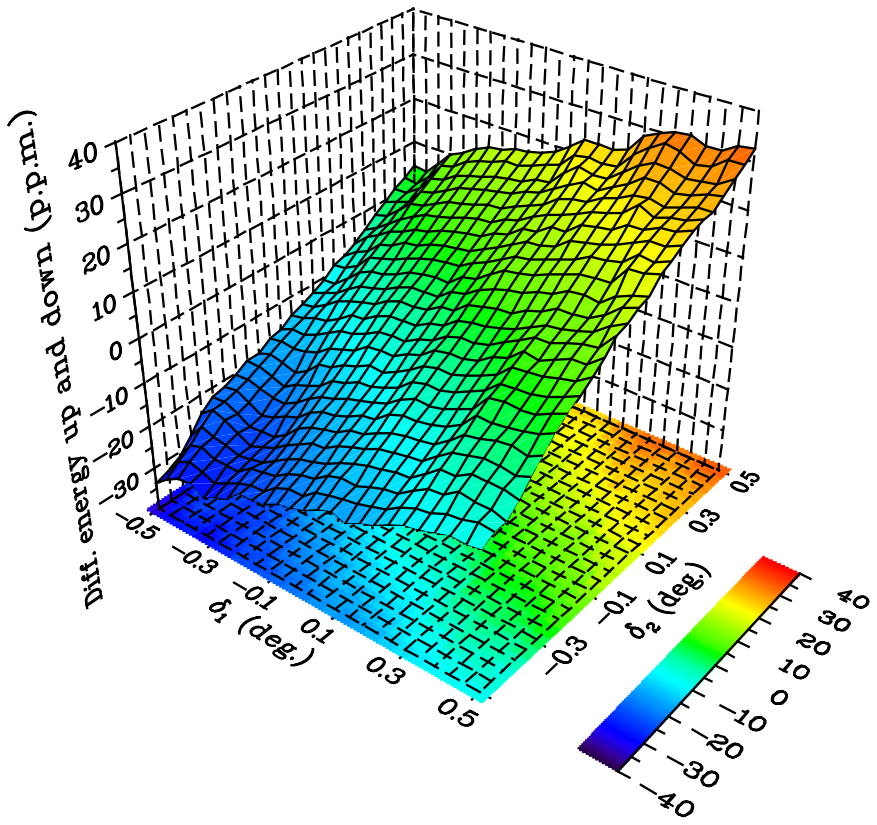

Figure 7.11: Simulation of the energy done for several values of crystal tilts - Plot of the energy difference between upper and lower masks for several values of δ_1 and δ_2.

$$\Delta E'_{\text{mask2}} = 33.3\{\delta_2 + \delta_1\,[1 - \cos(2\theta_{\text{B}})]\}\,. \tag{7.60}$$

These simulations were done without considering a vertical misalignment. The dependence on the crystal tilts in Eq. (7.60) can be verified by noticing that performing the difference between the lower and upper mask case, all terms of Eq. (7.59) vanishes, except the last term. The numerical coefficient in Eq. (7.60) (33.3) is related with the vertical misalignment made by the mask and was obtained by fitting the simulated values with the function $\{\delta_2 + \delta_1\,[1 - \cos(2\theta_{\text{B}})]\}$.

7.5.3 Both vertical misalignment and crystal tilt

Since the mask test is employed in both systematic errors (vertical misalignment and crystal tilts), it is convenient to study the case when both errors occurs simultaneously. As mentioned before, the parallel peak (parameter x_0^{para}) does not depend on vertical misalignment without crystals tilts. In Fig. 7.12 is displayed two plots of the parallel peak difference between lower and upper mask done for several values of crystal tilts and vertical misalignments: (a) is a shift of -6 mm in the entrance

and (b) is for 6 mm. These values correspond to a vertical misalignment , ξ, of -0.17° and 0.17°, respectively. An expression for the parallel peak difference with mask test in second crystal is given by

$$\Delta x^{para}_{\text{mask2}} = -1.82 \times 10^{-3}(\delta_1 + \delta_2)\,(\xi + 1.25)\ , \tag{7.61}$$

where all the angles are in degrees. Once again, the dependence on $(\delta_1 + \delta_2)$ is obtained from the last term of Eq. (7.27) by noting that it is the only non-vanishing term when the difference between a lower and upper mask is made. A shift on the parallel peak indicates that, at least, there are crystal tilts, with or without vertical misalignment. One reason for using the parallel peak for comparing the results of a mask, is because it has much more counts comparing with the antiparallel, so it reduces the statistical error of the fit. However, one needs to experimentally assure that the zero reference of the encoders is stable during the measurements, in order to conclude the existence of crystal tilts. Moreover, the $\delta_1 = -\delta_2$ case can be undetected by using the parallel position or the energy (Eq. (7.60)) with lower statistics. The ratio between the intensities (parameter A of Eq. (7.56)) of the lower and upper cases gives the complementary information for discarding that situation. This check, of course, requires stable X-ray sources during the measurements.

If the crystal reflectivity curve is known, the measured FWHM of the parallel peak can also give the indication if the crystal are aligned and vertically parallel. For the reflectivity given by the XOP, the parallel FWHM without crystal vertical tilts is (9.6±0.4) $\times 10^{-3}$ °. This value corresponds to the FWHM of the instrumental response function, which in energy units is equal to (0.6±0.2) eV. In Fig. 7.13 is represented the parallel FWHM shift as a function of the crystal tilts. This FWHM was obtained from Eq. (7.48) with the fit parameters σ and Γ. We notice that the function shape represented in Fig. 7.13 is approximately related with crystal tilts (values in degrees) by

$$\Delta FWHM^{\text{para}} = 8.64 \times 10^{-4} \times (\delta_1 + \delta_2)^2\ . \tag{7.62}$$

All simulations done shows, assuming a flat crystal, that crystal tilts are the only systematic errors that increases the parallel FWHM value.

The energy difference between the output energy and the input value depends on crystal tilts according to the plot of Fig. 7.14. For values of $\delta_1 \sim -\delta_2$, the output energy is higher than the input one, while for $\delta_1 \sim \delta_2$ is obtained a lower value. The vertical misalignment shifts the surface towards the direction defined by $\delta_1 = \delta_2$. Overall, the saddle shape of the surface in Fig. 7.14 is given approximately by Eq. (7.58) with Eq. (7.59). In conclusion, the results of Eqs. (7.60), (7.61) or (7.62) gives an indication of the amount of crystals tilts and vertical misalignment.

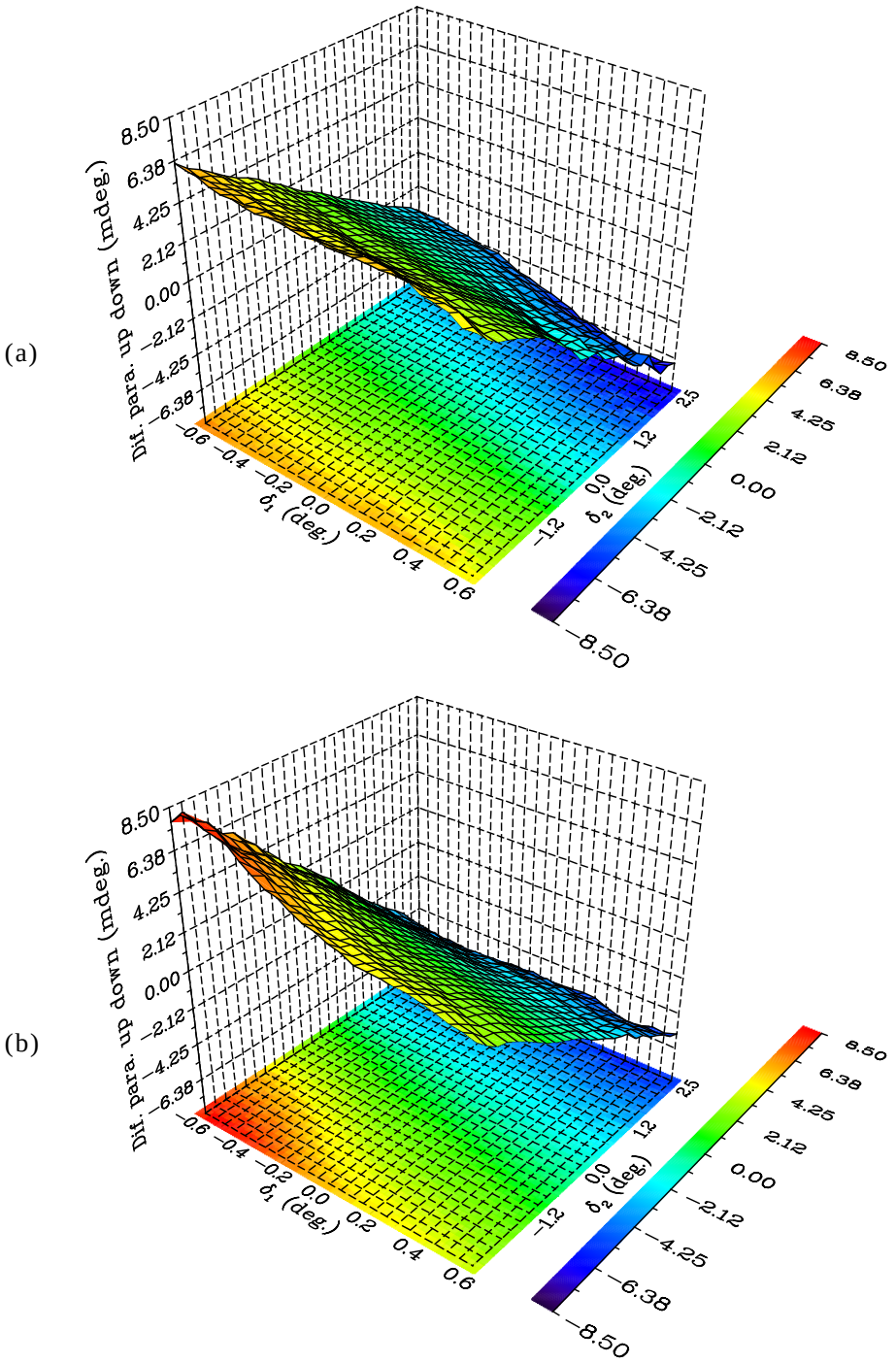

Figure 7.12: Simulation of the parallel peak done for several values of crystal tilts and vertical misalignment - Plot of the parallel peak difference between upper and lower masks for several values of δ_1 and δ_2. a) and b) corresponds to -0.17° and 0.17° vertical misalignment.

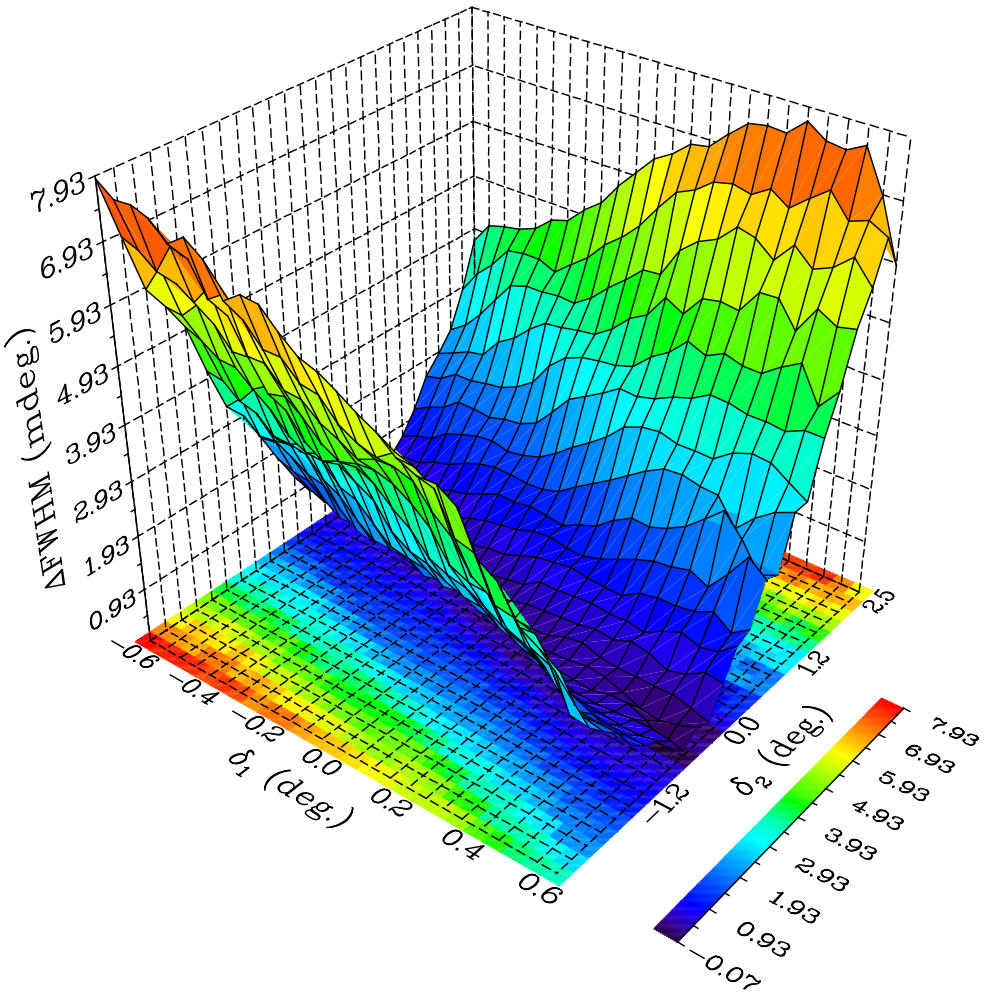

Figure 7.13: Simulation of the parallel FWHM done for several values of crystal tilts - Plot of the parallel FWHM shift from a value with no crystal tilts for several values of δ_1 and δ_2.

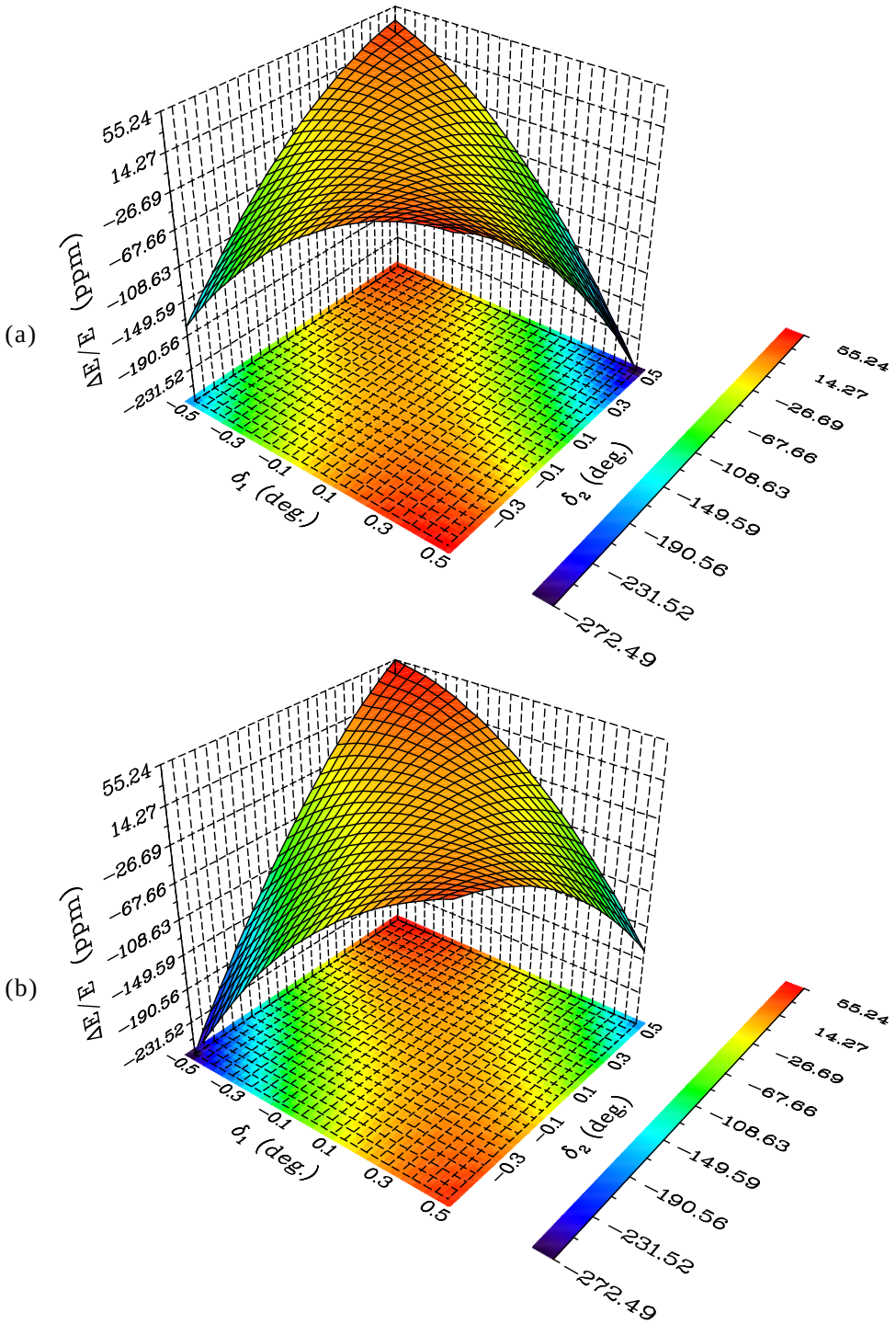

Figure 7.14: Simulation of the energy done for several values of crystal tilts and vertical misalignment - Plot of the energy difference between output and input energy for several values of δ_1 and δ_2. a) is for a vertical misalignment of -0.17° and b) for a 0.17° value.

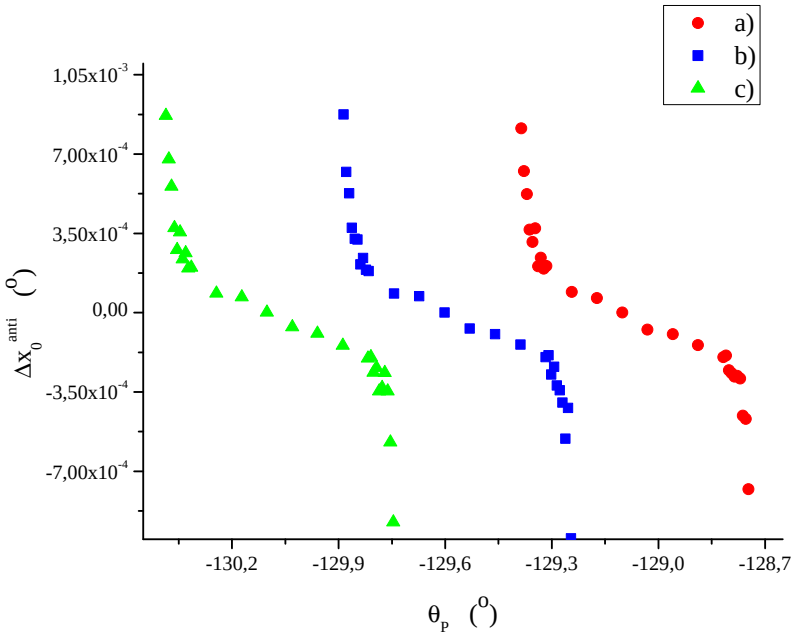

Figure 7.15: Simulation of the antiparallel shift done for several values of first crystal angle - Plot of the antiparallel shift due to horizontal error for several values of first crystal θ_P. (a), (b) and (c) are for the table positions 78.633°, 79.133° and 79.633°, respectively.

7.5.4 Horizontal geometrical error

The horizontal geometrical error is due to a decrease of the ϑ_{max} value, or an increase of the ϑ_{min} value. Since the antiparallel is dispersive, this might cause a shift on the antiparallel peak since one side of the rocking curve will have more counts compared with the other side. This effect can be due to an horizontal misalignment at the entrance collimator, crystals, detector window, or an horizontal misalignment between the table position and the first crystal.

The angular region $[\vartheta_{max}, \vartheta_{min}]$ can obtained by performing a first crystal scan, i.e., by analyzing the parallel and antiparallel rocking curves for several angles of the first crystal. We have simulated this scan taking into account an uniform focal distribution. As in previous Sec. 7.5.3, it was considered a monochromatic approximation on the wavelength distribution and both rocking curves were fitted using Voigt functions (Sec. 7.4.2). In Fig. 7.15 is represented the deviation of the antiparallel peak position (parameter x_0^{anti} of Eq. (7.56)) from its value without horizontal error, for several values of the first crystal and table positions obtained with simulation for the experiment geometry. The effect of horizontal errors is clear on the edges of the green, blue and red lines, where the deviance is higher. The plots (a), (b) and (c) are for table positions 78.633°, 79.133° and 79.633°, respectively, which indicates that this effect is independent of the table position.

For each table position there is an angular region of acceptance of the first crystal angle; outside this region the antiparallel peak is not observed. The angle of acceptance for a source with an uniform distribution and the current geometry is 0.64 °. This angle of acceptance can be also observed in

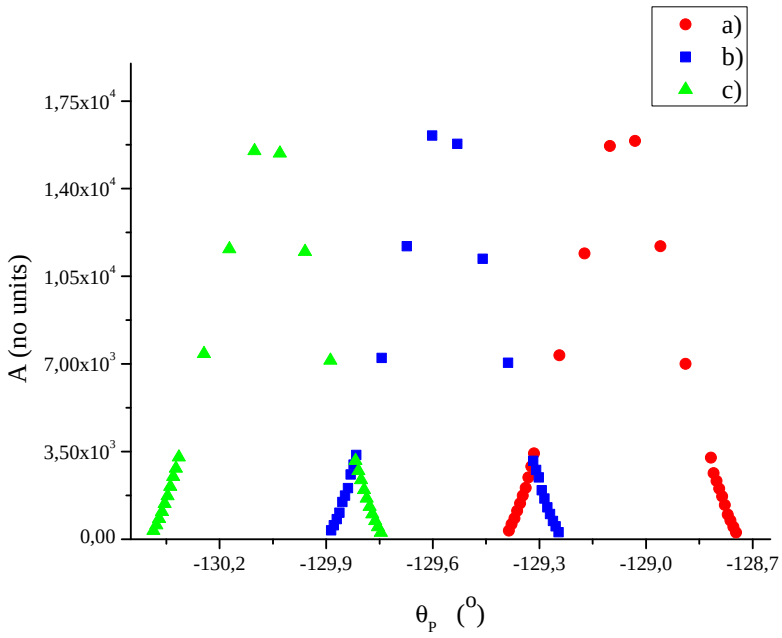

Figure 7.16: Simulation of the antiparallel amplitude done for several values of first crystal angle - Plot of the amplitude for several values of first crystal θ_P. (a), (b) and (c) are for table positions 78.633°, 79.133° and 79.633°, respectively.

Fig. 7.16, where it is represented the amplitude (fitting parameter A of Eq. (7.56)) for the same scan as in Fig. 7.15.

The shift of the antiparallel peak due to this effect also makes a maximum shift in the obtained energy of about 6 ppm.

In conclusion, the horizontal geometrical misalignment can be experimentally avoided by performing a first crystal scan. The measured intensity can be compared with the one of Fig. 7.16 . Then, the first crystal can be set on the optimal value of Fig. 7.15, where there are maximum intensity and minimal horizontal errors.

7.5.5 Crystals bent

The bending of the crystals is another source of geometrical systematic error in thick crystals. In this simulation it was assumed that the surface has a parabolic shape since it is considered that the amount of bending is at least an hundred times smaller then the size of the crystal. This is the first approximation term in a Taylor series considering a symmetric bend on the surface crystal. The surface equation according to this assumption is

$$w = R\left(1 - \left(\frac{y}{y_{\max}}\right)^2\right)\left(1 - \left(\frac{z}{z_{\max}}\right)^2\right), \tag{7.63}$$

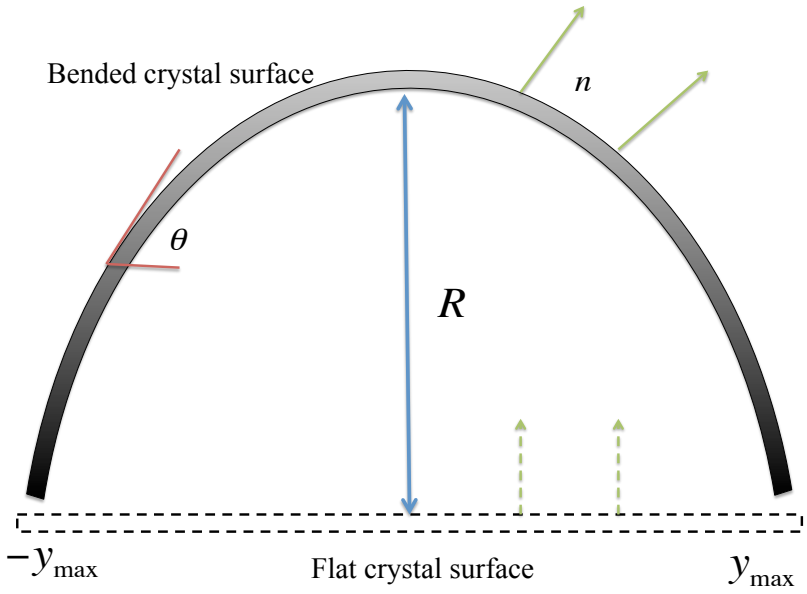

Figure 7.17: Horizontal slice of a bent crystal - The curved black surface is the bent crystal, while the dashed black rectangle is the crystal .

where R describes the amount of bending and the variables y and z are the horizontal and vertical positions on the flat crystal. $2y_{\max}$ and $2z_{\max}$ are the width and the height of the crystal.

This model introduces a rotation on the crystals unitary vectors, $\boldsymbol{n_1}$ and $\boldsymbol{n_2^{\pm}}$ (Eqs. (7.40) and (7.54)) that is dependent of the ray position on the crystal. In Fig. 7.17 is represented a slice of a bent crystal, where is showed the rotation of some unitary vectors (in green) due to the bend. The horizontal rotation that an unitary vector makes with respect to its position, is obtained by noticing that the partial derivative of Eq. (7.63) with respect to y is equal to $\tan(\theta)$, which for the magnitude of R, can be approximately equal to θ.Along with the horizontal rotation, there is also a vertical rotation of the unitary vector. This effect will not be considered since it is a correction in the terms $\varepsilon_1(\phi, \delta_1)$ and $\varepsilon_2^{\pm}\left(\phi, \delta_2^{\pm}\right)$ that already are corrections to the glancing angle. On the other hand, the glancing angle depends linearly (trough θ_C) on the horizontal rotation of the unitary vector.

Simulations show that are two very distinctive indications of the crystals bending. The first indication is a higher value of the parallel FWHM compared with one of a flat surface. Two peaks in the parallel rocking curve can be observed in an extreme case. In Fig. 7.18 is showed some parallel rocking curves obtained for a bent crystal that shows this effect. Each curve was obtained with different first crystal angles, which indicates that in case of a bent crystal, the shape of the parallel curve is dependent of the former variable. In detail, the parallel FWHM obtained after fit, which depends on the shape, is showed in Fig. 7.19 for several first crystal angles. The FWHM of the a), b) and c) rocking curves of Fig. 7.18, are shown at the angles a), b) and c) of Fig. 7.19. Along with the FWHM dependence, in Fig. 7.19 is showed an image plate of the first crystal at the points a), b) and c). Each

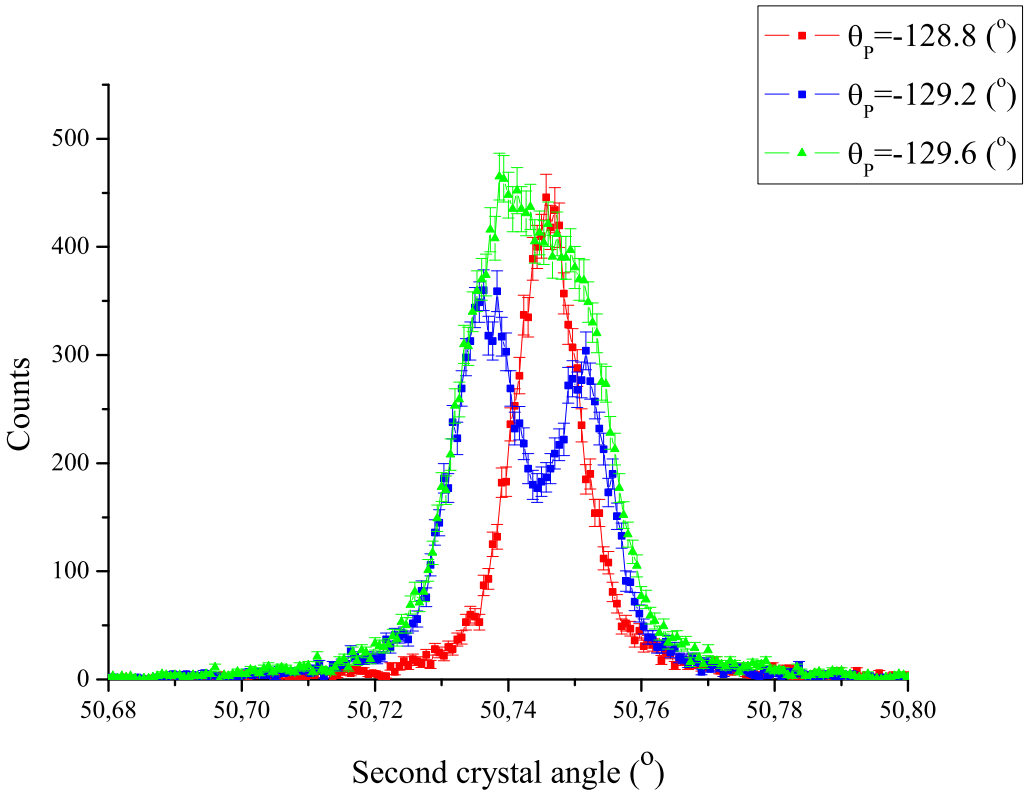

Figure 7.18: Simulated parallel rocking curves with bent crystals - Each curve was obtained with a different first crystal angle. a), b) and c) is for an angle of -129.6°, -129.2° and -128.8°, respectively. Moreover, each curve was shifted by a value equal to the difference between its first crystal angle and the one of b), in order to all curves being at the same position.

of this image plate represents the number of reflected rays at a given (y, z) position at the first crystal. This systematic error depends on the wavelength distribution. The wavelength distribution used in this simulation consists of four energies with equal probability and no broadening. Since this is an uniform distribution, each energy forms a circular spot at the acceptable ellipse of the image plate. This acceptable ellipse is the projection of the circular X-ray spot over the plane with angle θ_C. At the image plate of point a) is showed the ray's reflection position of three energies, where one is at the limit of the acceptable ellipse and the other two overlap at the center. As for the image plate of b) is showed the ray's reflection positions of two energies, while for the case of c), is the ray's reflection position of only one energy. Since with a bended crystal, the normal plane vector depends on the ray position and two different energies that are reflected from different positions on the crystal surface will have an additional difference in the glancing angle. This effect makes the parallel rocking curve being dispersive. As an example, the parallel curve b) in Fig. 7.18 have two peaks since for that first crystal angle and wavelength distribution, there are two reflected energies at different positions on the first crystal surface (see image plate b) of Fig. 7.19).

The simulations presented in Figs. 7.18 and 7.19 were done with a curvature, R, of 1.05 μm in both crystals. The change of the parallel FWHM at the point a) of Fig. 7.19, in function of the

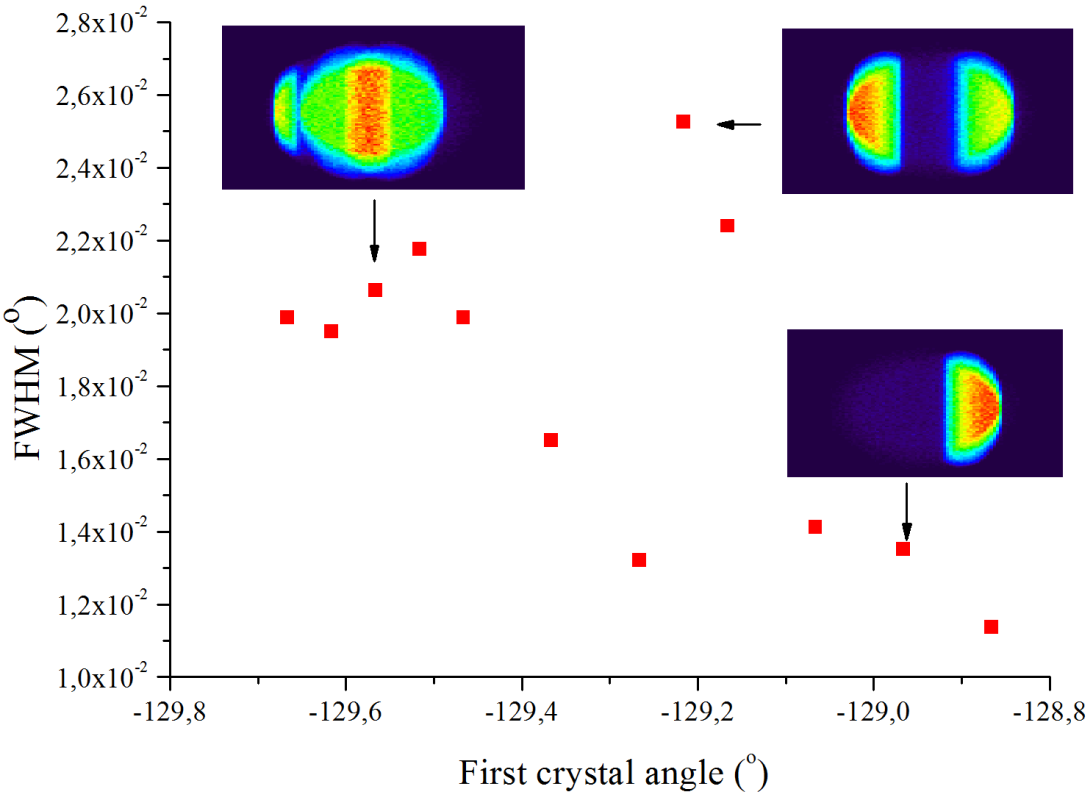

Figure 7.19: Parallel FWHM with a bent crystal for several values of first crystal angle - Along with the plot of the parallel FWHM with the rotation of the first crystal, it is showed image plots at the first crystal surface for several first crystal angles. a), b) and c) is for an angle of -129.6°, -129.2° and -128.8°, respectively.

curvature, is plotted in Fig. 7.20, where shows that for angles less than 0.1 μm, the effect of the bend is not observed. It also shows that the antiparallel FWHM depends much less on curvature than the parallel FWHM.

In conclusion, the systematic error can be experimentally detected by performing a first crystal rotation and observed the parallel FWMH obtained. A dependence of this quantity on the rotation is a clear evidence of a bent crystal.

7.5.6 Crystals miscut

Another systematic error is due to the asymmetric cut of the crystal defined in Sec. 7.1. This error arises can be detected if a crystal has an horizontal asymmetric cut by measuring the parallel peak position before and after turning the crystal up side down with the same face to the X-ray source. Although the parallel shift peak does not give the absolute angle of the miscut plane of the crystal, it gives the relative horizontal angle of the first crystal crystallographic plane with the second one

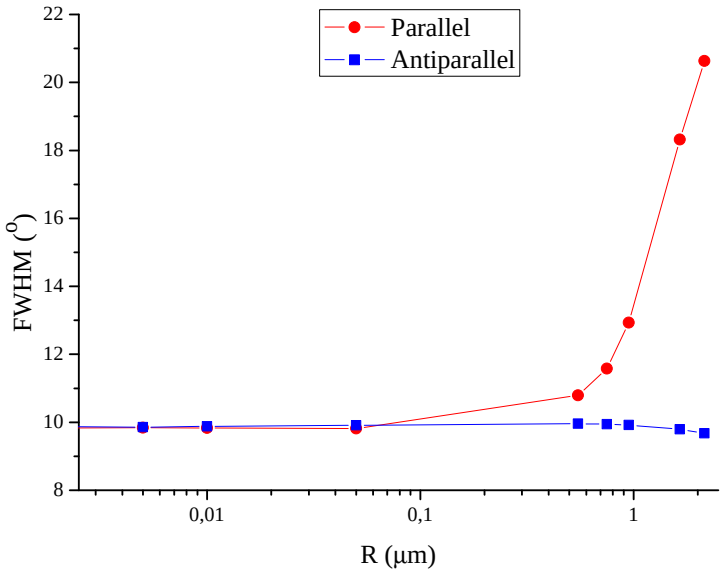

Figure 7.20: Simulation of FWHM done for several curvature values - The red point circle is for the parallel case, while the blue square is for the antiparallel curve.

as a reference. The shift of the parallel peak obtained from this procedure ($\Delta\theta_A$) depends on the asymmetric cut of both crystals as

$$\Delta\theta_A = \theta_{A1} + \theta_{A2} \,, \tag{7.64}$$

where θ_{A1} and θ_{A2} are the asymmetric cut of each crystal. If the crystals are cut from the same wafer, and consider $\theta_{A1} = \theta_{A2} = \theta_A$, then $\Delta\theta_A$ will have values $-2\theta_A$, 0 and $2\theta_A$ depending on the initial orientation of the crystals asymmetric cut to the coordinates system were the parallel peak is defined. Simulations shows that, if the change of the crystal reflectivity with this effect can be neglected (Eqs. (7.6) and (7.7)), then the output energy does not depend on this effect. Both parallel and antiparallel peaks shifts with the same value, as if the first crystal position were in a different position.

If the change of the crystal reflectivity can not being neglected, the width on the parallel and antiparallel rocking curves, $W_{P,AP}$, will be higher compared with the case of no asymmetric cut, $W^0_{P,AP}$. The changes given by

$$\Delta W_{P,AP} = W^0_{P,AP}\left(1 + \frac{\theta_A}{\tan(\theta_B)^2}\right) \,. \tag{7.65}$$

For a θ_B of 39.9° and a θ_A of 0.1°, the change in the width is 0.1 %.

7.5.7 Temperature miscalibrations

As mentioned in Sec. 7.3.2, the inter-planer distance d has a temperature dependence. Besides that, if the temperature originates some geometrical distortion, then, overall, the effect of geometrical change can be traced back to the previous geometrical systematic errors.

The temperature miscalibrations can be divided in two types. The first type is related with a stable, but wrong measurement, i.e., the measured temperature is not the real temperature at the crystal. While the second type of miscalibration consists of measuring the right temperature with instability from the parallel to the antiparallel mode. Simulations shows that, if the temperature is the same during the parallel to antiparallel scans, the d that must be included in Eq. (7.58) comes from Eq. (7.50) with the second crystal temperature. This can be intuitively expected since different temperatures on the first crystal have the same effect as a slightly different first crystal angle and, as discussed in Sec. 7.5.4, has a negligible effect on the obtained energy. If the measured temperature at the second crystal does not corresponds to the real one, then the obtained energy will be wrong by ±2.56 ppm for each degree Celsius bellow/above the true value. The numerical value of 2.56 is related with the lattice coefficient expansion, since $\Delta E/E = \Delta d/d = 2.56 \times 10^{-6}$.

As for the second type of miscalibrations, several simulations were done for temperatures of 20°, 25° and 30° at the first and second crystal in both parallel and antiparallel modes. The temperature used for the evaluation of d in Eq. (7.50), is the second crystal temperature at antiparallel mode. In Fig. 7.21 is plotted the difference between the output and input energy as a function of $T_2^{\text{anti-para}}$, which is the difference between the temperature in antiparallel and parallel modes of the second crystal. It was noticed that the energy difference changes approximately in a linear proportion with $T_2^{\text{anti-para}}$ and has a less dependence on the first crystal temperature. The linear coefficient is ~ 1.23 ppm/ °C.

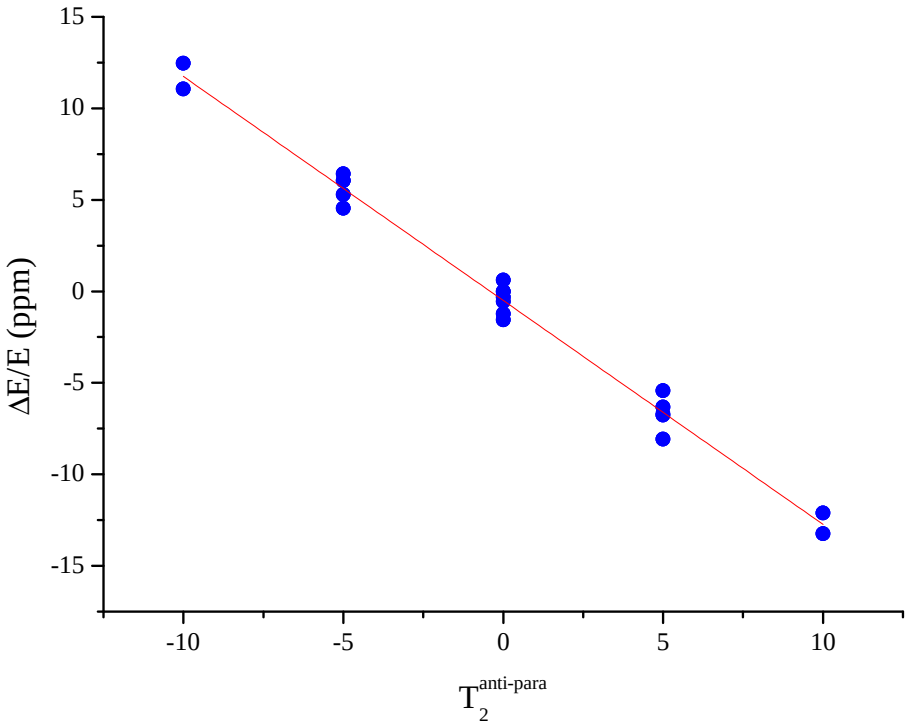

Figure 7.21: Simulation of the energy with different temperatures - Plot of the difference between the output and input energy (ppm) for several values of $T_2^{\text{anti-para}}$, where the last variable is the difference between the temperature in antiparallel and parallel modes.

Chapter 8

Experimental Results on Double Crystal Spectrometer

8.1 Study of Systematic Errors

It is a fact that the first time an experiment is performed, the results have little resemblance with the *true* physical values that an experimentalist pretend to measure. As the experiment is repeated, the instrument, with all it's components, is better understood, thus, leading to successive refinements of technique and method in each iteration. Therefore, the results gradually tends to a level of confidence that can be identified as a reliable description of the physical events or properties.

The DCS at SIMPA is no exception to this pattern. This section is addressed to the study of the systematic errors presented in the first measurements performed with this instrument. The results presented in Sec. 8.2 were obtained after achieving a level of confidence that the results had negligible systematic errors.

In Figs. 8.1 and 8.2 are presented examples of rocking curves obtained in the first measurements. The data of both spectra were acquired by summing individual back-and-forward scans of hundred bins during ten minutes in the parallel case and twenty minutes in the antiparallel case. For the parallel spectrum the number of scans was three, while in the antiparallel case were performed nine scans. The time interval that the second crystal stays in a given angle inside the bin region varies arbitrary from bin to bin, therefore, we measure the number of counts and the time spend in a bin. This is due to instabilities of the stepping motor movement. Therefore, in Figs. 8.1 and 8.2 is plotted the counts per second for each angular bin.

The dispersive antiparallel peak is due to the x rays emitted from the forbidden transition $1s2s^3\mathrm{S}_1 \rightarrow 1s^2\ {}^1\mathrm{S}_0$ in Ar^{16+} [259, 260, 261]. The electron in this transition decays by a metastable $M1$ decay

channel, being the decay natural width several orders smaller than an allowed $E1$ decay channel.

From Fig. 8.1 it is noticeable a larger parallel width compared with the simulated respective one. The agreement between measured and simulated values appears to be better in the antiparallel case. A fit with Voigt functions (Eq. (7.56)) on both sets of experimental data confirms of a possible systematic error. The parameters of the fit are tabulated in Table 8.1 for several measurements. It is evident from this table that the parallel width is larger than the antiparallel one. The fact that experimental antiparallel peak have agreement with simulation, gives an indication that the crystals have a negligible degree of mosaic, which otherwise would increase the width in both peaks.

As mentioned in Sec. 7.2.1.2, both anti- and parallel peaks must have the same width if the antiparallel peak has a narrow natural width (like a monochromatic source) since in that case it reduces to the DCS response function, which is the also the shape of the parallel peak. From the study in Sec. 7.5, we noticed that the systematic errors that could increase the parallel width are either related with the vertical alignment of the crystal, i.e., crystal tilts (Sec. 7.5.3), or with the properties of the crystal itself, like being bended (Sec. 7.5.5), or miscut (Sec. 7.5.6).

The option of the crystals being tilted was checked by doing alignments (Sec. 6.2.3) in different time periods and by the use of the Wyler zerotronic sensor in order to check the verticality and parallelism of the crystals. It was confirmed that the large parallel width was not due to crystals tilts.

Another possible reason for the large width is due to a miscut in the crystals. For that matter, we performed the method suggested in Sec. 7.5.6 in order to identify a possible miscut angle. The result of the measurements is presented in Fig. 8.3, which shows that the parallel peak position before and after several vertical flips of the first or second crystal. The values in Fig. 8.3 were subtracted by the expected value from simulation. The initial measurements given by the black dots indicates that the value of the parallel position is slowly changing with time, which is caused by slow drift of the encoder reference angle. However, the absolute Bragg angle is obtained from the angular difference between the parallel and antiparallel peaks, thus making the obtained Bragg angle independent of the encoder reference angle. The experimental results clearly indicate that the crystals have an horizontal asymmetric cut since whenever one of crystals is flipped the peak position changes by $\sim 0.18^{\circ}$. If both crystal have the same asymmetric cut, the value of the asymmetric angle is $\sim 5.55'$, according to Eq. (7.64), which was much higher than the one assured ($\sim 10''$) by the manufacturer. Therefore, the crystals were send back to that NIST in order to be recutted, etched, and again re-polished. Moreover, after the crystals returned from the manufacturer the same large width remained in the experimental results. Nevertheless, after that procedure there were good agreement between the experimental and simulated parallel positions, which did not changed when the crystals were flipped.

The remained systematic error that could cause the large parallel width was due to a bended crystal. Therefore, the next measurements were addressed to this hypothesis. As mentioned in Sec. 7.5.5, an amount of bending in both crystals makes the parallel peak dependent on the wavelength

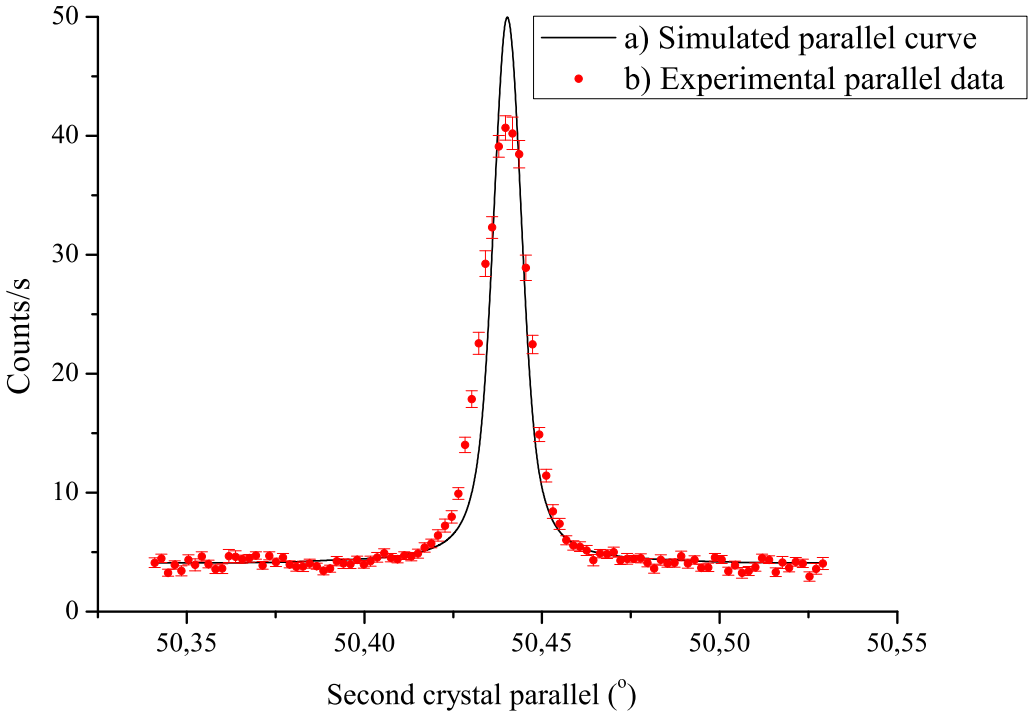

Figure 8.1: Measured parallel rocking curve - Plot of the counts/s for each position of the second crystal angle in parallel mode. The red dots (b) are experimental parallel data, while the black solid line (a) is a simulated profile.

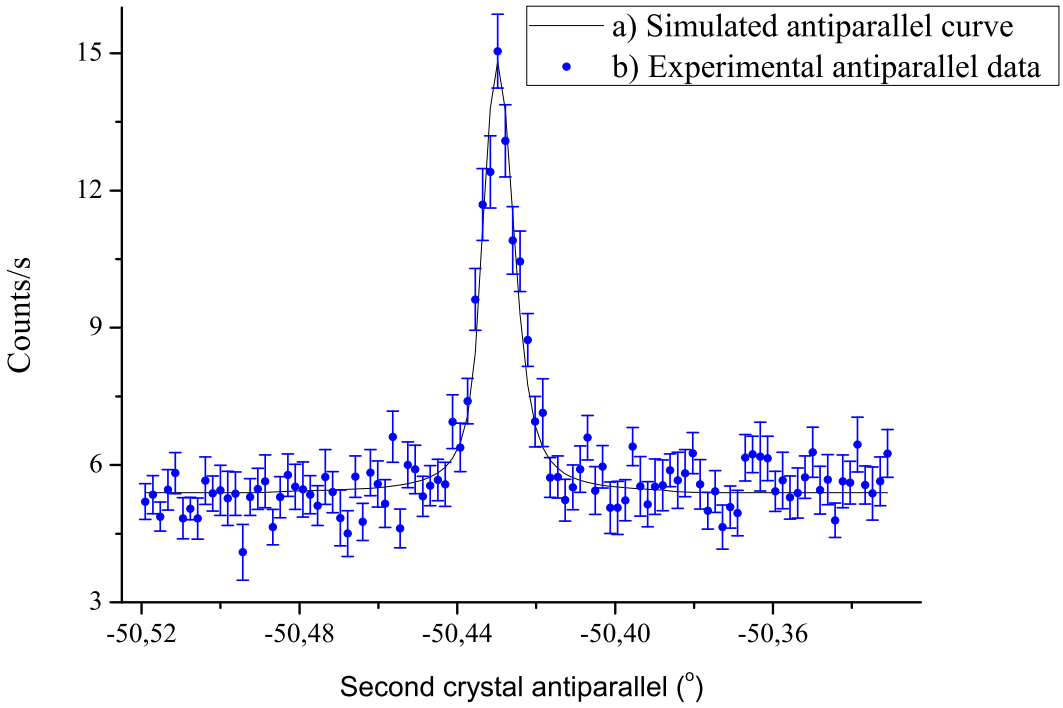

Figure 8.2: Measured antiparallel rocking curve - Plot of the counts/s for each position of the second crystal angle in antiparallel mode. The blue dots (b) are experimental antiparallel data, while the black solid line (a) is a simulated profile.

Parallel			
Intensity (s^{-1})	Position (°)	Total Width (°)	χ^2
28.6±0.7	50.44035±1.5(-4)	1.57(-2)± 9.7(-4)	1.46
35.1±0.7	50.44039±1.2(-4)	1.53(-2)± 8.7(-4)	1.41
23.9±0.7	50.44001±1.6(-4)	1.58(-2)± 7.7(-4)	1.12
42.8±0.8	50.44012±1.0(-4)	1.54(-2)±1.25(-3)	1.21
Antiparallel			
Intensity (s^{-1})	Position (°)	Total Width (°)	χ^2
7.8± 0.5	-50.42476± 3.1(-4)	1.10(-2)±6.4(-3)	1.08
4.5± 0.2	-50.42497± 2.2(-4)	1.01(-2)±7.1(-3)	1.00
5.0± 0.3	-50.42549± 2.8(-4)	1.05(-2)±5.5(-3)	1.14
9.1± 0.2	-50.42496± 1.4(-4)	1.16(-2)±2.6(-3)	1.06

Table 8.1: Parameters after fitting experimental data - Parameter obtained after fitting measured rocking curves with Voigt functions. These fits were performed on preliminary measurements.

distribution accepted by the first crystal. Moreover, this wavelength distribution depends on first crystal angle. Thus, in Fig. 8.4 is shown a plot of the measured parallel width for several values of the first crystal angle. Since the width decreases with the first crystal angle, we have an indication that the crystal was somehow bended. Moreover, in Fig. 8.5 is shown a parallel rocking curve for a given first crystal angle, where it seems to have two peaks. The simulations present in Sec. 7.5.5, shows an estimative of the bending in both crystals of $\sim 1.0\ \mu$m for such case. This was due to the back metal screws that were pressing the crystals to the supports. They were replaced by elastic nylon screws. After this procedure, we checked that the parallel width was independent of the first crystal angle, with a value equal to the antiparallel width and to the value of the response function. The result of this procedure is shown in Fig. 8.6, where is plotted the parallel width for several values of first crystal. In Fig. 8.7 is presented an example of a parallel spectrum. The fit was performed with a simulated profile and the agreement between that profile and the experimental data is very good with a reduced $\chi^2 \approx 1.2$, showing a good experimental setting, a good model of experiment and a near perfect quality of the crystals.

Once the parallel and antiparallel widths were understandable, we check if the system had some temperature miscalibration. In order to track the right temperature at the crystal surface, we measured the temperature at the crystal surface and at the point of the heater. The result of this procedure is shown in Fig. 8.8. Starting at 22.5 °C, we increased the temperature of the heater sensor so that the temperature at the crystal surface goes from 22.5 °C to 30 °C with two or three degrees steps in each hour. We noticed that the temperature difference between the two sensors could reach 50 °C, which indicates a bad thermal contact of the sensors. This problem was fixed using a pressing mechanism of the sensor towards the crystal surface. As a result, it were observed maximum variations of 0.5 °C.

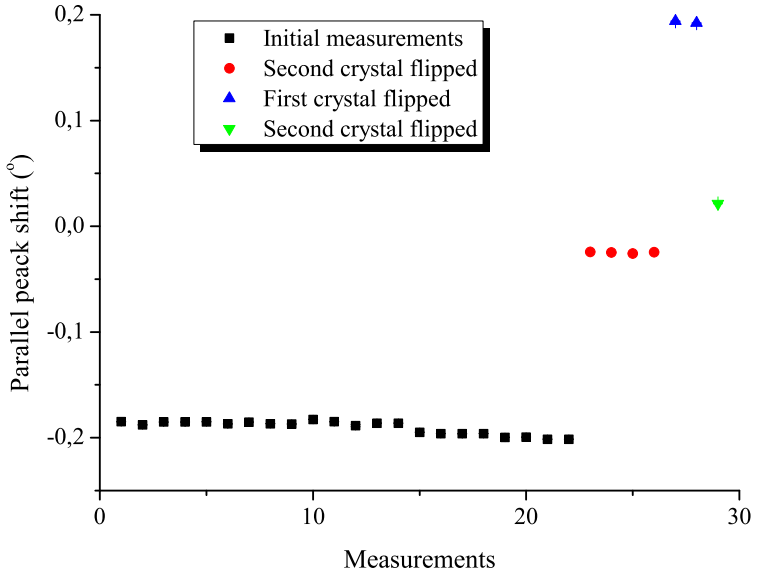

Figure 8.3: Measured parallel peak position - Plot of the measured parallel shift for several measurements. The value of a measured position was subtracted by the one expected from simulation. The first measurements are shown by the black squares. The results after flipping the second crystal are shown by red dots. The blue dots are after the first crystal being flipped and the last green point is for another flip of the second crystal.

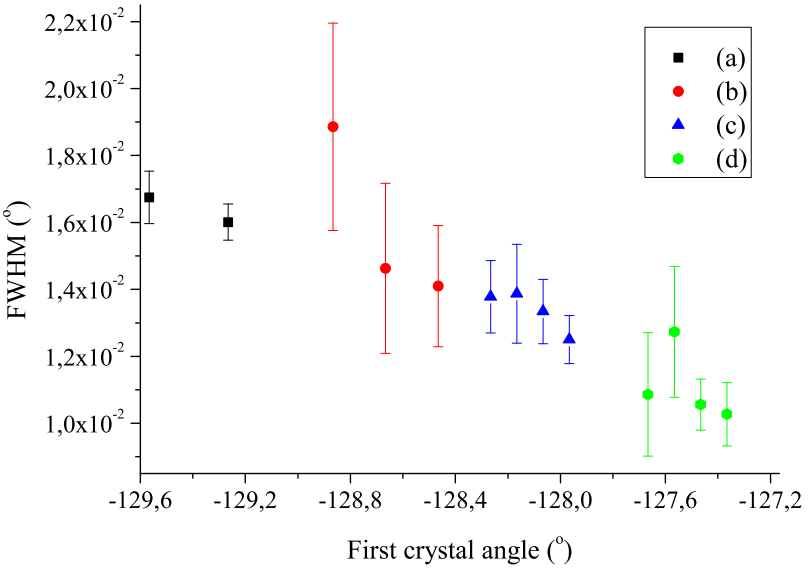

Figure 8.4: Parallel FWHM of measured rocking curves - Plot of the measured parallel FWHM with several values of first crystal angle. The points a) to d) correspond to different table positions with an unknown angle.

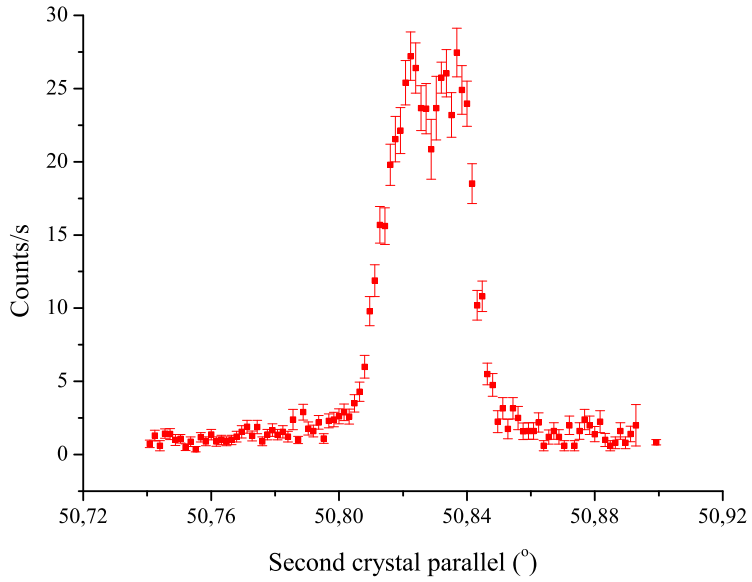

Figure 8.5: Parallel rocking curve for first crystal angle of -129.17^o - Plot of the counts/s for each position of the second crystal angle in parallel mode. Scan performed for a first crystal angle of 129.17^o.

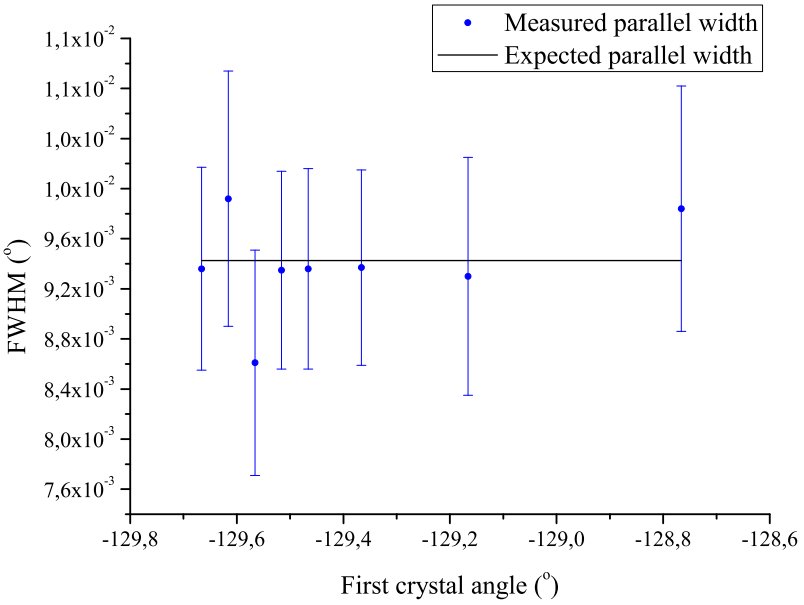

Figure 8.6: Parallel FWHM of measured rocking curves - Plot of the measured parallel FWHM with several values of first crystal.

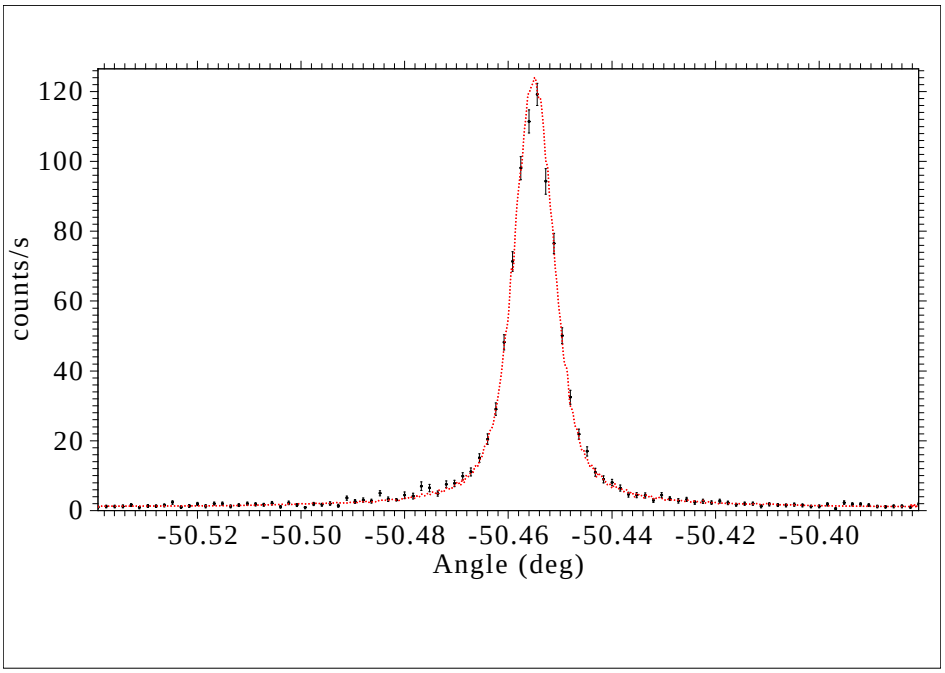

Figure 8.7: Parallel spectrum - Parallel spectrum made at a first crystal position optimized for the $M1$ with a acquisition time of 943 s.

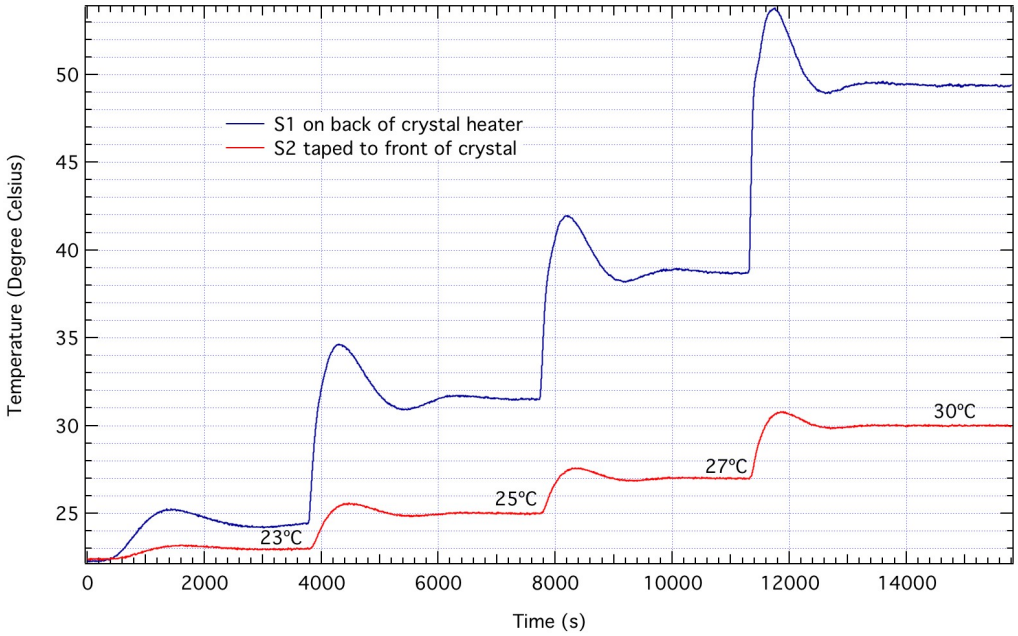

Figure 8.8: Temperature at different parts of crystal and support - The blue line corresponds to a temperature measurement at the second crystal heater, while the red line corresponds to the temperature at the second crystal surface. The measurement was performed in order to do two or three degrees steps at the crystal surface in each hour.

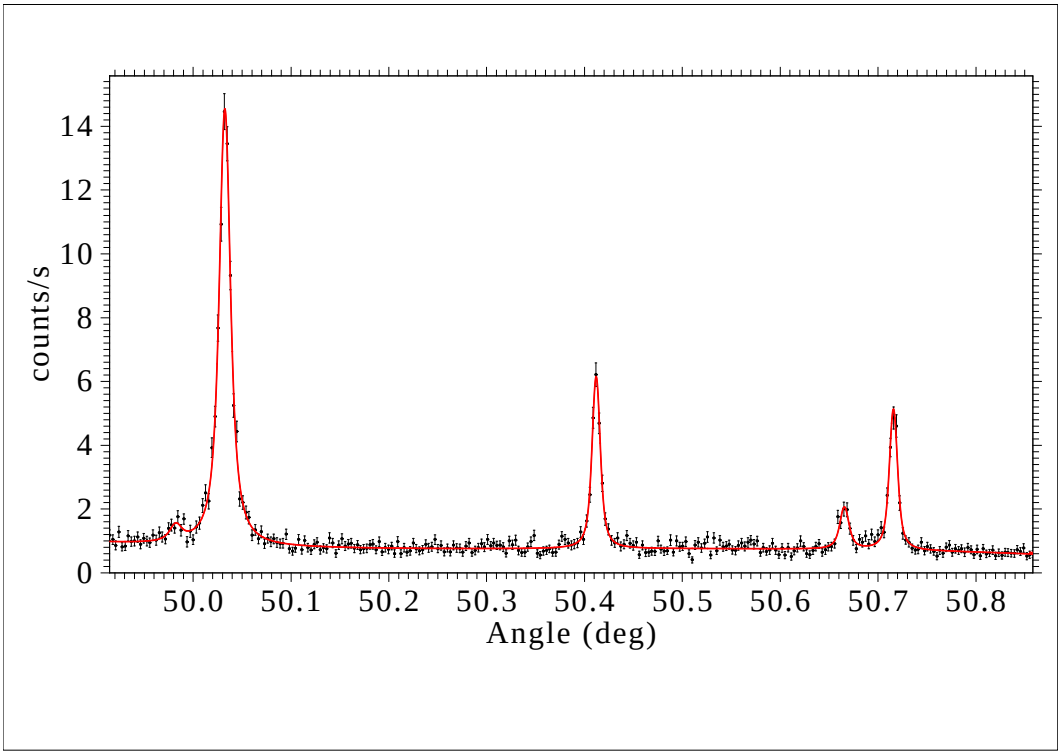

Figure 8.9: Experimental antiparallel rocking curve - The three lines corresponds to (left to right in plot): $1s^2 2s^2 2p\ ^1\mathrm{P}_1 \rightarrow 1s^2 2s^2\ ^1\mathrm{S}_0$ in Be-like Ar (Ar^{14+}); $1s2s\ ^3\mathrm{S}_1 \rightarrow 1s^2\ ^1\mathrm{S}_0$ $M1$ transition of He-like Ar (Ar^{16+}); and $1s2s2p\ ^2\mathrm{P}_{1/2,\ 3/2} \rightarrow 1s^2 2s\ ^2\mathrm{S}_{1/2}$ in Li-like Ar (Ar^{15+}).

In Fig. 8.9, we present the measured antiparallel rocking curves obtained with the DCS after checking for systematic errors. The angular region in the antiparallel rocking curve (Fig. 8.9) was chosen in a way that the spectrum includes peaks corresponding to transition energies of atomic transitions in Ar^{14+} (Be-like) , Ar^{15+} (Li-like) and Ar^{16+} (He-like) ions.

The highest peak on the left side of the spectrum (Fig. 8.9) corresponds to the transition $1s^2 2s^2 2p\ ^1\mathrm{P}_1 \rightarrow 1s^2 2s^2\ ^1\mathrm{S}_0$ of Be-like Ar (Ar^{14+}), while the centered one is the $1s2s\ ^3\mathrm{S}_1 \rightarrow 1s^2\ ^1\mathrm{S}_0$ $M1$ transition of He-like Ar (Ar^{16+}), as showed with better resolution in Fig. 8.10. The double peak on the right side of the spectrum corresponds to the doublet $1s2s2p\ ^2\mathrm{P}_{1/2,\ 3/2} \rightarrow 1s^2 2s\ ^2\mathrm{S}_{1/2}$ of Li-like Ar (Ar^{15+}). A detailed analysis of the obtained energies and widths of the allowed transitions is underway [257].

All the figures with rocking curves, presented in this section, clearly shows that the ECRIS provides high enough intensities for precision measurements of transitions in HCI with a DCS. The red line in Fig. 8.9 corresponds to simulated rocking curves fitted to the measured spectra. The fit of the simulated spectra to the measured data indicates very good agreement between the experiment and a simulation done for the *ideal* alignment of the spectrometer components.

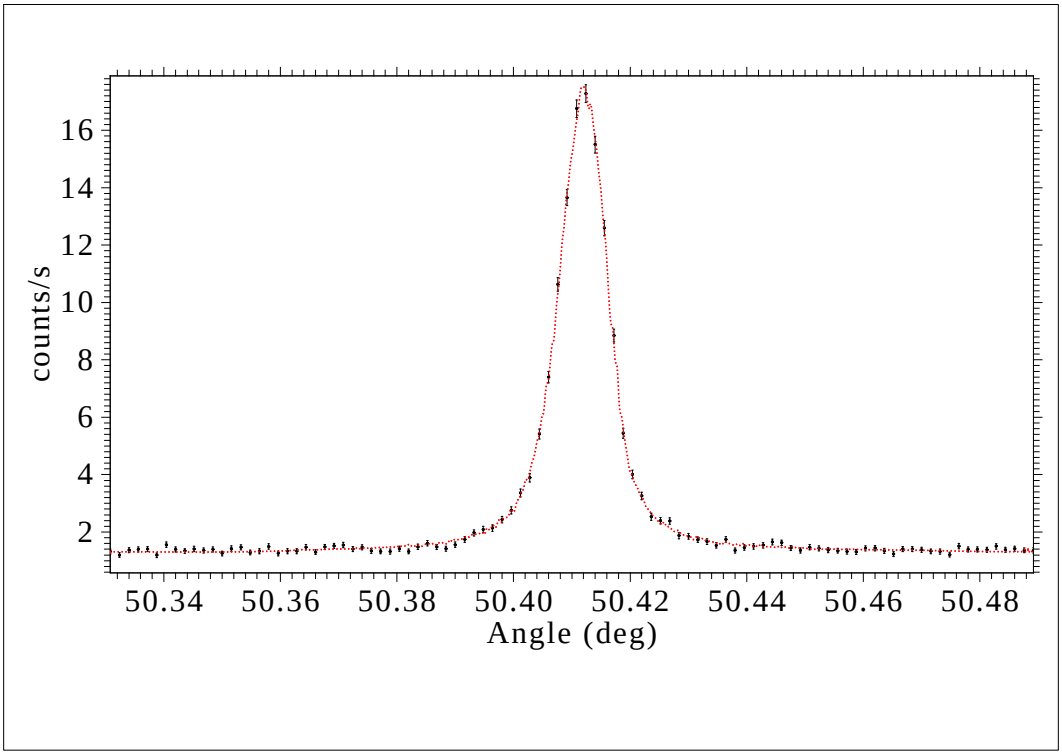

Figure 8.10: Antiparallel spectrum - Antiparallel spectrum made at a first crystal position optimized for the $M1$ with a acquisition time of 18239 s).

8.2 $1s2s\ ^3S_1 \rightarrow 1s^2\ ^1S_0$ in He-like Ar

In Fig. 8.10 is plotted a spectrum that corresponds to the $1s2s\ ^3S_1 \rightarrow 1s^2\ ^1S_0$ $M1$ transition with high statistics. The width of this spectrum has a slightly higher value than respective one of the parallel spectrum in Fig. 8.7. Since the antiparallel spectrum is dispersive, this additional amount of width comes from additional broadening of the wavelength distribution compared with a monochromatic source. The $M1$ transition has a negligible natural width, therefore, the observation of an additional broadening on the antiparallel side must then come from the Doppler effect. We found a Doppler broadening of 80.5(4.6) meV (FWHM) by averaging the gaussian width obtained by fitting a total of thirteen recorded spectra with simulated profiles corresponding to different widths and minimizing the χ^2. As for the fit parameter of the peak position, because of the slight asymmetry of the real profile (see discussion in Sec. 7.4.2), a small shift between the parameter obtained from simulation and Voigt profile is observed. This corresponds to a 14 meV (4.6 ppm) energy shift. To our knowledge, this is the first time that such a shift is observed and it has never been taken into account in previous X-ray standard measurements reported in the latest X-ray energy tables [199]. This sensitivity to the small asymmetry of the line is unique and due to the very small width of the $M1$ line.

Two different analyses of the experimental data were performed. In one, a Voigt profile was fitted to both experimental antiparallel and parallel spectra, as well as to high statistic simulated spectra. The experimental energy was then deduced from the energy used as input in the simulation. In the

Contribution	Value (eV)
Fit and extrapolation	0.0044
Angle encoder error	0.0036
Lattice spacing error	0.00012
Index of refraction	0.0016
Coefficient of thermal expansion	0.00019
X-ray polarization	0.00100
Energy-wavelength correction [90]	0.000078
Temperature (0.5°C)	0.0040
Total	0.0072

Table 8.2: Experimental uncertainty - Contributions to the uncertainty on the $1s2s\ ^3S_1 \rightarrow 1s^2\ ^1S_0$ $M1$ transition energy measurement (68 % confidence interval).

second method, the simulated profiles were directly used to fit the experimental lines and obtain the Bragg angle from which the line energy was obtained. Both methods provided the same result to high accuracy. The dependance of the measured transition energy on temperature is shown on Fig. 8.11. Weighted one- and two-parameter linear fits have been performed. The difference between the value at 22.5 °C obtained with those fits are combined to get an estimate of systematic errors. The list of contributions to the uncertainty is shown in Table 8.2. The uncertainty is limited by statistics, angle and temperature measurements.

The measured value for the $M1$ transition energy is 3104.1605(71) eV with an accuracy of 2.3 ppm. The comparison with theoretical results is shown in Table 8.3. The theoretical result of *Artemyev et. al.* [3] is 1.7σ below the experimental value. The list of contributions included in [3] and their uncertainty is also shown in Table 8.3. Our experimental accuracy is 0.7 % of the one-electron QED corrections, and 7.4 % of the self-energy correction to the electron-electron interaction. The finite size correction represents 2.7 ppm of the transition energy, barely larger than our uncertainty. Its uncertainty cannot influence the comparison between theory and experiment in this case.

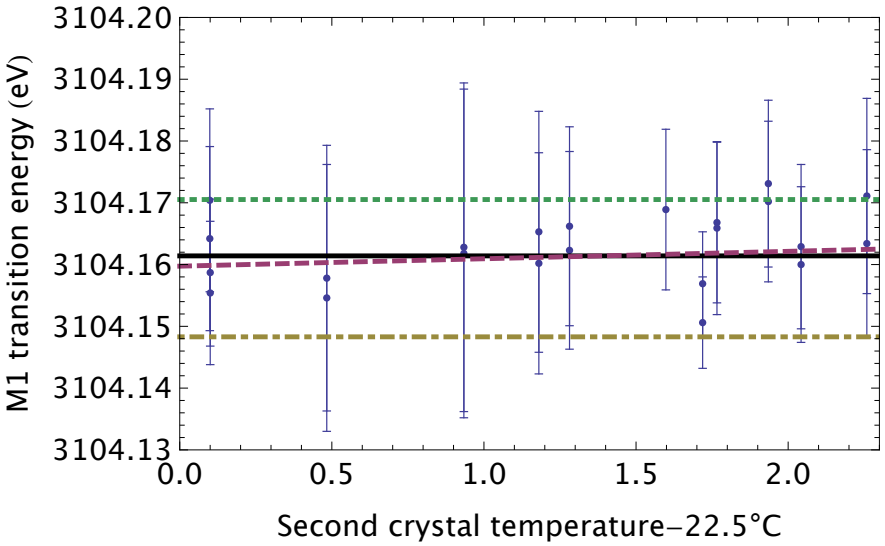

Figure 8.11: $M1$ transition energy - One and two parameter extrapolation of the $M1$ transition energy to the standard temperature (22.5 °C). Solid line: one parameter extrapolation, dashed line: two parameter extrapolation, dot-dashed line: Ref. [3], dotted line: MCDF calculation (see Table 8.3).

Contribution	$1s^2\,{}^1S_0$	$1s2s\,{}^3S_1$	Transition
Dirac	-4427.4154 (3)	-1108.0563	3319.3591 (3)
$\Delta E_{\rm int}$	305.6560	91.3873	-214.2687
$\Delta E^{\rm QED}_{\rm 1el}$	1.1310 (1)	0.1525	-0.9785 (1)
$\Delta E^{\rm QED}_{\rm 2el}$:			
Scr. SE	-0.1116	-0.0154	0.0962
Scr. VP	0.0072	0.0010	-0.0062
2-ph.exch.	0.0091 (1)	-0.0004 (1)	-0.0095 (2)
$\Delta E^{\rm QED}_{\rm ho}$	0.0009	0.0003	-0.0006
$\Delta E_{\rm rec}$	0.0575	0.0141	-0.0434
Total [3]	-4120.6653 (4)	-1016.5169 (1)	3104.1484 (4)
MCDF [257]			3104.171
Drake [262]			3104.138
RMBPT [2]			3104.189
RMBPT [18]			3104.06(19)
Experiment			3104.1605 (71)

Table 8.3: Comparison between theoretical and experimental values - Comparison between the levels $1s^2\,{}^1S_0$, $1s2s\,{}^3S_1$ and the measured transition energy (eV). Individual contributions are from Ref. [3]. Older calculations are updated for fundamental constants [90]. The MCDF calculation follows the procedure of Refs. [8, 263].

Chapter 9

Conclusion

An *ab initio* simulation based on the spectrometer geometry of the experiment was presented, which was compared with the most recent experiments and good agreement was found between them. These first measurements were performed in order to find possible misalignment in the system and within the statistics considered the alignment proved itself correct.

Due to the geometrical properties of the DCS, high precision measurements of X-ray transition energies in highly charge ions can be performed without external reference. These high precision measurements can enable direct tests of the QED theory in middle Z elements and can provide new X-ray standards based on narrow transitions of highly charged ions. It was demonstrated that the ECRIS has the necessary intensity for performing accurate measurements of HCI with a DCS.

We have performed the most accurate and absolute measurement of a X-ray transition energy in HCI and the total QED contribution (Table 8.3) was tested with an accuracy of 0.8 %.The Doppler broadening of the observed X-ray lines was calculated to be about 80 meV.

With this experiment we have established the first X-ray standard based on a narrow, symmetric line, that can be used to calibrate any instrument in the few KeV range to our quoted accuracy, without the problems associated with X-ray tubes based standards.

This system enables the investigation of core-excited ions with three and four electrons, namely the correlation and Auger shifts. Thanks to the well understood line shape of the DCS, it will be possible to obtain the intrinsic width of these transitions to a few percent accuracy. This will allow to study radiative and Auger contributions to the transition rate. In the future, with the use of higher performance ECRIS (larger plasma and higher electronic densities), improvements in the temperature controls and angle measurements accuracy of the DCS, it will be possible to obtain X-ray energies accuracy below 1 ppm and to perform measurements on heavier elements.

References

[1] G. Breit and E. Teller. **Metastability of Hydrogen and Helium Levels**. *Astrophys. J.*, **91**:215, 1940. 1, 2, 7

[2] D. R. Plante, W. R. Johnson, and J. Sapirstein. **Relativistic all-order many-body calculations of the $n = 1$ and $n = 2$ states of heliumlike ions**. *Phys. Rev. A*, **49**(5):3519, 1994. 1, 164

[3] A. N. Artemyev, V. M. Shabaev, V. A. Yerokhin, G. Plunien, and G. Soff. **QED calculation of the $n = 1$ and $n = 2$ energy levels in He-like ions**. *Phys. Rev. A*, **71**(6):062104, 2005. 1, 163, 164

[4] W. R. Johnson and G. Soff. **The Lamb Shift in Hydrogen-like Atoms, $1 \leq Z \leq 110$**. *At. Data Nucl. Data Tables*, **33**:405, 1985. 1, 14

[5] M. H. Chen, K. T. Cheng, and W. R. Johnson. **Relativistic configuration-interaction calculations of $n = 2$ triplet states of heliumlike ions**. *Phys. Rev. A*, **47**(5):3692, 1993. 1

[6] W. R. Johnson and J. Sapirstein. **Relativistic many-body perturbation theory applied to $n = 2$ triplet states of heliumlike ions**. *Phys. Rev. A*, **46**(5):R2197, 1992. 2

[7] J. Hata and I. P. Grant. **MCDF calculations of wavelenghts and radiative lifetimes in helium-like ions**. *J. Phys. B*, **14**:2111–2114, 1981. 2

[8] P. Indelicato. **Multiconfiguration Dirac-Fock Calculations of Transition Energies in Two Electron Ions with $10 < Z < 92$**. *Nucl. Instrum. and Meth. Phys. B*, **31**:14, 1988. 2, 77, 93, 164

[9] J. P. Desclaux. **A Multiconfiguration Relativistic Dirac-Fock Program**. *Comp. Phys. Commun.*, **9**:31–45, 1975. 2, 77, 93

[10] G. W. F. Drake. **Theory of relativistic Magnetic Dipole Transitions: Lifetime of the Metastable 2^3S of the Heliumlike Ions**. *Phys. Rev. A*, **3**(3):908–915, 1971. 2

[11] W. R. Johnson. **Radiative Decay Rates of Metastable One-Electron Atoms**. *Phys. Rev. Lett.*, **29**(17):1123–1126, 1972. 2

[12] J. P. Santos, F. Parente, and P. Indelicato. **Application of B-splines finite basis sets to relativistic two-photon decay rates of $2s$ level in hydrogenic ions**. *Eur. Phys. J. D*, **3**(1):43–52, 1998. 2, 8, 30, 34, 54

[13] J. G. Li, P. Jönsson, G. Gaigalas, and C. Z. Dong. **Hyperfine induced $1s2s\ ^1\mathrm{S}_0 \rightarrow 1s^2\ ^1\mathrm{S}_0$ $M1$ transition of He-like ions**. *Eur. Phys. J. D*, **51**(3):313–317, 2009. 2

[14] A. Derevianko and W. R. Johnson. **Two-photon decay of $2\ ^1\mathrm{S}_0$ and $2\ ^3\mathrm{S}_1$ states of heliumlike ions**. *Phys. Rev. A*, **56**(2):1288–1294, 1997. 3, 92, 93

[15] S. Trotsenko, A. Kumar, A. V. Volotka, D. Banaś, H. F. Beyer, H. Bräuning, S. Fritzsche, A. Gumberidze, S. Hagmann, S. Hess, P. Jagodziński, C. Kozhuharov, R. Reuschl, S. Salem, A. Simon, U. Spillmann, M. Trassinelli, L. C. Tribedi, G. Weber, D. Winters, and T. Stöhlker. **Spectral Shape of the Two-Photon Decay of the $2^1\mathrm{S}_0$ State in He-Like Tin**. *Phys. Rev. Lett.*, **104**(3):033001, 2010. 3, 9

[16] A. H. Gabriel and C. Jordan. **Helium-like ion forbidden line emission from the sun**. *Phys. Lett. A*, **32**(3):166–167, 1970. 3

[17] A. H. Gabriel and C. Jordan. **Long Wavelength Satellites to the He-like Ion Resonance Lines in the Laboratory and in the Sun**. *Nature*, **221**(5184):947–949, 1969. 3

[18] E. Lindroth and S. Salomonson. **Relativistic calculation of the $2^3\mathrm{S}_1 - 1\ ^1\mathrm{S}_0$ magnetic dipole transition rate and transition energy for heliumlike Argon**. *Phys. Rev. A*, **41**(9):4659–4669, 1990. 3, 39, 164

[19] P. Indelicato. **Correlation and Negative Continuum effects for the relativistic $M1$ transtion in two-electron ions using the multiconfiguration Dirac-Fock method**. *Phys. Rev. Lett.*, **77**(16):3323–3326, 1996. 3, 34, 39

[20] W. R. Johnson, D. R. Plante, and J. Sapirstein. **Relativistic Calculations of Transition Amplitudes in the Helium Isoelectronic Sequence**. *Advances In Atomic, Molecular, and Optical Physics*, **Volume 35**:255–329, 1995. 3

[21] M. Mizushima. **$\Delta S = \pm 1$ Magnetic Quadrupole Radiative Transitions in Atoms and Molecules**. *J. Phys. Soc. Jpn.*, **21**:2335, 1966. 3

[22] R. H. Garstang. **Magnetic-quadrupole radiation and solar coronal de-excitation**. *Astr. Soc. Paci.*, **81**:488–495, 1969. 3

[23] P. Indelicato, F. Parente, and R. Marrus. **Effect of the hyperfine structure on the 2^3P_1 and the 2^3P_0 lifetime in heliumlike ions**. *Phys. Rev. A*, **40**(7):3505–3514, 1989. 3

[24] W. R. Johnson, K. T. Cheng, and D. R. Plante. **Hyperfine structure of 2^3P levels of helium-like ions**. *Phys. Rev. A*, **55**(4):2728–2742, 1997. 3

[25] R. Marrus and P. J. Mohr. **Forbiden Transitions in One- and Two-Electron Atoms**. *Adv. At. Mol. Phys.*, **14**:181–224, 1978. 3

[26] E. Träbert. **In pursuit of highly accurate atomic lifetime measurements of multiply charged ions**. *J. Phys. B*, **43**(7):074034, 2010. 3

[27] M. Göppert-Mayer. **Über Elementarakte mit zwei Quantensprüngen**. *Ann. Phys.*, **401**:273–294, 1931. 7

[28] J. L. Spitzer and J. L. Greenstein. **Continuous Emission from Planetary Nebulae**. *Astrophys. J.*, **114**:407, 1951. 7, 55, 68

[29] J. Shapiro and G. Breit. **Metastability of $2s$ States of Hydrogenic Atoms**. *Phys. Rev.*, **113**(1):179, 1959. 7

[30] S. Seager, D. D. Sasselov, and D. Scott. **A New Calculation of the Recombination Epoch**. *Astrophys. J. Lett.*, **523**(1):L1–L5, 1999. 7

[31] J. Chluba and R. A. Sunyaev. **Induced two-photon decay of the $2s$ level and the rate of cosmological hydrogen recombination**. *Astron. Astrophys.*, **446**:39–42, 2006. 8

[32] C. Schwob, L. Jozefowski, B. de Beauvoir, L. Hilico, F. Nez, L. Julien, F. Biraben, O. Acef, J. J. Zondy, and A. Clairon. **Optical Frequency Measurement of the 2S-12D Transitions in Hydrogen and Deuterium: Rydberg Constant and Lamb Shift Determinations**. *Phys. Rev. Lett.*, **82**(25):4960, 1999. 8, 88

[33] B. de Beauvoir, C. Schwob, O. Acef, L. Jozefowski, L. Hilico, F. Nez, L. Julien, A. Clairon, and F. Biraben. **Metrology of the hydrogen and deuterium atoms: Determination of the Rydberg constant and Lamb shifts**. *Eur. Phys. J. D*, **12**(1):61–93, 2000. 8, 9

[34] H. Gould and R. Marrus. **Lamb shift and the lifetime of the $2^2S_{1/2}$ state of hydrogenlike argon ($Z = 18$)**. *Phys. Rev. A*, **28**(4):2001–2025, 1983. 8

[35] W. Perrie, A. J. Duncan, H. J. Beyer, and H. Kleinpoppen. **Polarization Correlation of the Two Photons Emitted by Metastable Atomic Deuterium: A Test of Bell's Inequality**. *Phys. Rev. Lett.*, **54**(16):1790, 1985. 8

[36] A. Aspect, J. Dalibard, and G. e. Roger. **Experimental Test of Bell's Inequalities Using Time- Varying Analyzers**. *Phys. Rev. Lett.*, **49**(25):1804, 1982. 8

[37] T. Tsujibayashi, M. Itoh, J. Azuma, M. Watanabe, O. Arimoto, S. Nakanishi, H. Itoh, and M. Kamada. **Two-Photon Spectroscopy of Core Excitons in Barium Fluoride Using Synchrotron Radiation and Laser Light**. *Phys. Rev. Lett.*, **94**(7):076401, 2005. 8

[38] P. T. C. So, C. Y. Dong, B. R. Masters, and K. M. Berland. **Two-Photon Excitation Fluorescence Microscopy**. *Annu. Rev. Biomed. Eng.*, **2**(1):399–429, 2000. 8

[39] S. Fujiyoshi, M. Fujiwara, and M. Matsushita. **Visible Fluorescence Spectroscopy of Single Proteins at Liquid-Helium Temperature**. *Phys. Rev. Lett.*, **100**(16):168101, 2008. 8

[40] M. A. Bouchiat and C. Bouchiat. **Parity violation induced by weak neutral currents in atomic physics. part II**. *J. Phys.*, **36**(6):493–509, 1975. 8

[41] M. A. Bouchiat and C. Bouchiat. **I. Parity violation induced by weak neutral currents in atomic physics**. *J. Phys.*, **35**(12):899–927, 1974. 8

[42] E. G. Drukarev and A. N. Moskalev. **Parity Nonconservation Effects in 2-Photon Transitions in Hydrogen-Atom**. *JETP*, **73**(6):2060–2066, 1977. 8, 54

[43] M. Maul, A. Schäfer, W. Greiner, and P. Indelicato. **Prospects for Parity-nonconservation Experiments with Highly Charged Heavy Ions**. *Phys. Rev. A*, **53**(6):3915–3925, 1996. 8

[44] D. R. Dounas-Frazer, K. Tsigutkin, D. English, and D. Budker. **Atomic parity violation in $J = 0 \to 0$ two-photon transitions**. *Phys. Rev. A*, **84**(2):023404, 2011. 8

[45] A. Schäfer, G. Soff, P. Indelicato, B. Müller, and W. Greiner. **Prospects for an atomic parity-violation experiment in U^{90+}**. *Phys. Rev. A*, **40**(12):7362–7365, 1989. 8

[46] L. Labzowsky and A. Prozorov. **Parity Nonconservation Effects in the Highly Charged Ions**. *J. Phys.: Conf. Ser.*, **72**:012010, 2007. 8

[47] S. Weinberg. **A Model of Leptons**. *Phys. Rev. Lett.*, **19**(21):1264, 1967. 8

[48] J. C. Pati and A. Salam. **Unified Lepton-Hadron Symmetry and a Gauge Theory of the Basic Interactions**. *Phys. Rev. D*, **8**(4):1240, 1973. 8

[49] M. G. Kozlov, D. English, and D. Budker. **Symmetry-suppressed two-photon transitions induced by hyperfine interactions and magnetic fields**. *Phys. Rev. A*, **80**(4):042504, 2009. 8

[50] D. English, V. V. Yashchuk, and D. Budker. **Spectroscopic Test of Bose-Einstein Statistics for Photons**. *Phys. Rev. Lett.*, **104**(25):253604, 2010. 8

[51] E. Lamour, C. Prigent, B. Eberhardt, J. P. Rozet, and D. Vernhet. **2E1 Ar^{17+} decay and conventional radioactive sources to determine efficiency of semiconductor detectors**. *Rev. Sci. Instrum.*, **80**(2):023103, 2009. 8

[52] C. Szymanowski, V. Véniard, R. Taïeb, and A. Maquet. **Relativistic calculation of two-photon bound-bound transition amplitudes in hydrogenic atoms**. *Phys. Rev. A*, **56**(1):700, 1997. 9, 30, 88

[53] J. H. Tung, X. M. Ye, G. J. Salamo, and F. T. Chan. **Two-photon decay of hydrogenic atoms**. *Phys. Rev. A*, **30**(3):1175–1184, 1984. 9, 76, 77, 82, 84

[54] S. Klarsfeld. **Radiative Decay of Metastable Hydrogenic Atoms**. *Phys. Lett.*, **30A**:382, 1969. 9

[55] V. Florescu. **Two-photon emission in the $3s \to 1s$ and $3d \to 1s$ tranitions of hydrogen-like atoms**. *Phys. Rev. A*, **30**(5):2441–2448, 1984. 9

[56] X. Mu and B. Crasemann. **Two-Photon Transitions in Atomic Inner Shells: A Relativistic self-consistent-field calculation with applications to Mo, Ag, and Xe**. *Phys. Rev. A*, **38**(9):4585–4596, 1988. 9

[57] X.-M. Tong, J.-M. Li, L. Kissel, and R. H. Pratt. **Two-photon transitions in atomic inner shell: Relativistic and atomic-screening effects**. *Phys. Rev. A*, **42**(3):1442–14491, 1990. 9

[58] A. Surzhykov, P. Koval, and S. Fritzsche. **Angular correlations in the two-photon decay of hydrogenlike ions: Relativistic Green's-function approach**. *Phys. Rev. A*, **71**(2):022509, 2005. 9, 30, 42, 68

[59] L. N. Labzowsky, A. V. Shonin, and D. A. Solovyev. **QED calculation of $E1M1$ and $E1E2$ transition probabilities in one-electron ions with arbitrary nuclear charge**. *J. Phys. B*, **38**(3):265, 2005. 9, 35, 39, 40, 53, 54, 55, 66, 67

[60] S. P. Goldman and G. W. F. Drake. **Relativistic two-photon decay rates of $2s_{1/2}$ hydrogenic ions**. *Phys. Rev. A*, **24**(1):183–191, 1981. 9, 24, 28, 53, 67, 85

[61] H. M. T. Nganso and M. G. K. Njock. **Use of Dirac-Coulomb Sturmians of the first order for relativistic calculations of two-photon bound-bound transition amplitudes in hydrogen-like ions**. *J. Phys. B*, **40**(5):807, 2007. 9

[62] A. V. Volotka, A. Surzhykov, V. M. Shabaev, and G. Plunien. **Interelectronic-interaction effects on the two-photon decay rates of heavy He-like ions**. *Phys. Rev. A*, **83**(6):062508, 2011. 9

[63] F. Fratini, M. C. Tichy, T. Jahrsetz, A. Buchleitner, S. Fritzsche, and A. Surzhykov. **Quantum correlations in the two-photon decay of few-electron ions**. *Phys. Rev. A*, **83**(3):032506, 2011. 9, 10

[64] F. Fratini, S. Trotsenko, S. Tashenov, T. Stöhlker, and A. Surzhykov. **Photon-photon polarization correlations as a tool for studying parity nonconservation in heliumlike uranium**. *Phys. Rev. A*, **83**(5):052505, 2011. 9, 10, 69

[65] M. Fischer, N. Kolachevsky, M. Zimmermann, R. Holzwarth, T. Udem, T. W. Hänsch, M. Abgrall, J. Grünert, I. Maksimovic, S. Bize, H. Marion, F. P. D. Santos, P. Lemonde, G. Santarelli, P. Laurent, A. Clairon, C. Salomon, M. Haas, U. D. Jentschura, and C. H. Keitel. **New Limits on the Drift of Fundamental Constants from Laboratory Measurements**. *Phys. Rev. Lett.*, **92**(23):230802, 2004. 9

[66] M. Niering, R. Holzwarth, J. Reichert, P. Pokasov, T. Udem, M. Weitz, T. W. Hänsch, P. Lemonde, G. Santarelli, M. Abgrall, P. Laurent, C. Salomon, and A. Clairon. **Measurement of the Hydrogen 1S- 2S Transition Frequency by Phase Coherent Comparison with a Microwave Cesium Fountain Clock**. *Phys. Rev. Lett.*, **84**(24):5496, 2000. 9, 88

[67] C. G. Parthey, A. Matveev, J. Alnis, B. Bernhardt, A. Beyer, R. Holzwarth, A. Maistrou, R. Pohl, K. Predehl, T. Udem, T. Wilken, N. Kolachevsky, M. Abgrall, D. Rovera, C. Salomon, P. Laurent, and T. W. Hänsch. **Improved Measurement of the Hydrogen $1S - 2S$ Transition Frequency**. *Phys. Rev. Lett.*, **107**(20):203001, 2011. 9

[68] D. J. Bamford, L. E. Jusinski, and W. K. Bischel. **Absolute two-photon absorption and three-photon ionization cross sections for atomic oxygen**. *Phys. Rev. A*, **34**(1):185, 1986. 9

[69] S. Kröll and W. K. Bischel. **Two-photon absorption and photoionization cross-section measurements in the $5p^5 6p$ configuration of xenon**. *Phys. Rev. A*, **41**(3):1340, 1990. 9

[70] C. Dorrer, F. Nez, B. de Beauvoir, L. Julien, and F. Biraben. **Accurate Measurement of the $2^3\mathbf{S}_1 - 3^3\mathbf{D}_1$ Two-Photon Transition Frequency in Helium: New Determination of the $2^3\mathbf{S}_1$ Lamb Shift**. *Phys. Rev. Lett.*, **78**(19):3658–3661, 1997. 9

[71] C. Eichhorn, S. Fritzsche, S. Löhle, A. Knapp, and M. Auweter-Kurtz. **Time-resolved fluorescence spectroscopy of two-photon laser-excited 8p, 9p, 5f, and 6f levels in neutral xenon**. *Phys. Rev. E*, **80**(2):026401, 2009. 9

[72] G. Doumy, C. Roedig, S. K. Son, C. I. Blaga, A. D. DiChiara, R. Santra, N. Berrah, C. Bostedt, J. D. Bozek, P. H. Bucksbaum, J. P. Cryan, L. Fang, S. Ghimire, J. M. Glownia, M. Hoener, E. P. Kanter, B. Krässig, M. Kuebel, M. Messerschmidt, G. G. Paulus, D. A. Reis, N. Rohringer, L. Young, P. Agostini, and L. F. DiMauro. **Nonlinear Atomic Response to Intense Ultrashort X Rays**. *Phys. Rev. Lett.*, **106**(8):083002, 2011. 10

[73] P. Shaw, U. Arp, A. Henins, and S. Southworth. **X-ray polarization detector (abstract)**. *Rev. Sci. Instrum.*, **67**(9), 1996. 10

[74] S. Fritzsche, P. Indelicato, and T. Stöhlker. **Relativistic quantum dynamics in strong fields: photon emission from heavy, few-electron ions**. *J. Phys. B*, **38**(9):S707, 2005. 10, 101

[75] S. Tashenov, T. Stöhlker, D. Banaś, K. Beckert, P. Beller, H. F. Beyer, F. Bosch, S. Fritzsche, A. Gumberidze, S. Hagmann, C. Kozhuharov, T. Krings, D. Liesen, F. Nolden, D. Protic, D. Sierpowski, U. Spillmann, M. Steck, and A. Surzhykov. **First Measurement of the Linear Polarization of Radiative Electron Capture Transitions**. *Phys. Rev. Lett.*, **97**(22):223202, 2006. 10

[76] Th. Stöhlker, U. Spillmann, D. Banaś, H. F. Beyer, J. Cl. Dousse, S. Chatterjee, S. Hess, C. Kozhuharov, M. Kavcic, T. Krings, D. Protić, R. Reuschl, J. Szlachetko, S. Tashenov, and S. Trotsenko. **A 2D position sensitive germanium detector for spectroscopy and polarimetry of high-energetic x-rays**. *J. Phys.: Conf. Ser.*, **58**(1):411, 2007. 10

[77] P. Amaro, A. Surzhykov, F. Parente, P. Indelicato, and J. P. Santos. **Calculation of two-photon decay rates of hydrogen-like ions by using B-polynomials**. *J. Phys. A: Math. Theor.*, **44**(24):245302, 2011. 11

[78] A. Surzhykov, J. P. Santos, P. Amaro, and P. Indelicato. **Negative-continuum effects on the two-photon decay rates of hydrogenlike ions**. *Phys. Rev. A*, **80**(5):052511, 2009. 11, 34

[79] P. Amaro, J. P. Santos, F. Parente, A. Surzhykov, and P. Indelicato. **Resonance effects on the two-photon emission from hydrogenic ions**. *Phys. Rev. A*, **79**(6):062504, 2009. 11, 34, 85

[80] A. Surzhykov, P. Indelicato, J. P. Santos, P. Amaro, and S. Fritzsche. **Two-photon absorption of few-electron heavy ions**. *Phys. Rev. A*, **84**(2):022511, 2011. 12, 42

[81] J. P. Santos. *Radiative and Non-Radiative relativistic Transitions in Atomic Systems*[1]. PhD thesis, Faculdade de Ciências e Tecnologia da Universidade Nova de Lisboa, 1998. 12, 54

[82] H. A. Bethe and E. E. Salpeter. *Quantum Mechanics of One- and Two-Electron Atoms*. Springer-Verlag, Berlin, 1957. 12, 17

[83] W. Greiner. *Relativistic Quantum Mechanics*. Springer-verlag, Berlin, 1990. 12, 13, 17, 33, 40

[84] M. Weissbluth. *Atoms and Molecules*. Academic Press, New York, 1978. 12, 92

[85] A. I. Akhiezer and V. B. Berestetskii. *Quantum Electrodynamics*. Interscience Publishers, New York, 1965. 12, 17, 18, 19, 20, 22, 23, 24, 27, 54, 82

[86] P. A. M. Dirac. **The Quantum Theory of the Electron**. *Proc. R. Soc. London, Ser. A*, **117**(778):610–624, 1928. 12

[1] No URL found

[87] P. A. M. Dirac. **The Quantum Theory of the Electron. Part II**. *Proc. R. Soc. London, Ser. A*, **118**(779):351–361, 1928. 12

[88] O. Klein. **Quantentheorie und fünfdimensionale Relativitätstheorie**. *Z. Phys. A*, **37**(12):895–906, 1926. 12

[89] W. Gordon. **Der Comptoneffekt nach der Schrödingerschen Theorie**. *Z. Phys. A*, **40**(1):117–133, 1926. 12

[90] P. J. Mohr, B. N. Taylor, and D. B. Newell. **CODATA recommended values of the fundamental physical constants: 2006**. *Rev. Mod. Phys.*, **80**(2):633, 2008. 12, 54, 101, 132, 163, 164

[91] J. D. Jackson. *Classical Electrodynamics*. John Wiley & Sons, New York, 1975. 13, 24

[92] D. M. Brink and G. R. Satchler. *Angular momentum*. Clarendon Press, New York, 1994. 14, 24, 47, 51, 52

[93] P. A. M. Dirac. **A Theory of Electrons and Protons**. *Proc. R. Soc. London, Ser. A*, **126**(801):360–365, 1930. 16

[94] C. D. Anderson. **The Positive Electron**. *Phys. Rev. A*, **43**:491494, 1933. 16

[95] W. E. Lamb and R. C. Retherford. **Fine Structure of the Hydrogen Atom by a Microwave Method**. *Phys. Rev.*, **72**(3):241, 1947. 17

[96] H. A. Bethe. **The Electromagnetic Shift of Energy Levels**. *Phys. Rev.*, **72**(4):339, 1947. 17

[97] P. J. Mohr. **Self-Energy Radiative Corrections in Hydrogen-Like Systems**. *Ann. Phys.*, **88**:26–51, 1974. 18

[98] G. Soff and P. J. Mohr. **Vacuum polarization in a strong external field**. *Phys. Rev. A*, **38**(10):5066–5075, 1988. 18

[99] I. Goidenko, L. Labzowsky, A. Nefiodov, G. Plunien, and G. Soff. **Second-Order Electron Self-Energy in Hydrogenlike Ions**. *Phys. Rev. Lett.*, **83**(12):2312–2315, 1999. 18

[100] G. Plunien, T. Beier, G.Soff, and H. Persson. **Exact two-loop vacuum polarization correction to the Lamb shift in hydrogenlike ions**. *Eur. Phys. J. D*, **1**:177–185, 1997. 18

[101] P. Beiersdorfer. **Testing QED and atomic-nuclear interactions with high- Z ions**. *J. Phys. B*, **43**(7):074032, 2010. 18

[102] V. M. Shabaev. **Rayleigh-Schrödinger perturbation theory for a relativistic atom**. *Theor. Math. Phys.*, **82**(1):57–62, 1990. 18

[103] A. N. Artemyev, T. Beier, G. Plunien, V. M. Shabaev, G. Soff, and V. A. Yerokhin. **Vacuum-polarization screening corrections to the energy levels of heliumlike ions**. *Phys. Rev. A*, **62**(2):022116, 2000. 18

[104] P. J. Mohr and J. Sapirstein. **Evaluation of two-photon exchange graphs for excited states of highly charged heliumlike ions**. *Phys. Rev. A*, **62**:052501, 2000. 18

[105] P. Indelicato and P. J. Mohr. **Coordinate-space approach to the bound-electron self-energy: Self-energy screening calculation**. *Phys. Rev. A*, **63**(5):052507, 2001. 18

[106] R. P. Feynman. **The theory of positrons**. *Phys. Rev.*, **76**(6):749–768, 1949. 19

[107] R. P. Feynman. **Space-Time Approach to Quantum Electrodynamics**. *Phys. Rev.*, **76**(6):769, 1949. 19

[108] S. Tomonaga. **On a Relativistically Invariant Formulation of the Quantum Theory of Wave Fields**. *Prog. Theor. Phys.*, **1**, 1946. 19

[109] J. Schwinger. **Quantum Electrodynamics. I. A Covariant Formulation**. *Phys. Rev.*, **74**(10):1439–1461, 1948. 19

[110] J. Schwinger. **Quantum Electrodynamics. II. Vacuum Polarization and Self-energy**. *Phys. Rev.*, **75**(4):651–679, 1949. 19

[111] J. Schwinger. **Quantum Electrodynamics. III. The electromagnetic properties of the electronradiative corrections to scattering**. *Phys. Rev.*, **76**(6):790–817, 1949. 19

[112] F. J. Dyson. **The S Matrix in Quantum Electrodynamics**. *Phys. Rev.*, **75**(11):1736, 1949. 19

[113] I. P. Grant. **Gauge invariance and relativistic radiative transitions**. *J. Phys. B*, **7**(12):1458–1475, 1974. 26, 28, 47, 49

[114] R. A. Swainson and G. W. F. Drake. **A unified treatment of the non-relativistic and relativistic hydrogen atom II: the Green functions**. *J. Phys. A: Math. Gen.*, **24**(1):95, 1991. 30

[115] A. Maquet, V. e. Véniard, and T. A. Marian. **The Coulomb Green's function and multiphoton calculations**. *J. Phys. B*, **31**(17):3743, 1998. 30

[116] J. Sapirstein and W. R. Johnson. **The use of basis splines in theoretical atomic physics**. *J. Phys. B*, **29**(22):5213, 1996. 30, 34

[117] O. Zatsarinny and K. Bartschat. **B-spline Breit-Pauli R-matrix calculations for electron collisions with neon atoms**. *J. Phys. B*, **37**(10):2173, 2004. 30

[118] H. Bachau, E. Cormier, P. Decleva, J. E. Hansen, and F. Martin. **Applications of B -splines in atomic and molecular physics**. *Rep. Prog. Phys.*, **64**(12):1815, 2001. 30

[119] C. W. A. Fletcher. *Computational Galerkin Methods*. Springer, New York, 1984. 31

[120] W. R. Johnson, S. Blundell, and J. Sapirstein. **Finite Basis sets for Dirac equation constructed from B splines**. *Phys. Rev. A*, **37**(2):307–315, 1988. 31, 33, 34

[121] E. Anderson, Z. Bai, C. Bischof, S. Blackford, J. Demmel, J. Dongarra, J. D. Croz, A. Greenbaum, S. Hammarling, A. McKenney, and D. Sorensen. *LAPACK Users' Guide*. Society for Industrial and Applied Mathematics, Philadelphia, 1999. 32

[122] S. P. Goldman. **Variational representation of the Dirac-Coulomb Hamiltonian with no spurious roots**. *Phys. Rev. A*, **31**(6):3541, 1985. 33

[123] A. Igarashi. **B-Spline Expansions in Radial Dirac Equation**. *J. Phys. Soc. Jpn.*, **75**:114301, 2006. 33

[124] K. Beloy and A. Derevianko. **Application of the dual-kinetic-balance sets in the relativistic many-body problem of atomic structure**. *Comp. Phys. Commun.*, **179**(5):310–319, 2008. 33

[125] I. P. Grant. **B-spline methods for radial Dirac equations**. *J. Phys. B*, **42**(5):055002, 2009. 33

[126] V. M. Shabaev, I. I. Tupitsyn, V. A. Yerokhin, G. Plunien, and G. Soff. **Dual Kinetic Balance Approach to Basis-Set Expansions for the Dirac Equation**. *Phys. Rev. Lett.*, **93**(13):130405, 2004. 33, 34

[127] A. Chodos, R. L. Jaffe, K. Johnson, C. B. Thorn, and V. W. Weisskopf. **New extended model of hadrons**. *Phys. Rev. D*, **9**(3471), 1974. 33

[128] C. de Boor. *A Pratical Guide to Splines*. Springer-Verlag, New York, 1978. 34, 35

[129] W. R. Johnson, M. Idrees, and J. Sapirstein. **Second-order energies and third-order matrix elements of alkali-metal atoms**. *Phys. Rev. A*, **35**(8):3218, 1987. 34

[130] C. F. Fischer and W. Guo. **Spline algorithms for the hartree-fock equation for the helium ground state**. *J. Comput. Phys.*, **90**(2):486–496, 1990. 34

[131] C. F. Fischer and M. Idrees. **Spline algorithms for continuum functions**. *Comput. Phys.*, **3**(3):53–58, 1989. 34

[132] Y. Qiu and C. F. Fischer. **Integration by Cell Algorithm for Slater Integrals in a Spline Basis**. *J. Comput. Phys.*, **156**(2):257–271, 1999. 34

[133] M. I. Bhatti, K. D. Coleman, and W. F. Perger. **Static polarizabilities of hydrogen in the B-spline basis set**. *Phys. Rev. A*, **68**(4):044503, 2003. 34

[134] P. Indelicato. **Projection operators in Multiconfiguration Dirac-Fock calculations: Application to the ground state of heliumlike ions.** *Phys. Rev. A*, **51**(2):1132–1145, 1995. 34

[135] B. R. Gelbaum. *Modern Real and Complex Analysis*. Wiley-Interscience, New York, 1995. 35

[136] D. D. Bhatta and M. I. Bhatti. **Numerical solution of KdV equation using modified Bernstein polynomials**. *Appl. Math. Comput.*, **174**(2):1255–1268, 2006. 35

[137] M. I. Bhatti and P. Bracken. **Solutions of differential equations in a Bernstein polynomial basis**. *J. Comput. Appl. Math.*, **205**(1):272–280, 2007. 35, 38

[138] S. Bhattacharya and B. N. Mandal. **Use of Bernstein polynomials in numerical solutions of Volterra integral equations**. *Appl. Math. Sci.*, **2**(33-36):1773–1787., 2008. 35

[139] M. I. Bhatti and W. F. Perger. **Solutions of the radial Dirac equation in a B-polynomial basis**. *J. Phys. B*, **39**(3):553, 2006. 35

[140] J. J. Sakurai. *Advanced Quantum Mechanics*. Addison-Wesley, Reading, 1967. 39

[141] M. Boca and V. Florescu. **Relativistic effects in the time evolution of an one-dimensional model atom in a laser pulse**. *Eur. Phys. J. D*, **46**(1):15–20, 2008. 39

[142] S. Selsto, E. Lindroth, and J. Bengtsson. **Solution of the Dirac equation for hydrogenlike systems exposed to intense electromagnetic pulses**. *Phys. Rev. A*, **79**(4):043418, 2009. 39

[143] A. Derevianko, I. M. Savukov, W. R. Johnson, and D. R. Plante. **Negative-energy contributions to transition amplitudes in heliumlike ions**. *Phys. Rev. A*, **58**(6):4453, 1998. 39

[144] L. Borowska, A. Surzhykov, T. Stöhlker, and S. Fritzsche. **Angular correlations in the two-photon decay of aligned hydrogenlike ions**. *Phys. Rev. A*, **74**(6):062516, 2006. 42

[145] V. V. Balashov, A. N. Grum-Grzhimailo, and N. M. Kabachnik. *Polarization and Correlation Phenomena in Atomic Collisions*. Springer, Verlag, 2000. 42, 43

[146] R. W. Dunford, E. P. Kanter, B. Krässig, S. H. Southworth, L. Young, P. H. Mokler, and T. Stöhlker. **Two-photon decay in gold atoms following photoionization with synchrotron radiation**. *Phys. Rev. A*, **67**:054501, 2003. 44

[147] F. Low. **Natural Line Shape**. *Phys. Rev.*, **88**(1):53, 1952. 44

[148] J. Chluba and R. A. Sunyaev. **Two-photon transitions in hydrogen and cosmological recombination**. *Astron. & Astrophys.*, **480**(3):629–645, 2008. 44

[149] C. M. Hirata. **Two-photon transitions in primordial hydrogen recombination**. *Phys. Rev. D*, **78**(2):023001, 2008. 44

[150] G. W. F. Drake. **Energy level calculations and $E1M1$ two photon transition rates in two electron U^{90+}**. *Nucl. Instrum. and Meth. Phys. B*, **9**:465–470, 1985. 44

[151] I. M. Savukov and W. R. Johnson. **Two-photon $E1M1$ decay of 2^3P_0 states in heavy heliumlike ions**. *Phys. Rev. A*, **66**(6):062507, 2002. 44

[152] E. Lötstedt and U. D. Jentschura. **Correlated two-photon emission by transitions of Dirac-Volkov states in intense laser fields: QED predictions**. *Phys. Rev. A*, **80**(5):053419, 2009. 44

[153] L. N. Labzowsky and A. V. Shonin. **QED theory of cascades and two-photon transitions and calculation of the $E1$-$M1$ transition probability in two-electron highly charged ions**. *Phys. Rev. A*, **69**(1):012503, 2004. 44, 45, 54, 66, 67

[154] U. D. Jentschura. **Non-uniform convergence of two-photon decay rates for excited atomic states**. *J. Phys. A: Math. Theor.*, **40**(9):F223, 2007. 44, 46, 85, 86

[155] U. D. Jentschura and A. Surzhykov. **Relativistic calculation of the two-photon decay rate of highly excited ionic states**. *Phys. Rev. A*, **77**(4):042507, 2008. 44, 46, 86

[156] O. Y. Andreev, L. N. Labzowsky, G. Plunien, and D. A. Solovyev. **QED theory of the spectral line profile and its applications to atoms and ions**. *Phys. Rep.*, **455**(4-6):135–246, 2008. 45

[157] R. P. Saxon and J. o. r. Eichler. **Theoretical calculation of two-photon absorption cross sections in atomic oxygen**. *Phys. Rev. A*, **34**(1):199, 1986. 51

[158] U. Czarnetzki, K. Miyazaki, T. Kajiwara, K. Muraoka, M. Maeda, and H. F. Döbele. **Comparison of various two-photon excitation schemes for laser-induced fluorescence spectroscopy in atomic hydrogen**. *J. Opt. Soc. Am. B*, **11**(11):2155–2162, 1994. 51

[159] B. R. Marx, J. Simons, and L. Allen. **The effect of laser linewidth on two-photon absorption rates**. *J. Phys. B*, **11**(8):L273, 1978. 51

[160] N. L. Manakov, A. V. Meremianin, A. Maquet, and J. P. J. Carney. **Photon-polarization effects and their angular dependence in relativistic two-photon bound-bound transitions**. *J. Phys. B*, **33**(20):4425, 2000. 52

[161] N. L. Manakov, A. V. Meremianin, and A. F. Starace. **Multipole expansions of irreducible tensor sets and some applications**. *J. Phys. B*, **35**(1):77, 2002. 52

[162] L. Labzowsky, D. Solovyev, G. Plunien, and G. Soff. **Two-photon $E1M1$ and $E1E2$ transitions between $2p$ and $1s$ levels in hydrogen**. *Eur. Phys. J. D*, **37**(3):335–343, 2006. 53, 54, 55

[163] W. H. Press, B. P. Flannery, S. A. Teukolsky, and W. T. Vetterling. *Numerical Recipes*. Cambridge University Press, Cambridge, 1986. 60, 129, 130, 136

[164] C. N. Yang. **On the Angular Distribution in Nuclear Reactions and Coincidence Measurements**. *Phys. Rev.*, **74**(7):764, 1948. 68

[165] A. N. Grum-Grzhimailo. **On the angular distributions in molecular photoionization beyond the dipole approximation**. *J. Phys. B*, **36**(12):2385, 2003. 68

[166] K. L. Reid. **Photonelectron angular distributions**. *Annu. Rev. Phys. Chem.*, **54**(1):397–424, 2003. 68

[167] S. H. Southworth, P. H. Kobrin, C. M. Truesdale, D. Lindle, S. Owaki, and D. A. Shirley. **Photoelectron and Auger electron asymmetries: Alignment of $Xe^{+2}D_{5/2}$ by photoionization**. *Phys. Rev. A*, **24**(4):2257, 1981. 68

[168] C. K. Au. **Effect of higher multipole transitions in the two-photon decay spectrum of metastable hydrogen**. *Phys. Rev. A*, **14**(1):531–533, 1976. 68

[169] J. H. Tung, A. Z. Tang, G. J. Salamo, and F. T. Chan. **2-Photon Absorption of Atomic-Hydrogen from 2 Light-Beams**. *J. Opt. Soc. Am. B*, **3**(6):837–848, 1986. 76, 87, 89

[170] V. Florescu, S. Patrascu, and O. Stoican. **Systematic study of $1s - ns$ and $1s - nd$ two-photon transitions of hydrogenlike atoms**. *Phys. Rev. A*, **36**(5):2155, 1987. 77

[171] A. Quattropani, F. Bassani, and S. Carillo. **Two-photon transitions to excited states in atomic hydrogen**. *Phys. Rev. A*, **25**:3079–3089, 1982. 77

[172] O. Gorceix, P. Indelicato, and J. P. Desclaux. **MCDF studies of two electron ions: I. Electron-electron interaction**. *J. Phys. B*, **20**:639–650, 1987. 77, 93

[173] J. D. Cresser, A. Z. Tang, G. J. Salamo, and F. T. Chan. **Lifetime of excited atomic states**. *Phys. Rev. A*, **33**(3):1677, 1986. 82, 95

[174] V. Florescu, I. Schneider, and I. N. Mihailescu. **Comment on "Lifetime of excited atomic states"**. *Phys. Rev. A*, **38**(4):2189, 1988. 82

[175] U. D. Jentschura, J. Evers, C. H. Keitel, and K. Pachucki. **A problematic set of two-loop self-energy corrections**. *New J. Phys.*, **4**:49, 2002. 82

[176] D. Solovyev, V. Dubrovich, A. V. Volotka, L. Labzowsky, and G. Plunien. **Two-photon decays of highly excited states in hydrogen**. *J. Phys. B*, **43**(17):175001, 2010. 85

[177] D. Solovyev and L. Labzowsky. **Two-photon approximation in the theory of electron recombination in hydrogen**. *Phys. Rev. A*, **81**(6):062509, 2010. 85

[178] D. Solovyev, V. Sharipov, L. Labzowsky, and G. Plunien. **Influence of external electric fields on multi-photon transitions between the $2s$, $2p$ and $1s$ levels for hydrogen and antihydrogen atoms and hydrogen-like ions**. *J. Phys. B*, **43**(7):074005, 2010. 85

[179] U. D. Jentschura. **Two-photon decays reexamined: cascade contributions and gauge invariance**. *J. Phys. A: Math. Theor.*, **41**(15):155307, 2008. 86

[180] Y. Gontier and M. Trahin. **On the Multiphoton Absorption in Atomic Hydrogen**. *Phys. Lett.*, **36A**(6):463–464, 1971. 87

[181] G. A. Bickel and G. A. McRae. **Determination of the 1s-2s two-photon excitation cross-section in atomic hydrogen**. *Spectrochim. Acta Part B*, **55**(1):57–63, 2000. 87, 88

[182] A. Antognini, F. D. Amaro, F. Biraben, J. M. R. Cardoso, C. A. N. Conde, D. S. Covita, A. Dax, S. Dhawan, L. M. P. Fernandes, and T. W. Hansch. **Powerful fast triggerable 6 [mu]m laser for the muonic hydrogen 2S-Lamb shift experiment**. *Opt. Commun.*, **253**(4-6):362, 2005. 88

[183] C. G. Parthey, A. Matveev, J. Alnis, R. Pohl, T. Udem, U. D. Jentschura, N. Kolachevsky, and T. W. Hänsch. **Precision Measurement of the Hydrogen-Deuterium $1S - 2S$ Isotope Shift**. *Phys. Rev. Lett.*, **104**(23):233001, 2010. 88

[184] J. P. Santos, P. Patte, F. Parente, and P. Indelicato. **Spontaneous relativistic two-photon decay rate mathematical expression in heliumlike systems**. *Eur. Phys. J. D*, **13**(1):27–31, 2001. 91, 92

[185] J. Chluba and R. A. Sunyaev. **Two-photon transitions in hydrogen and cosmological recombination**. *Astron. Astrophys.*, **480**:629, 2008. 95

[186] J. S. Borbely, M. C. George, L. D. Lombardi, M. Weel, D. W. Fitzakerley, and E. A. Hessels. **Separated oscillatory-field microwave measurement of the $2\,^3P_1$–$2\,^3P_2$ fine-structure interval of atomic helium**. *Phys. Rev. A*, **79**(6):060503, 2009. 101

[187] M. Smiciklas and D. Shiner. **Determination of the Fine Structure Constant Using Helium Fine Structure**. *Phys. Rev. Lett.*, **105**(12):123001, 2010. 101

[188] K. Pachucki and V. A. Yerokhin. **Fine Structure of Heliumlike Ions and Determination of the Fine Structure Constant**. *Phys. Rev. Lett.*, **104**(7):070403, 2010. 101

[189] R. Pohl, A. Antognini, F. Nez, F. D. Amaro, F. Biraben, J. a. o. M. R. Cardoso, D. S. Covita, A. Dax, S. Dhawan, L. M. P. Fernandes, A. Giesen, T. Graf, T. W. Hänsch, P. Indelicato, L. Julien, C.-Y. Kao, P. Knowles, E.-O. Le Bigot, Y.-W. Liu, J. e. A. M. Lopes, L. Ludhova, C. M. B. Monteiro, F. Mulhauser, T. Nebel, P. Rabinowitz, J. M. F. dos Santos, L. A. Schaller, K. Schuhmann, C. Schwob, D. Taqqu, J. F. C. A. Veloso, and F. Kottmann. **The size of the proton**. *Nature*, **466**(7303):213–216, 2010. 101

[190] C. Brandau, C. Kozhuharov, A. Müller, W. Shi, S. Schippers, T. Bartsch, S. Böhm, C. Böhme, A. Hoffknecht, H. Knopp, N. Grün, W. Scheid, T. Steih, F. Bosch, B. Franzke, P. H. Mokler, F. Nolden, M. Steck, T. Stöhlker, and Z. Stachura. **Precise Determination of the $2s_{1/2}$-$2p_{1/2}$ Splitting in Very Heavy Lithiumlike Ions Utilizing Dielectronic Recombination**. *Phys. Rev. Lett.*, **91**(7):073202, 2003. 101

[191] P. Beiersdorfer, H. Chen, D. B. Thorn, and E. Träbert. **Measurement of the Two-Loop Lamb Shift in Lithiumlike U^{89+}**. *Phys. Rev. Lett.*, **95**(23):233003–4, 2005. 101

[192] R. D. Thomas, N. C. David, and G. M. Edmund. **Improved Measurement of the $1s2s\ ^1S_0$-$1s2p\ ^3P_1$ Interval in Heliumlike Silicon**. *Phys. Rev. Lett.*, **100**(24):243001, 2008. 101

[193] M. Trassinelli, A. Kumar, H. F. Beyer, P. Indelicato, R. Märtin, R. Reuschl, Y. S. Kozhedub, C. Brandau, H. Bräuning, S. Geyer, A. Gumberidze, S. Hess, P. Jagodzinski, C. Kozhuharov, D. Liesen, U. Spillmann, S. Trotsenko, G. Weber, D. F. A. Winters, and T. Stöhlker. **Observation of the $2p_{3/2} \rightarrow 2s_{1/2}$ intra-shell transition in He-like uranium**. *Europhys. Lett.*, **87**(6):63001, 2009. 101

[194] A. Gumberidze, T. Stöhlker, D. Banaś, K. Beckert, P. Beller, H. F. Beyer, F. Bosch, S. Hagmann, C. Kozhuharov, D. Liesen, F. Nolden, X. Ma, P. H. Mokler, M. Steck, D. Sierpowski, and S. Tashenov. **Quantum Electrodynamics in Strong Electric Fields: The Ground-State Lamb Shift in Hydrogenlike Uranium**. *Phys. Rev. Lett.*, **94**(22):223001, 2005. 101

[195] G. Plunien, B. Müller, W. Greiner, and G. Soff. **Nuclear Polarization in Heavy Atoms and Superheavy Quasiatoms**. *Phys. Rev. A*, **43**(11):5853–5866, 1991. 101

[196] H. Bruhns, J. Braun, K. Kubiček, J. R. C. Lopez-Urrutia, and J. Ullrich. **Testing QED Screening and Two-Loop Contributions with He-Like Ions**. *Phys. Rev. Lett.*, **99**(11):113001, 2007. 101

[197] C. T. Chantler, D. Paterson, L. T. Hudson, F. G. Serpa, J. D. Gillaspy, and E. Takács. **Absolute measurement of the resonance lines in heliumlike vanadium on an electron-beam ion trap**. *Phys. Rev. A*, **62**(4):042501, 2000. 102

[198] D. F. Anagnostopoulos, D. Gotta, P. Indelicato, and L. M. Simons. **Low-Energy X-Ray Standards from Hydrogenlike Pionic Atoms**. *Phys. Rev. Lett.*, **91**(24):240801, 2003. 102, 105

[199] R. D. Deslattes, E. G. Kessler, P. Indelicato, L. de Billy, E. Lindroth, and J. Anton. **X-ray transition energies: new approach to a comprehensive evaluation**. *Rev. Mod. Phys.*, **75**(1):35–99, 2003. 102, 162

[200] W. C. Röntgen. **On a New Kind of Rays**. *Nature*, **53**:274–276, 1896. 102

[201] A. Sommerfeld. **Theoretisches ber die Beugung der Röntgenstrahlen**. *Physikalische Zeitschrift*, **2**:55–60, 1900. 103

[202] B. Peter. **History and progress in the accurate determination of the Avogadro constant**. *Rep. Prog. Phys.*, **64**(12):1945, 2001. 103

[203] M. v. Laue. **Interferenzen-Erscheinungen bei Röntgenstrablen**[1]. *Münchener sitzungsberichte*, **363**, 1912. 103

[204] M. Laue and F. Tank. **Die Gestalt der Interferenzpunkte bei den Röntgenstrahlinterferenzen**. *Ann. Phys.*, **346**(10):1003–1011, 1913. 103

[205] W. L. Bragg. **The Specular Reflection of X-rays**. *Nature*, **90**:410, 1912. 103

[206] W. H. Bragg and W. L. Bragg. *X-rays and crystal structure*. Bell, London, 1915. 103

[207] A. H. Compton and S. K. Allison. *X-Ray in Theory and Experiment*. Van Nostrand, New York, 1935. 103, 120

[208] A. H. Compton. **Reflection Coefficient of a Monochromatic X-rays from Rock Salt and Calcite**. In Physical Review, editor, *Minutes of the Washington Meeting*, **10**, page 95, 1917. 103

[209] B. Davis and W. M. Stempel. **An Experimental Study of the Reflection of X-Rays from Calcite**. *Phys. Rev.*, **17**(5):608, 1921. 103

[210] A. H. Compton. **A Precision X-ray Spectrometer and the Wavelength of Mo K alpha**. *Rev. Sci. Instrum.*, **2**(7):365–376, 1931. 103

[211] J. H. Williams and S. K. Allison. **Design of a Double X-ray Spectrometer**. *J. Opt. Soc. Am*, **18**:473–478, 1929. 103

[212] B. Davis and H. Purks. **Measurement of the Mo.K Doublet Distances by Means of the Double X-Ray Spectrometer**. *Proc. Natl. Acad. Sci.*, **13**(6), 1927. 103

[1] No URL found

[213] B. Davis and H. Purks. **Additional Lines in the K Series of Molybdenum and the Natural Breadth of Spectral Lines**. *Proc. Natl. Acad. Sci.*, **14**(2), 1928. 103

[214] M. M. Schwarzschild. **Theory of the Double X-Ray Spectrometer**. *Phys. Rev.*, **32**(2):162, 1928. 103

[215] J. A. Bearden and J. S. Thomsen. **The Double-Crystal X-ray Spectrometer: Corrections, Errors, and Alignment Procedure**. *J. Appl. Cryst.*, **4**:130, 1971. 103, 125, 137

[216] R. D. Deslattes. **Two-Crystal, Vacuum Monochromator**. *Rev. Sci. Instrum.*, **38**(5):616–620, 1967. 103, 106

[217] M. Hart and K. H. Lloyd. **Measurement of strain and lattice parameter in epitaxic layers**. *J. Appl. Cryst*, **8**:42–44, 1975. 103

[218] A. Fukuhara and Y. Takano. **Determination of strain distributions from X-ray Bragg reflexion by silicon single crystals**. *Acta Crystallogr. Sect. A*, **33**(1):137–142, 1977. 103

[219] K. Barla, R. Herino, G. Bomchil, J. C. Pfister, and A. Freund. **Determination of lattice parameter and elastic properties of porous silicon by X-ray diffraction**. *J. Cryst. Growth*, **68**(3):727–732, 1984. 103

[220] J. A. Bearden and A. Henins. **Precision Measurement of Lattice Imperfections with a Photographic Two-Crystal Method**. *Rev. Sci. Instrum.*, **36**:334, 1965. 103

[221] K. Godwod, R. Kowalczyk, and Z. Szmid. **Application of a precise double X-ray spectrometer for accurate lattice parameter determination**. *Phys. Stat. Sol. A*, **21**(1):227–234, 1974. 103

[222] A. Okazaki and M. Kawaminami. **Accurate Measurement of Lattice Constants in a Wide Range of Temperature: Use of White X-Rays and Double-Crystal Diffractometry**. *Jpn. J. Appl. Phys.*, **12**:783, 1972. 103

[223] E. G. Kessler, G. L. Greene, M. S. Dewey, R. D. Deslattes, H. Borner, and F. Hoyler. **High accuracy, absolute wavelength determination of capture gamma-ray energies for $E \leq 5$ MeV and the direct determination of binding energies in light nuclei**. *J. Phys. G: Nucl. Phys.*, **14**(S):S167, 1988. 103

[224] M. S. Dewey, E. G. Kessler, G. L. Greene, R. D. Deslattes, F. Sacchetti, C. Petrillo, A. Freund, H. G. Börner, S. Robinson, and P. Schillebeecks. **Structure factors in germanium at 0.342 and 1.382 MeV**. *Phys. Rev. B*, **50**(5):2800, 1994. 103

[225] T. Mooney, E. Lindroth, P. Indelicato, E. Kessler, and R. D. Deslattes. **Precision measurements of K and L transitions in xenon: Experiment and Theory for the K, L and M levels**. *Phys. Rev. A*, **45**(3):1531–1543, 1992. 103, 125

[226] M. Ohno and R. E. LaVilla. **Xenon L emission spectra and many-electron effects in core levels**. *Phys. Rev. A*, **45**(7):4713, 1992. 103

[227] D. D. Dietrich, A. Simionovici, M. H. Chen, G. Chandler, C. J. Hailey, P. O. Egan, P. H. Mokler, S. Reusch, and D. H. H. Hoffmann. **Beam-foil spectroscopy of $n = 3$ to $n = 2$ transitions in highly stripped bismuth**. *Phys. Rev. A*, **41**(3):1450, 1990. 103

[228] Z. Liu, S. Sugata, K. Yuge, M. Nagasono, K. Tanaka, and J. Kawai. **Correlation between chemical shift of Si K alpha lines and the effective charge on the Si atom and its application in the Fe-Si binary system**. *Phys. Rev. B*, **69**(3):035106, 2004. 103

[229] T. Tochio, Y. Ito, and K. Omote. **Broadening of the x-ray emission line due to the instrumental function of the double-crystal spectrometer**. *Phys. Rev. A*, **65**(4):042502 (6), 2002. 103

[230] U. Bonse and M. Hart. **An X-ray Interferometer**. *Appl. Phys. Lett.*, **6**(8):155, 1965. 104

[231] M. Hart. **An ångström ruler**. *J. Phys. D*, **1**(11):1405, 1968. 104

[232] R. D. Deslattes and A. Henins. **X-Ray to Visible Wavelength Ratios**. *Phys. Rev. Lett.*, **31**(16):972–975, 1973. 104

[233] P. Becker, K. Dorenwendt, G. Ebeling, R. Lauer, W. Lucas, R. Probst, H.-J. Rademacher, G. Reim, P. Seyfried, and H. Siegert. **Absolute Measurement of the (220) Lattice Plane Spacing in a Silicon Crystal**. *Phys. Rev. Lett.*, **46**(23):1540–1543, 1981. 104

[234] E. Massa, G. Mana, U. Kuetgens, and L. Ferroglio. **Measurement of the lattice parameter of a silicon crystal**. *New J. Phys.*, **11**(5):053013, 2009. 104

[235] R. Geller. *Electron Cyclotron Resonance Ion Sources and ECR Plasmas*. Institute of Physics, Bristol, 1996. 105

[236] D. F. Anagnostopoulos, S. Biri, D. Gotta, A. Gruber, P. Indelicato, B. Leoni, H. Fuhrmann, L. M. Simons, L. Stingelin, A. Wasser, and J. Zmeskal. **On the characterisation of a Bragg spectrometer with X-rays from an ECR source**. *Nucl. Instr. and Meth. Phys. A*, **545**:217, 2005. 105

[237] A. Gumberidze, M. Trassinelli, N. Adrouche, C. I. Szabo, P. Indelicato, F. Haranger, J. M. Isac, E. Lamour, E. O. Le Bigot, J. Merot, C. Prigent, J. P. Rozet, and D. Vernhet. **Electronic temperatures, densities, and plasma x-ray emission of a 14.5 GHz electron-cyclotron resonance ion source**. *Rev. Sci. Instrum.*, **81**(3):033303–10, 2010. 105, 106, 120

[238] C. Bieth, J. L. Bouly, J. C. Curdy, S. Kantas, P. Sortais, P. Sole, and J. L. Vieux-Rochaz. **Electron cyclotron resonance ion source for high currents of mono- and multicharged ion and general purpose unlimited lifetime application on implantation devices**. *Rev. Sci. Instrum.*, **71**(2):899–901, 2000. 106

[239] A. Gumberidze, D. Attia, C. I. Szabo, P. Indelicato, A. Vallette, and S. Carmo. **Trapping of highly charged ions with an electrostatic ion trap**. *J. Phys.: Conf. Ser.*, **163**(1):012110, 2009. 106

[240] I. H. Hutchinson. *Principles of Plasma Diagnostics*. Cambridge University Press, Cambridge, 1987. 106

[241] S. Schlesser. *Spectroscopie X d'ions très chargés et niveaux d'énergie de l'hydrogène pionique*. PhD thesis, Université Pierre et Marie Curie (Paris VI), 2009. 108, 109

[242] E. G. Kessler, A. Henins, R. D. Deslattes, L. Nielsen, and M. Arif. **Precision comparison of the lattice parameters of silicon monocrystals**. *J. Res. Natl. Inst. Stand. Technol.*, **99**(1), 1994. 109

[243] C. G. Darwin. **XXXIV. The theory of X-ray reflexion**. *Phil. Mug.*, **27**(158):315–333, 1914. 113, 115

[244] P. P. Ewald. **Zur Begründung der Kristalloptik**. *Ann. Phys.*, **359**(23):519–556, 1917. 113

[245] J. A. Prins. **Die Reflexion von Röntgenstrahlen an absorbierenden idealen Kristallen**. *Z. Phys. A*, **63**(7):477–493, 1930. 113

[246] M. Laue. **Die dynamische Theorie der Röntgenstrahlinterferenzen in neuer Form**. *Ergebn. Exakten Naturwiss.*, **10**:133–158, 1931. 114

[247] W. H. Zachariasen. *Theory of X-ray diffraction in crystals*. Dover Publications, New York, 1967. 114, 126

[248] R. J. Dejus and M. S. d. Rio. **XOP: A graphical user interface for spectral calculations and xray optics utilities**. *Rev. Sci. Instrum.*, **67**, 1996. 115, 132

[249] A. M. Afanas'ev, R. M. Imamov, and E. K. Mukhmedzhanov. **Asymmetric X-Ray Diffraction**. *Crystallogr. Rev.*, **3**(2):157–226, 1992. 116

[250] S. K. Allison and J. H. Williams. **Experiments on the Reported Fine Structure and the Wave-Length Separation of the K beta Doublet in the Molybdenum X-Ray Spectrum**. *Phys. Rev.*, **35**(2):149, 1930. 117

[251] L. V. Azároff. *X-ray Spectroscopy*. McGraw-Hill, New York, 1974. 122

[252] R. Bracewell. *The Fourier Transform & Its Applications*. McGraw-Hill, New York:, 2000. 124

[253] J.-S. Lee. **Monte Carlo Simulation of Voigt Distribution in Photon Diffusion Problems**. *Astrophys. J., Suppl. Ser.*, **187**, 1974. 131

[254] J. J. Olivero and R. L. Longbothum. **Empirical fits to the Voigt line width: A brief review**. *J. Quant. Spectrosc. Radiat. Transfer*, **17**(2):233–236, 1977. 131

[255] Y. Okada and Y. Tokumaru. **Precise determination of lattice parameter and thermal expansion coefficient of silicon between 300 and 1500 K**. *J. Appl. Phys.*, **56**(2):314–320, 1984. 132

[256] P. R. Bevington and D. K. Robinson. *Data Reduction and Error Analysis for the Physical Sciences*. McGraw-Hill, New York, 2003. 136

[257] P. Indelicato and *et.al.*. **To be publish**. 137, 161, 164

[258] P. Indelicato. *Contribution à l'étude expérimentale et théorique des ions lourds à un et deux électrons*[1]. PhD thesis, Université Pierre et Marie Curie (Paris VI), 1987. 137

[259] M. C. Martins, A. M. Costa, J. P. Santos, P. Indelicato, and F. Parente. **Interpretation of X-ray spectra emitted by Ar ions in an ECR ion source**. *J. Phys. B*, **34**(4):533–543, 2001. 153

[260] G. Douysset, H. Khodja, A. Girard, and J. P. Briand. **Highly charged ion densities and ion confinement properties in an electron-cyclotron-resonance ion source**. *Phys. Rev. E*, **61**(3):3015–3022, 2000. 153

[261] P. Indelicato, S. Boucard, D. S. Covita, D. Gotta, A. Gruber, A. Hirtl, H. Fuhrmann, E. O. Le Bigot, S. Schlesser, J. M. F. dos Santos, L. M. Simons, L. Stingelin, M. Trassinelli, J. Veloso, A. Wasser, and J. Zmeskal. **Highly charged ion X-rays from Electron-Cyclotron Resonance Ion Sources**. *Nucl. Instrum. and Meth. Phys. A*, **580**(1):8–13, 2007. 153

[262] G. W. F. Drake. **High precision variational calculations for the $1s^2\ ^1$S state of H^- and the $1s^2\ ^1$S, $1s2s\ ^1$S and $1s2s\ ^3$S states of helium**. *Nucl. Instr. and Meth. in Phys. Res. B*, **31**(1-2):7–13, 1988. 164

[263] P. Indelicato, O. Gorceix, and J. P. Desclaux. **Multiconfigurational Dirac-Fock studies of two electron ions: II. Radiative corrections and comparison with experiment.** *J. Phys. B*, **20**:651, 1987. 164

[264] C. Kittel. *Introduction to Solid State Physics*. John Wiley & Sons, New York, 2004. 190

[1] No URL found

[265] H. MICHELS. **Data Plotting Software DISLIN**, 2011. 200

Appendix A

Crystal Structure

A material named crystal belongs to a class of solids with certain distinct characteristic properties. Such properties includes the fact of having a cleavage along certain planes with a impact, or producing X-ray diffraction patterns. This is a direct consequence of the atomic or moleculer periodicity in the material. This can be observed in Fig. A.1, where is represented the internal structure of an ideal crystal with only one type of atom with four bounds. This is a typical structure of the fourteen group elements, such as carbon (C), silicon (Si), and germanium (Ge), which have four valence electrons. In the case of carbon, the crystal structure in Fig. A.1 corresponds to a crystal of diamond. Due to its periodic internal structure, a crystal is refereed as an homogeneous and an anisotropic material. The homogeneity of the crystal means that the observed physical properties do not depend on the chosen solid volume. A crystal is not an isotropic material since its physical properties depends on certain directions. Such properties includes thermal expansion, dielectric constant or thermal and electric conductivities. Crystals are formed from the molted or vapor state or from solutions. When formed in an unconfined space under right conditions of growth, they usually are bounded by plane surfaces, which are called crystal faces.

Due to its internal periodic structure, it is convenient to define a unit cell. A unit cell consist of a box containing one or more atoms or molecules which defines the minimal structure that is repeated by translation along the crystal. For the diamond-like structure illustrated in Fig. A.1, the unit cell is showed in Fig. A.2. On that unit cell, each atom is connected to the other four atoms in a tetrahedral geometry that is showed in green in Fig. A.2. The edge of the unit cell is defined as the lattice parameter, a. The crystal structure showed in Fig. A.1 is obtained from multiple translations of the unit cell in Fig. A.2. In terms of Bravais classification, this unit cell is a diamond face centered cubic unit cell (fcc) with four atoms at the center of the tetrahedrons defined by the center face and corner atoms. Other types of unit cells associated with other crystal structures, like simple cubic or body centered cubic, as well as, a description of crystallography, can be found in the textbook of Kittel

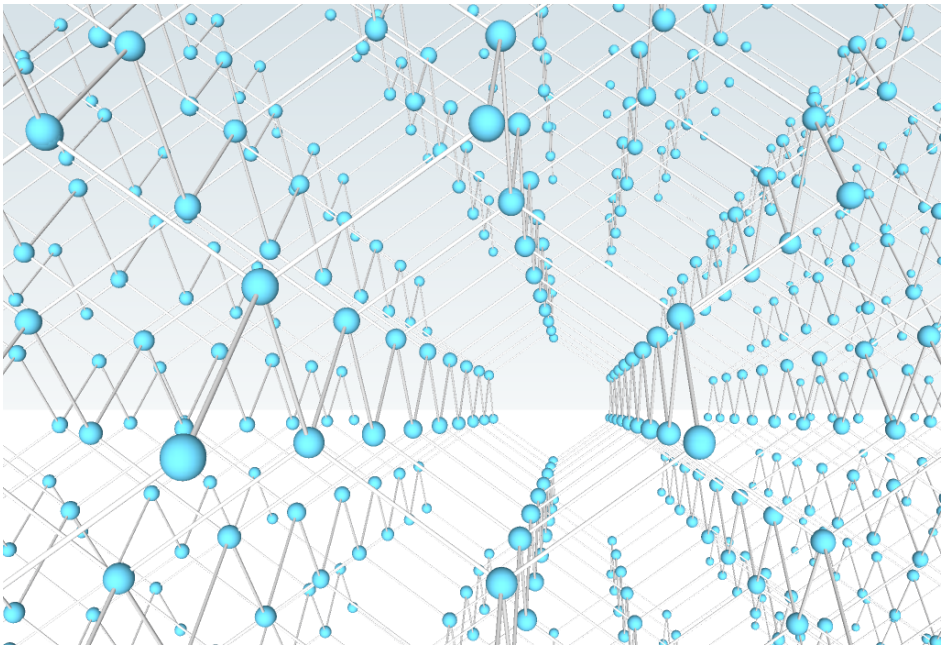

Figure A.1: Crystal internal structure - The atoms or molecules in a crystal are arranged in space as a periodic order. In this case, the atoms of the crystal are only of one type of element that belong to the fourteen group. This crystal can be diamond-like C or a mono-crystal of Si or Ge.

[264]. Along with the unit cell, the atomic planes in the crystal structure are described by a three-value Miller index notation (hkl). By definition, (hkl) denotes a plane that intercepts the unit cell at three points, ma/h, ma/k, and ma/l, where m is a positive integer constant. In Fig. A.3 are showed the (111) planes in green and the (220) planes in brown. Not all the Miller indices are allowed in a given crystal structure. The selection rules for a given crystal structure can be found in Ref. [264]. For a diamond face centered cubic unit cell, the allowed Miller indices follows the condition: (all odd) $\vee$ (all even $\wedge h + k + l = 4n$), where n is a integer. Examples of allowed Miller indices are (111), (220), (333) and (444).

Since the plane intercepts the unit cell at a/h, a/k and a/l, a vector $\boldsymbol{B_{hkl}}$ perpendicular to the plane will also be perpendicular to the vectors defined by $\hat{\boldsymbol{y}}a/k - \hat{\boldsymbol{x}}a/h$ and $\hat{\boldsymbol{z}}a/l - \hat{\boldsymbol{y}}a/k$, and hence, it is parallel to their vector product, which is

$$\boldsymbol{B_{hkl}} = \frac{a^2}{hkl}(h\hat{\boldsymbol{x}} + k\hat{\boldsymbol{y}} + l\hat{\boldsymbol{z}}) = \frac{a^3}{hkl}\bar{\boldsymbol{B}}_{\boldsymbol{hkl}} \,. \tag{A.1}$$

Since there is a plane between the points ma/h and $(m+1)a/h$, the inter-planar distance between two near planes will be the projection of the line defined by those points along the direction given by the vector of Eq. (A.1). The result is given by

$$d_{hkl} = \frac{1}{\left|\bar{\boldsymbol{B}}_{\boldsymbol{hkl}}\right|} = \frac{a}{\sqrt{h^2 + k^2 + l^2}} \,. \tag{A.2}$$

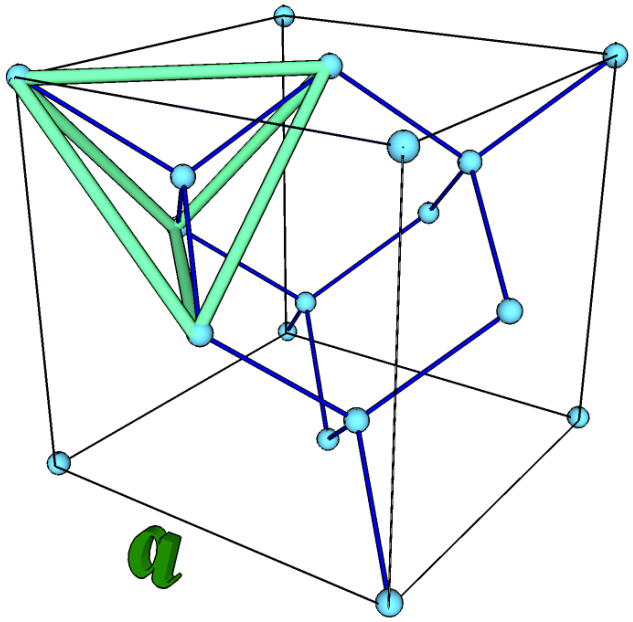

Figure A.2: Unit cell diamond cubic structure - The unit cell consists of an atom on each corner and at each face center (fcc Bravais lattice). A tetrahedral in green is formed with an atom at the corner along with nearest atoms at the faces. At the center of the tetrahedral is located an additional atom. a is the lattice parameter.

With the use of the vector defined by Eq. (A.1), it is possible to obtain an elementary formulation of the diffraction pattern. A plane wave of monochromatic electromagnetic radiation incident upon the grating will be scattered in all directions. Due to the crystal periodic structure, the maximum diffraction occur in directions that originates path differences equal to an integer number of wavelengths. This lead to the grading equation

$$\boldsymbol{k_r} - \boldsymbol{k_0} = 2\pi n \bar{\boldsymbol{B}}_{hkl} \,, \tag{A.3}$$

where n is an integer associated with the integer number of wavelengths, and $k_{r,0} = 2\pi/\lambda$ are the scattered (r) and incident wave (0) wavenumbers. As an example, Eq. (A.3) can be applied to the simple net presented in Fig. A.4 where shows, with the use of Eq. (A.2), that the Bragg equation (6.1) and Eq. (A.3) are equivalent equations.

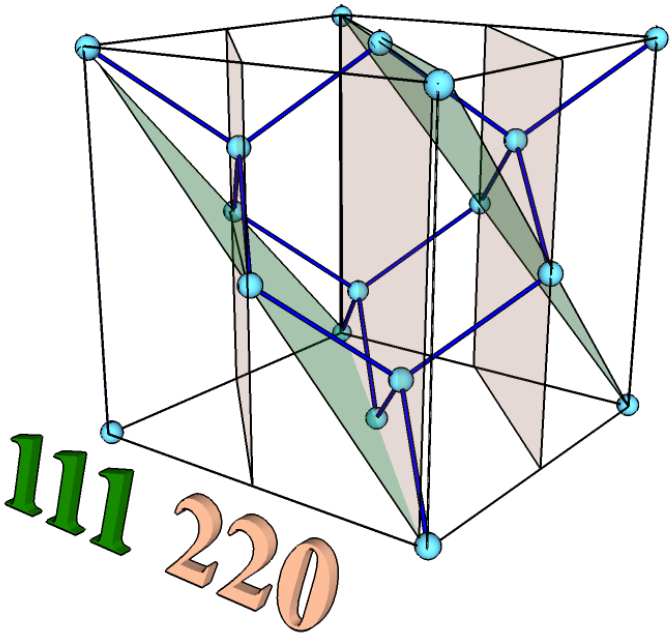

Figure A.3: Miller planes - The plane (111) is represented in green while the plane (220) is in brown.

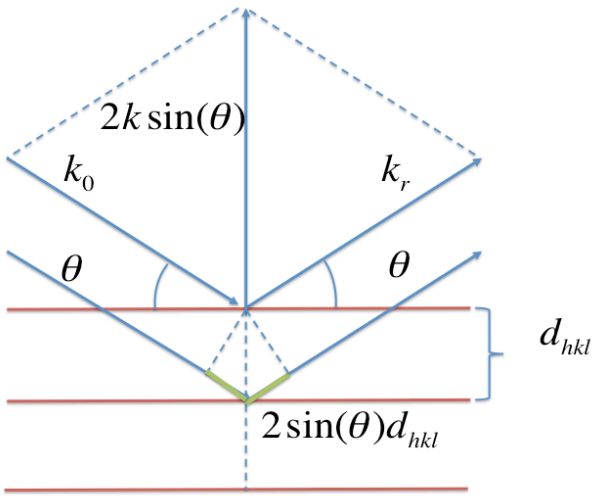

Figure A.4: 2d simple representation of a crystal structure - The wavenumber vector difference is $2k\sin(\theta)$. The condition of maximum diffraction, Eq. (A.3), sets $2k\sin(\theta)$ equal to $2\pi n\left|\bar{\boldsymbol{B}}_{\boldsymbol{hkl}}\right|$, which is equivalent to Bragg equation (6.1) or the path difference in green being equal to an integer number of wavelengths.

Appendix B

Simulation Input and Output Data

B.1 Input Data

The data needed for the simulation code is provided by two files and one widget. The first file contains the reflectivity (obtained from XOP), while the second one contains the values of the several input variables necessary for the simulation. The reflectivity file, "*Plot_crystall_responce_600_600.txt*", consists of two columns with values associated to the angle $\alpha - \theta_B$ in μrads and the reflectivity (no units). An example of these values is ploted in Fig. 7.2. The variables used in the simulation are in the input file "*DCrystal_input.input*". In the beginning of the simulation, the program reads the input files and prompts a confirmation widget (Fig. B.1), where the user can confirm or change some input values. A list of the input variables are given bellow, following the order of the input file.

***mode_bragg_geo* (Boolean)–** The double crystal can be used in both Laue (F) or Bragg modes (T) (see Fig. 7.1). The case of the Bragg mode has more variables options and more debug effort.

***imh, imk, iml* (Integers)–** Miller indices (*hkl*) as in Eq. (A.1).

***crystal_Si* (Boolean)–** Option for using a Si crystal (T) or a Ge one (F). In case of this variable being true, the lattice parameter a in Eq. (A.2) is set so that the d_{220} is equal to the measured value. Otherwise, is set for the lattice parameter of Ge obtained from XOP, a = 5.65735 Å.

***see_para* (Boolean)–** A parallel spectrum is simulated in case of a true option (V). Otherwise (F), the output file for the parallel spectrum has zero counts.

***see_anti* (Boolean)–** Same as *see_para*, but for the antiparallel spectrum.

***Make_Vertical* (Boolean)–** Option that considers all rays moving in horizontal planes (F) or starting with a random angle (T) towards the horizontal plane. For the false option, the variable ϕ in Eq.

(7.35) has a zero value (F). Otherwise (V), a ray start with a random number (region defined by the geometry $U[\phi_{\min}, \phi_{\max}]$). This variable is used for debug purposes and should be true.

***Make_Horizontal* (Boolean)–** Same as *Make_Vertical*, but for the vertical plane. ϑ can have value 0 (F) or a random number (T). Used for debug purposes and should be true.

***angle_aprox* (Integer: 0, 1, 2)–** Several approximations are considered for both first and second crystals glancing angles, $\alpha_1(\vartheta, \phi, \delta_1)$ and $\alpha_2^{\pm}\left(\vartheta, \phi, \beta, \delta_1, \delta_2^{\pm}\right)$. For a complete simulation, this variable have a value of zero (no approximation as in Eq. (7.38)), and other values are only considered for debug purposes. A value of two is for the approximations Eqs. (7.17) and (7.20), while a value of one is for a second order approximation in ϕ at Eq. (7.38).

***fitting* (Boolean)–** This option considers a fit of the simulated spectrums with a Voigt function (Sec. 7.4.2). The spectrums are fitted with Voigt functions using the Levenberg-Marquard method. This option is automatically false if *see_para* or *see_anti* are false.

***TrueVoigt* (Boolean)–** Option that consider the case of a true Voigt function (Sec. 7.4.2) (T) or a pseudo-Voigt as the fit function (F). The pseudo-Voigt function consists of a linear combination of a Lorentzian (Eq. (7.42)) and a Gaussian (Eq. (7.44)). This option is used for debug purposes and should be true.

***Simple_simu* (Boolean)–** This option considers a simple (T) or a complete (F) simulation. In a simple simulation, the position of the table is not considered, neither, the ray position at the crystal surface, where it ray is reflected. This option also sets *angle_aprox* equal to zero in case of false. This option is for debug purposes and should be false. For a complete simulation all variables are considered. Otherwise, only some variables are taking into account in the simulation.

***center_1crys* (Boolean)–** In case of this option being true, the X-ray spot is vertically centered at the first crystal. The vertical orientation of the tube that connects the source to the spectrometer (between point 17) and 20) of Fig. 6.4), is automatically made for that purpose through the variable *S_shi_ver_A* (details further on).

***center_2crys* (Boolean)–** Same as *center_1crys* for the second crystal. The first crystal vertical tilt, δ_1 (*tilt_C1*), is changed automatically for that purpose.

***mask_C1* (Integer: 0, 1, 2)–** Option that considers a vertical mask in the first crystal. The option zero is for the case without mask, one is for a mask covering the lower part and two is for the upper part.

***mask_C2* (Integer: 0, 1, 2)–** Same as *mask_C1*, but for the second crystal.

***print_scan* (Boolean)–** Graphical option for exporting images of the rocking curve (T) in "pdf" format, , such as the one in Fig. B.2.

center_Mask **(Boolean)–** Option that considers a center mask on first crystal (T). This mask consist of a rectangular window that restricts the rays at the center of the crystal. The width is the same as the first crystal width, however, the height is twelve mm which is the same as the tube between point 17) and 20) of Fig. 6.4.

make_mask_test **(Boolean)–** Option to repeat the calculation for several values of mask_C2 and store the output data.

type_source **(Char: U, P, G)–** Type of the source used in simulation. "U" is for an uniform source, "P" for a point source and "G" is for a Gaussian source distribution. This option is for debug purposes and should be "U".

LT_aper **(Real)–** Length (cm) of the long tube defined between point 17) and 20) of Fig. 6.4.

dist_T_Cr1 **(Real)–** Distance (cm) from point 17) of Fig. 6.4 to the first crystal.

dist_Cr1_Cr2 **(Real)–** Distance (cm) between the two crystals.

dist_Cr2_Det **(Real)–** Distance (cm) between second crystal and detector.

S_aper **(Real)–** Diameter (cm) of the tube in point 17) of Fig. 6.4.

S_aper_var **(Real)–** In case of a Gaussian source distribution (*type_source* with "G"), this is the σ of the distribution (cm).

S_sour **(Real)–** Diameter (cm) of the X-ray emission region.

S_shi_hor_B **(Real)–** Horizontal Shift (cm) of the long tube at the point 20) of Fig. 6.4.

S_shi_hor_A **(Real)–** Horizontal Shift (cm) of the long tube at the point 17) of Fig. 6.4.

S_shi_ver_B **(Real)–** Vertical Shift (cm) of the long tube at the point 20) of Fig. 6.4.

S_shi_ver_A **(Real)–** Vertical Shift (cm) of the long tube at the point 17) of Fig. 6.4. In case of *center_1crys* being true, this value is ignored.

y_first_crys **(Real)–** Length (cm) of the first and second crystals. The crystals were considered with the same dimensions.

z_first_crys **(Real)–** Height (cm) of the first and second crystals.

ydetc **(Real)–** Length (cm) of the detector.

zdetc **(Real)–** Height (cm) of the detector.

shift_det_ver **(Real)–** Vertical shift (cm) of the detector with respect to the central line.

Exp_crys1 **(Real)–** First crystal angle (°). In case of a complete simulation (*Simple_simu* is false), this angle is the first crystal angle, as if it was measured in the experiment with the zero reference (θ_F at point 3 of Sec. 6.2.3). Otherwise, is $90 - \theta_C$ with θ_C defined as in Figure 7.3.

teta_table **(Real)–** Angle of the table θ_T (°) as defined at point 3 of Sec. 6.2.3.

OffsetRotCry1 **(Real)–** Offset angle (°) for the first crystal difference from the zero position (crystal surface perpendicular to the optical axis).

teta_detec_para **(Real)–** Angle of the detector in parallel position (°).

teta_detec_anti **(Real)–** Angle of the detector in antiparallel position (°).

tilt_C1 **(Real)–** First crystal vertical tilt, δ_1 (°). In case of *center_2crys* or *make_CurveTilt* being true, this value is ignored.

tilt_C2 **(Real)–** Second crystal vertical tilt, δ_2 (°). In case of *make_CurveTilt* being true, this value is ignored.

xsi **(Real)–** Vertical misalignment (°) ξ in Eqs. (7.28) and (7.34). It is only considered if *Simple_simu* is true.

center_1cry_at **(Real)–** If *center_1crys* is true, this variable is the position of the X-ray spot at the first crystal.

center_2cry_at **(Real)–** Same as *center_1cry_at*, but for the second crystal.

make_CurveTilt **(Boolean)–** This option takes account an experimental measured tilt in the axis of the crystals (T). In case of this variable being true, the values of *tilt_C1* and *tilt_C2* are replaced by the ones obtained from Eq. (7.9). This variable has priority over *center_1crys* for defining the value of *tilt_C1*.

phas_tilt1 **(Real)–** Parameter θ_{phase} of Eq. (7.9) for the first crystal.

phas_tilt2 **(Real)–** Parameter θ_{phase} of Eq. (7.9) for the second crystal.

offsettilt1 **(Real)–** Parameter δ_{axis} of Eq. (7.9) for the first crystal.

offsettilt2 **(Real)–** Parameter δ_{axis} of Eq. (7.9) for the second crystal.

consttilt1 **(Real)–** Parameter δ_{offset} of Eq. (7.9) for the first crystal.

consttilt2 **(Real)–** Parameter δ_{offset} of Eq. (7.9) for the second crystal.

MakeDislin **(Boolean)–** In case of this option being false, disables any graphical output, except the confirmation widget.

make_graph_profile **(Boolean)–** Display a graphical output of the rocking curves (Fig. B.2).

make_image_plates **(Boolean)–** Display an image-plate of various points of the spectrometer, such as the entrance, the first and second crystal, or the detector at the graphical output (Fig. B.2).

make_imageC1_After_refle **(Boolean)–** The image plate of the rays at the first crystal can be before (F) or after (V) the reflection.

make_imageC2_After_refle **(Boolean)–** Same as *make_imageC1_After_refle*, but for the second crystal.

delta_angl **(Real)–** Plot range of β for both parallel and antiparallel rocking curves.

shift_disp_window **(Real)–** Shift of the plot range. If is equal to zero, the parallel peak is centered in the plot.

nubins **(Integer)–** Number of bins used to plot the rocking curves.

nbeams **(Integer)–** Number of rays that enters the spectrometer for a given position of the rocking curve β.

Unit_energy **(Char: "eV", "A")–** Units used for quantifying the variables. "eV" is for eV, while "A" is for Angstroms.

linelamda **(Real)–** Energy of the transition that by decay emits a x-ray.

naturalwidth **(Real)–** FWHM of the Lorentzian associated with the natural width of the decay (Γ_1 in Eq. (7.42)).

T_crystal_1_para **(Real)–** Temperature of the first crystal at the parallel setting (C°).

T_crystal_1_anti **(Real)–** Temperature of the first crystal at the antiparallel setting (C°).

T_crystal_2_para **(Real)–** Temperature of the second crystal at the parallel setting (C°).

T_crystal_2_anti **(Real)–** Temperature of the second crystal at the antiparallel setting (C°).

gauss_Doop **(Real)–** FWHM of the Gaussian associated with the natural width of the decay (Eq. (7.46)). σ is related with the FWHM according to Eq. (7.46).

make_more_lines **(Boolean)–** Option that considers more than one transition at the wavelength profile. In case of this variable being true, the variables *linelamda* and *naturalwidth* that describes a single emission, are not considered and the next variables that describes four emissions are taken into account.

linelamda(i) **(Real)–** Energy of the *i* transition that by electron decay emits a X-ray.

naturalwidth(i) **(Real)–** FWHM of the Lorentzian associated with the natural width of the *i* decay (Γ_i in Eq. (7.42)).

p(i)_ener **(Real)–** Probability of the photon being from the *i* decay. *p(4)_ener* is set so that the sum of the four probabilities is one.

Do_background **(Boolean)–** An uniform distribution is added to the wavelength distribution (V). For efficiency purposes this option should be false. Only considered for the debug process.

Curve_crystall **(Boolean)–** This option (V) considers a bended crystal according to Sec. 7.5.5.

R_cur_crys_1 **(Real)–** Value of curvature radii, R_1^C, for the first crystal (cm).

R_cur_crys_2 **(Real)–** Value of curvature radii, R_2^C, for the second crystal (cm).

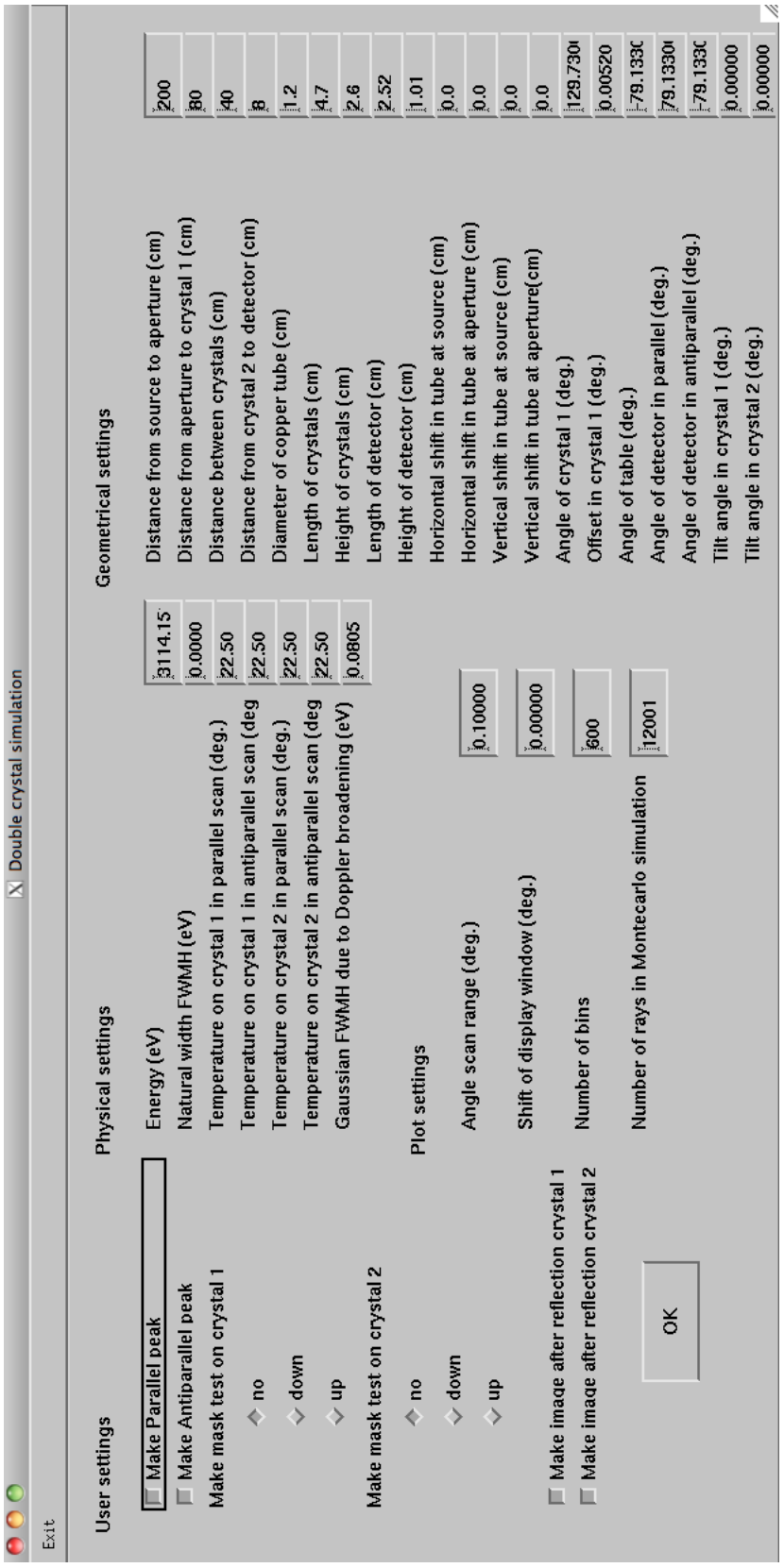

Figure B.1: Simulation graphical input - In this widget, some variables used in simulation are listed and could be changed. The initial values of the widget are read from the input file.

B.2 Output Data

The simulation output consists of three files, a graphical output and additional information in the console terminal. The information in the terminal consists of the approximate positions given by Eqs. (7.28) and (7.34). This information is useful for the user if he/she does not know where the parallel and antiparallel peaks are located. If the plot range of the rocking curves are chosen so that the plots do not include the peaks, then the simulation reduces the number of rays to reduce the computation time in order to visualize the images at the crystals. Then, the user can use this information to choose a better plot range. The simulation can run without the graphical output. This option is indicated for huge numbers of rays (10^8). In case this option is considered, a graphical output window that is represented in Fig. B.2 is prompted. In Fig. B.2, is represented a snapshot of the simulation with the second crystal angle at half of rocking curve. There are only rays at the upper half of the detector due to the use of a lower mask in the second crystal. All the graphical displays were included in the simulation program using the Fortran 90/95 interface code DISLIN [265]. Two files, "*Histogram_antiparallel.txt*" and "*Histogram_parallel.txt*", contain the simulated parallel and antiparallel rocking curves, i.e., a number of counts in function of the second crystal rotation. The file "*general_output.txt*" contains a repetition of the input variables and the result of a fitting process. In this process, the rocking curves are fitted using Voigt functions (Sec. 7.4.2) and the output parameters are printed in that file.

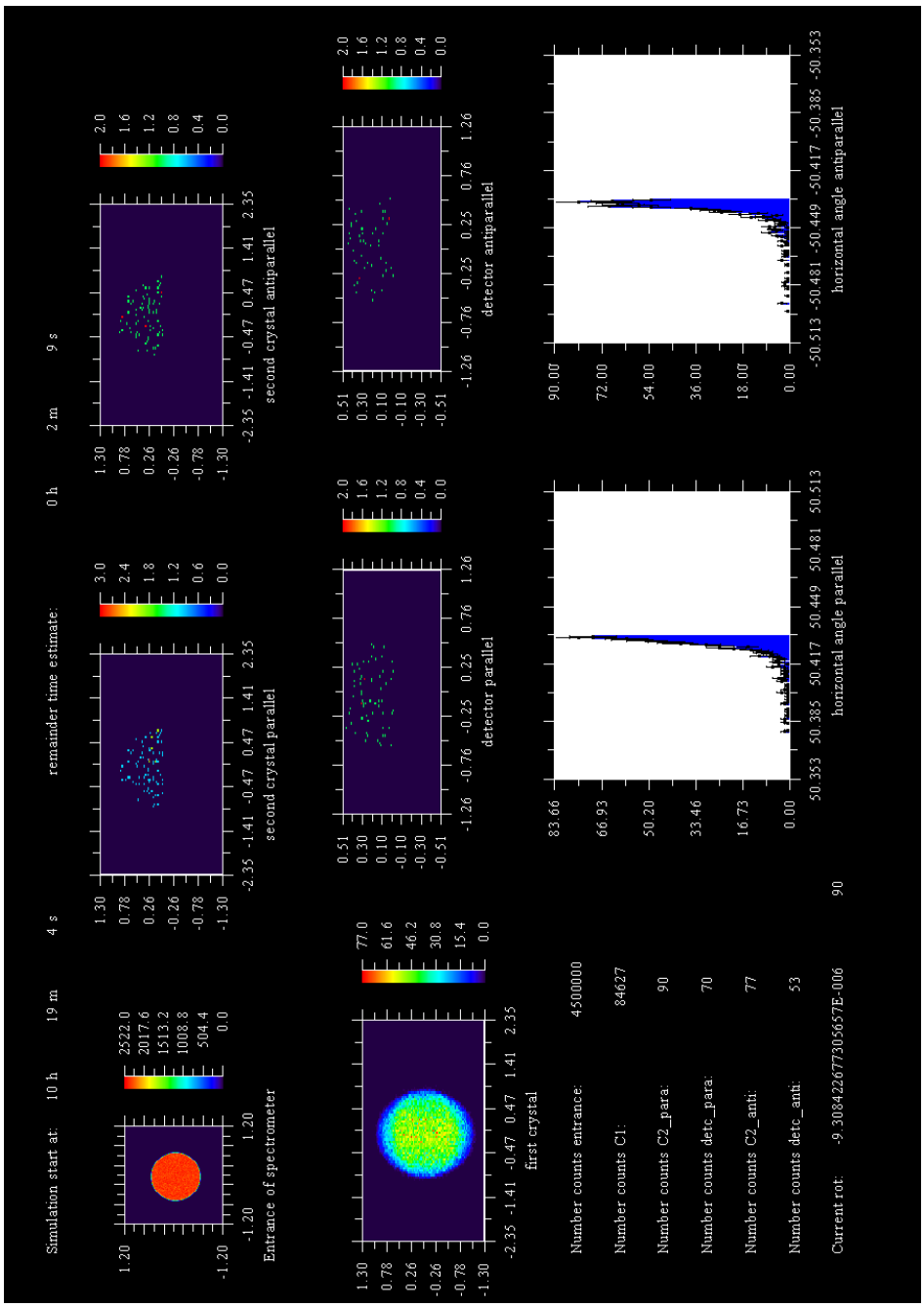

Figure B.2: Simulation graphical output - On the top (image rotated clockwise), is indicated the time when the simulation stars and an estimative of the necessary time to finish. At the "entrance of spectrometer" window (below the starting time), is showed graphically the number of rays passing at the point 17 of Fig. 6.4. At the "first crystal", is the number of incident or reflected (user option) rays. The "second crystal parallel" and "second crystal parallel" windows shows the number of incident or reflected rays at the second crystal being at parallel or antiparallel settings, for an angle of the rocking curve. Moreover, the number of rays that reaches the detector for an angle of the rocking curve is given at the "detector parallel" and "detector antiparallel" windows. At the bottom left is the total ray number that had passed the spectrometer and the first crystal. The next lines are addressed for the ray number that passes the second crystal and detector in parallel/antiparallel setting for a given value of the rocking curve β. The value of β, is given by "current rot". At the bottom right is the simulated rocking curves for parallel and antiparallel settings.